



Max-Planck-Institut  
für Polymerforschung

Max Planck Institute  
for Polymer Research



JOHANNES GUTENBERG  
UNIVERSITÄT MAINZ

# **Small Molecule Organic Semiconductors as Efficient Visible Light-active Photocatalysts**

## **Dissertation**

Zur Erlangung des Grades  
„Doktor der Naturwissenschaften“  
im Promotionsfach Chemie

dem Fachbereich Chemie, Pharmazie und Geowissenschaften  
der Johannes Gutenberg-Universität Mainz

**Lei Wang**

Geboren in Yining, China

Mainz, July 2017



Dekan:

1. Gutachter:

2. Gutachter:

Tag der mündlichen Prüfung: 25-09-2017

## **Affidavit**

I hereby confirm that I have completed the present dissertation independently and without inadmissible external support. I have not used any sources or tools other than those indicated and have identified literal and analogous quotations.

Furthermore, I confirm that this thesis has not yet been submitted as part of another examination process neither in identical nor in similar form.

Place, date:

Signature:



# Einführung

Diese Arbeit befasst sich mit neuen konzeptionellen Designs für die Entwicklung von niedermolekularen organischen Halbleitern als effiziente Photokatalysatoren für organische Photoredox-Reaktionen. Sichtbares Licht wurde als Energiequelle benutzt. Ziel der Arbeit war es, eine neue Klasse von metallfreien Photokatalysatoren auf Basis von organischen Halbleitern als Alternative von traditionellen Übergangsmetallkomplexen zu etablieren und deren Einsatzbereich zu untersuchen und zu erweitern.

Zunächst wurde ein allgemeines Konstruktionsprinzip von niedermolekularen organischen Halbleitern präsentiert, um entscheidende Anforderungen zu erfüllen wie: 1) Absorption im sichtbaren Bereich, 2) ausreichendes Photoredoxpotential und 3) lange Lebensdauer der photogenerierten Exzitonen. Die photokatalytische Aktivität wurde anhand der intermolekularen C-H-Funktionalisierung von elektronenreichen Heteroarenen mit Malonaten demonstriert. Eine mechanistische Studie über den lichtinduzierten Elektronentransfer zwischen dem organischen Photokatalysator, dem Substrat und dem Opferreagenz wurde beschrieben. Mit ihrem einstellbaren Absorptionsbereich und ihrer definierten energetischen Bandstruktur stellen die niedermolekularen organischen Halbleiter eine neue Klasse von metallfreien Photokatalysatoren für organische Reaktionen unter Bestrahlung mit sichtbarem Licht dar.

Anschließend wurde ein weit verbreitetes Problem bei organischen Photoredox-Reaktionen untersucht, nämlich der essentielle Einsatz eines Opferreagenzes, das als Elektronendonator fungiert. Dabei wurde ein neues Konzept von photokatalytischen Systemen vorgestellt, wobei anstatt eines organischen Halbleiters als Einzelsystem ein kooperatives Katalysatorpaar eingesetzt wurde. Fortgeschrittene photophysikalische Untersuchungen zeigten, dass eine effiziente intermolekulare Ladungsseparation innerhalb des kooperativen Halbleiterpaars stattfindet und dadurch der Einsatz des Opferreagenzes als zusätzlicher Elektronendonator nicht benötigt wurde.

Als nächstes wurde der Einsatz der organischen Halbleiter für aromatische C-C-Bindungsformationen untersucht. Hier wurde die Grundstruktur der organischen Halbleiter präzise modifiziert, so dass ein extrem hohes LUMO (lowest unoccupied molecular orbital) von ca. -2.04 V vs. SCE erreicht wurde. Diverse Arylhalide konnten erfolgreich reduziert werden. Die dadurch entstandenen Arylradikale wurden für die danach folgende C-C-Bindungsformation eingesetzt.

Als letztes wurden organische Halbleiter für licht-kontrollierbare ATRP (atom transfer radical polymerization) eingesetzt. Ein besonderes Augenmerk galt der Anpassung der Reduktionspotentiale von allen Reaktionskomponenten, nämlich Photokatalysator, Initiator und Additiven. Kontrollierbare Polymerisationen sowohl zu reinen Polymeren also auch zu Blockcopolymeren wurden erfolgreich demonstriert.

## Abstract

In this thesis, small molecule organic semiconductors (SMOS) containing electron donor and acceptor moieties have been designed as metal-free, visible light-active and stable photocatalysts for organic transformation reactions as a promising alternative to the traditional transition metal complexes.

First, a general structural design principle of the small molecule organic semiconductor-based photocatalysts has been established following crucial requirements: (i) visible light absorption; (ii) sufficient photoredox potential; (iii) long lifetime of photogenerated excitons. Using a C-H functionalization reaction between electron-rich heteroaromatics and malonate derivatives as the model reaction, the structural design principle of the SMOSs was demonstrated. A mechanistic study focusing on the variation of the photoredox potential of the catalysts and sacrificial reagents was conducted. It could be demonstrated that the catalytic efficiency of the small molecule organic semiconductor were absolutely comparable with the state-of-the-art photocatalytic systems consisting of transition metal complexes.

Second, an important issue for photo-redox reactions, i.e. the mandatory use of electron donating sacrificial reagents, has been addressed. Here, a new conceptual study using a double photocatalyst system made of cooperative organic semiconductor couples was conducted. By the cooperative photocatalyst design, an extra intermolecular electron transfer could occur between the OSs, leading to enhanced photo-generated electron/hole separation and thereby more stable reductive and oxidative species which can give out one electron to the diethyl bromomalonate or get one electron back from the intermediate directly. The C-H functionalization reaction between electron-rich heteroaromatics and malonate derivatives can be conducted successfully without triphenylamine as sacrificial reagent. Advanced photophysical studies illustrate the excitons separation process between OS couples in a direct way. Precisely tuning the energy levels of the photocatalysts will improve the excitons separation process, further influence the reaction rate.

Aromatic carbon-carbon bond formation reactions could be successfully conducted via the reductive dehalogenation of various aryl halides by a designed OS with a high reduction potential of -2.04 V vs. SCE.

An additional study for light-controlled atom transfer radical polymerization using organic semiconductor photocatalysts was carried out. The living nature of the polymerization process was confirmed by the controllable growth of the molecular weight in a light “on-off” cycle, successful synthesis of the chain extension and di-block copolymer and the defined molecular weight distribution of the polymer chain.

## Acknowledgement

*To all I used to love, am loving and will love.*

## Table of Contents

<b>1 Introduction and Motivation .....</b>	<b>1</b>
<b>2 Aim of Work.....</b>	<b>2</b>
<b>3 Theoretical Background.....</b>	<b>3</b>
3.1 Photocatalysts .....	3
3.1.1 Brief introduction of photocatalysts .....	3
3.1.2 Visible light-active photocatalysts .....	4
3.1.2.1 Transition metal complexes .....	4
3.1.2.2 Organic dyes .....	6
3.1.2.3 Extended conjugated structures as photocatalysts.....	7
3.1.2.4 Macromolecular organic semiconductor-based phototcatalysts.....	8
3.2.1 Net reductive reactions .....	9
3.2.2 Net oxidative reactions .....	11
3.2.3 Redox neutral reactions .....	13
3.2.3.1 Radical formation from cleavage of C-halide bond .....	14
3.2.3.2 Radical formation from the cleavage of C-N <sub>2</sub> BF <sub>4</sub> and C-SO <sub>2</sub> Cl bonds .....	15
3.2.3.3 Radical formation from electron deficient compounds.....	16
3.2.3.4 Radical formation via the reduction of alkene .....	16
3.2.3.5 Radical formation via oxidation of alkyl amine .....	17
3.2.3.6 Radical formation from the oxidation of –COOH bond.....	18
3.2.3.7 Radical formation from the oxidation of alkene.....	19
3.3 Organic semiconductors .....	20
3.3.1 Brief introduction of organic semiconductors .....	20
3.3.2 Electronic properties .....	22
3.3.3 Applications of organic semiconductors .....	24
<b>4 Characterization Techniques.....</b>	<b>25</b>

4.1 Ultraviolet-visible spectroscopy .....	25
4.2 Cyclic voltammetry .....	25
4.3 Fluorescence quenching .....	27
4.4 Time-resolved fluorescence spectroscopy .....	27

## 5 Results and Discussions .....28

5.1 Structural design principle of small molecule organic semiconductors for metal-free, visible light-promoted photocatalysis.....	28
5.1.1 Motivation .....	29
5.1.2 Design of the D-A type small molecule organic semiconductors for photocatalyst .....	30
5.1.3 Physical properties of the designed photocatalysts in series 1 .....	31
5.1.4 Electron transfer test between the photocatalyst in series 1 and $\alpha$ -bromoacetophenones ....	33
5.1.5 Photocatalytic C-H functionalization of electron-rich heteroaromatics with diethyl bromomalonate.....	38
5.1.6 Factor that influences the C-H functionalization reaction.....	41
5.1.7 Fluorescence lifetime of SMOSs .....	48
5.1.8 Conclusion .....	49
5.2 Sacrificial reagent-free photoredox catalysis using cooperative organic semiconductor couples .....	49
5.2.1 Motivation .....	50
5.2.2 Design of the catalyst couples .....	51
5.2.3 Physical properties of OS couples .....	54
5.2.4 Photocatalytic C-C bond formation .....	59
5.2.5 Attempt to improve the catalytic efficiency .....	68
5.2.6 Conclusion .....	72
5.3 Feasibility study of the small molecule organic semiconductors as photocatalysts for challenging reactions: molecular design for metal-free and photocatalytic aromatic C-C bond formation reaction...	72
5.3.1 Motivation .....	72
5.3.2 Catalytic cycle design .....	74
5.3.3 Screening of the reaction condition .....	78
5.3.4 Screening of the aryl iodides and aromatic ring .....	79
5.3.5 Examination of the mechanism .....	82
5.3.6 Conclusion .....	84

5.4 Visible light-controlled atom transfer radical polymerization (ATRP) catalyzed by small molecule organic semiconductors.....	84
5.4.1 Motivation .....	84
5.4.2 The role of sacrificial reagent .....	86
5.4.3 Energy level study in the proposed catalytic cycle .....	88
5.4.4 Optimization of polymerization condition .....	89
5.4.5 Living nature of the ATRP .....	95
5.4.6 Improvement of the ATRP catalyzed by small molecule organic semiconductor .....	101
5.4.7 Conclusion .....	105

## **6 Experimental Section..... 106**

6.1 Structural design principle of small molecule organic semiconductors for metal-free, visible light-promoted photocatalysis.....	106
6.1.1 Materials and methods .....	106
6.1.2 Synthesis of the small molecule organic semiconductors.....	107
6.1.3 Synthesis of sacrificial reagent.....	110
6.1.4 Fluorescence quenching experiments.....	110
6.1.5 General procedure of the dehalogenation reaction using the small molecule organic semiconductors .....	111
6.1.6 General procedure of the intermolecular C–H functionalization of electron-rich heterocycles with malonates catalyzed by the organic semiconductors.....	111
6.1.7 Products data.....	112
6.2 Sacrificial reagent-free photoredox catalysis using cooperative organic semiconductor couples ....	115
6.2.1 Materials and methods .....	115
6.2.2 Synthesis of the organic semiconductors.....	116
6.2.3 General procedure for the sacrificial reagent free and photocatalytic C-C coupling reactions using cooperative photocatalyst systems .....	122
6.2.4 Comparison control experiment for the C-C coupling reaction between 3-methylbenzofuran and ethyl bromoacetate using Th-BTz-Th as catalyst and 4-methoxytriphenylamine as sacrificial reagent.....	122
6.2.5 Products NMR data: .....	122
6.3 Feasibility study of the small molecule organic semiconductors as photocatalysts for challenging reactions: molecular design for metal-free and photocatalytic aromatic C-C bond formation reaction.	124



6.3.1 Materials and methods. ....	124
6.3.2 Synthesis of the molecular organic semiconductors and sacrificial reagent.....	125
6.3.3 Absorption and fluorescence spectrum of photocatalyst Py-BTz-Py.....	126
6.3.4 Product characterization .....	127
6.3.5 NMR spectrum of the isolate products .....	136
6.4 Atom transfer radical polymerization (ATRP) catalyzed by visible-light-absorbed small molecule organic semiconductors.....	165
6.4.1 Materials and methods .....	165
6.4.2 Fluorescence quenching experiments.....	165
6.4.3 General procedure for polymerization .....	165
<b>7 Conclusion .....</b>	<b>166</b>
<b>8 List of Abbreviations.....</b>	<b>168</b>
<b>9 References .....</b>	<b>170</b>
<b>10 List of Related Publications.....</b>	<b>193</b>

## List of Figures

Figure 2.1 Illustration of donor and acceptor-based organic semiconductors (OSs). The charge separation results into electron/hole pair as reducing and oxidizing sites of the catalyst. D: donor unit, A: acceptor unit, S: substrates. ....	2
Figure 3.1 Solar spectrum and distribution reaching the earth surface. ....	4
Figure 3.2 Examples of transition metal based photocatalysts. ....	5
Figure 3.3 Illustration of the light absorption and electron transfer process in $\text{Ru}(\text{bpy})_3^{2+}$ . ....	6
Figure 3.4 Illustration of components in an organic dye. ....	6
Figure 3.5 Examples of photocatalysts based on organic dyes. ....	7
Figure 3.6 Examples of photocatalysts based on conjugated structures. ....	7
Figure 3.7 Examples of chemical structures of conjugated porous polymers. ....	8
Figure 3.8 Illustration of the electron transfer process in photocatalytic cycle. ....	9
Figure 3.9 Illustration of the catalytic cycle of net reductive reaction. A, B and C are different chemical groups. ....	10
Figure 3.10 Examples of net reductive reactions. ....	11
Figure 3.11 Illustration of the catalytic cycle of net oxidative reactions. A, B and C are different chemical groups. ....	12
Figure 3.12 Examples of net oxidative reactions. ....	13
Figure 3.13 Representative mechanisms for the redox neutral reactions. A, B, C and D are different chemical groups. ....	14
Figure 3.14 Illustration of the radical addition reaction with cleavage of C-halide bond. ....	14
Figure 3.15 Examples of the trifluoromethylation reaction. ....	15
Figure 3.16 Illustration of radical formation from $\text{C-N}_2\text{BF}_4$ and $\text{C-SO}_2\text{Cl}$ bonds. ....	15
Figure 3.17 Examples of electron deficient compounds. ....	16
Figure 3.18 Illustration of the radical formation process from diphenyliodonium salts and Togni (I) reagent. ....	16
Figure 3.19 Illustration of the mechanism for [2+2] cycloaddition reaction. ....	17
Figure 3.20 Illustration of the formation of $\alpha$ -aminoalkyl radicals. ....	17
Figure 3.21 Illustration of the mechanism for the reaction between amine and alkene and cyanoarene (E is short for electron withdrawing group). ....	18
Figure 3.22 Illustration of the mechanism in bond formation via decarboxylation process. ....	19
Figure 3.23 Illustration of the mechanism for anti-Markovnikov addition reaction. ....	20

Figure 3.24 Illustration of $\sigma$ and $\pi$ bonds formation in $sp^2$ hybridization.....	21
Figure 3.25 Illustration of the molecular orbitals formation in butadiene.....	21
Figure 3.26 Illustration of the energy levels in organic semiconductors.....	22
Figure 3.27 (a) Chemical structure of $\beta$ -carotene and Lycopene; (b) illustration of band gap decreases	
Figure 3.28 Function principle of OSCs.....	24
Figure 4.1 Illustration of a typical cyclic voltammogram.....	26
Figure 5.1 Absorption spectrum of the SMOSs in series 1. ....	32
Figure 5.2 Illustration of the HOMO/LUMO levels of SMOSs in series 1.....	32
Figure 5.3 Illustration of the mechanism for the dehalogenation reaction. ....	33
Figure 5.4 Rates of the light-induced dehalogenation reaction of $\alpha$ -bromoacetophenone using SMOSs as photocatalysts; reaction condition: $\alpha$ -bromoacetophenone (1 mmol, 1 equiv.), hantzsch ester (1.1 mmol, 1.1 equiv.), <i>N,N</i> -diisopropylethylamine (2 mmol, 2 equiv.), catalyst (1 mol%) and 2 ml DMF.....	34
Figure 5.5 Fluorescence quenching of Ph-BT with (a) diisopropylethylamine and (b) diethyl bromomalonate, and (c) Stern-Volmer curve.....	36
Figure 5.6 Fluorescence quenching of Ph-BT-Ph with (a) diisopropylethylamine and (b) diethyl bromomalonate, and (c) Stern-Volmer curve.....	37
Figure 5.7 Fluorescence quenching of Th-BT-Th with (a) diisopropylethylamine and (b) diethyl bromomalonate, and (c) Stern-Volmer curve.....	37
Figure 5.8 Absorption spectrum of Th-BO-Th, Th-BT-Th, and Th-BS-Th (ca. $10^{-5}$ mol/ml in DCM).....	39
Figure 5.9 Illustration of the mechanism for intermolecular C-H functionalization reaction.....	39
Figure 5.10 (a) Fluorescence quenching of Th-BO-Th with triphenylamine and (b) Stern-Volmer curve. .	42
Figure 5.11 (a) Fluorescence quenching of Th-BT-Th with triphenylamine and (b) Stern-Volmer curve...	42
Figure 5.12 (a) Fluorescence quenching of Th-BS-Th with triphenylamine and (b) Stern-Volmer curve...	43
Figure 5.13 (a) Fluorescence quenching of Th-BT-Th with 4-methyl- <i>N,N</i> -diphenylaniline and (b) Stern-Volmer curve.....	43
Figure 5.14 (a) Fluorescence quenching of Th-BT-Th with 4-methoxyl- <i>N,N</i> -diphenylaniline and (b) Stern-Volmer curve.....	43
Figure 5.15 HOMO and LUMO band positions of the SMOSs in series 2 and redox potentials of substrates and sacrificial reagents. ....	44
Figure 5.17 Reaction time comparisons for different substrates with various triphenylamine-based sacrificial reagents using Th-BO-Th and Th-BS-Th as catalysts. ....	46
Figure 5.18 Reaction time comparisons for different substrates with various triphenylamine-based sacrificial reagents using Th-BT-Th as model catalyst. ....	47

Figure 5.19 (a) Fluorescence-delay spectra of the SMOs and (b) HOMO (bottom) and LUMO (top) of Th-BT-Th calculated at the B3LYP/6-31G* level.....	48
Figure 5.20 Difference between (a) conventional single organic photocatalyst system with direct electron/hole recombination, sacrificial reagent needed; (b) cooperative photocatalyst system with enhanced electron/hole separation, no sacrificial reagent needed. OS: organic semiconductor; SA: sacrificial reagent; S: substrate. ....	51
Figure 5.21 Structure and HOMO LUMO levels (vs. SCE) of the OS molecules in both designed photocatalyst couples.....	52
Figure 5.22 Reductive potentials of (a) Th-BT-Th, (c) Th-BTz-Th and (e) TA-BT-TA and oxidative potential of (b) Th-BT-Th, (d) Th-BTz-Th and (f) TA-BT-TA determined via cyclic voltammetry (vs. SCE). ....	53
Figure 5.23 (a) Normalized absorption spectrum and (b) fluorescence spectrum of Th-BT-Th, Th-BTz-Th and TA-BT-TA. ....	54
Figure 5.24 Steady state fluorescence quenching within the photocatalyst couples in solution. The ratios of the OSs were 1:1 for both couples. Excitation wavelength: (a) 450 nm, (b) 500 nm. ....	55
Figure 5.25 Time-resolved fluorescence quenching within the photocatalyst couples in solution. The ratios of the OSs were 1:1 for both couples. Excitation wavelength: 400 nm.....	56
Figure 5.26 Time-resolved photoluminescence decays in the pristine materials and in the photocatalyst couples in solution. The ratios of the OSs were 1:1 for both couples. (a) Couple 1 and (b) couple 2. Excitation wavelength: 400 nm.....	57
Figure 5.27 Decay associated spectra (DAS) derived by a global fitting analysis of the TRPL data. (a) Couple 1 and (b) couple 2. ....	58
Figure 5.28 Jablonski diagram illustrates energy and charge transfer in the photocatalyst couples, respectively. Excitation wavelength: 400 nm. EET: excitation energy transfer; ET: electron transfer. ....	59
Figure 5.29 Fluorescence quenching spectra of (a)Th-BT-Th, (b)TA-BT-TA (c)Th-BTz-Th with diethyl bromomalonate and (d) Stern-Volmer analysis of quenching rate between Th-BTz-Th and diethyl bromomalonate. ....	62
Figure 5.30 Fluorescence quenching for (a) cooperative catalyst system 1 (Th-BTz-Th and Th-BT-Th) and (c) cooperative catalyst system 2 (Th-BTz-Th and TA-BT-TA) with diethyl bromomalonate and Stern-Volmer analysis of (b) cooperative couple 1 and (d) couple 2 with diethyl bromomalonate. ....	63
Figure 5.31 Reductive potentials of (a) diethyl bromomalonate and (b) ethyl bromoacetate (potentials given vs. SCE).....	64
Figure 5.32 Study of the electron transfer pathway using comparative substrates with different reduction potentials. Interm.: intermediate.....	65
Figure 5.33 C-C coupling between 3-methylbenzofuran and ethyl bromoacetate using couple 2 (Th-BTz-Th/TA-BT-TA) as cocatalyst, Conversion: ~ 4%.....	66

Figure 5.34 C-C coupling between 3-methylbenzofuran and ethyl bromoacetate using Th-BTz-Th as catalyst and 4-methoxytriphenylamine as sacrificial reagent. Reaction conditions: 1 equiv. (0.38 mmol) heteroaromate, 2 equiv. ethyl bromomalonate, 0.1 equiv. photocatalyst in 2.5 mL DMF, white LED, 12 h. ....	67
Figure 5.35 UV/vis absorption and fluorescence spectra of the connected photocatalyst system TA-BT-TA@Th-BTz-Th.....	69
Figure 5.36 Fluorescence spectra of C6-connected Th-BTz-Th@TA-BT-TA and unconnected photocatalyst couple 2 containing Th-BTz-Th and TA-BT-TA under same molar ratio and concentration. ....	69
Figure 5.37 Study of the impact of the OS ratio on the reaction conversion. ....	70
Figure 5.38 Comparison between cooperative photocatalyst couple 2 with the C6-connected molecule Th-BTz-Th@TA-BT-TA .....	70
Figure 5.39 Fluorescence quenching of (a) unconnected and (c) connected Th-BTz-Th/TA-BT-TA with diethyl bromomalonate and Stern-Volmer analysis of (b) unconnected and (d) connected Th-BTz-Th/TA-BT-TA with diethyl bromomalonate. ....	71
Figure 5.40 Pre-designed mechanism for organic semiconductor photocatalyst catalyzed C-H cross coupling reactions. ....	75
Figure 5.41 Molecular engineering of OS type photocatalysts.....	76
Figure 5.42 Proper energy levels designed for catalytic cycle. ....	77
Figure 5.43 Screening of the Ar-I and Ar for the photocatalytic C-C bond formation.....	80
Figure 5.44 Reductive potential of (a) 4-iodoanisole, (b) iodobenzene, (c) methyl 4-iodobenzoate, (d) 4-iodobenzonitrile, (e) 4-bromobenzonitrile and (f) 4-chlorobenzonitrile.....	81
Figure 5.45 Fluorescence quenching of (a) Py-BTz-Py with tri(4-methoxylohenyl)amine and (c) methyl 4-iodobenzoate, Stern-Volmer analysis of (b) Py-BTz-Py with tri(4-methoxylohenyl)amine and (d) methyl 4-iodobenzoate. [M]: concentration of the amine or the substrate. ....	82
Figure 5.46 Aryl radical trapping experiment using TEMPO. Reaction conditions: methyl 4-iodobenzoate (0.38 mmol, 1 equiv.), tributylamine (1.9 mmol, 5 equiv.), TEMPO (1.9 mmol, 5 equiv.), organic semiconductor photocatalyst (5%, 0.019 mmol), in 2.5 ml DMSO. ....	83
Figure 5.47 Proposed mechanism for the light-controlled ATRP process catalyzed by OS type photocatalysts.....	86
Figure 5.48 Illustration of the probably suitable OS type catalysts using in ATRP.....	86
Figure 5.49 Fluorescence quenching of Ph-BT-Ph with (a) triphenylamine, (b) ethyl $\alpha$ -bromophenyl acetate, and (c) Stern-Volmer analysis.....	87
Figure 5.50 (a) Reductive potential of initiator ethyl $\alpha$ -bromophenyl acetate, (b) reductive potential of polymer chain end C-Br bond, (c) oxidative potential of sacrificial reagent triphenylamine, (d) reductive	

potential of initiator 1-iodoperfluorohexane, and (e) reductive potential of polymer chain end C-I bond, estimated by the analogue ethyl iodoacetate. .... 88

Figure 5.51 Gel permeation chromatography traces of PMMA40 synthesized (a) with sacrificial reagent and (b) without sacrificial reagent. Reaction condition: MMA 5.6 mmol, 2.5% mol Initiator ethyl  $\alpha$ -bromophenyl acetate, 0.1% Th-BTz-Th as photocatalyst, 10% mol triphenylamine or not in 1.5 ml DMF with a white LED as light source..... 89

Figure 5.52 Gel permeation chromatography traces of PMMA40 and chain extended PMMA40 synthesized (a) with ethyl  $\alpha$ -bromophenyl acetate as initiator and (b) with 1-iodoperfluorohexane as initiator. Reaction condition for the PMMA40: MMA 5.6 mmol, 2.5% mol Initiator, 0.1% Th-BTz-Th as photocatalyst, 10% mol triphenylamine in 1.5 ml DMF with a white LED as light source (5 hours reaction time for Br initiator and 20 h for the I initiator). Reaction condition for the chain extended PMMA40: MMA 5.6 mmol, 100 mg purified macroinitiator, 0.1% Th-BTz-Th as photocatalyst, 20% mol triphenylamine in 1.5 ml DMF with a white LED as light source (5 hours reaction time for Br initiated PMMA40 and 20h for the I initiated PMMA40). .... 90

Figure 5.53 Proposed elimination side reaction. .... 91

Figure 5.54 (a) Gel permeation chromatography trace vs. reaction time, (b) molecular weight and molecular weight distribution vs. conversion, (c) conversion vs. reaction time and (d)  $\ln([M]_0/[M])$  as a function of time. Reaction condition: MMA 5.6 mmol, 2.5% mol Initiator ethyl  $\alpha$ -bromophenyl acetate, 0.1% Th-BTz-Th as photocatalyst, 10% mol triphenylamine, 20% LiBr in 1.5 ml DMF. .... 92

Figure 5.55 (a) Gel permeation chromatography trace vs. reaction time, (b) molecular weight and molecular weight distribution vs. conversion, (c) conversion vs. reaction time, and (d)  $\ln([M]_0/[M])$  as a function of time. Reaction condition: MMA 5.6 mmol, 2.5% mol Initiator ethyl  $\alpha$ -bromophenyl acetate, 0.1% TA-BT-TA as photocatalyst, 10% mol triphenylamine, 20% LiBr in 1.5 ml DMF. .... 93

Figure 5.56 (a) Gel permeation chromatography trace vs. reaction time, (b) molecular weight and molecular weight distribution vs. conversion, (c) conversion vs. reaction time and (d)  $\ln([M]_0/[M])$  as a function of time. Reaction condition: MMA 5.6 mmol, 2.5% mol Initiator ethyl  $\alpha$ -bromophenyl acetate, 0.1% Ph-BT-Ph as photocatalyst, 10% mol triphenylamine, 20% mol LiBr in 1.5 ml DMF. .... 94

Figure 5.57(a) Conversion of the monomer within the controlled light “on-off” cycle, (b) relative molecular weight of each “on-off” cycle and (c) gel permeation chromatography trace at different time point. .... 96

Figure 5.58 (a) Gel permeation chromatography traces of PMMA before and after chain extension, and (b) Gel permeation chromatography traces of PMMA and PMMA-*b*-PBMA. .... 97

Figure 5.59 MALDI-TOF spectrum of the PMMA synthesized with the standard condition: MMA 5.6 mmol, 2.5% mol Initiator ethyl  $\alpha$ -bromophenyl acetate, 0.1% Ph-BT-Ph as photocatalyst, 10% mol triphenylamine, 20% LiBr in 1.5 ml DMF. .... 98

Figure 5.60 MALDI-TOF spectrum of the PMMA synthesized without LiBr: MMA 5.6 mmol, 2.5% mol Initiator ethyl $\alpha$ -bromophenyl acetate, 0.1% Ph-BT-Ph as photocatalyst, 10% mol triphenylamine in 1.5 ml DMF. ....	99
Figure 5.61 Gel permeation chromatography traces of the polymer in Table 5.8.....	101
Figure 5.62 (a) Gel permeation chromatography trace vs. reaction time (b) molecular weight and molecular weight distribution vs. conversion (c) conversion vs. reaction time and (d) $\ln([M]_0/[M])$ as a function of time. Reaction condition: MMA 5.6 mmol, 2.5% mol initiator 1-iodoperfluorohexane, 0.1% Ph-BT-Ph as photocatalyst, 10% mol triphenylamine, 20% LiI in 1.5 ml DMF. ....	105
Figure 5.63 The “ideal” potential conditions for the ATRP process catalyzed by small molecule organic semiconductor with low reductive potentials. ....	104
Figure 5.64 (a) Gel permeation chromatography trace vs. reaction time, (b) molecular weight and molecular weight distribution vs. conversion, (c) conversion vs. reaction time and (d) $\ln([M]_0/[M])$ as a function of time. Reaction condition: MMA 5.6 mmol, 2.5% mol initiator ethyl $\alpha$ -bromophenyl acetate, 0.1% Ph-BT-Ph as photocatalyst, 10% mol triphenylamine, 20% LiI in 1.5 ml DMF.....	105

## List of Tables

Table 5.1 Photocatalytic dehalogenation reaction of different haloketones using Th-BT-Th as catalyst. ....	35
Table 5.2 Fluorescence quenching constants ( $K_{sv}$ ) of different photocatalysts using diisopropylethylamine as reductant.....	38
Table 5.3 Photocatalytic C-C bond formaton via C-H functionalization of electron rich heteroaromates with diethyl bromomalonate using the SMOSs as photocatalysts. ....	40
Table 5.4 $K_{sv}$ of fluorescence quenching with different catalysts and reductants.....	42
Table 5.5 Photocatalytic C-C bond formation between diethyl bromomalonate and heteroaromates using different photocatalysts systems .....	61
Table 5.6 Reaction condition optimization of aromatic cross coupling reaction .....	78
Table 5.7 Results of the ATRP conducted with different catalysts. ....	95
Table 5.8 Results of the OS catalyzed atom transfer radical polymerization.....	100



## 1 Introduction and Motivation

Unlike the well-studied thermal catalysts that require heat to maintain the reactivity, photocatalysts have emerged in recent year as a new kind of catalyst which can be activated by light instead of heat.<sup>1-7</sup> The word “photocatalyst” is a combination of “photo” and “catalyst” to highlight the specific character for this kind of catalyst requiring light for its activation.

Photochemistry or photocatalysis are promising tools to induce versatile chemical transformation. The energy source for chemical transformation changed from heating for normal catalytic reaction to light for a photocatalyst, which is quit abundant in a cheap, clean and renewable manner in nature from sun. Inspired by light driven chemical reactions in nature, namely the photosynthesis process, the chemists have developed various photocatalytic systems in the past years. One of the most famous homogeneous photocatalysts are transition metal complexes like *fac*-Ir(ppy)<sub>3</sub>, Ir[(ppy)<sub>2</sub>(dtbbpy)]PF<sub>6</sub>, Ru(bpy)<sub>3</sub>Cl<sub>2</sub> and etc.<sup>6, 8</sup> The high efficiency of catalytic reactivity is proved by tremendous chemical reactions with light as a simple driven force.<sup>9-12</sup> However, considering the high price and toxicity of transition metal iridium and ruthenium, pure organo-photocatalysts based on organic dyes are emerged as an alternative to the transition metal complexes, which are also proved with a high efficiency for light driven chemical reactions.<sup>13-16</sup> However, drawbacks still exist, since the dyes are bleaching under light irradiation and are difficult to functionalize. Therefore, the development of a new kind of homogeneous photocatalyst system is of great demand.

Organic semiconductors with optic and electronic properties, which originate from their special delocalized  $\pi$  orbitals<sup>17-19</sup>, have been developed in recent years. Light absorption induced electron transfer from the highest occupied molecular orbital (HOMO) to the lowest unoccupied molecular orbital (LUMO) via charge separation is the main driving force for organic solar cells.<sup>20-21</sup> Although the light absorption and electron transfer processes of organic semiconductors have been well studied, the application of organic semiconductors as visible

light-active and efficient photocatalysts has been less reported so far. Therefore, the main target of this dissertation is to design new photocatalytic systems based on organic semiconductors with specific properties as visible light absorption, tunable photoredox potential, and long live excited state for organic photoredox reactions.

## 2 Aim of Work

The main objective of this work is to develop small molecule organic semiconductors as new photocatalysts according to the following principles: (i) visible light absorption; (ii) sufficient photoredox potential; (iii) long lifetime of photogenerated excitons.

To realize the targets of this work, different combinations of organic donor and acceptor units will be chosen for the investigation of structure-property-relationship by analyzing their optical and electronic properties. Specific photoredox reactions will also be chosen as model reaction to individually study the possible electron transfer between the photo-generated electron/hole pair and the substrate (Figure 2.1), in order to obtain the mechanistic insights of the photocatalytic cycle. Important factors, which can influence the photocatalytic efficiency, will be also investigated using advanced photophysical methods such as photoluminescence decay.

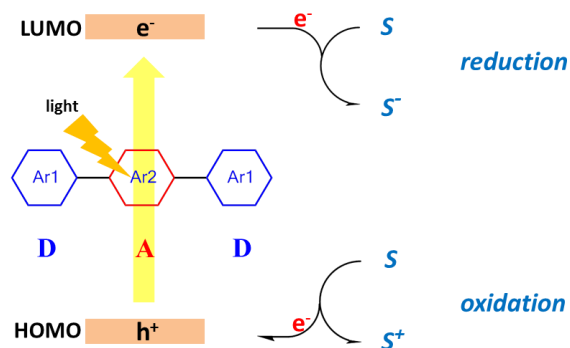


**Figure 2.1** Illustration of donor and acceptor-based organic semiconductors (OSs). The charge separation results into electron/hole pair as reducing and oxidizing sites of the catalyst. **D**: donor unit, **A**: acceptor unit, **S**: substrates.

Furthermore, the feasibility of the designed organic semiconductor-based photocatalysts will be investigated for challenging reactions such as aromatic C-C bond formation or light-controlled radical polymerization. The structural design of the organic semiconductors on the molecular level will be undertaken to reach extreme high photoredox potentials.

## 3 Theoretical Background

### 3.1 Photocatalysts

#### 3.1.1 Brief introduction of photocatalysts

Based on the definition of “photocatalysis” suggested by the International Union of Pure and Applied Chemistry (IUPAC), *“change in the rate of a chemical reaction or its initiation under the action of ultraviolet, visible or infrared radiation in the presence of a substance—the photocatalyst—that absorbs light and is involved in the chemical transformation of the reaction partners”*, the most remarkable step for photocatalytic reactions should be the light energy absorption and utilization for driving chemical reactions. Photochemistry and photocatalysis offer a sustainable and green alternative to the traditional thermal reaction conditions for chemical production.<sup>22-24</sup> Motivated by the photosynthesis process in nature, various photocatalyst systems have been developed for a wide range of applications such as water splitting<sup>25-28</sup>, pollutants and bacteria removing<sup>29-33</sup> or chemicals producing<sup>4, 34-35</sup>.

The sun is the most abundant and sustainable energy source. The solar spectrum is divided into three regions based on wavelength: ultraviolet light in 300-400 nm, visible light in 400-700 nm and infrared light in the region higher than 700nm (Figure 3.1). Compared to the ultraviolet light, which only accounts for ca. 4% of the solar energy, visible light owns not only a much larger energy content of over ca. 40%, but also the highest intensity in the solar spectrum. However, given the fact that most of the organic molecules cannot absorb in visible light region, additional visible light-mediating or transferring reagents are highly needed. Therefore, the development of visible light-active photocatalytic systems is highly necessary.

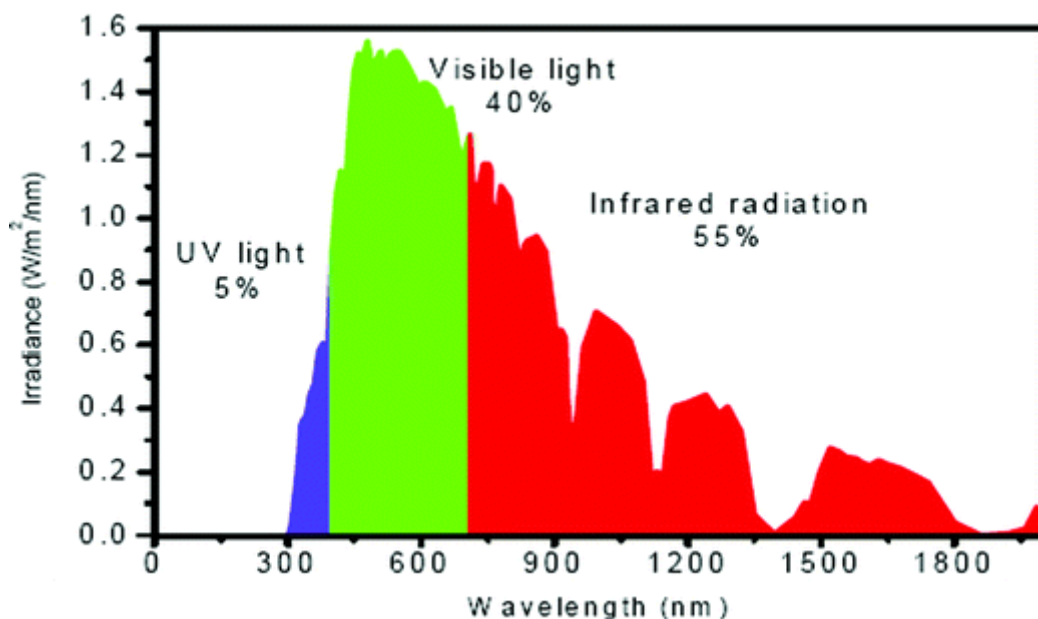


Figure 3.1 Solar spectrum and distribution reaching the earth surface.

### 3.1.2 Visible light-active photocatalysts

In the last two decades, two main categories of visible light photocatalysts have been developed: transition metal complexes<sup>6, 36</sup> and organic dyes<sup>13, 37</sup>. Very recent studies on copper-containing photocatalysts have also been reported.<sup>38</sup> Conjugated structures were reported as an alternative to the metal complexes and organic dyes.<sup>39-45</sup> Lately, conjugated porous polymers have emerged as metal-free and heterogeneous photocatalysts.<sup>46-49</sup>

#### 3.1.2.1 Transition metal complexes

In recent years, transition metal complex-based photocatalysts consisting iridium or ruthenium have been intensely studied. Widely used examples are *fac*-Ir(ppy)<sub>3</sub>, Ir[(ppy)<sub>2</sub>(dtbbpy)]PF<sub>6</sub>, or Ru(bpy)<sub>3</sub>Cl<sub>2</sub> etc. (Figure 3.2). Due to their strong absorption in the visible region, long excited state life time and sufficient redox potentials, the transition metal complexes have been used in a vast number of chemical reactions.<sup>6, 36</sup> Additionally, by variation of the ligands, the redox potentials of the metal complexes can be adjusted.<sup>50</sup>

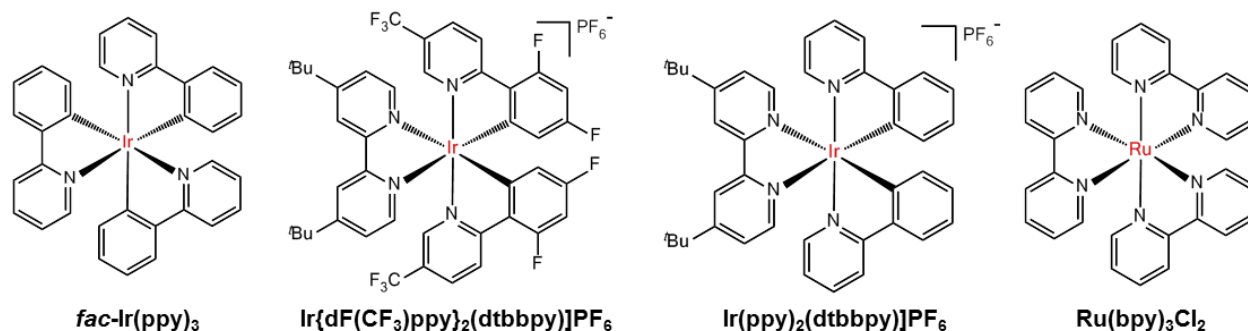


**Figure 3.2 Examples of transition metal based photocatalysts.**

The photocatalytic ability of the transition metal complex originates from its specific molecular orbitals (Figure 3.3). Taking Ru(bpy)<sub>3</sub><sup>2+</sup> as an example, under light irradiation, the electrons are excited from the metal-centered  $t_{2g}$  orbital to the ligand-centered  $\pi^*$  orbital via a metal to ligand charge transfer (MLCT) process. After the intersystem crossing process, a more stable triplet state can be formed. The reaction of the stable triplet electrons with the substrates via single electron transfer (SET) process will form the reduced or oxidized intermediates for further steps in the catalytic cycle. However, significant drawbacks are still associated to the transition metal complexes, for example the high costs and toxicity of *Ir* and *Ru* as noble metals, limited catalyst alternatives, and the difficulty to functionalize them; all these drawbacks lead to an impossible wide utilization. Developing cheap and metal-free photocatalysts remains a challenge for the chemists and materials scientists.

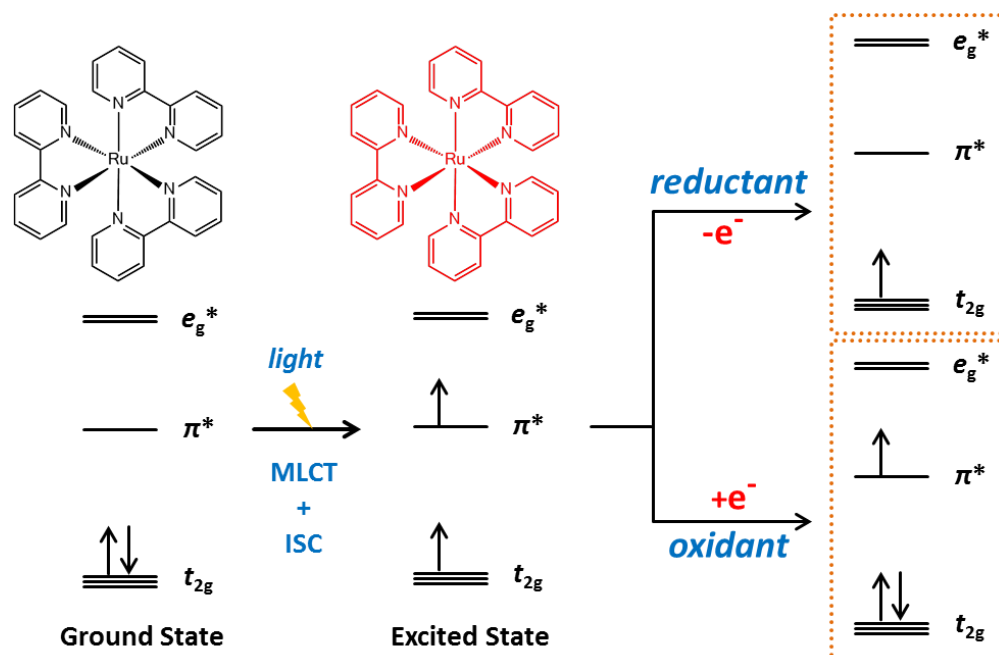


Figure 3.3 Illustration of the light absorption and electron transfer process in  $\text{Ru}(\text{bpy})_3^{2+}$ .

### 3.1.2.2 Organic dyes

A dye is a colored substance due to the ability of light absorption under specific wavelengths. The composition of organic dyes can be simply divided into three main parts as shown in Figure 3.4: the chromogen, the chromophore and the auxochrome. The chromogen is a chemical compound that is either colored or could be made colored by suitable substitution; the chromophore is a chemical group that is used for the creation of color in compounds (the chromogen); and the auxochrome is a substituent group to further influence the color of dyes.

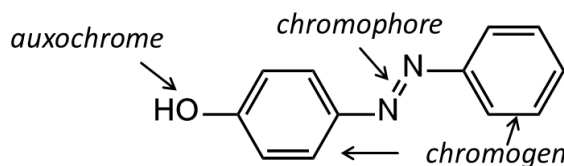
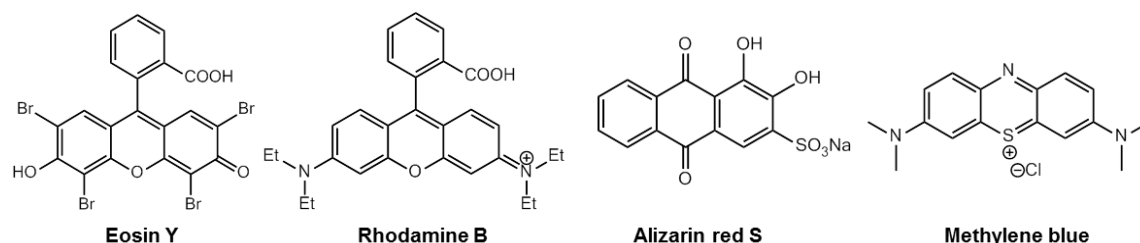


Figure 3.4 Illustration of components in an organic dye.

Under light irradiation, the electron can be excited from the lower energy levels to the higher ones. Examples are the  $\pi \rightarrow \pi^*$  transitions in  $\text{C}=\text{C}$  or  $\text{C}\equiv\text{C}$  chromophores, or  $\pi \rightarrow \pi^*$ ,  $n \rightarrow \pi^*$  and

$n \rightarrow \sigma^*$  transitions in  $C=O$ ,  $C\equiv N$  or  $N=N$  chromophores. However, in order to be able to absorb visible light, a larger conjugated structure with combination of the chromophoric groups, is needed. According to this construction principle, a vast number of organic dyes have been synthesized, which possess not only broad absorption range, but also high absorption coefficients. Important examples, such as eosin Y, rhodamine B, alizarin red S, methylene blue, have been applied as metal-free photocatalysts for versatile photoredox reactions (Figure 3.5).<sup>51-58</sup>



**Figure 3.5 Examples of photocatalysts based on organic dyes.**

### 3.1.2.3 Extended conjugated structures as photocatalysts

Other non-ionic and extended conjugated aromatic compounds have also been used for photoredox reactions. Few studies have been reported such as  $\alpha$ -sexithiophene ( $\alpha$ -6T)<sup>44</sup>, perylene<sup>43</sup>, or N,N-diaryl dihydrophenazine and its derivatives<sup>39-42, 45</sup> as pure organic photocatalysts (Figure 3.6).

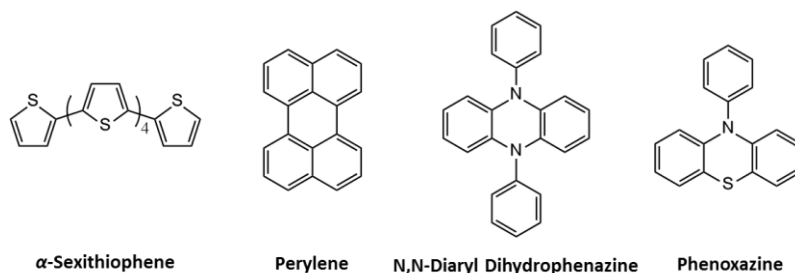


**Figure 3.6 Examples of photocatalysts based on conjugated structures.**

### 3.1.2.4 Macromolecular organic semiconductor-based photocatalysts

Conjugated porous polymers (CPP) have emerged in the last four years as a new kind of semiconducting materials with specific nano-structures (Figure 3.7). The permanent pore structure as well as the electronic properties of CPPs shows its great potential in photocatalysis application. Numerous CPPs were synthesized and proved to be efficient and stable catalyst for visible light promoted chemical transformations.

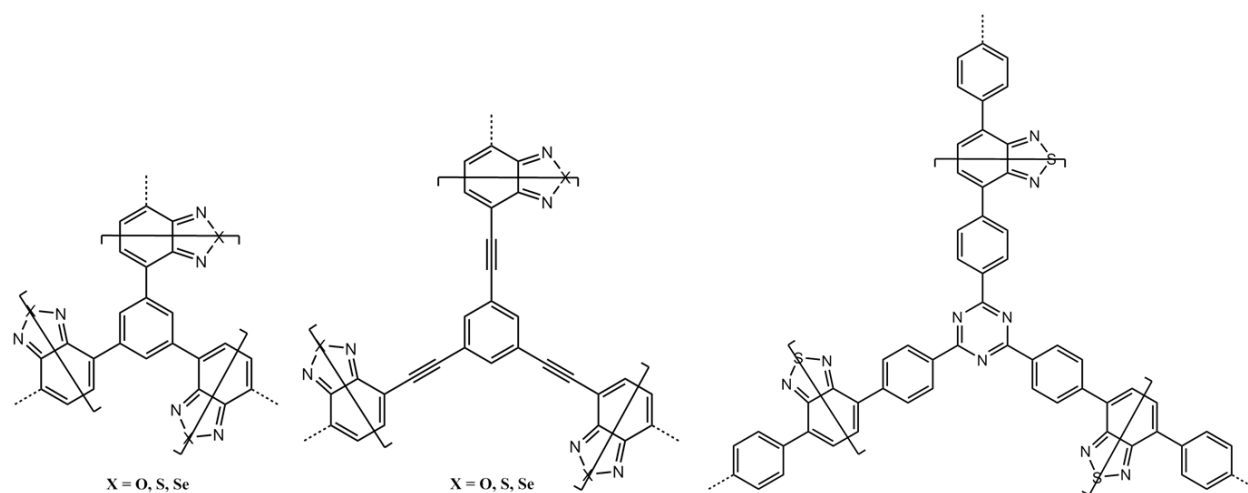


**Figure 3.7** Examples of chemical structures of conjugated porous polymers.

## 3.2 Photocatalytic reaction mechanism in organic synthesis

The photocatalytic reactions can be simply divided into three main categories: net reductive reactions, net oxidative reactions and redox neutral reactions. Definition of reduction or oxidation is based on the electron transfer process from the photocatalyst to the substrate as shown in Figure 3.8: when the substrate receives one electron from the excited photocatalyst, a reductive mechanism is carried out. The opposite direction of the electron transfer is considered as oxidation, where the substrate is oxidized. This unique single electron transfer process is the fundamental step for the successful chemical transformations.



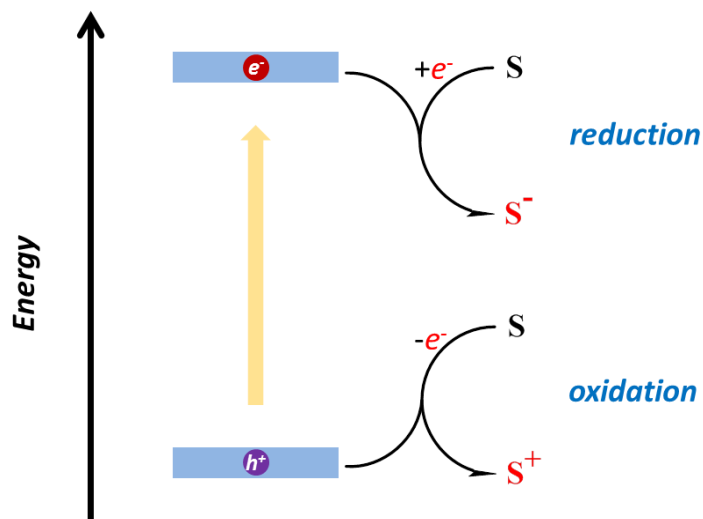
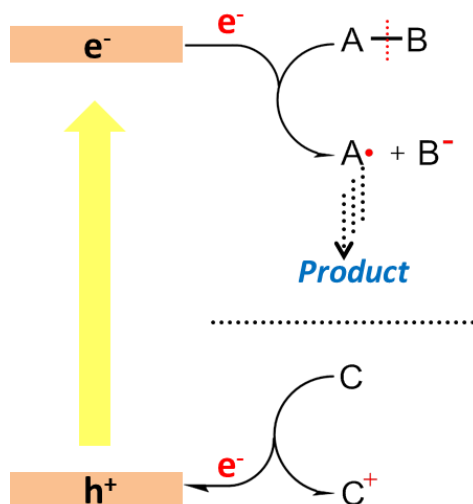


Figure 3.8 Illustration of the electron transfer process in photocatalytic cycle.

### 3.2.1 Net reductive reactions

For photoredox reactions, an interaction between the excited photocatalyst and substrates via the single electron transfer process is the key step to form the desired activated intermediate for further transformations. For the net reductive reaction, the only useful part of the catalytic cycle is the electron transfer from the photocatalyst to the substrate. So, in order to bring the photocatalyst back to its ground state, an additional electron donor (sacrificial reagent) is needed to donate one electron to the photocatalyst (Figure 3.9).



**Figure 3.9 Illustration of the catalytic cycle of net reductive reaction. A, B and C are different chemical groups.**

Figure 3.10 shows some classic examples of net reductive reactions. Most of the substrates involved in the net reductive reactions own a chemical bond that can receive electrons from the photocatalyst, such as C-halide<sup>37, 59-61</sup>,  $-\text{NO}_2$ <sup>62-64</sup>,  $-\text{N}_3$ <sup>65</sup>, sulfonium<sup>66-67</sup> and sulfonyl groups<sup>68-69</sup>, epoxide and aziridine<sup>70-72</sup>, etc. The most common reaction for net reductive process is the cleavage of the C-halide bond. In a typical reaction cycle, one electron is transferred from the photocatalyst to the substrate, forming a carbon radical and halogen ion. The carbon radical can further extract one hydrogen atom to form the dehalogenated C-H product. Cyclic structures can be formed via the addition reaction of the radical and an unsaturated bond.<sup>73-75</sup> New C-C bonds can also be formed via the combination of two generated radicals.<sup>76</sup> Double bonds can be formed if the cleavage of two adjacent C-halide groups occurred simultaneously.<sup>44, 77-78</sup> Other examples of the net reductive reaction are the reduction of  $-\text{NO}_2$  or  $-\text{N}_3$  groups into  $-\text{NH}_2$  using electron-donating sacrificial reagents. Positively charged sulfonium groups can also receive one electron, leading to the cleavage of the C-S bond. Other examples with similar mechanism are for example the cleavage of the  $\text{C-SO}_2\text{Ph}$  or  $\text{N-NH}_2$  to form the C-H and  $-\text{N-H}$  bonds with  $\text{PhSO}_2^-$  and  $\text{NH}_2^-$  ions as by-products.

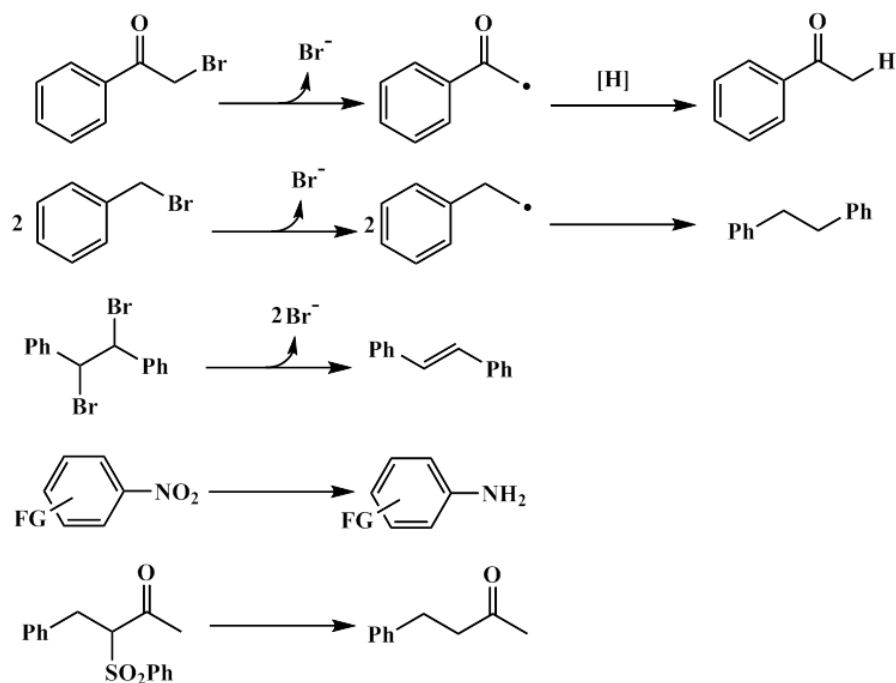
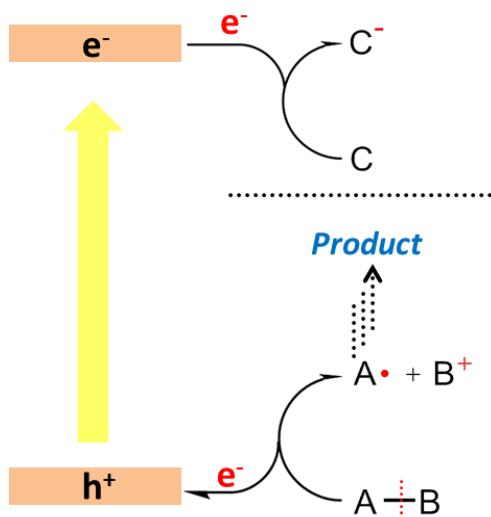


Figure 3.10 Examples of net reductive reactions.

### 3.2.2 Net oxidative reactions

For net oxidative reactions, the most significant process of the catalytic cycle is the electron transfer from the substrate to the photocatalysts in the excited state. In net oxidative reactions, an extra electron accepting reagent is usually needed in order to bring the photocatalyst back to its ground state (Figure 3.11).<sup>79</sup>



**Figure 3.11 Illustration of the catalytic cycle of net oxidative reactions. A, B and C are different chemical groups.**

Molecular oxygen often acts as efficient electron acceptor for the photocatalysts, leading to the formation of its anionic radical, i.e. superoxide ( $\text{O}_2^-$ ), which can either directly act as oxidant or further extract one hydrogen atom to form the  $\text{H}_2\text{O}_2$  as another oxidant species.<sup>80</sup> The substrates that can be oxidized always contain an electron sufficient aromatic ring or atoms, such as benzene rings<sup>54, 81-83</sup> or amines<sup>84-86</sup>. The reconstruction of the oxidized substrate is necessary for the formation of the final product. One example can be demonstrated by the photocatalytic Aza-Henry reaction as shown in Figure 3.12. The oxidation of the amine forms first the aminium radical cation, and after losing a hydrogen atom on the adjacent carbon atom, it will form the iminium ion, which can further react with nucleophiles to directly form new bonds at the  $\alpha$ -position of the amine. This  $\alpha$ -position bond formation reaction has been used for different bond formation reaction using various nucleophiles such as cyanide<sup>87</sup>, enol silanes<sup>88</sup>, ketones<sup>89</sup>, dialkyl phosphates<sup>90</sup>, or alkyne<sup>91</sup>. For other reactions, ring formation can also be achieved by using triphenyl amine as substrate, which leads to the intramolecular ring closing mechanism with carbazole as final product.<sup>84</sup> The oxidation of aromatic rings can offer a useful platform for further substitution reactions. The oxidized aromatic rings can either undergo the reconstruction process for further reactions, such as oxidation of benzylic alcohols

to aldehydes<sup>82</sup>, or can react with the nucleophiles to form new chemical bond like direct bromination on aromatic systems<sup>54, 81, 83</sup>.

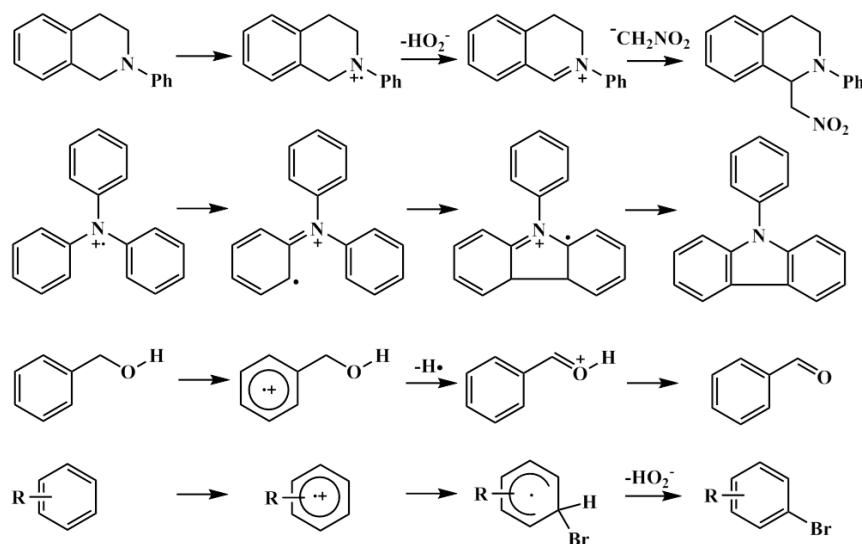


**Figure 3.12** Examples of net oxidative reactions.

### 3.2.3 Redox neutral reactions

Compared to the net reductive or oxidative reactions, redox neutral reactions are predominant. The proposed mechanism for the redox neutral reactions is shown in Figure 3.13. During the redox neutral catalytic cycle, the substrate undergoes both the reductive and oxidative processes, which means both electron accepting and donating processes are completed by substrate or its reconstructed intermediate during the closed catalytic cycle.

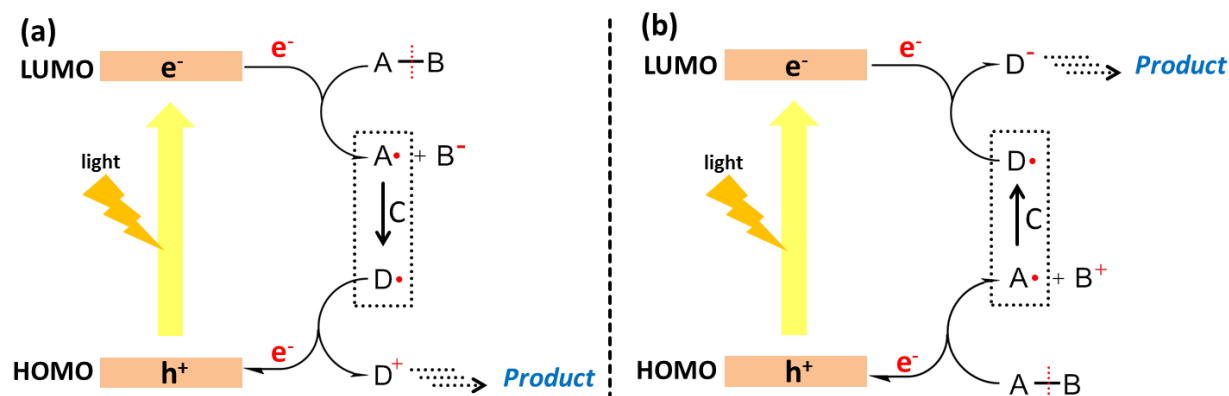


Figure 3.13 Representative mechanisms for the redox neutral reactions. A, B, C and D are different chemical groups.

### 3.2.3.1 Radical formation from cleavage of C-halide bond

C-halide bond is a good candidate for the electron accepting step to form the carbon radical and halogen anion (Figure 3.14). Unlike the net redox reactions, the radical formed here further reacts with unsaturated bond to form the new radical (intermediate), and then form the final product after giving out one electron and the reconstruction of the intermediate.

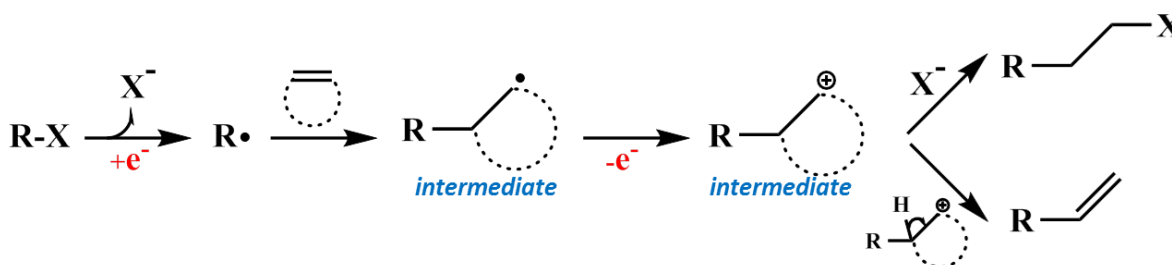


Figure 3.14 Illustration of the radical addition reaction with cleavage of C-halide bond.

Numerous reactions are designed depending on this catalytic cycle for different purpose. The halogen could be chloride<sup>92-94</sup>, bromine<sup>95-97</sup>, or iodine<sup>98-99</sup>, and the unsaturated bond could be double bond<sup>100-101</sup>, triple bond<sup>102</sup>, or aromatic rings<sup>103-104</sup>. The interesting part for this kind of reaction is its ability to provide an access for the synthesis of aromatic cross coupling product<sup>94</sup>

and fluoroalkylated product<sup>12</sup> as shown in Figure 3.15, which has great application in organic synthesis and medicine respectively.

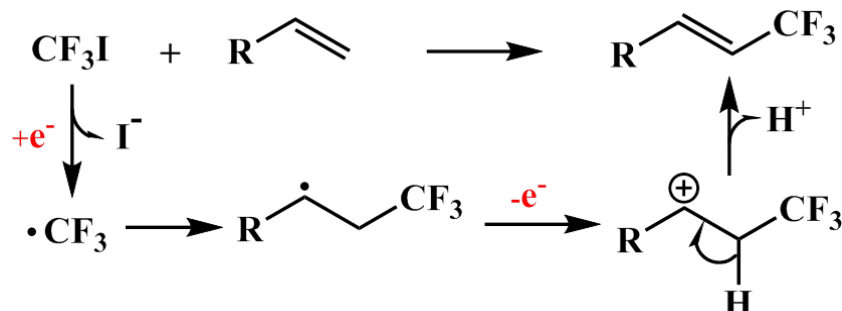


Figure 3.15 Examples of the trifluoromethylation reaction.

### 3.2.3.2 Radical formation from the cleavage of C-N<sub>2</sub>BF<sub>4</sub> and C-SO<sub>2</sub>Cl bonds

Compared to the C-halide bond, C-N<sub>2</sub>BF<sub>4</sub> and C-SO<sub>2</sub>Cl bonds are more active due to their lower reductive potentials, and the practical production of by-products in gas form (Figure 3.16). The C-N<sub>2</sub>BF<sub>4</sub> and C-SO<sub>2</sub>Cl bonds have been chosen as good precursor alternatives for the formation of radical intermediates compared to the C-halides.

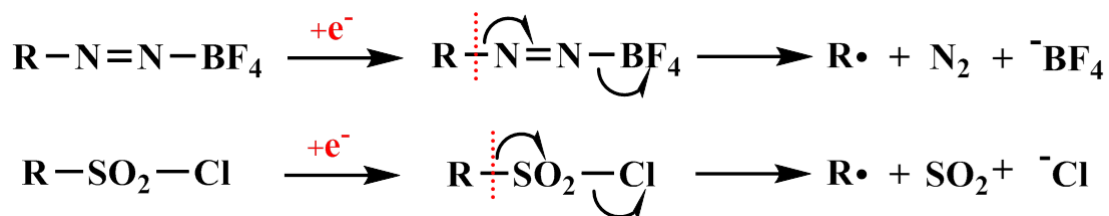
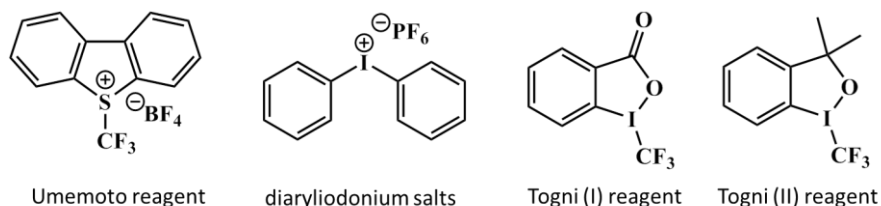


Figure 3.16 Illustration of radical formation from C-N<sub>2</sub>BF<sub>4</sub> and C-SO<sub>2</sub>Cl bonds.

Many reactions were accomplished using substrates that contain C-N<sub>2</sub>BF<sub>4</sub><sup>105-111</sup> and C-SO<sub>2</sub>Cl bonds<sup>112-116</sup>. Several cross-coupling, trifluoromethylation, and ring closing reactions were carried out with good to excellent yields.

### 3.2.3.3 Radical formation from electron deficient compounds

Some organic salts were utilized as active electron-accepting units to form the desired radical. Examples are diaryliodonium salts<sup>117-120</sup> and Umemoto reagent<sup>121-126</sup> as shown in Figure 3.17. Some reagents, such as Togni reagent that contain high oxidation state atoms can also be used as proper substrates to release radical after accepting one electron<sup>127-130</sup>.



**Figure 3.17** Examples of electron deficient compounds.

The formation mechanism of the active radicals is illustrated in Figure 3.18.

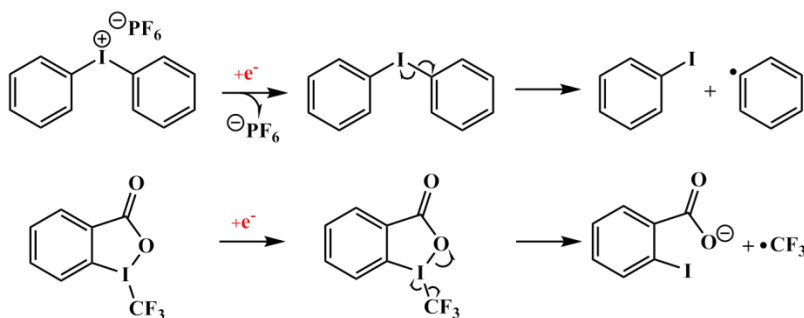


**Figure 3.18** Illustration of the radical formation process from diphenyliodonium salts and Togni (I) reagent.

### 3.2.3.4 Radical formation via the reduction of alkene

The alkenes that contain an electron withdrawing substitution are good candidates to form the radical anion via accepting one electron for subsequent reactions. Widely used alkenes are aryl enone.<sup>131</sup> The proposed mechanism is shown in Figure 3.19. The coordination of a Lewis acid, like  $\text{LiBF}_4$ , is required to improve the electron transfer process.<sup>132-134</sup> The radical formed here



can undergo both inter- or intramolecular [2+2] cycloaddition pathways to afford cyclic products.<sup>135-136</sup> An improved stereo-selectivity control can be achieved when using chiral Lewis acid as cocatalyst.<sup>137-139</sup>

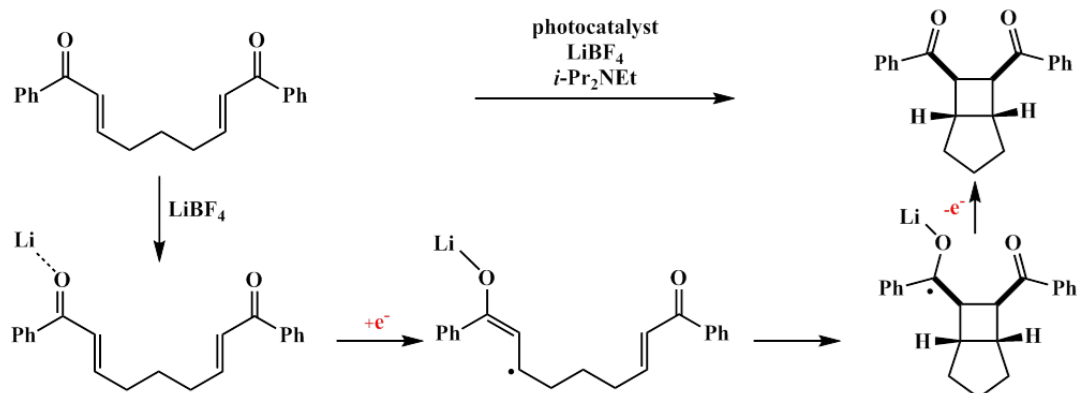


**Figure 3.19** Illustration of the mechanism for [2+2] cycloaddition reaction.

### 3.2.3.5 Radical formation via oxidation of alkyl amine

Another synthetic alternative for the formation of the radical is via the oxidation process, i.e. via the electron transfer from the substrate to the excited photocatalyst (Figure 3.13b). The substrates for this purpose usually contain an alkyl amine group, which can be oxidized and then be reconstructed to form the radical on the adjacent carbon.<sup>115, 140-147</sup> The efficiency of the radical formation process can be improved via changing the substitution on the  $\alpha$ -carbon from hydrogen to silyl or carboxyl.<sup>139, 148-153</sup>

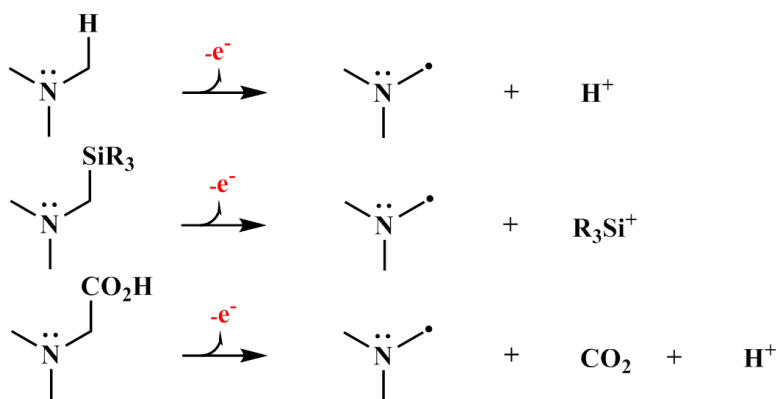


**Figure 3.20** Illustration of the formation of  $\alpha$ -aminoalkyl radicals.

In order to complete the catalytic cycle, the left half cycle should contain the electron accepting process, so the unsaturated bonds used here are always electron accepting compounds<sup>154-158</sup> or double bonds with electron withdrawing groups<sup>159-162</sup>. Examples are shown in Figure 3.21. The electron withdrawing group in alkene can stabilize the negative carbon ion, which makes the reduction of the radical intermediate to the corresponding anion exothermically.<sup>163-165</sup> Also, the electron deficient cyanoarene can be used as counterpart due to their ability to accept electron to form the intermediate that can add with amino alkyl radicals.<sup>166</sup>

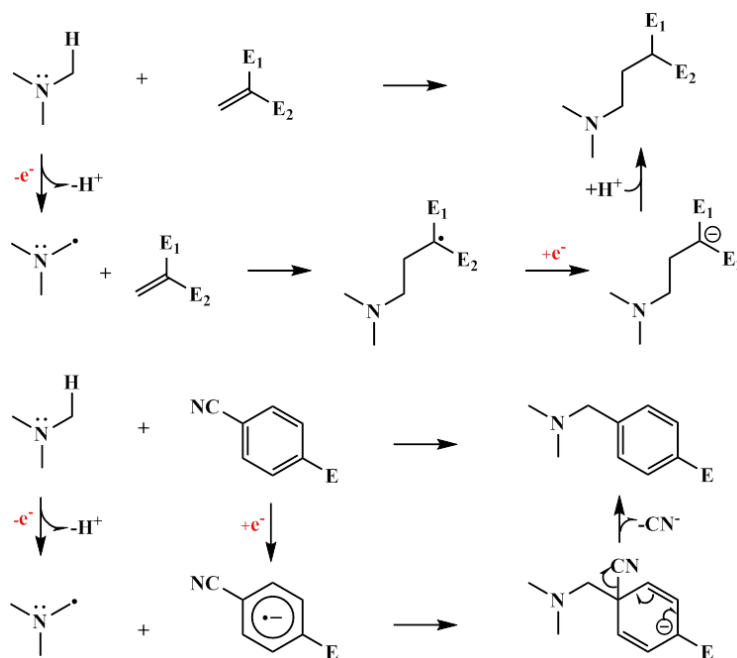


**Figure 3.21** Illustration of the mechanism for the reaction between amine and alkene and cyanoarene (E is short for electron withdrawing group).

### 3.2.3.6 Radical formation from the oxidation of –COOH bond

The substrate that contains a carboxylic acid group can be oxidized by the proper photocatalyst, and the resultant carboxyl radical is expected to rapidly extrude CO<sub>2</sub> to produce desired radical precursor.<sup>167-168</sup> The counterpart should be an electron accepting substrate, so the total electron is balanced in the catalytic cycle.<sup>153, 169-170</sup> For most of the decarboxylation reactions, a cocatalyst is always needed (Figure 3.22). The role of this cocatalyst is to accept an electron

from the catalyst to form the ligated Ni(0) species, which has an ability to react with an alkyl radical and then can insert into the C-Br bond. The desired product was formed via the elimination process. The C-X bond containing substrate could be the alkyl<sup>171</sup>, alkene<sup>172-173</sup> or aromatic one<sup>168, 174-175</sup>.

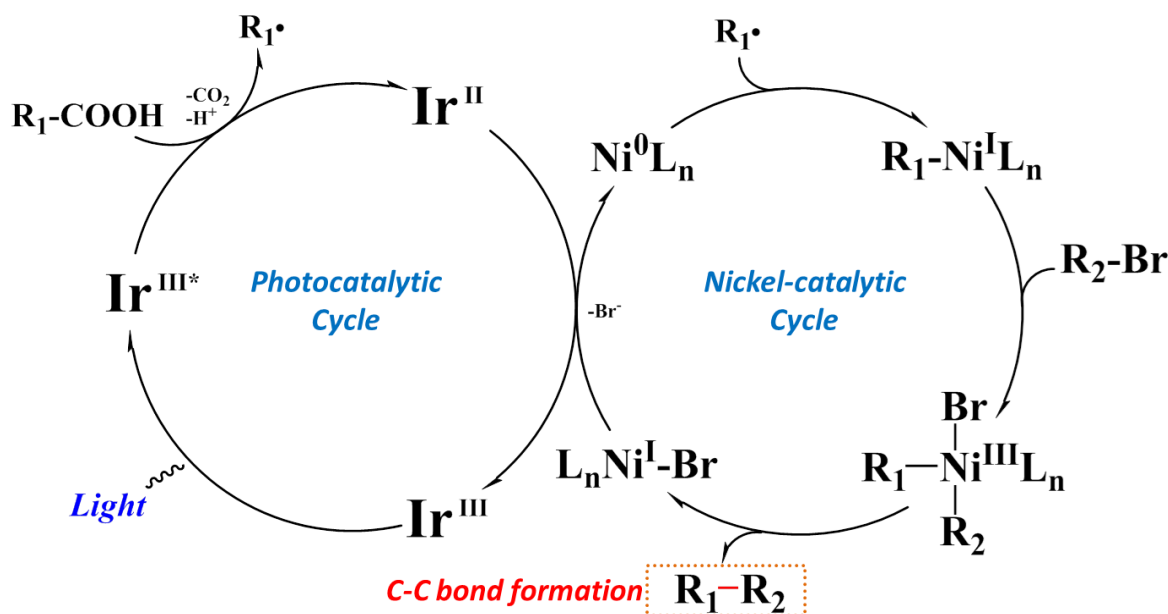


Figure 3.22 Illustration of the mechanism in bond formation via decarboxylation process.

### 3.2.3.7 Radical formation from the oxidation of alkene

Alkenes can be oxidized by the photocatalyst in its excited state, however, the oxidative potential of alkenes is usually high (Figure 3.23). Substitution of the alkene with electron donating groups can lower the energy that is required for oxidation, which will make the radical formation process easier.<sup>176</sup> Oxidation of the alkene will form the radical cation as precursor, which can react with the nucleophiles to form the adduct product.<sup>177-180</sup> After abstracting one hydrogen atom from a hydrogen donor, the final anti-Markovnikov addition product is obtained. The hydrogen donor used here should be regarded as an assistant catalyst since it also works as an electron accepting partner.<sup>181</sup>

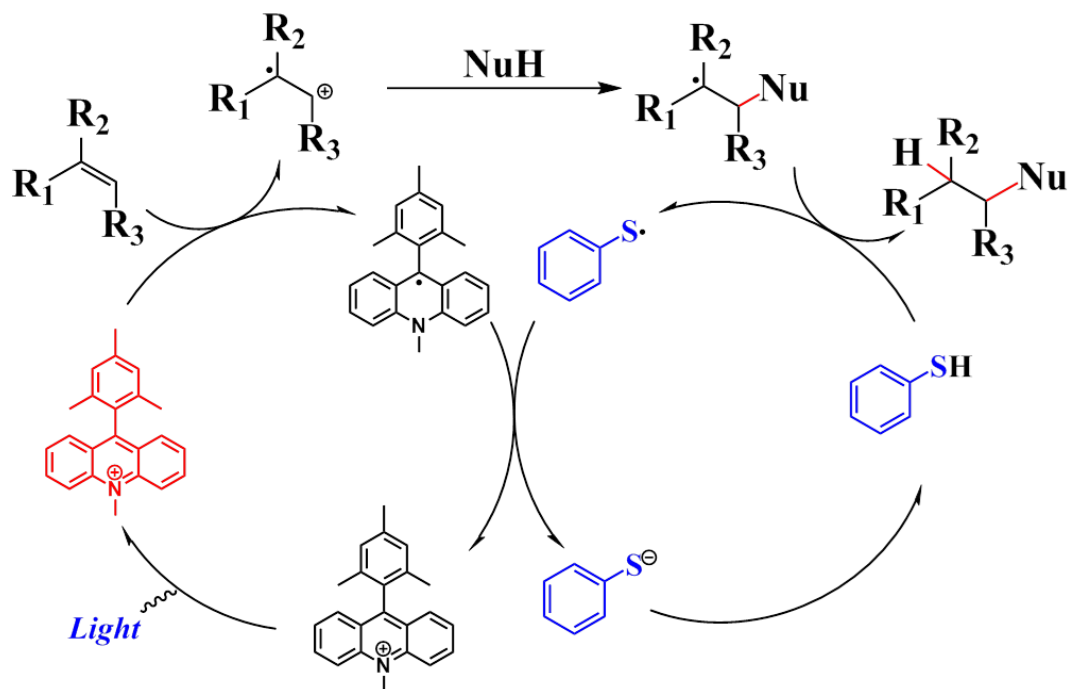
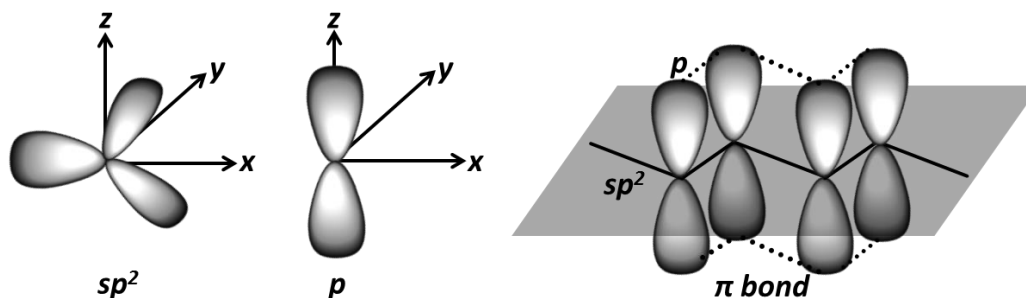


Figure 3.23 Illustration of the mechanism for anti-Markovnikov addition reaction.

### 3.3 Organic semiconductors

#### 3.3.1 Brief introduction of organic semiconductors

The most significant character for organic semiconductors is the unsaturated chemical bonds. The word “conjugate” is commonly used to describe the specific combination of the unsaturated double or triple bonds. Most of the conjugated  $\pi$ -electron systems possess the  $sp^2$  hybridization of the carbon orbitals. The hybridization results into three  $sp^2$  orbitals in  $xy$  plane and a  $p$  orbital in  $z$  axis. The backbone is formed via the combination  $sp^2$  orbitals within different carbons and the left  $p$  orbitals will form a  $\pi$  bond. Compared to the  $\sigma$  bond, the  $\pi$  bonds are significantly weak and have a rather delocalized nature as shown in Figure 3.24.



**Figure 3.24** Illustration of  $\sigma$  and  $\pi$  bonds formation in  $sp^2$  hybridization.

The specific conjugated  $\pi$  bonds are responsible for their semiconducting electronic properties. The onset of the absorption can be predicted by the energy level difference between the highest occupied molecular orbital (HOMO) and the lowest unoccupied molecular orbital (LUMO) as shown in Figure 3.25. This energy difference is called band gap. The starting wavelength of the absorption spectrum is determined by:

$$\Delta E_{\text{band gap}} = hc/\lambda$$

where  $h$  is the Planck constant,  $c$  is the speed of light and  $\lambda$  is the wavelength. After light absorption, the total energy of OSs raises due to the antibonding molecular orbital is occupied, and this state is called excited state.

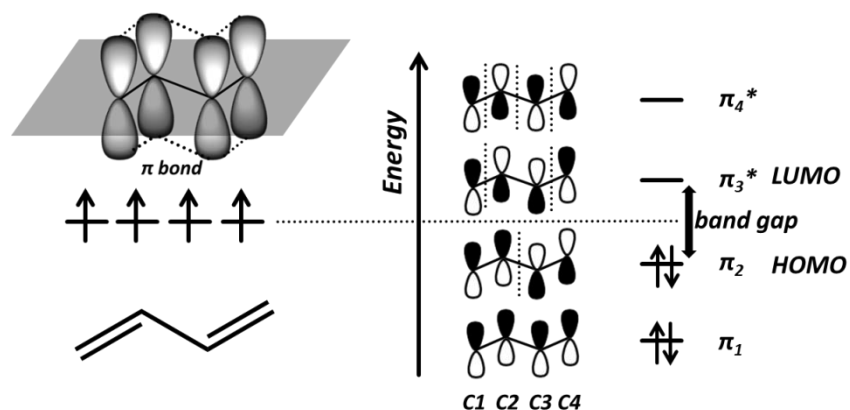


**Figure 3.25** Illustration of the molecular orbitals formation in butadiene.

### 3.3.2 Electronic properties

The most important properties for organic semiconductors are light absorption and electron transfer. Owing to the delocalized  $p$  electrons in the  $\pi$  orbital, the light can be absorbed by the organic semiconductors via the electron transfer from the bonding orbital to the antibonding orbital. This will result in the formation of the excited state of organic semiconductors. The detailed process for the light absorption process is illustrated in Figure 3.26. Usually, the ground state is a singlet state ( $S_0$ ), light absorption leads to the electron transfer to the first excited state ( $S_1$ ). Then the excited organic semiconductors can go back to the ground state again via whether a radiative light emitting (fluorescence) process or nonradiative transition process. The lifetime for the  $S_1$  state is always 1-10 ns. Also, during the excited state, a small fraction of singlet state ( $S_1$ ) can be converted into triplet state via intersystem crossing process. Compared to the singlet state, the triplet state owns a longer lifetime with a magnitude of milliseconds. Two pathways were considered to distinguish the triplet state: a radiative light emitting (phosphorescence) process or a nonradiative transition process.

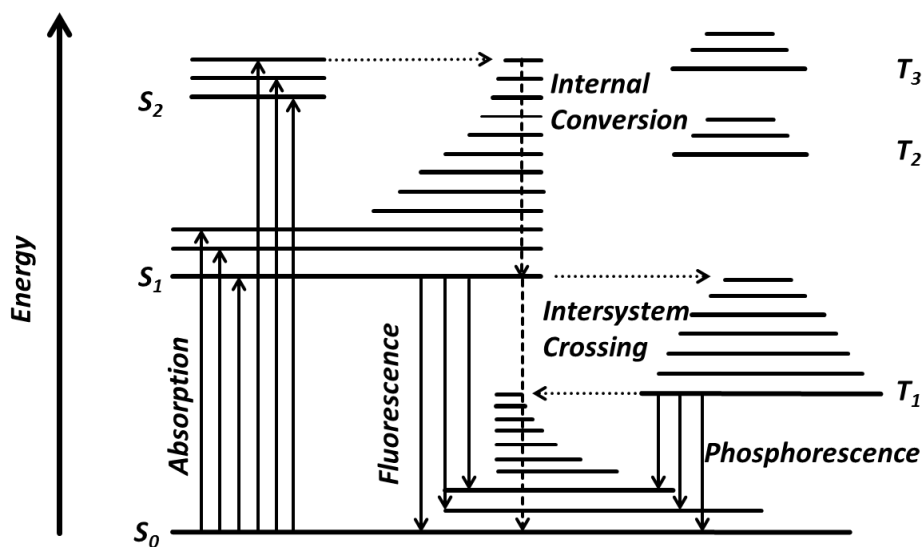


**Figure 3.26** Illustration of the energy levels in organic semiconductors.

The absorption spectrum of the organic semiconductors can be tuned via varying the conjugated  $\pi$  bonds. One method is to extend the unsaturated bond in the backbone structure. By increasing the conjugated units, the absorbed wavelength can be extended into the longer

range (Figure 3.27a and 3.27b).<sup>182</sup> This method can be demonstrated by comparing the light absorption differences between  $\beta$ -carotene and lycopene. Compared to the  $\beta$ -carotene, which has nine continuous alternative single-double bonds and results in the absorption onset at around 520 nm, lycopene has eleven continuous alternative single-double bonds and results in the absorption onset at around 560 nm. The other way to tune the energy levels in organic semiconductor is via the regular alternation of conjugated strong donor (D) and acceptor (A) moieties in a conjugated backbone.<sup>183-184</sup> Donors are a kind of hetero aromatic rings with an electron sufficient O, S or N atom, and acceptors are a kind of aromatic rings with a strong electron withdrawing group, like  $-C=O$ ,  $-C=N-$ . The reconstruction of the HOMO/LUMO levels while the combination of the donor and acceptor will result in the formation of new energy levels that has a smaller band gap than before (Figure 3.27c and 3.27d).<sup>185</sup> This D-A type organic semiconductors are widely used since the versatile energy levels can be achieved via the simple combination of different donor and acceptor units.

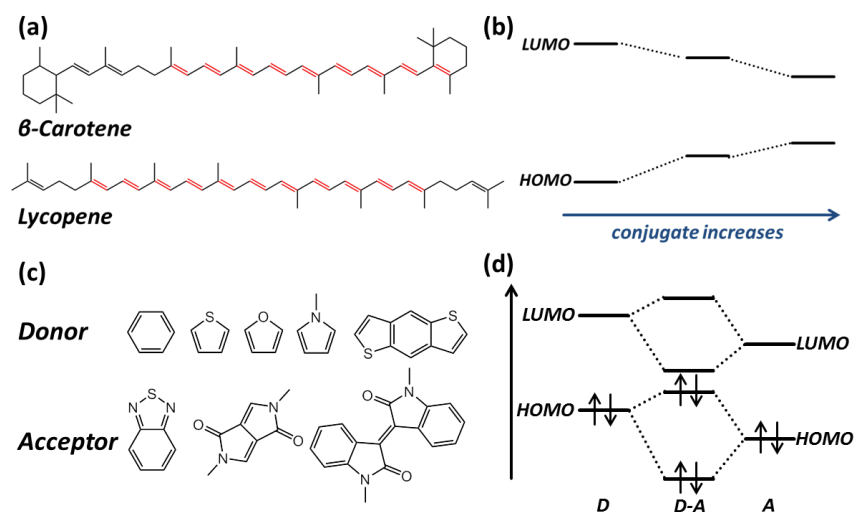


**Figure 3.27** (a) Chemical structure of  $\beta$ -carotene and Lycopene; (b) illustration of band gap decreases with increasing conjugated structure; (c) examples of donor and acceptor unit; and (d) illustration of energy levels hybridization in D-A type organic semiconductors.

### 3.3.3 Applications of organic semiconductors

Organic semiconductors have been widely used for the fabrication of organic thin film transistors (OTFTs)<sup>186-188</sup>, organic solar cells (OSCs)<sup>189-191</sup>, and organic light emitting diodes (OLEDs)<sup>192</sup> due to their excellent advantages in tuning electronic properties via chemical structure modification, low cost for processing and the ability for coating on soft matrix. Among these, directly converting light into electricity via OSCs is considered as one of the most promising and important application for organic semiconductors, since they provide an alternative solution to the increasing global energy need by using a cheap, clean and renewable source from sun. Great improvement of the power conversion efficiency (PCE) is achieved by bulk heterojunction, which is a mixture of the donor materials and acceptor material in nanoscale.<sup>20-21</sup>

The light harvesting and electricity converting process can be divided into four main steps as shown in Figure 3.28: (1) one electron is excited from the highest occupied molecular orbital (HOMO) to the lowest unoccupied molecular orbital (LUMO) via light absorption to form the excitons, (2) diffusion of the excitons to the surface between donor and acceptor, (3) due to the LUMO level difference between the donor and the acceptor, the electron can transfer from the LUMO of the donor to the LUMO of the acceptor to form the charge transfer (CT) state, which will further form the free holes and electrons, (4) gathering of the electrons and holes on the respective electrode.

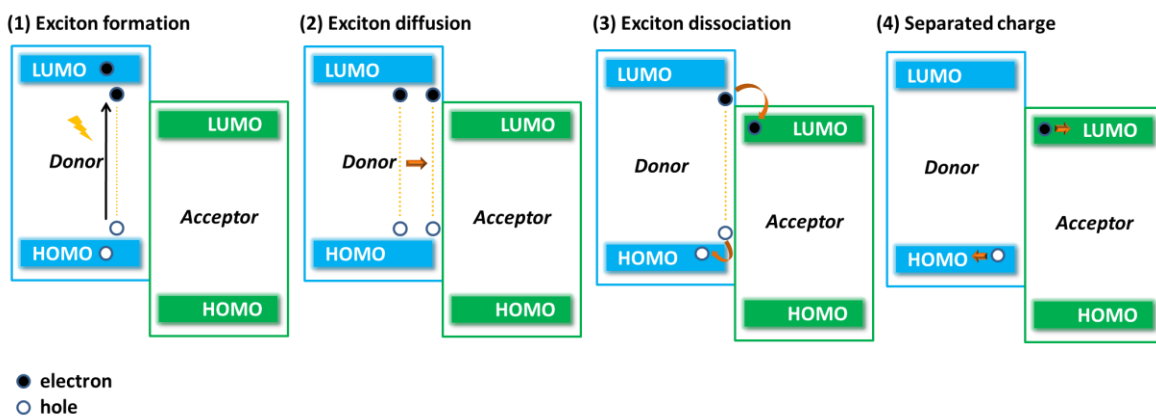


**Figure 3.28** Function principle of OSCs.



Compared to the direct conversion of light energy into the electricity via exciton separation process, the light energy can be also used as driving force for chemical transformations. In the so-called catalytic cycle using possible organic semiconductor-containing photocatalysts, two main processes for the utilization of photo energy are the excited state formation of the photocatalysts via light absorption and subsequent electron transfer to or from the substrate for activation. A similar model of the light-generated charge separation for the organic solar cells can be taken to applicate in photocatalysis, however, the electron donor and acceptor materials should be fused together. Compared to the well-studied organic metal complex and the organic dye type photocatalyst, reports on organic semiconductor photocatalyst are still rare. It is therefore our plan to develop this class of metal-free materials as efficient photocatalytic systems.

## 4 Characterization Techniques

### 4.1 Ultraviolet-visible spectroscopy

The ultraviolet-visible (UV-Vis) spectroscopy presents the range of wavelength that can be absorbed by a sample in ultraviolet and visible regions. In a typical UV-Vis measurement, light with a specific wavelength range passes through the sample and the detector records the non-absorbed light. Compared to the blank sample, the final absorption spectrum will show not only the wavelength that can be absorbed by the sample, but also the intensity. ***The absorption spectrum is a direct indicator for organic semiconductors to determine the light source in photocatalytic reactions.***

### 4.2 Cyclic voltammetry

Cyclic voltammetry (CV) is an electrochemical measurement that is widely used for determining the electronic properties of the materials. For soluble samples, the CV measurement is usually conducted in solutions that contain the sample and electrolyte. A standard CV setup employs

an electric cell with three electrodes: working electrode, counter electrode and reference electrode. In a measurement, a potential that linearly increases then linearly decreases as a cycle is applied between the working electrode and reference electrode, and the current between the working electrode and counter electrode is recorded. The data was given as a plot of current (y axis) versus applied potential (x axis). Depending on the potential applied in cell, the electrode can abstract electrons from the analyte or can give out electrons to the analyte, which will result in the oxidation or reduction of the analyte respectively. The onset of i-v curve is used in this dissertation to determine the minimums potential that is required for oxidizing or reducing the substrates. And also, the HOMO or LUMO of small molecule organic semiconductor is settled with the onset of i-v curve. ***The main purpose of the CV measurement is to determine the energy levels of the photocatalysts and all substrates in a catalytic cycle.***

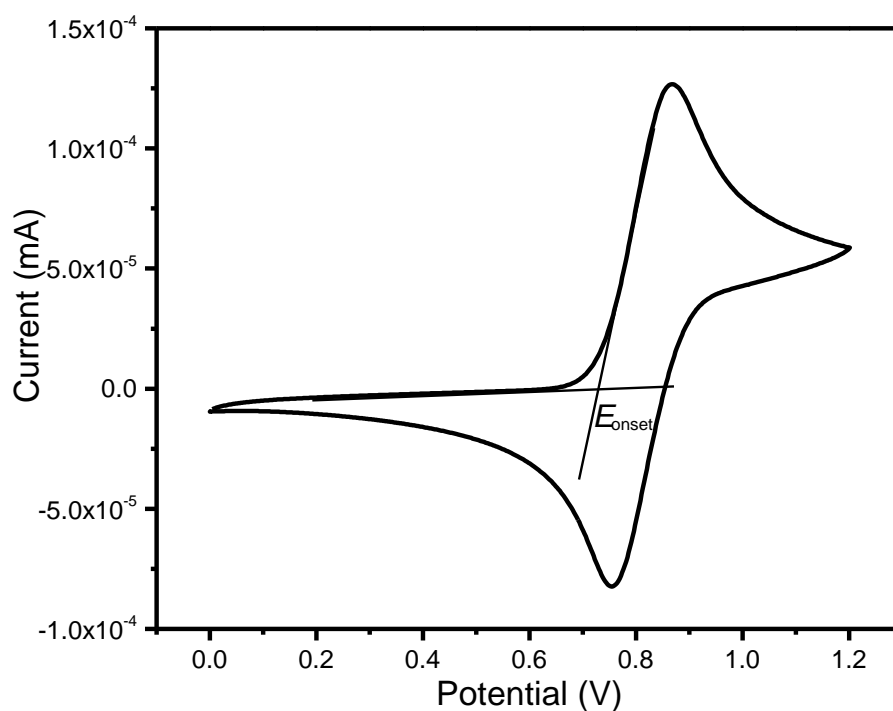


**Figure 4.1** Illustration of a typical cyclic voltammogram.

### 4.3 Fluorescence quenching

Fluorescence is the radiative emission of the excited materials. In a typical measurement, a monochrome light source (excited wavelength) passes through the solution of sample to form the excited state, and then the emitted light is recorded by a detector placed at a different angle. Quenching is a process that will decrease the intensity of the fluorescence produced by a sample. The fluorescence quenching experiment is a direct measurement to determine whether the excited sample has an interaction with the added substrate. This technique shows the competition between two deactivation pathways for an excited sample: emission and electron transfer. Increasing the concentration of the added substrate, the fluorescence of the sample will decrease, which can be described by the Stern-Volmer equation:

$$I_0/I = 1 + K_{sv}[Q]$$

where  $I_0$  is the fluorescence intensity of the pure sample,  $I$  is the fluorescence intensity of the sample with specific concentration of quencher,  $K_{sv}$  is the Stern–Volmer constant and  $[Q]$  is the concentration of quencher. Only if the interaction between the excited sample and added substrate existed, the fluorescence can be quenched. ***In this dissertation, the fluorescence quenching experiment is used to determine the interaction between the photocatalyst and all the substrates in a photocatalytic reaction.***

### 4.4 Time-resolved fluorescence spectroscopy

Time-resolved fluorescence spectroscopy is an advanced extension of fluorescence spectroscopy, which gives the plot about the fluorescence intensity decay of the given sample as a function of time after pulsed excitation. It is used to determine the fluorescence lifetime of excited singlet state, where the intensity of the fluorescence can be determined by the following equation:

$$I = I_0 e^{-t/\tau}$$

where  $I_0$  is the fluorescence intensity at  $t = 0$  and  $\tau$  is the lifetime of singlet state. The lifetime  $\tau$  is a reciprocal of rate constant for total decay pathways. For one that the fluorescence is the only way for deactivation of the excited state,  $\tau$  equals to  $1/k_f$ , and the plot of  $\ln I$  versus  $t$  is in a linear relationship. ***In this dissertation, time-resolved fluorescence spectroscopy is used to***

***determine the lifetime of the excited photocatalysts, it will give us the information about the sustained time period of singlet state which is the main state utilized for electron transfer between the excited photocatalyst and substrates.***

## **5 Results and Discussions**

The chapter of results and discussions is divided into four sections. In chapter 5.1, the main purpose is to establish a structural design principle of the D-A type small molecule organic semiconductors (SMOS) as visible light-active photocatalysts by investigating important factors such as absorption range, energy band structure, or lifetime of the excitons that can influence the catalytic efficiency. In the next three chapters, chapter 5.2, 5.3 and 5.4, the main purpose is to further investigate the feasibility of the organic semiconductors as photocatalysts in chosen challenging reactions. In particular, chapter 5.2 deals with a new conceptual study on the so-called cooperative photocatalyst systems, in which the charge separation process can be enhanced via intermolecular electron and hole transfer between the cooperative photocatalysts and thereby delivering long-living excitons formation for a sacrificial reagent-free purpose. In chapter 5.3, via the structure optimization of the organic semiconductors, an extremely high reductive potential OS photocatalyst was synthesized to meet the demand for the radical formation from common arene halides, which can further form aromatic C-C bonds with other arenes. In chapter 5.4, the organic semiconductors are designed to successfully catalyze controllable atom transfer radical polymerization (ATRP) via the energy levels modification of not only the photocatalyst, but also the initiator, active polymer chain end and sacrificial reagent.

### **5.1 Structural design principle of small molecule organic semiconductors for metal-free, visible light-promoted photocatalysis**

In the following chapter, two series of electron-donor and acceptor-type organic semiconductor molecules were synthesized to meet crucial requirements, such as 1) absorption range in the

visible region, 2) sufficient photoredox potential, and 3) long lifetime of photogenerated excitons. The utilization of the organic semiconductors as photocatalysts showed good efficiency for both the dehalogenation of  $\alpha$ -bromoacetophenone and intermolecular radical C-C coupling reactions. Through detailed examination, it is proved that electrons could successfully transfer between the catalyst and substrates, which indicates the promising perspective of semiconductors as photocatalyst. Due to the defined energy levels of the organic semiconductors, the potential difference ("over potential") between the photocatalyst and substrate is found to be the dominated reason that determines the total reaction time. The chapter is based on and adapted from the published article: *Angew. Chem. Int. Ed.* 2016, 55, 9783–9787, DOI: 10.1002/anie.201603789.

### 5.1.1 Motivation

Organic semiconductors have gained tremendous interest for applications in organic light emitting diodes (OLEDs)<sup>192</sup>, organic solar cells (OSCs)<sup>189-190</sup> and organic thin film transistors (OTFTs)<sup>188, 193</sup> because of their unique optical and electronic properties originated from its  $\pi$ -conjugated structure. Among these, organic solar cells, which can directly harvest energy from sunlight, are regarded as a promising means to meet the increasing demand for clean and renewable energies. It is commonly believed that a consequence of photoexcitation, exciton diffusion and then exciton dissociation is involved to transform the light into electricity, namely, a photo induced free electron formation process.

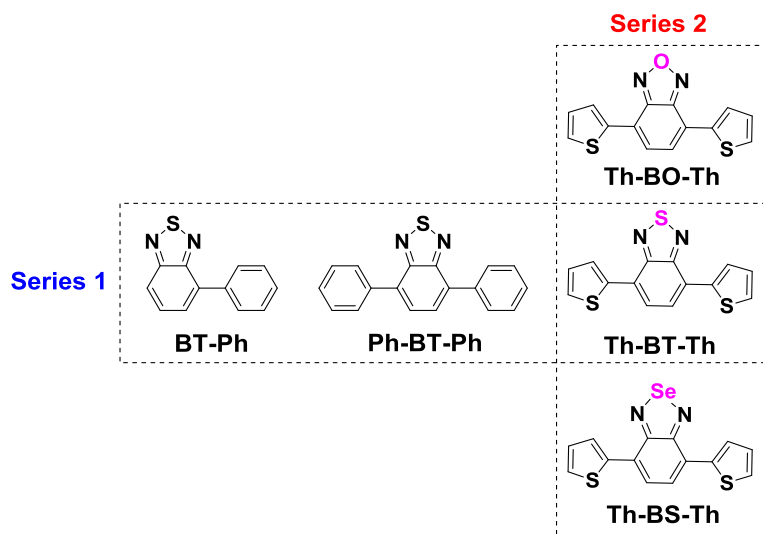
Photocatalysts, which are developed in recent years as a new strategy for chemical synthesis under mild and environmentally benign conditions, also involve a light activation, then a single-electron-transfer (SET) process, which means that the excited state formed after light absorption and the photocatalyst can work as an electron donor as well as an electron acceptor depends on the specific catalytic cycle.<sup>6-8, 13</sup> The most famous one is the organometallic complex based on costly and toxic noble metal ruthenium and iridium, such as  $\text{Ru}(\text{bpy})_3\text{Cl}_2$ , *fac*- $\text{Ir}(\text{ppy})_3$  and  $\text{Ir}(\text{ppy})_2(\text{dtbbpy})\text{PF}_6$  (bpy = bipyridine, ppy = 2-phenyl-pyridine, dtbbpy = 4,4'-di-tert-

butyl-2,2'-bipyridine).<sup>50, 139, 170, 194-196</sup> Also, a series of simple, inexpensive and metal-free organic dyes are tested to achieve the same desired transformation, and are proved to be efficient photocatalysts for versatile reactions.<sup>37, 52, 55, 58, 81, 197</sup>

Although, noble metal based organometallic complexes and organic dyes are suitable to work as efficient photocatalyst, it is still under strong demand to find a new category of photocatalyst that occupies versatile chemical and physical properties such as chemical structure, absorption spectrum, oxidative/reductive potentials, as well as easy modification of the catalyst for different utilizing purposes. Given the fact that same process is occupied at the very beginning by both organic semiconductors for solar cells and photocatalysts, namely photoexcitation then charge separation, it motivates us to think that using specific substrates instead of the acceptor materials as electron delivery stuff can also result in efficient electron-transfer process to initiate the reaction, then organic semiconductors might be treated as a promising new category of photocatalyst.

### 5.1.2 Design of the D-A type small molecule organic semiconductors for photocatalyst

The requirements for D-A type small molecule organic semiconductors as organic molecular photocatalysts are described as below: 1) absorption range in the visible region, 2) sufficient light generated redox potential, and 3) long lifetime of the photo generated excitons. The structures of the SMOSs are displayed in Scheme 1. Containing the same benzothiadiazole (BT) unit as the electron-acceptor moiety, series 1 represents different electron-donor variations, such as single phenyl ring (BT-Ph), two phenyl rings (Ph-BT-Ph), and two thiophene units (Th-BT-Th). In comparison, series 2 shows the opposite structural design principle using thiophene as the electron donor unit in combination with different benzochalcogenadiazoles, such as benzooxadiazole (Th-BO-Th), benzothiadiazole (Th-BT-Th), and benzoselenadiazole (Th-BS-Th) as the electron acceptor.



**Scheme 5.1 Structures of the two series of the small molecule organic semiconductors.**

### 5.1.3 Physical properties of the designed photocatalysts in series 1

Since the kind and number of the donor unit are different in series 1, the absorption spectrum differs from each other (Figure 5.1). Compared to the BT-Ph, BT connected with two phenyl ring result in an absorption in a longer wavelength region, and this is further improved with a strong donor thiophene, which has a broad absorption spectrum at the longest wavelength region. Since the light source we used here is a house hold bulb, which is a white light that has a broad emitting spectrum, Th-BT-Th seems to be able to capture more photons compared to the Ph-BT and Ph-BT-Ph, which may accelerate the reaction.

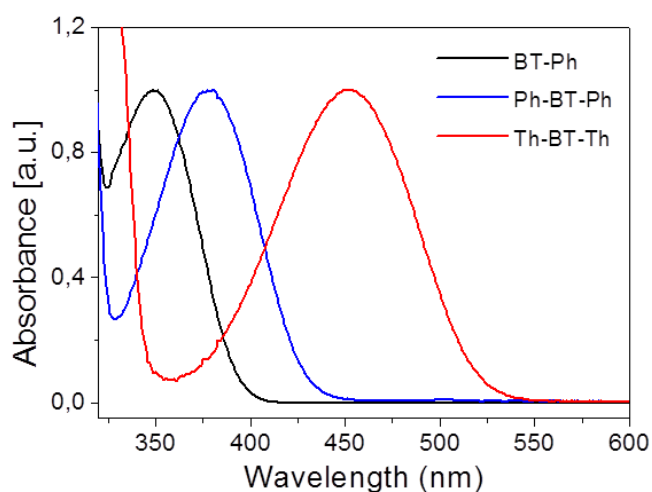


**Figure 5.1 Absorption spectrum of the SMOSs in series 1.**

Altering the donor results not only in varying the absorption spectrum, but also the energy levels of the SMOSs in series 1, namely the HOMO/LUMO levels. BT-Ph owns the highest band gap with a reductive potential of -1.35 V vs SCE and an oxidative potential of +1.83 V vs SCE. Th-BT-Th owns the lowest band gap with a reductive potential of -1.15 V vs SCE and oxidative potential of +1.12 V vs SCE as shown in Figure 5.2.

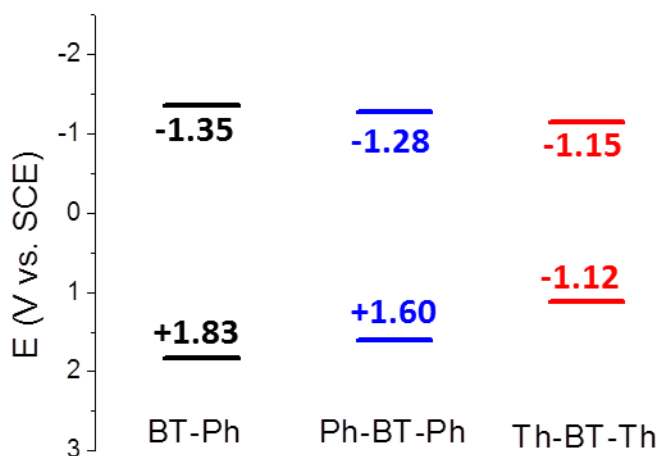
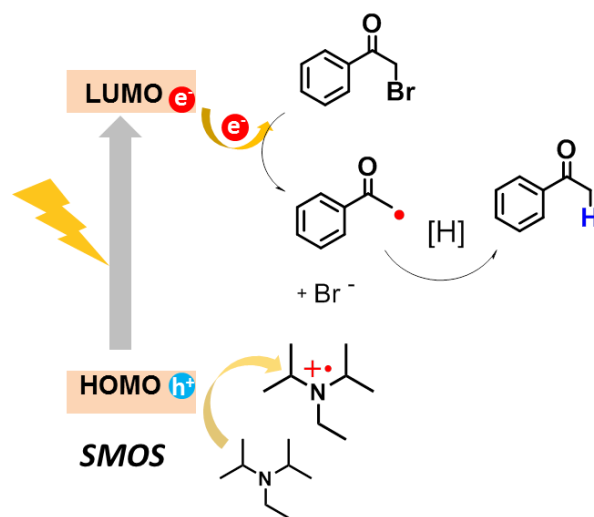


**Figure 5.2 Illustration of the HOMO/LUMO levels of SMOSs in series 1.**



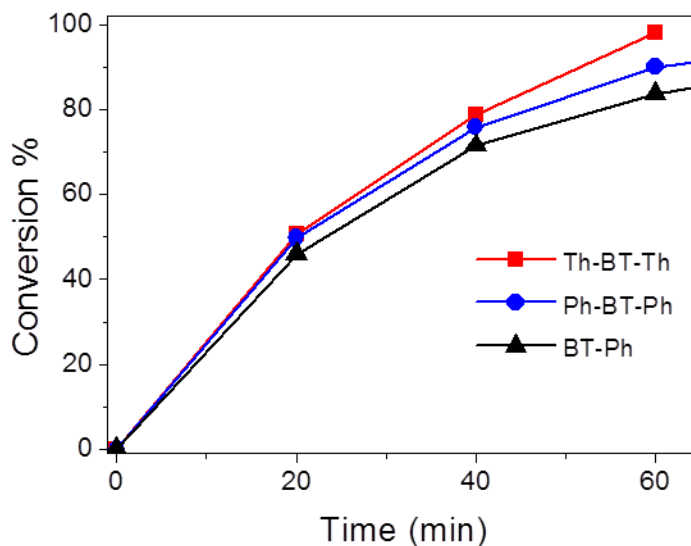
#### 5.1.4 Electron transfer test between the photocatalyst in series 1 and $\alpha$ -bromoacetophenones

To separately investigate the electron transfer from the photo-catalyst onto the halide, we conducted first the light-induced dehalogenation reaction of haloketone derivatives such as  $\alpha$ -bromoacetophenones using the SMOSs of series 1 as photocatalysts and diisopropylethylamine (DIEPA) as the electron-donating sacrificial reagent. The mechanism is shown in Figure 5.3. After light absorption, the electron transfer from the HOMO to LUMO formed the excited state. With the electron delivered from a sacrificial reagent, the hole on the HOMO is occupied and the electron on the LUMO is transferred to the substrate for the cleavage of the C-Br bond to form the carbon radical. The radical is further reacted with a hydrogen atom donor to form the final dehalogenation product.



**Figure 5.3** Illustration of the mechanism for the dehalogenation reaction.

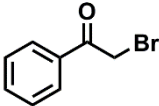
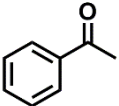
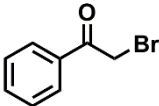
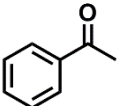
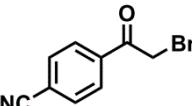
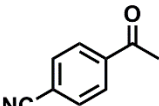
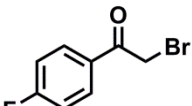
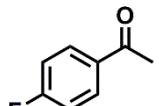
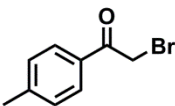
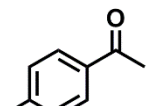
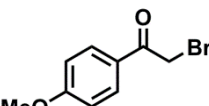
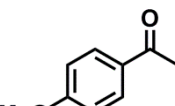
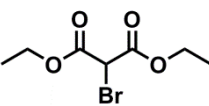
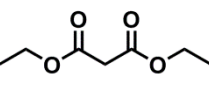
The electron transfer process is the key process for the dehalogenation reaction, and also an indicator for the possibility of the D-A type small molecule organic semiconductors as photocatalyst. Under the irradiation of a household energy saving light bulb (23 W), Th-BT-Th exhibited the highest reaction rate (Figure 5.4), reaching full conversion within one hour with a low catalyst load (1 mol%), followed by Ph-BT-Ph. With BT-Ph as photocatalyst, a longer reaction time of ca. 2 h was required.



**Figure 5.4** Rates of the light-induced dehalogenation reaction of  $\alpha$ -bromoacetophenone using SMOSs as photocatalysts; reaction condition:  $\alpha$ -bromoacetophenone (1 mmol, 1 equiv.), hantzsch ester (1.1 mmol, 1.1 equiv.), *N,N*-diisopropylethylamine (2 mmol, 2 equiv.), catalyst (1 mol%) and 2 ml DMF.

The success of the dehalogenation reaction is further tested by changing the Br-containing substrates with Th-BT-Th as photocatalyst, and the result is shown in Table 5.1.

**Table 5.1 Photocatalytic dehalogenation reaction of different haloketones using Th-BT-Th as catalyst.**

Entry	Substrate	Product	Reaction time[h] <sup>a</sup>	Yield[%] <sup>b</sup>
1			1	76
2 <sup>c</sup>			1	trace
3			1	83
4			1.5	77
5			3	80
6			3	86
7			2.5	87

<sup>a</sup>Reaction time determined by <sup>1</sup>H NMR analysis by reaching full conversion. <sup>b</sup>Isolated yield after purification over SiO<sub>2</sub>. <sup>c</sup>No DIEPA.

The difference in HOMO/LUMO levels may also influence the reaction rate, so the fluorescence quenching experiment is conducted to determine the interaction between the excited photocatalyst and the substrate: Br containing substrate and DIPEA (Figure 5.5-5.7). It was shown that the fluorescence of the SMOSs could be gradually quenched by adding the amine, while the addition of diethyl bromomalonate did not affect the fluorescence. This result indicates that for the SMOS-based systems, the excited electron could not be transferred directed to diethyl bromomalonate without employing an electron donor. This further indicates that the electron originated from the sacrificial reagent via oxidative extraction by the photogenerated hole. Similar light-induced electron mediation has been demonstrated by employing polymeric systems as photocatalysts.<sup>46, 198</sup>

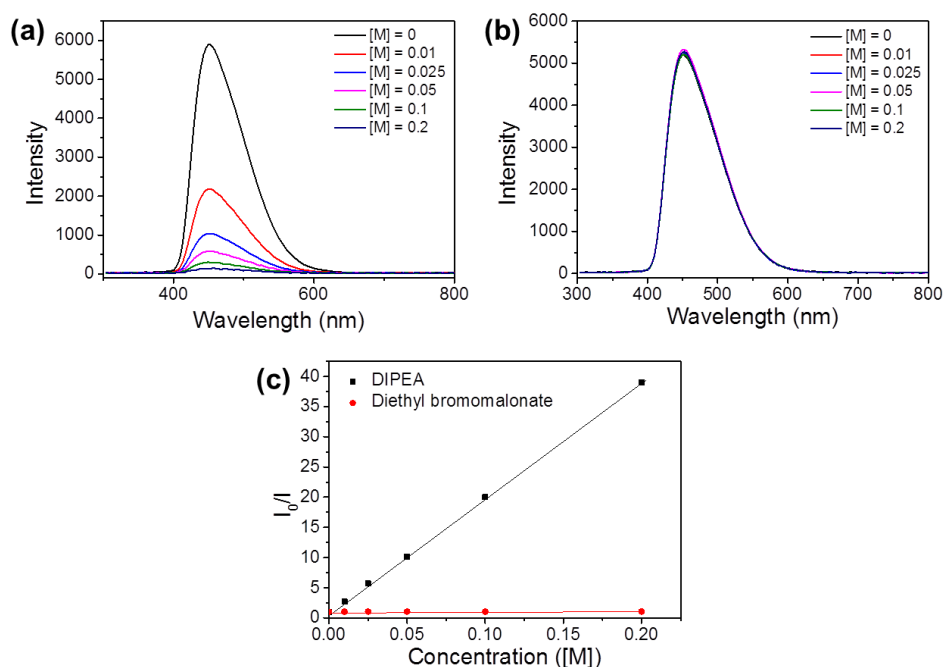


**Figure 5.5 Fluorescence quenching of Ph-BT with (a) diisopropylethylamine and (b) diethyl bromomalonate, and (c) Stern-Volmer curve.**

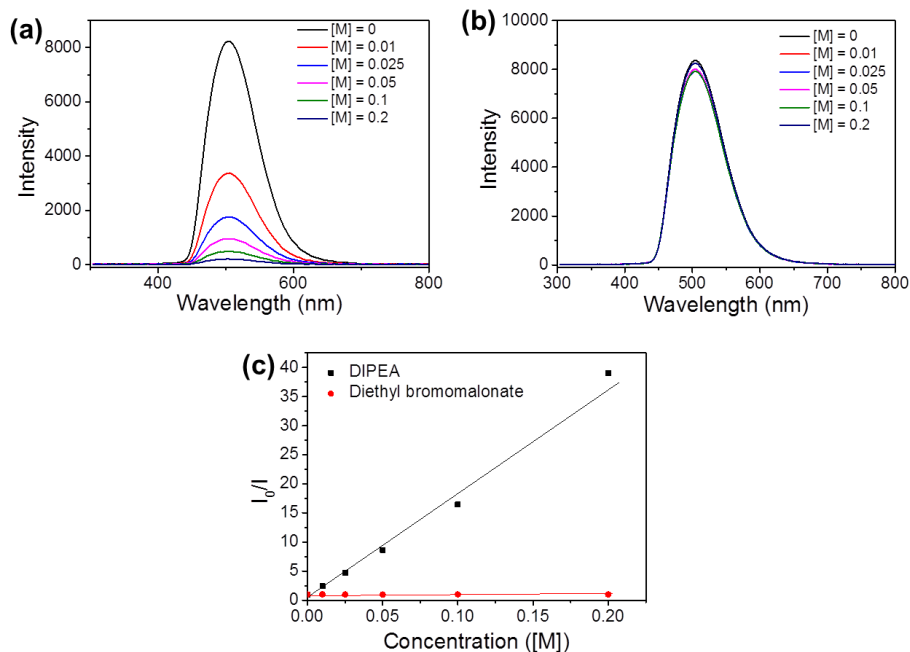


**Figure 5.6** Fluorescence quenching of Ph-BT-Ph with (a) diisopropylethylamine and (b) diethyl bromomalonate, and (c) Stern-Volmer curve.

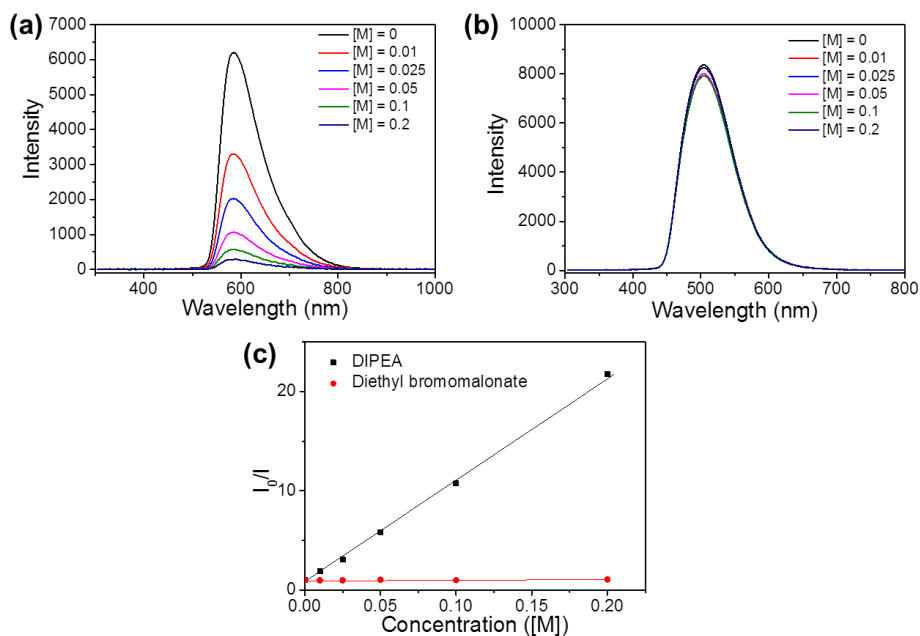


**Figure 5.7** Fluorescence quenching of Th-BT-Th with (a) diisopropylethylamine and (b) diethyl bromomalonate, and (c) Stern-Volmer curve.

From the rate constants for the fluorescence quenching between the SMOSs in series 1 and DIPEA, we found that the quenching is in a quicker rate if the HOMO energy is higher. Significantly, the highest oxidative and reductive potentials of Ph-BT (-1.35 V and +1.83 V vs. saturated calomel electrode (SCE)) did not lead to the highest reaction rate within the series. This is because the redox potentials of all three catalysts are sufficient enough for the oxidation of DIPEA (+0.52V vs. SCE) and for the reduction of  $\alpha$ -bromoacetophenone (-0.99 V vs. SCE). The superior catalytic activity of Th-BT-Th should be rather attributed to its broader absorption range in the visible region up to 550 nm, while Ph-BT and Ph-BT-Ph mainly absorb in the UV and blue region.

**Table 5.2 Fluorescence quenching constants ( $K_{sv}$ ) of different photocatalysts using diisopropylethylamine as reductant**

photocatalyst	quenching constant
Ph-BT	$K_{sv} = 190.68$
Ph-BT-Ph	$K_{sv} = 188.79$
Th-BT-Th	$K_{sv} = 104.19$

### 5.1.5 Photocatalytic C-H functionalization of electron-rich heteroaromatics with diethyl bromomalonate

To complete the reaction cycle of the photocatalytic intermolecular C-H functionalization, we then tested the functionalization reaction of 3-methylindole and diethyl bromomalonate using series 2 catalysts with similar absorption ranges in the visible region. The absorption spectrum of the OSs in series 2 is shown in Figure 5.8.

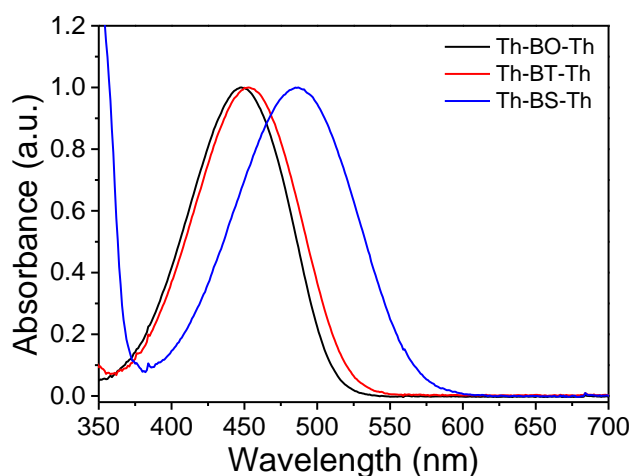


**Figure 5.8** Absorption spectrum of Th-BO-Th, Th-BT-Th, and Th-BS-Th (ca.  $10^{-5}$  mol/ml in DCM).

The reaction mechanism is shown in Figure 5.9.<sup>199</sup> The first step is also the formation of the radical, but the radical here further added with a double bond to form a new radical. This intermediate then gave out one electron to the oxidized sacrificial reagent, and after reconstruction formed the final product.

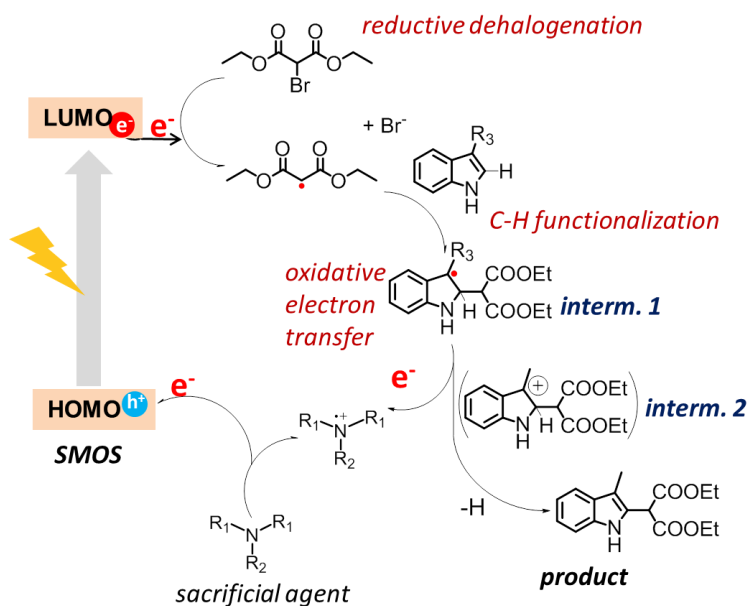


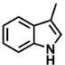
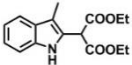
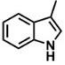
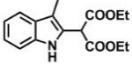
**Figure 5.9** Illustration of the mechanism for intermolecular C-H functionalization reaction.

A blue LED lamp (460 nm, 1.2 Wcm<sup>-2</sup>) was used as light source to accelerate the reaction rate. Unlike for the dehalogenation reaction, triphenylamine was used instead of DIPEA to avoid the hydrogen abstraction process by the diethyl malonate radical and to increase the final yield. The results are listed in Table 5.3. It was shown that all three SMOSs could catalyze the reaction in high conversion and yields, with Th-BT-Th again being the most efficient photocatalyst within series 2 using 3-methylindole as model substrate (Table 5.3, entry 2). Additionally, using BT-Ph and Ph-BT-Ph as catalyst lead either to no or a very low yield of product (Table 5.3, entry 7 and 8), demonstrating the absorption in the visible range is indispensable. Note that the catalytic efficiency of Th-BT-Th is comparable with the state-of-art photocatalysts based on transition metals, such as [Ru(bpy)<sub>3</sub>]Cl<sub>2</sub>, for the same type of photoredox reactions.

**Table 5.3 Photocatalytic C-C bond formaton via C-H functionalization of electron rich heteroaromates with diethyl bromomalonate using the SMOSs as photocatalysts.**

entry	catalyst	substrates	products	time [h]	conv. [%] <sup>a</sup>	yield [%] <sup>b</sup>
1	Th-BO-Th			15	>99	82
2	Th-BT-Th			0.75	>99	86
3	Th-BS-Th			14	>99	85
4	Th-BT-Th			2	>99	78
5	Th-BT-Th			2	>99	87
6	Th-BT-Th			1	>99	90



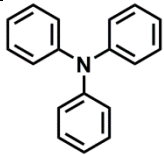
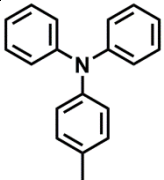
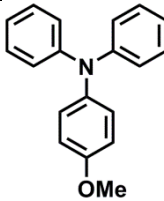
7	Ph-BT			6	0	-
8	Ph-BT-Ph			6	20	5

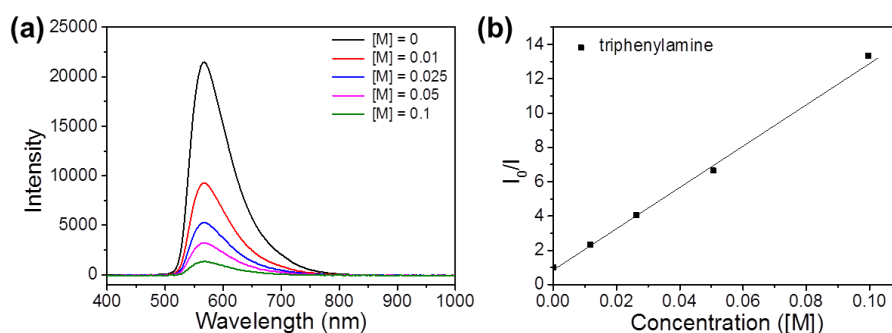
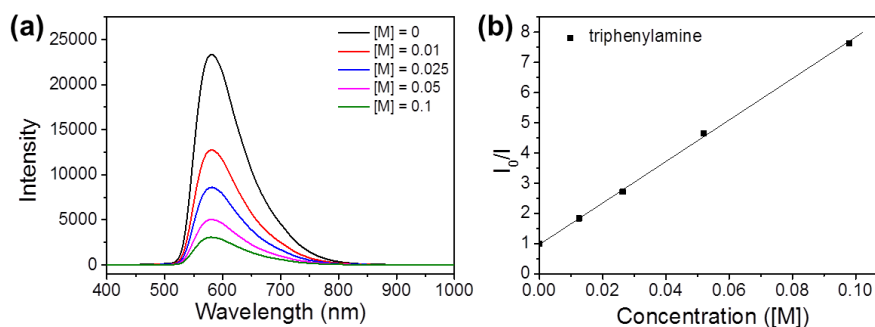
[a] Reaction conditions: 1 equiv (0.38 mmol) heteroarene, 2 equiv diethyl bromomalonate, 2 equiv 4-methoxy-N,N-diphenylaniline, 1 mol% photocatalyst in 2.5 mL DMF, blue LED ( $\lambda=460$  nm). [b] Determined by GC-MS. [c] Yield of isolated product after purification over  $\text{SiO}_2$ .

### 5.1.6 Factor that influences the C–H functionalization reaction

The superior catalytic efficiency of Th-BT-Th corresponded well with its redox potential, which is sufficient to both reduce diethyl bromomalonate ( $E_{\text{red}} = -1.0$  V vs. SCE) and oxidize triphenylamine ( $E_{\text{oxi}} = +0.89$  V vs. SCE). In comparison, despite the high oxidation potentials of Th-BO-Th ( $E_{\text{oxi}} = +1.24$  V vs. SCE) and Th-BS-Th ( $E_{\text{oxi}} = +1.02$  V vs. SCE), their reduction potentials with  $-1.06$  V and  $-1.08$  V (vs. SCE) appeared insufficient to reduce diethyl bromomalonate, indicating that the reductive half cycle might be the rate-determining step. The fluorescence quenching experiment is conducted to verify the influence of the interaction between the excited SMOSs and sacrificial reagent (Table 5.4 and Figure 5.10-5.14). The quenching constant increases with increasing of the potential difference between the oxidative potential of sacrificial reagent and the HOMO of the SMOSs. Although Th-BO-Th owns the quickest interaction with triphenylamine, the overall reaction rate is quickest for Th-BT-Th, which also confirmed that overall reaction rate is mainly determined by the LUMO level.

**Table 5.4  $K_{SV}$  of fluorescence quenching with different catalysts and reductants.**

Quencher			
			
Photocatalyst			
Th-BO-Th	$K_{SV} = 123.52$	-	-
Th-BT-Th	$K_{SV} = 68.1$	$K_{SV} = 82.13$	$K_{SV} = 107.8$
Th-BS-Th	$K_{SV} = 35.7$	-	-

**Figure 5.10 (a) Fluorescence quenching of Th-BO-Th with triphenylamine and (b) Stern-Volmer curve.****Figure 5.11 (a) Fluorescence quenching of Th-BT-Th with triphenylamine and (b) Stern-Volmer curve.**

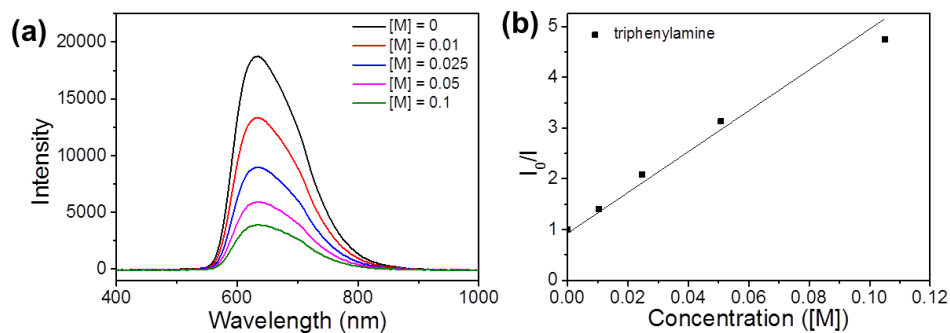


**Figure 5.12 (a) Fluorescence quenching of Th-BS-Th with triphenylamine and (b) Stern-Volmer curve.**

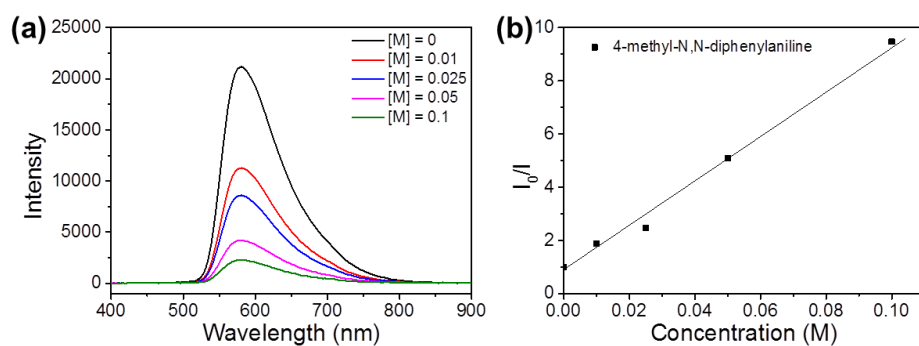


**Figure 5.13 (a) Fluorescence quenching of Th-BT-Th with 4-methyl-N,N-diphenylaniline and (b) Stern-Volmer curve.**

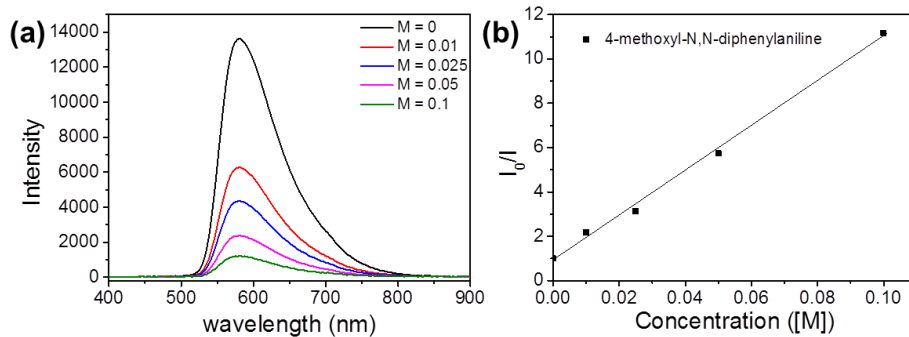


**Figure 5.14 (a) Fluorescence quenching of Th-BT-Th with 4-methoxyl-N,N-diphenylaniline and (b) Stern-Volmer curve.**

The HOMO/LUMO band positions of the SMOs and the reduction and oxidation potentials of the substrates and the sacrificial reagents are displayed in Figure 5.15. To obtain more insight of the reaction mechanism and to investigate the concrete electron-transfer pathway in the catalytic cycle, we verified the role of the sacrificial reagent. It was reported that the sacrificial reagents could be replaced by bases to neutralize hydrogen halides formed as by-products during the catalytic cycle.<sup>116</sup> However, using  $K_2HPO_4$ ,  $CsCO_3$ ,  $K_2CO_3$ , or  $KHCO_3$  as the base for our system did not lead to any consumption of 3-methylindole, confirming the role of the amine not only as a base, but also most likely for mediating the electron transfer from the radical intermediate **1** formed after the C-H functionalization of 3-methylindole with the malonate radical back to the photo-generated hole of the photocatalyst in the full catalytic cycle (Figure 5.9). To support this idea, we tested 4-nitro-N,N-diphenylaniline with an oxidative potential of +1.15 V (vs. SCE) as sacrificial reagent. By using Th-BT-Th ( $E_{oxi} = +1.12$  V vs. SCE) as photocatalyst, no product could be determined, confirming that the oxidation potential of Th-BT-Th was not sufficient enough to oxidize 4-nitro-N,N-diphenylaniline, making the electron transfer from the amine to the HOMO level of the catalyst impossible (Figure 5.15). Also the reaction rate difference between the SMOs in series 2 can be partly explained by the LUMO level, that a higher LUMO results in a quicker reaction rate.

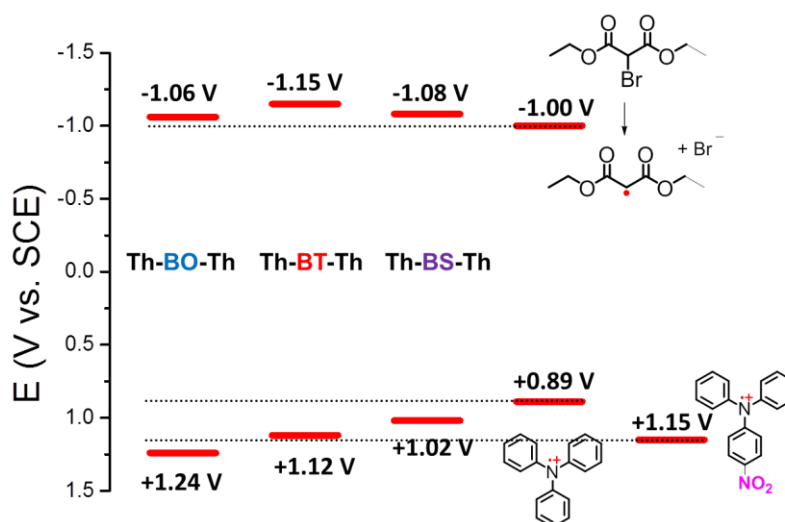


**Figure 5.15** HOMO and LUMO band positions of the SMOs in series 2 and redox potentials of substrates and sacrificial reagents.

Furthermore, two triphenyl amine derivatives, 4-methyl-N,N-diphenylaniline ( $E_{\text{oxi}} = +0.82$  V vs. SCE) and 4-methoxy-N,N-diphenylaniline ( $E_{\text{oxi}} = +0.74$  V vs. SCE) were employed to manipulate the electron-transfer process from the radical intermediate onto the oxidized amine. As illustrated in Figure 5.15, the reaction times of 90 min and 360 min of both amines, respectively, were slower than that of triphenylamine ( $E_{\text{oxi}} = +0.89$  V vs. SCE) with 45 min, despite the quenching rate of the Th-BT-Th with triphenylamine is the lowest one (Table 5.4). This further confirmed the electron-transfer pathway as illustrated in Figure 5.9 as the main electron transfer pathway. The other possibility of direct electron transfer from the radical intermediate or eventually from the indole should rather play a minor role within the catalytic cycle. The oxidation potential of the radical intermediate 1 to its oxidized cation intermediate 2 was calculated to be  $-0.34$  V vs. SCE, making the triphenyl amine radical cation the most efficient oxidant with a theoretical over potential of  $+1.23$  V.

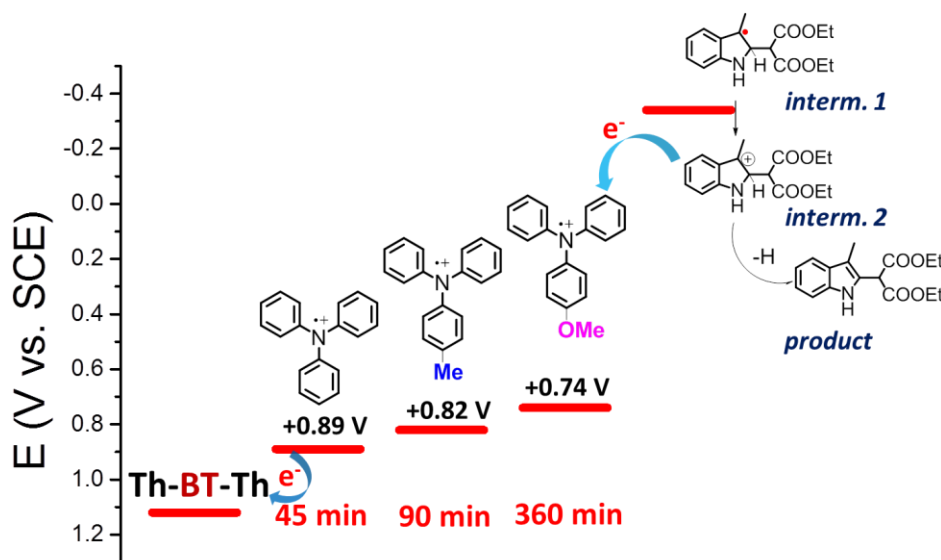


**Figure 5.16 Comparison of reaction times with different triphenylamine-based sacrificial reagents using Th-BT-Th as catalyst.**

This phenomenon is further tested by changing the photocatalyst and substrates (Figure 5.17 and Figure 5.18). When changing the Th-BT-Th into Th-BO-Th and Th-BS-Th, and changing the 3-methyl indole into 1-methyl indole and 2,3-benzofuran, the same reaction rate differs

happened, which confirmed our conclusion that the “over potential” is a key factor that will influence the reaction rate.

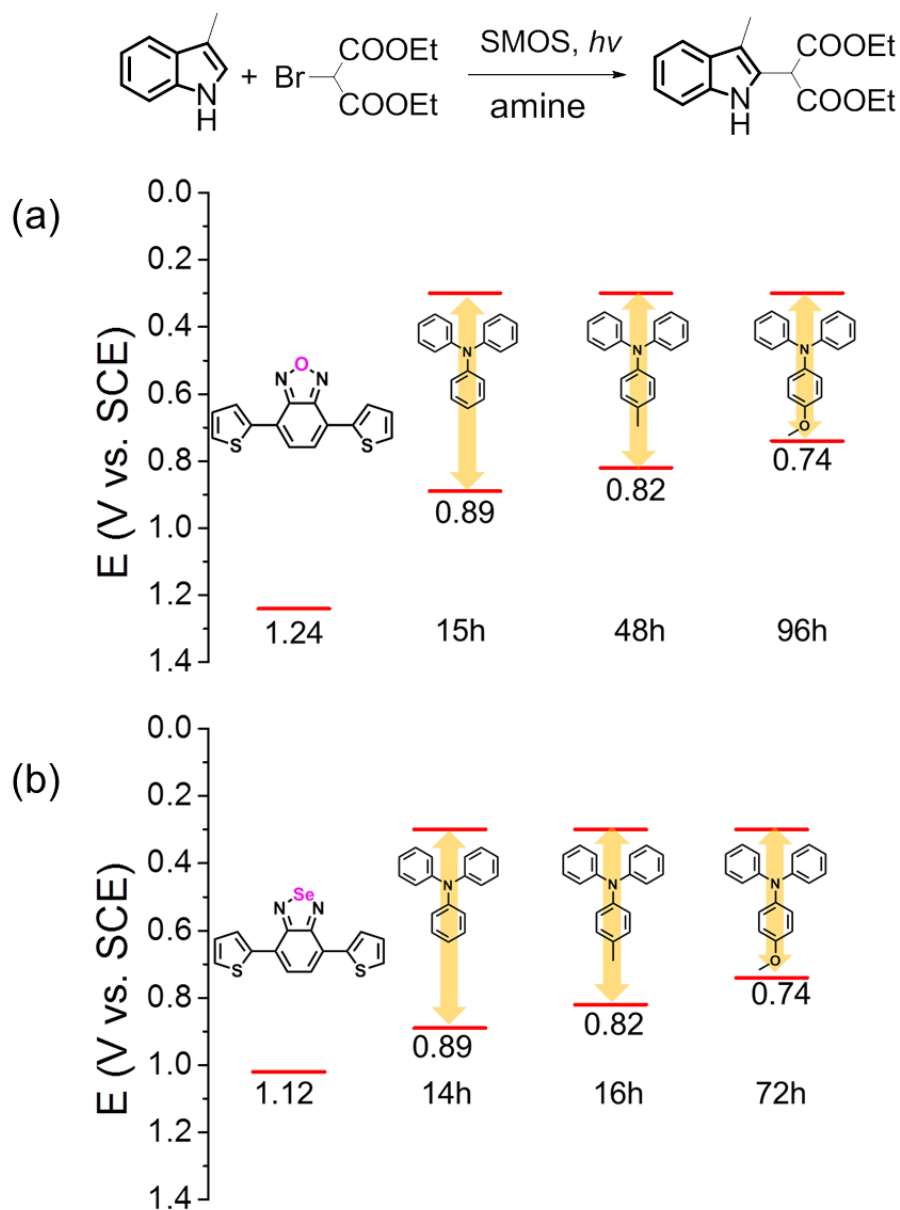


**Figure 5.17** Reaction time comparisons for different substrates with various triphenylamine-based sacrificial reagents using **Th-BO-Th** and **Th-BS-Th** as catalysts.

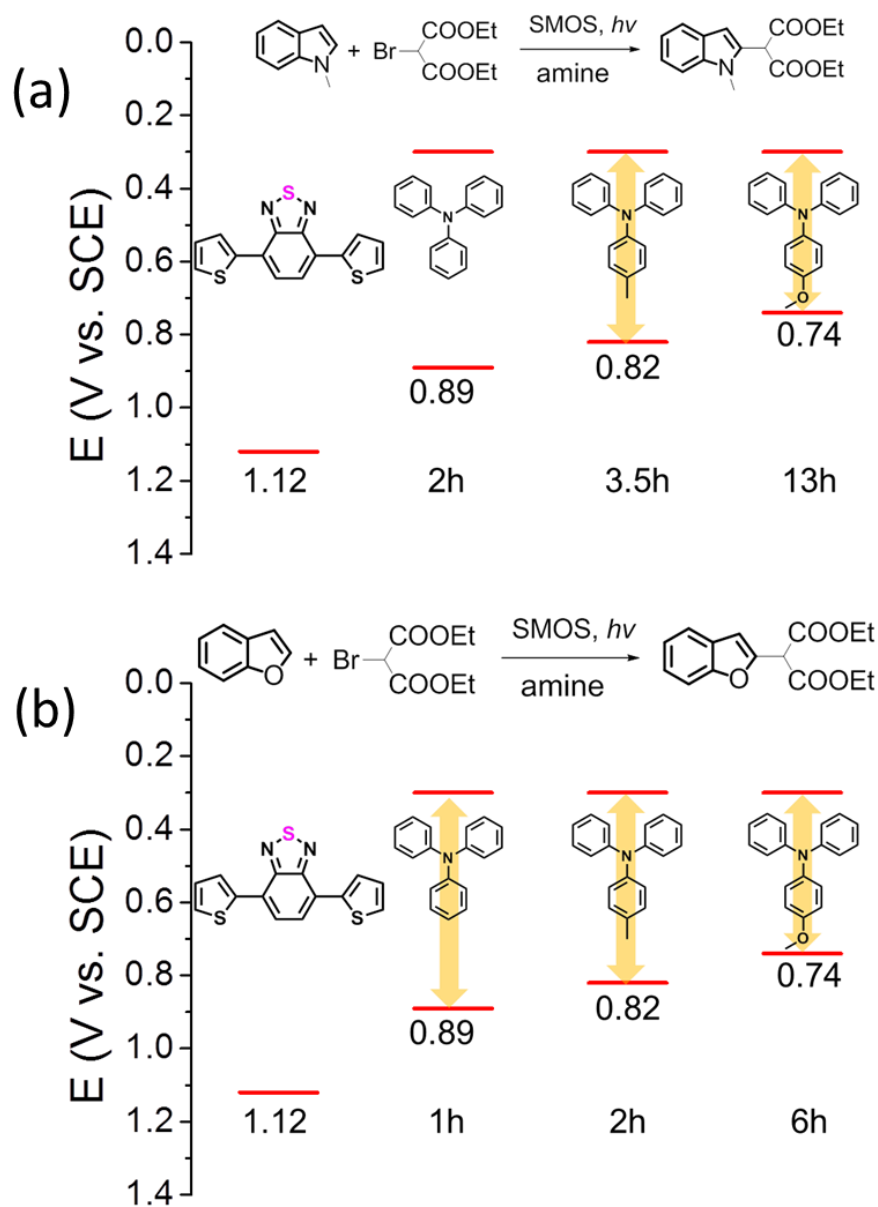
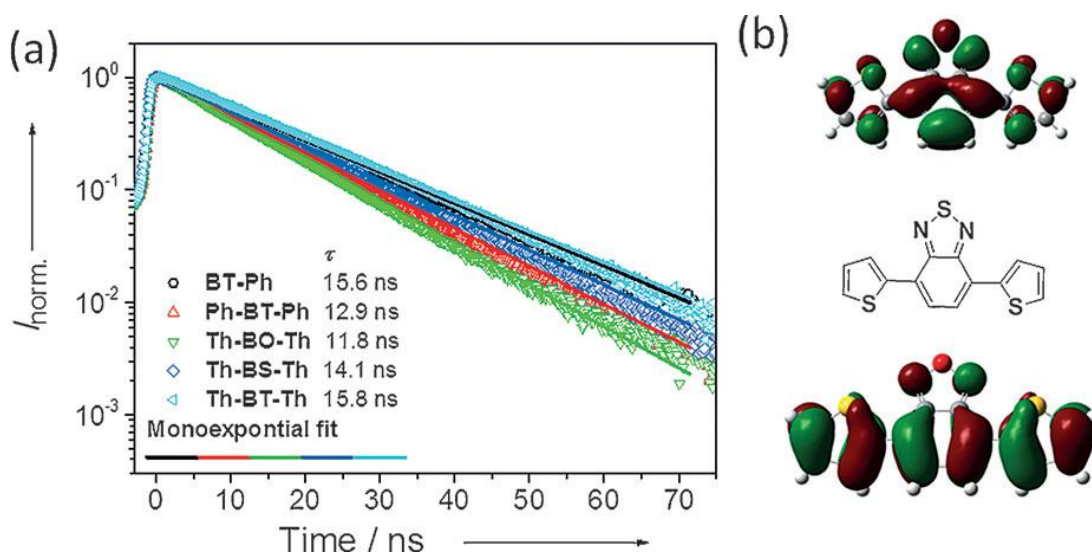


Figure 5.18 Reaction time comparisons for different substrates with various triphenylamine-based sacrificial reagents using Th-BT-Th as model catalyst.

### 5.1.7 Fluorescence lifetime of SMOs

Time-resolved photoluminescence spectroscopy revealed long fluorescence lifetimes for all SMOs ranging from around 12 to 16 ns, indicating long-living photo generated excitons for both series (Figure 5.19a). Furthermore, two tendencies could also be observed: 1) series 2 with absorption range mainly in the visible region exhibited much higher reaction yields than series 1 which has absorption mainly in the UV region; 2) Th-BT-Th with the longest fluorescence lifetime of 15.8 ns showed the highest photocatalytic efficiency. Theoretical calculations using the density functional theory (DFT) at B3LYP/6-31G\* level showed that the electron densities are mainly focused on the electron donating thiophene and -withdrawing benzothiadiazole moieties on the HOMO and LUMO for Th-BT-Th (Figure 5.19b). This clearly demonstrates that the D-A type molecules could exhibit longer exciton lifetimes, than oligomers based on only donor moieties, such as thiophene, which usually exhibit fluorescence lifetimes shorter than 1 ns.<sup>200</sup> These observations further confirmed that all three parameters, that is, absorption range, sufficient energy band position, and long exciton lifetime are required for highly efficient visible-light-driven catalytic reactions using SMOs.



**Figure 5.19 (a) Fluorescence-delay spectra of the SMOs and (b) HOMO (bottom) and LUMO (top) of Th-BT-Th calculated at the B3LYP/6-31G\* level.**



### 5.1.8 Conclusion

In summary, we have developed donor–acceptor (D–A) based small-molecule organic semiconductors (SMOSs) as a new class of pure organic and metal-free photocatalytic systems with tunable absorption range, defined and appropriate energy band positions, and long exciton lifetimes. The photocatalytic activity could be well controlled via variation of the electron-donor and -acceptor combination in the molecular structure. Using the intermolecular C-H functionalization of electron-rich heteroaromatics with malonate derivatives as a model reaction, the structural design principle of the SMOSs was demonstrated. The catalytic efficiency of the SMOSs was comparable to that of state-of-art catalysts, such as  $[\text{Ru}(\text{bpy})_3]\text{Cl}_2$ . Furthermore, the mechanistic insight of the light-induced electron transport between the organic photocatalyst, substrate, and the sacrificial electron-donating reagent confirmed that not only the finely controlled redox potential of the photocatalyst, but also the oxidation potential of the amine-based sacrificial reagent could enhance the catalytic efficiency. With their tunable absorption range, defined and controllable redox potential, long-lived photo-generated excitons, and pure organic nature, the SMOSs could offer a promising class of metal-free and visible light active photocatalysts for chemical reactions.

## 5.2 Sacrificial reagent-free photoredox catalysis using cooperative organic semiconductor couples

In the following chapter, a sacrificial reagents-free photoredox catalysis designed by using cooperative photocatalyst systems consisting of organic semiconductor couples is reported. The cooperative photocatalytic system is designed to undergo intermolecular electron transfer, and thereby overcoming the need for an extra electron donor. As a model reaction, the carbon-carbon formation reaction between electron-rich heteroaromatics and malonates, which usually required electron-donating sacrificial reagents, was conducted to demonstrate the feasibility and photocatalytic activity of the cooperative photocatalyst couple under visible light irradiation. A significant reaction rate improvement from trace conversion for single catalyst

system to over 90% via using cooperative catalyst couple was achieved. A mechanistic study revealed the light-induced electron transfer between the photocatalysts and substrate.

### 5.2.1 Motivation

Sacrificial reagents, which act as electron donor species, are of great importance for photocatalytic redox reactions including chemical transformation and water decomposition into hydrogen and oxygen.<sup>6, 201-202</sup> Especially for semiconductor-catalyzed reactions, the catalytic efficiency can be largely improved while the photo-generated holes can be scavenged by the sacrificial reagent molecules and the charge recombination can be reduced. However, the use of an usually excessive amount of sacrificial reagents during the catalytic cycle, mostly amines, often leads to undesired oxidized side products and is especially troublesome for product purification.<sup>203</sup> To overcome the above-mentioned challenge and to maintain reduced charge recombination within the semiconductor-based photocatalyst, an enhanced photo-generated electron transfer pathway should be developed.

Organic semiconductor (OS)-containing photocatalytic systems can offer a promising solution for the above-mentioned challenge. Currently, OS photocatalysts have emerged as a promising alternative to the traditional metal-containing photocatalysts due to their highly tunable electronical properties via flexible structural design. Recent research activities have demonstrated a vast number of structural design methods of small molecule<sup>13, 37, 58, 94, 204-205</sup> or macromolecular OS systems<sup>46-47, 206-213</sup> as efficient photocatalysts for visible light-promoted photoredox reactions. Nevertheless, most developed OS photocatalysts, similar to traditional transition metal complexes<sup>50, 111, 139, 170, 194-195, 214</sup>, are single photocatalytic systems. The photocatalytic ability of the OS system originates from the photo-generated electron/hole pair, which can function as the reductive and oxidative species. To maintain an efficient electron transfer from the ground to the excited state of the OS, extra sacrificial reagents are needed due to direct recombination of the electron/hole pair. However in organic photovoltaic (OPV) devices, the efficiency can be enhanced by separating the electron donor (D) and acceptor (A) materials in solid state (Figure 5.20a). The electron/hole recombination can be delayed in the bulk-heterojunction (BHJ) manner.<sup>191, 215-218</sup> We envision that this principle ought to be

transferred into a new photocatalyst design using a complementary double-photocatalyst system in order to prevent the necessary use of extra electron donor, i.e. sacrificial reagents.

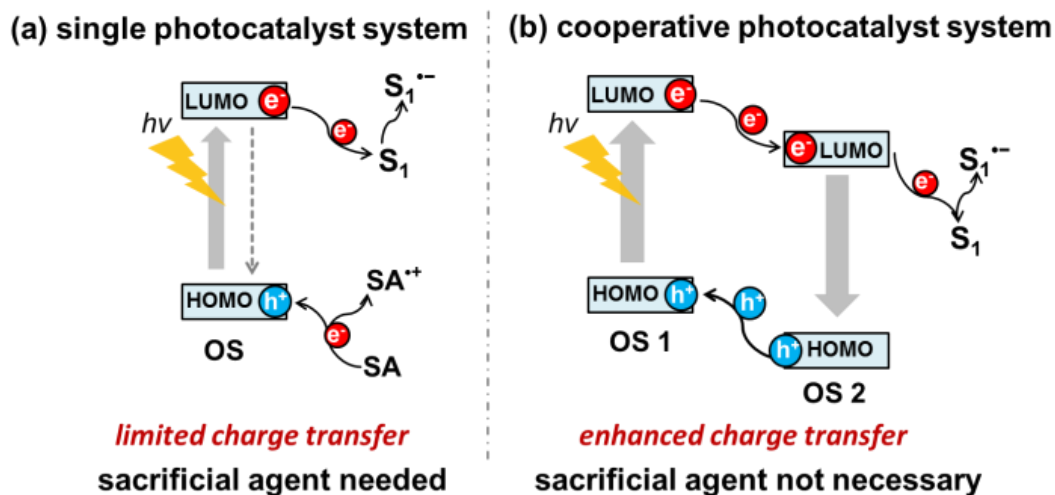
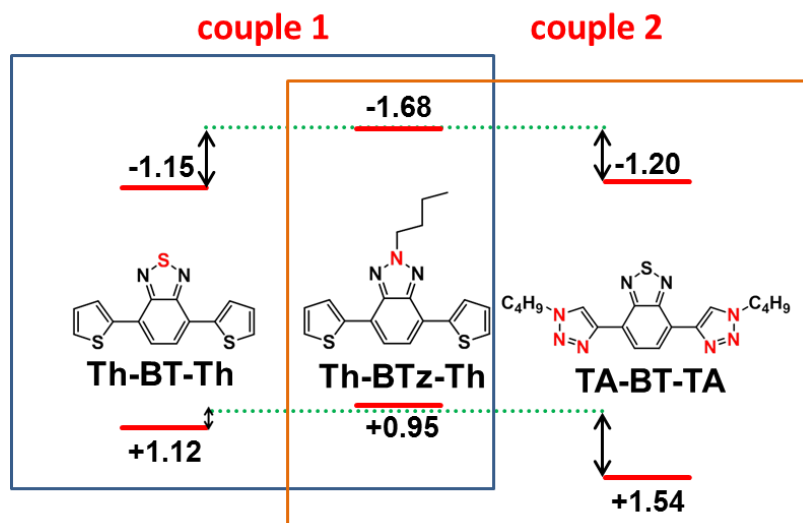


Figure 5.20 Difference between (a) conventional single organic photocatalyst system with direct electron/hole recombination, sacrificial reagent needed; (b) cooperative photocatalyst system with enhanced electron/hole separation, no sacrificial reagent needed. OS: organic semiconductor; SA: sacrificial reagent; S: substrate.

### 5.2.2 Design of the catalyst couples

In this study, three molecular organic semiconductors (OS), in particular, 4,7-di(thiophen-2-yl)benzo[c][1,2,5]thiadiazole (Th-BT-Th), 2-butyl-4,7-di(thiophen-2-yl)-2H-benzo[d][1,2,3]triazole (Th-BTz-Th), and 4,7-bis(1-butyl-1H-1,2,3-triazol-4-yl)benzo[c][1,2,5]thiadiazole (TA-BT-TA) were designed. The structures and energy band positions of the OSs are shown in Figure 5.21.



**Figure 5.21 Structure and HOMO LUMO levels (vs. SCE) of the OS molecules in both designed photocatalyst couples.**

The three OSs possessed different highest occupied molecular orbital (HOMO) and lowest unoccupied molecular orbital (LUMO) band positions, which could be determined via cyclic voltammetry. As shown in Figure 5.22, Th-BTz-Th exhibited a significantly high LUMO level at -1.68 V vs. saturated calomel electrode (SCE), followed by TA-BT-TA with -1.20 V vs. SCE and Th-BT-Th with -1.15 V vs. SCE. In comparison, TA-BT-TA exhibited the lowest HOMO level at +1.54 V vs. SCE, followed by Th-BT-Th with +1.12 V vs. SCE and Th-BTz-Th with +0.95 V vs. SCE. Given the different energy band positions, we assembled the three OSs in two photocatalyst couples for this study, particularly, Th-BTz-Th/Th-BT-Th for cooperative photocatalyst couple 1 and Th-BTz-Th/TA-BT-TA for couple 2.

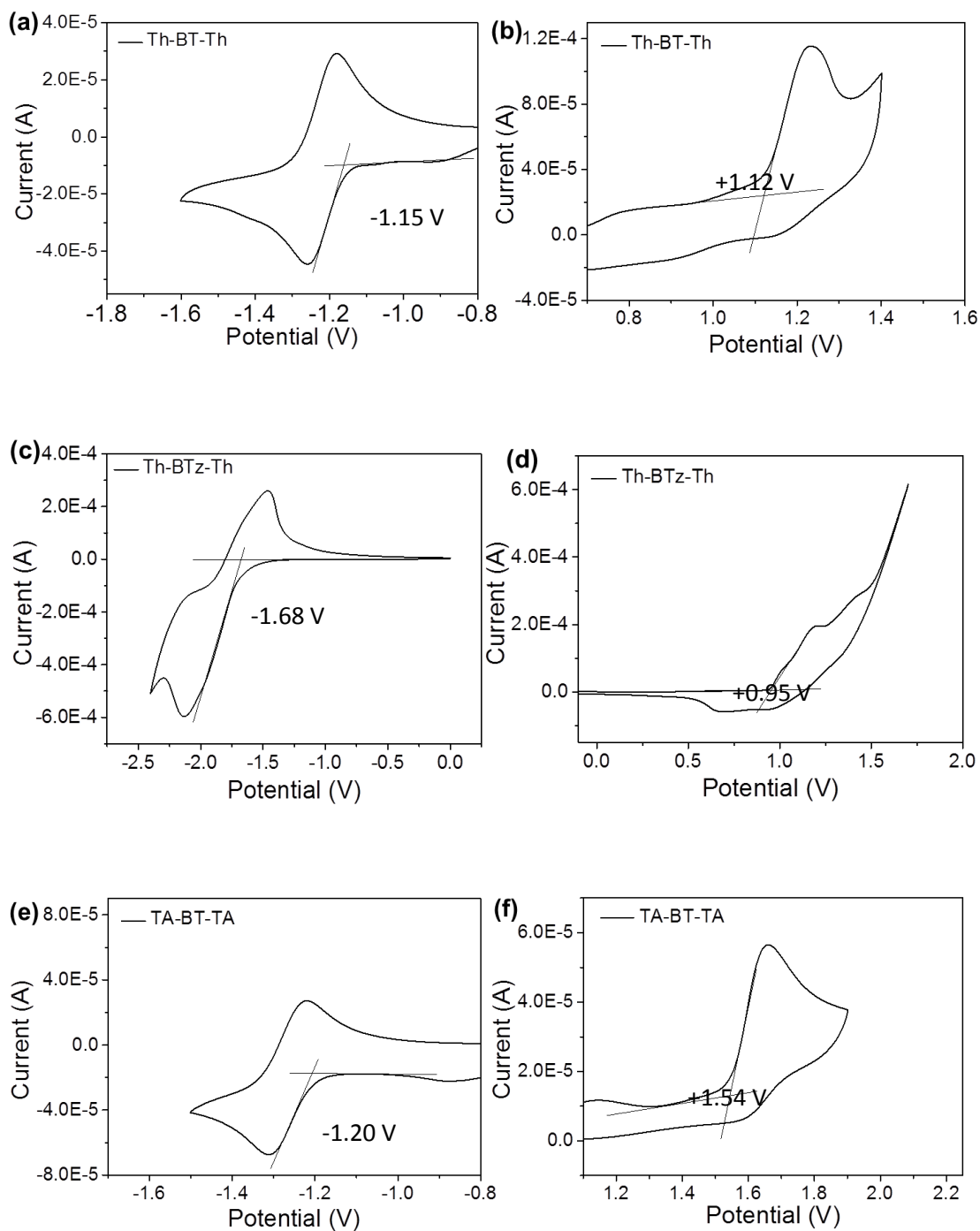


**Figure 5.22 Reductive potentials of (a) Th-BT-Th, (c) Th-BTz-Th and (e) TA-BT-TA and oxidative potential of (b) Th-BT-Th, (d) Th-BTz-Th and (f) TA-BT-TA determined via cyclic voltammetry (vs. SCE).**

### 5.2.3 Physical properties of OS couples

The absorption and fluorescence spectrums of Th-BT-Th, Th-BTz-Th and TA-BT-TA were shown in Figure 5.23.

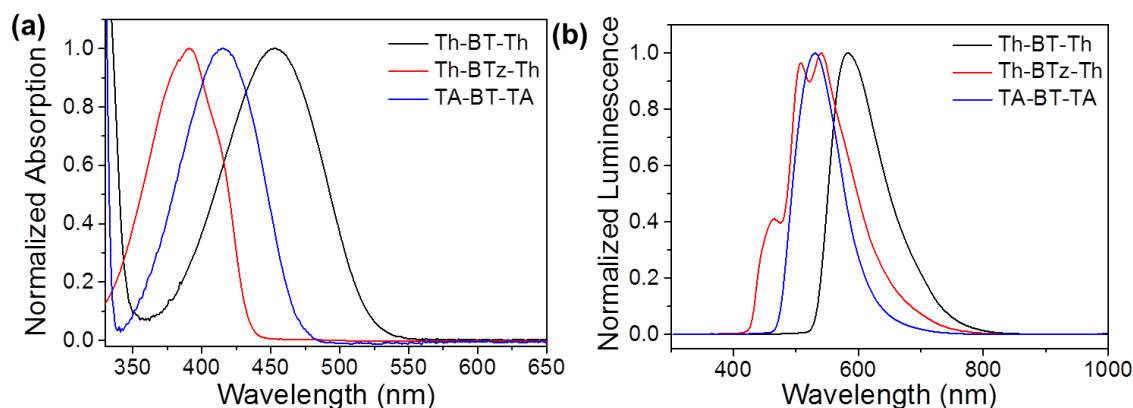


**Figure 5.23 (a) Normalized absorption spectrum and (b) fluorescence spectrum of Th-BT-Th, Th-BTz-Th and TA-BT-TA.**

Steady-state fluorescence quenching experiments in steady states were conducted and the results are shown in Figure 5.24. They showed that by only exciting Th-BT-Th (at 500 nm) or TA-BT-TA (at 450 nm) in both couples, the fluorescence intensity of couple 2 exhibited a larger decrease in PL intensity than that of couple 1, indicating an enhanced electron transfer within couple 2, which was likely caused by the larger distance between the two HOMO levels.

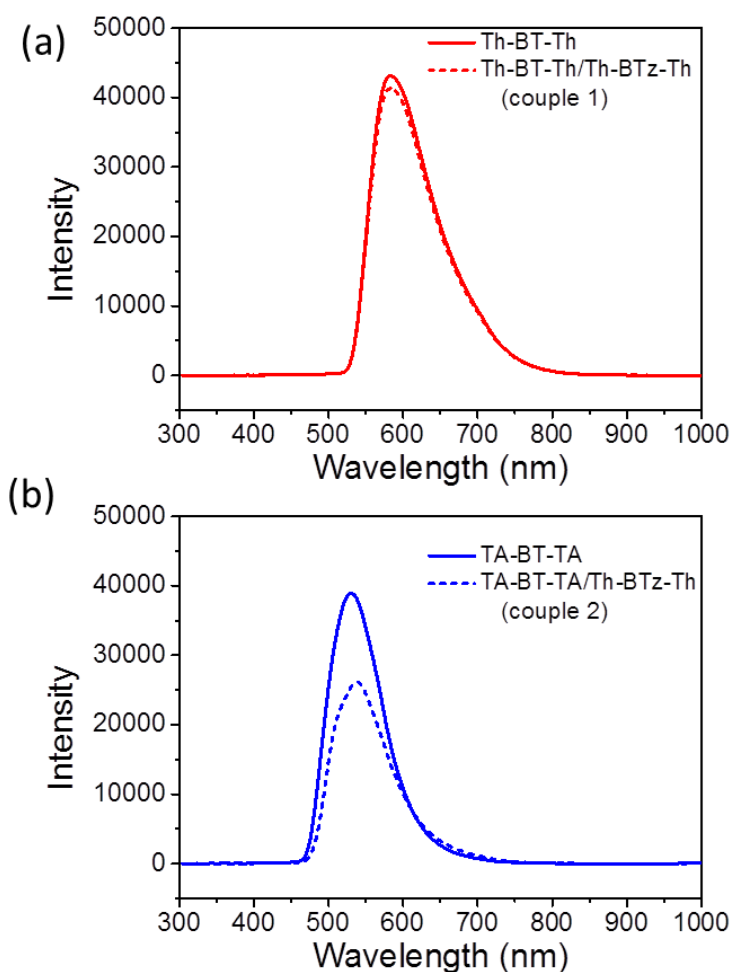


**Figure 5.24 Steady state fluorescence quenching within the photocatalyst couples in solution. The ratios of the OSs were 1:1 for both couples. Excitation wavelength: (a) 450 nm, (b) 500 nm.**

To further study the photo-induced charge transfer within the couples, time-resolved photoluminescence spectroscopy was conducted to characterize the photo-excited dynamics within the OS couples. The PL measurements of the pristine materials and a 1:1 (mol %) blend were all performed in DMF solution with excitation at 400 nm. The PL decays were collected at the emission maximum for each component OS.

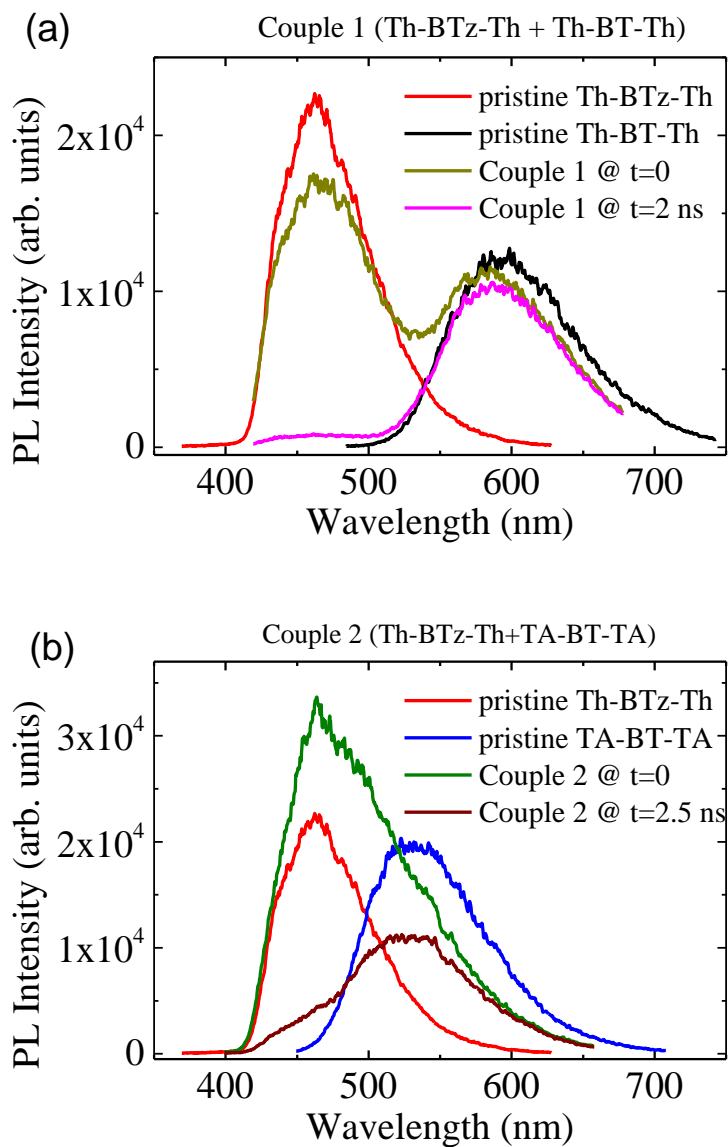


**Figure 5.25 Time-resolved fluorescence quenching within the photocatalyst couples in solution. The ratios of the OSs were 1:1 for both couples. Excitation wavelength: 400 nm.**



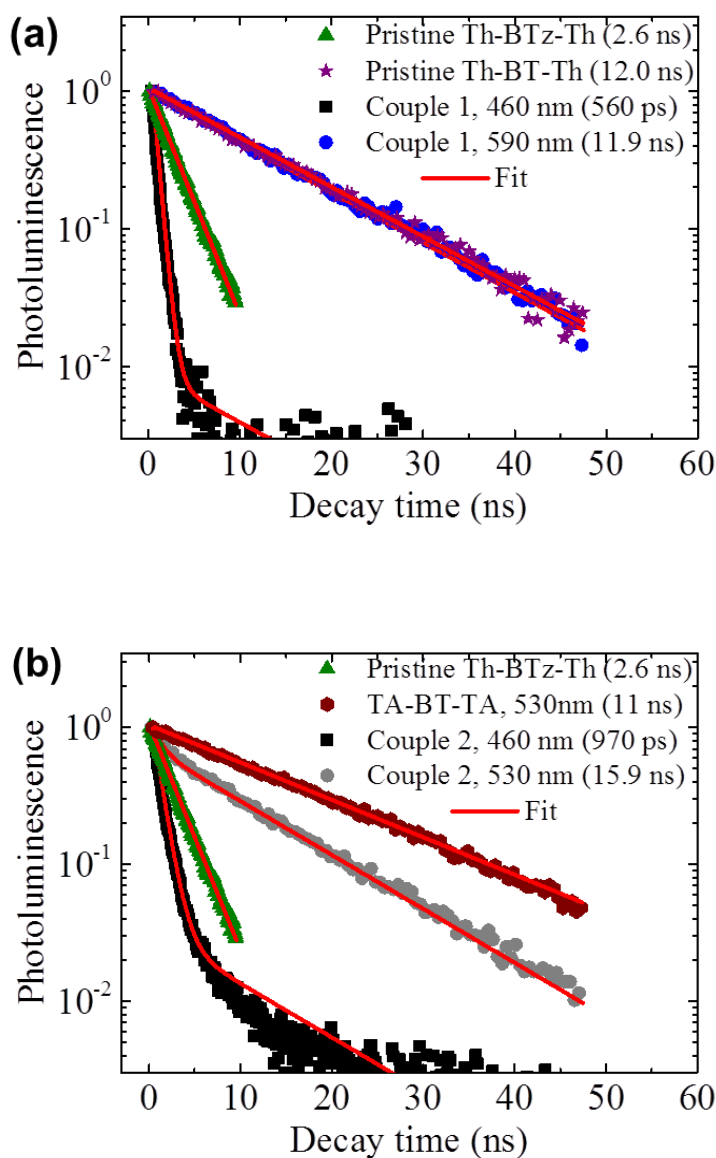


**Figure 5.26 Time-resolved photoluminescence decays in the pristine materials and in the photocatalyst couples in solution. The ratios of the OSs were 1:1 for both couples. (a) Couple 1 and (b) couple 2. Excitation wavelength: 400 nm.**

The fluorescence features of the different component materials overlap with each other. Therefore, decay associated spectra (DAS) were derived by a global fitting analysis of the TRPL data (Figure 5.27). This allows us to characterize the spectral distribution and lifetime of each

emitting species, particularly for the measurements of couple 1 and couple 2. In couple 1 (Figure 5.27a), one can see that DAS 1, centered at 460 nm, matches exactly with the fluorescence spectrum of Th-BTz-Th and decays in 0.6 ns, which is quenched with respect to the pristine donor (2.6 ns). DAS 2, which is centered at 590 nm, matches with the fluorescence spectrum of Th-BT-Th and decays with the same lifetime, as the pristine Th-BT-Th sample with 11.9 ns exhibiting no quenching. This indicates that in couple 1, likely the excitation energy transfer (EET) from Th-BTz-Th to Th-BT-Th dominates the excited state dynamics, as illustrated in Figure 5.28a. In couple 2 (Figure 5.27b), the DAS 1, centered at 460 nm, is again originating from Th-BTz-Th and decays in 0.97 ns, which is quenched with respect to the pristine Th-BTz-Th (2.6 ns). DAS 2, centered at 530 nm, is assigned to the emission of TA-BT-TA and has a decay time of 10.6 ns. Here, the fluorescence of both Th-BTz-Th and TA-BT-TA are quenched with respect to the pristine materials. This indicates an electron transfer from Th-BTz-Th to TA-BT-TA and an enhanced charge transfer within couple 2 (Figure 5.28b).

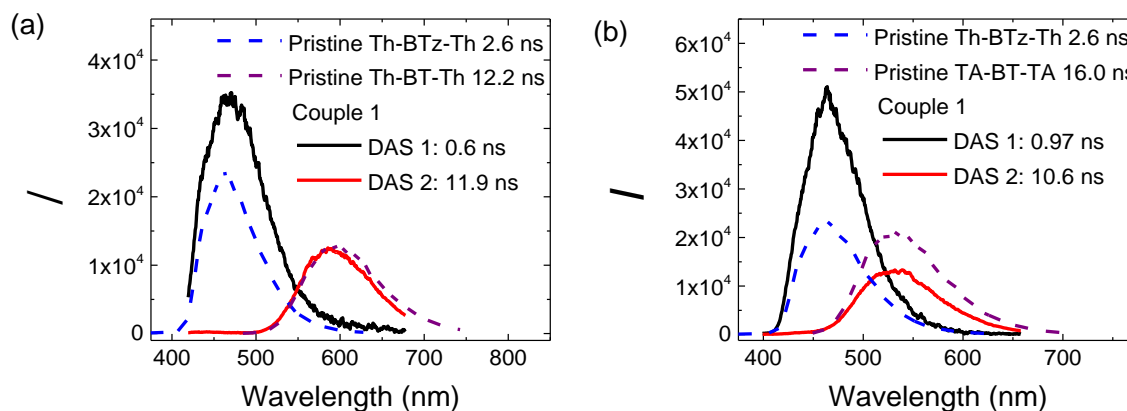


**Figure 5.27** Decay associated spectra (DAS) derived by a global fitting analysis of the TRPL data. (a) Couple 1 and (b) couple 2.

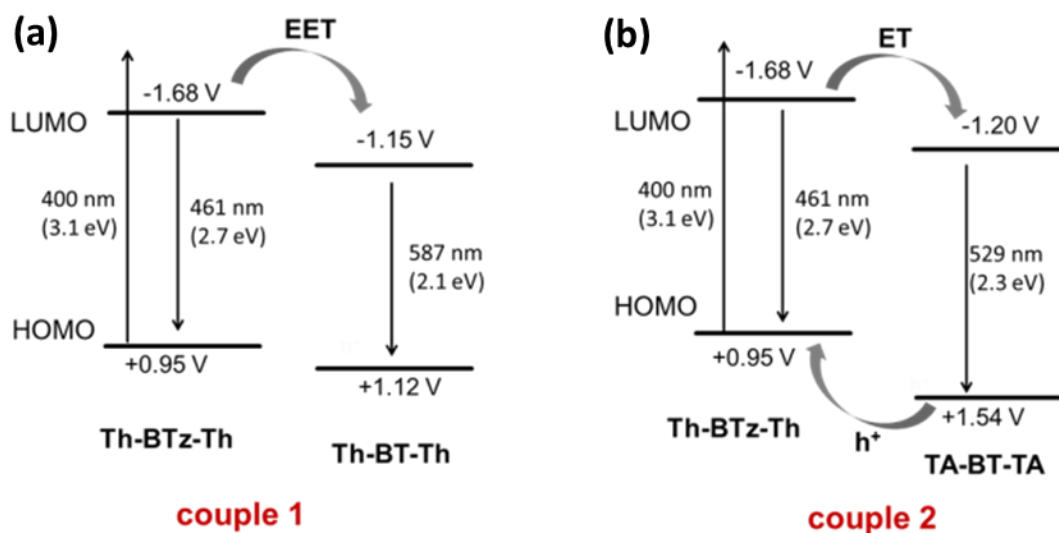


Figure 5.28 Jablonski diagram illustrates energy and charge transfer in the photocatalyst couples, respectively. Excitation wavelength: 400 nm. EET: excitation energy transfer; ET: electron transfer.

#### 5.2.4 Photocatalytic C–C bond formation

We chose the photocatalytic carbon-carbon formation reaction between electron-rich heteroarenes and malonates as model reaction.<sup>199</sup> Previous studies demonstrated the mandatory use of sacrificial reagents, mostly amines, which ought not to only act as electron donor, but also as electron mediator between the radical intermediate and the photo-generated hole of the photocatalyst. We first tested the three designed OSs as single photocatalyst system without using a sacrificial reagent. As expected, by using 3-methylbenzofuran and diethyl bromomalonate in the model reaction, no product was obtained using Th-BT-Th and TA-BT-TA as photocatalysts (entries 1-2 in Table 1). Interestingly, using Th-BTz-Th as photocatalyst led to a slight conversion of 9%. This indicates that a minimal electron transfer could still occur between the photocatalyst and the substrate, which corresponds with the highest LUMO level of Th-BTz-Th among the three OSs and thereby the largest over potential for the reduction of diethyl bromomalonate. In contrast, by using both cooperative photocatalyst couples, the product could be obtained in significantly higher conversions, in particular, 43% for couple 1 and 93% for couple 2, respectively (Table 5.5, entries 4-5). This is in

agreement with the photophysical study (Figure 5.27), indicating that the enhanced charge transfer between Th-BTz-Th and TA-BT-TA in couple 2 led to a better catalytic efficiency than that of couple 1 containing Th-BTz-Th and Th-BT-Th. The reason could lie on the larger HOMO energy gap ( $\Delta E_{HOMO} = 0.59$  V) between Th-BTz-Th and TA-BT-TA than that ( $\Delta E_{HOMO} = 0.17$  V) in couple 1 between Th-BTz-Th and Th-BT-Th. It is also worth to note that further scope reactions with other substrates led to high product yields using couple 2 as phototocatalyst, demonstrating a general feasibility of the cooperative photocatalyst design.

Further investigation of the catalytic efficiency is conducted with a fluorescence quenching experiment. No linear decrease of the fluorescence can be seen when increasing the concentration of the diethyl bromomalonate in the solution of Th-BT-Th and TA-BT-TA. Only Th-BTz-Th can be quenched by diethyl bromomalonate with a really small rate constant, which is consistent with the result before a slight conversion of 9% of starting compound can be got when using Th-BTz-Th alone as the photocatalyst (Figure 5.29). In contrast, the fluorescence of both photocatalyst couples could be gradually quenched by adding diethyl bromomalonate (Figure 5.30), confirming the possible electron transfer between the photocatalyst couple and the substrate.

**Table 5.5 Photocatalytic C–C bond formation between diethyl bromomalonate and heteroaromates using different photocatalysts systems**

Entry	Catalyst	Substrate	Product	Conv [%] <sup>b</sup>
1	Th-BT-Th			trace
2	TA-BT-TA			0
3	Th-BTz-Th			9
4	Couple 1			43
5	Couple 2			93
6 <sup>c</sup>	Couple 2			78
7 <sup>c</sup>	Couple 2			92
8 <sup>c</sup>	Couple 2			85
9 <sup>d</sup>	Th-BTz-Th/TA-BT-TA (2:1)			72
10 <sup>d</sup>	Connected cat.			31

<sup>a</sup>Reaction conditions: 1 equiv. (0.38 mmol) heteroaromate, 2 equiv. diethyl bromomalonate, 0.1 equiv. photocatalyst in 2.5 mL DMF, white LED, 24 h. <sup>b</sup>Determined by GC-MS. <sup>c</sup>48h. <sup>d</sup>0.05 equiv. photocatalyst, 24h.

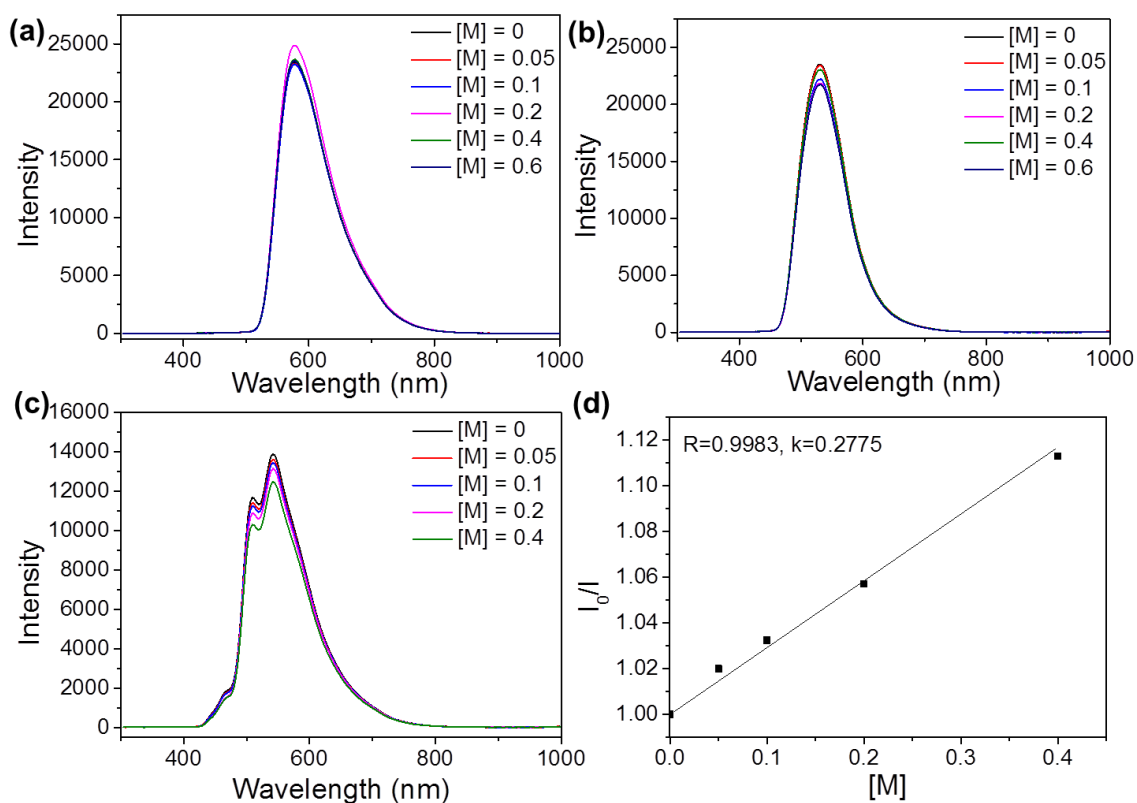


**Figure 5.29** Fluorescence quenching spectra of (a)Th-BT-Th, (b)TA-BT-TA (c)Th-BTz-Th with diethyl bromomalonate and (d) Stern-Volmer analysis of quenching rate between Th-BTz-Th and diethyl bromomalonate.

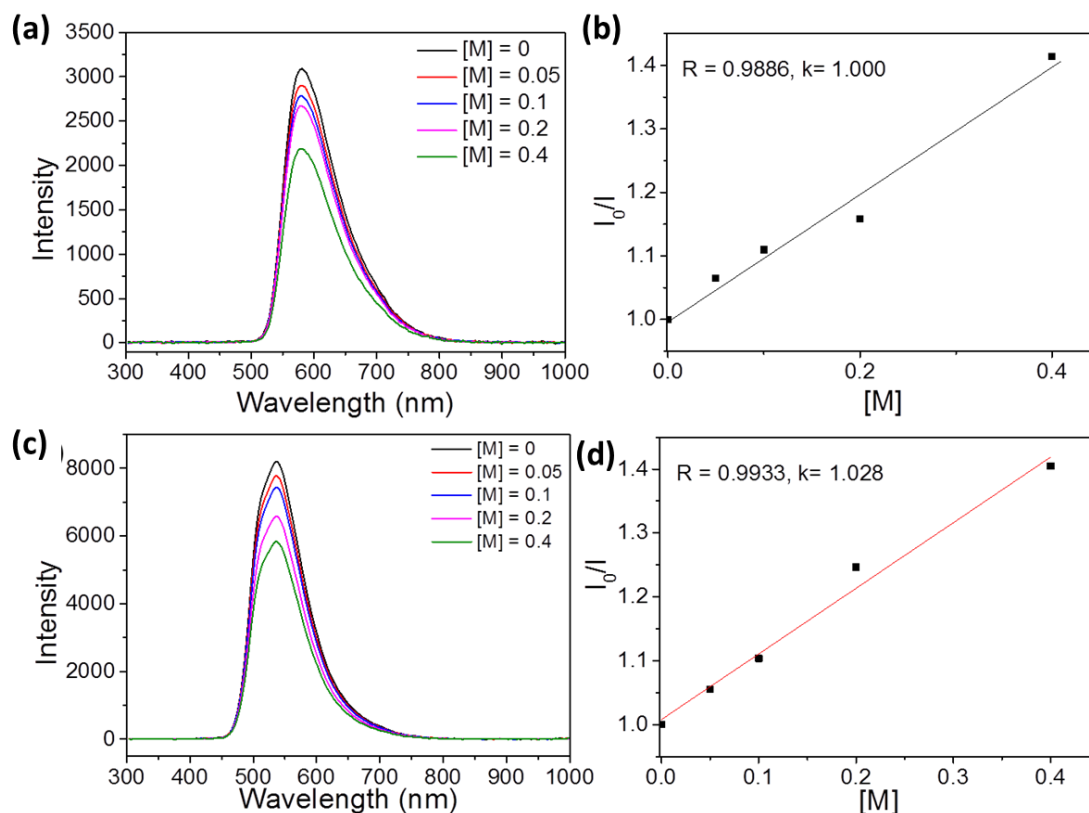


**Figure 5.30** Fluorescence quenching for (a) cooperative catalyst system 1 (Th-BTz-Th and Th-BT-Th) and (c) cooperative catalyst system 2 (Th-BTz-Th and TA-BT-TA) with diethyl bromomalonate and Stern-Volmer analysis of (b) cooperative couple 1 and (d) couple 2 with diethyl bromomalonate.

To precisely study the concrete electron transfer process within the catalytic cycle, we then employed ethyl bromoacetate as substrate, which possessed a reduction potential of -1.43 V vs. SCE (Figure 5.31b) that is higher than diethyl bromomalonate (-1.00 V vs. SCE) (Figure 5.31a).

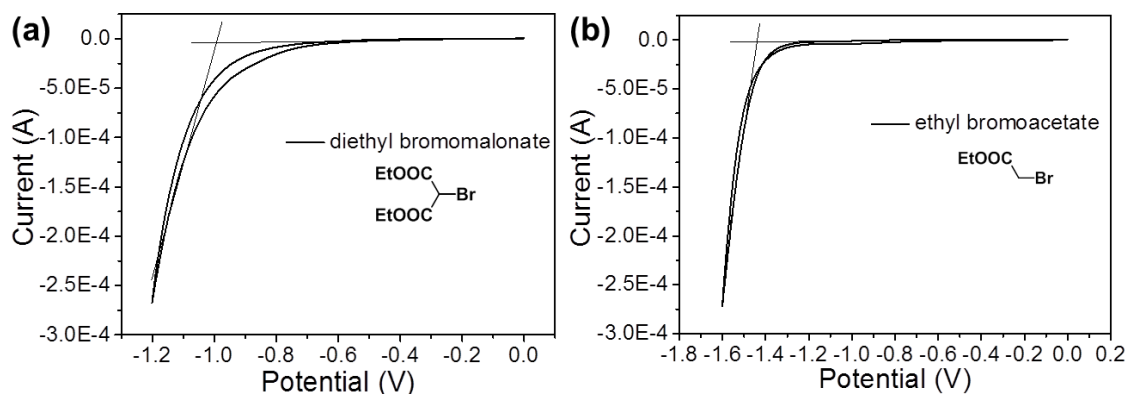


**Figure 5.31 Reductive potentials of (a) diethyl bromomalonate and (b) ethyl bromoacetate (potentials given vs. SCE)**

By using couple 2 as photocatalyst, it could be determined that only traces of the final product could be obtained (Figure 5.33). This reveals that the photo-generated electron could indeed only transferred from the LUMO of Th-BTz-Th (-1.68 V vs. SCE) to the LUMO of TA-BT-TA (-1.20 V vs. SCE) in the first step, from which the further electron transfer to the higher reduction level of ethyl bromoacetate was not possible as shown in Figure 5.32. Additionally, a direct electron transfer from Th-BTz-Th to ethyl bromoacetate could not occur either. In comparison, diethyl bromomalonate ( $E_{\text{red.}} = -1.00$  V vs. SCE) could be reduced via electron transfer originated from the LUMO of TA-BT-TA, leading to the formation of the malonate radical, which further reacts with 3-methylbenzofuran to form the final product in the following step of the catalytic cycle.



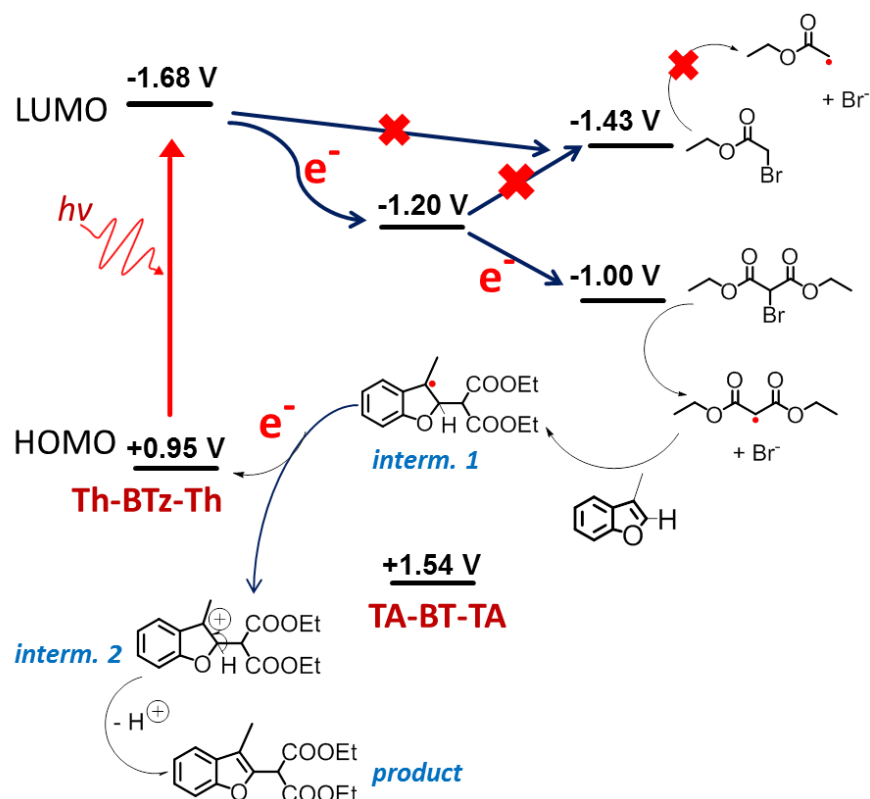


**Figure 5.32** Study of the electron transfer pathway using comparative substrates with different reduction potentials. Interm.: intermediate.

An additional model reaction using both Th-BTz-Th as the single photocatalyst system and triphenylamine as sacrificial reagent led to the formation of the finally desired product, confirming that a direct electron transfer from Th-BTz-Th to ethyl bromoacetate was only possible in the absence of TA-BT-TA as shown in Figure 5.34.

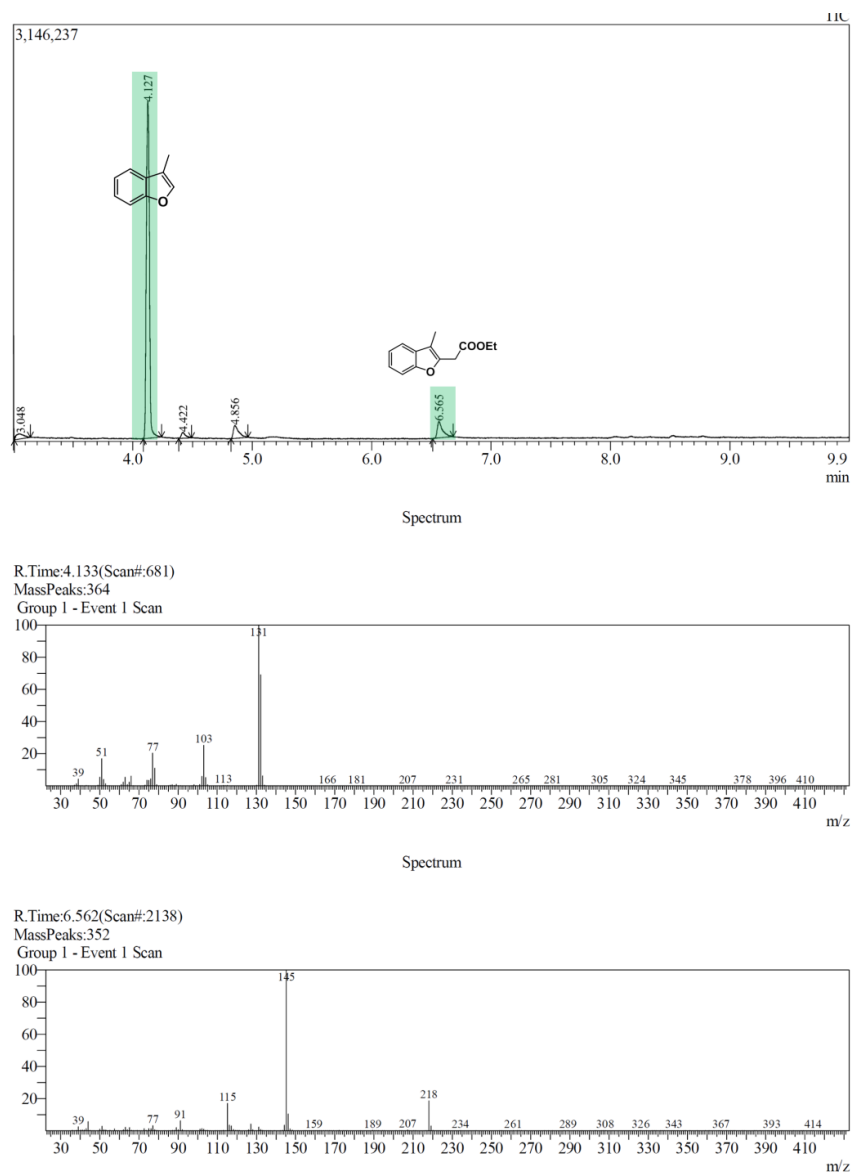


**Figure 5.33 C-C coupling between 3-methylbenzofuran and ethyl bromoacetate using couple 2 (Th-BTz-Th/TA-BT-TA) as cocatalyst, Conversion: ~ 4%.**

## Results and Discussions

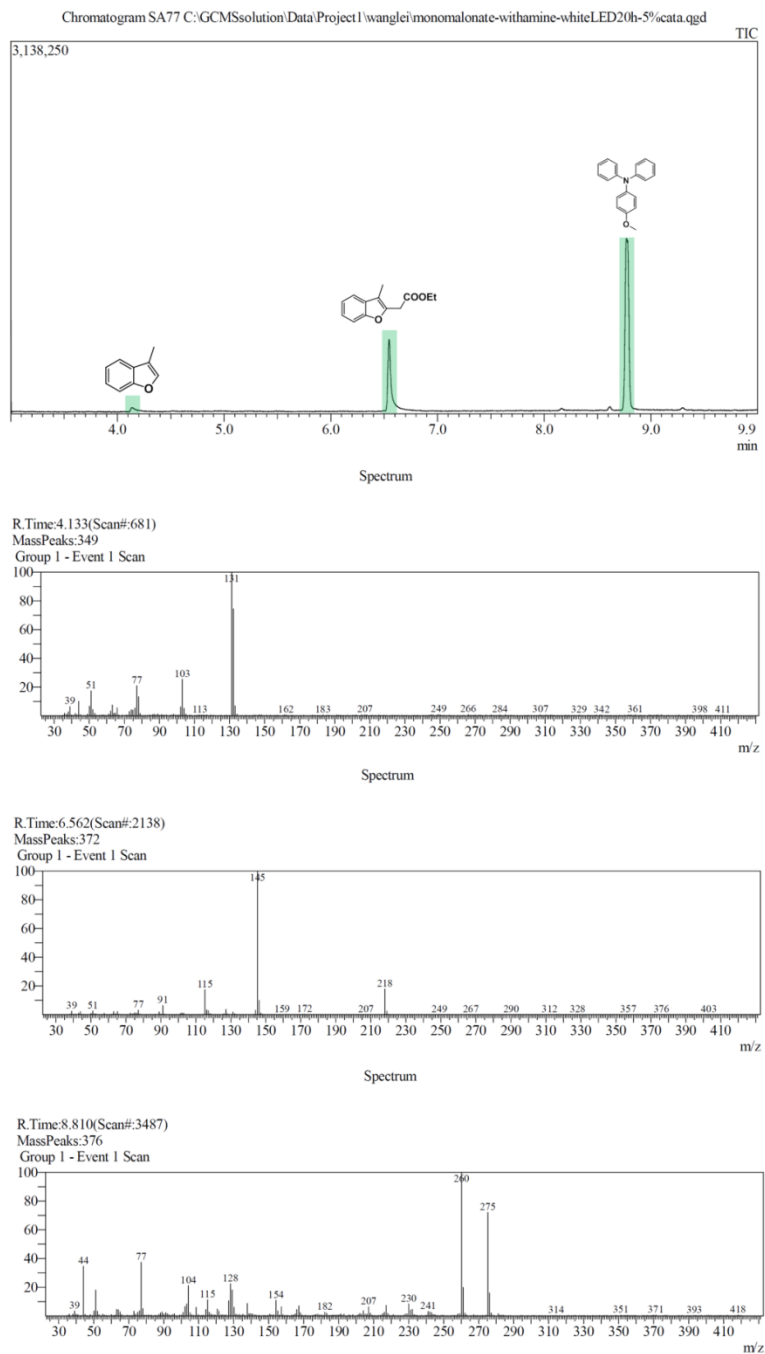
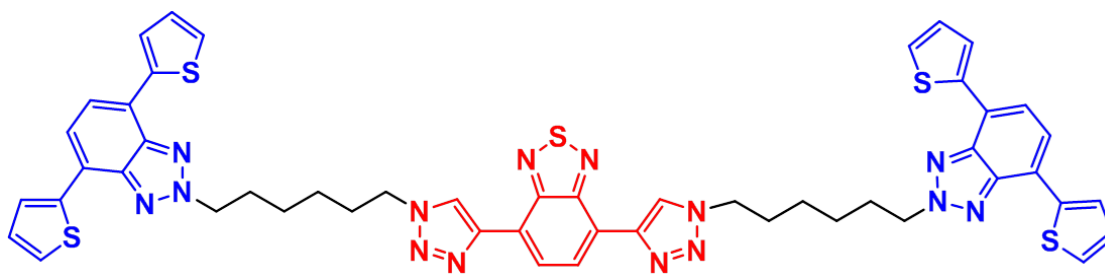


**Figure 5.34 C-C coupling between 3-methylbenzofuran and ethyl bromoacetate using Th-BTz-Th as catalyst and 4-methoxytriphenylamine as sacrificial reagent. Reaction conditions: 1 equiv. (0.38 mmol) heteroaromate, 2 equiv. ethyl bromomalonate, 0.1 equiv. photocatalyst in 2.5 mL DMF, white LED, 12 h.**

### 5.2.5 Attempt to improve the catalytic efficiency

The photo-induced electron transfer within the cooperative photocatalyst couple usually occurs based on the rather random contact between the two OSs in the liquid reaction medium. To create a non-random contact and thereby a more defined electron transfer process, we then connected Th-BTz-Th and TA-BT-TA via a C6 alkyl chain as molecular bridge as a control photocatalyst. As displayed in Scheme 2, a large molecule of Th- BTz-Th@TA-BT-TA containing both OSs in couple 2 was synthesized.



**Scheme 5.2 Chemical structure of Th-BTz-Th@TA-BT-TA.**

The absorbance spectrum of Th-BTz-Th@TA-BT-TA is a combination of both Th-BTz-Th and TA-BT-TA, but the fluorescence mainly comes from TA-BT-TA. Due to the spectrum overlap between the fluorescence of Th-BTz-Th and absorbance of TA-BT-TA, the fluorescence of Th-BTz-Th is strongly quenched by energy transfer process.

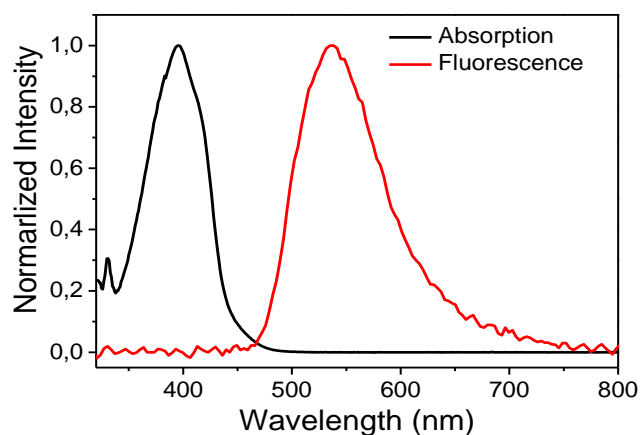


**Figure 5.35** UV/vis absorption and fluorescence spectra of the connected photocatalyst system TA-BT-TA@Th-BTz-Th.

Remarkably, under the same concentration and ratio, the fluorescence intensity of Th-BTz-Th/TA-BT-TA strongly decreased after connection compared to their unconnected form as couple 2 (Figure 5.36). This result suggests a strong interaction between two OSs inside the large molecule.

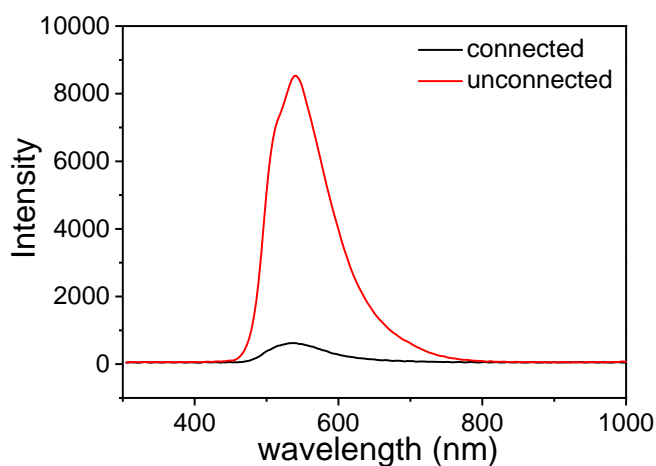


**Figure 5.36** Fluorescence spectra of C6-connected Th-BTz-Th@TA-BT-TA and unconnected photocatalyst couple 2 containing Th-BTz-Th and TA-BT-TA under same molar ratio and concentration.

A study on the impact of Th-BTz-Th/TA-BT-TA in couple 2 on their photocatalytic efficiency showed that the highest reaction rate was achieved by a ratio of 2:1 for Th-BTz-Th/TA-BT-TA (Figure 5.37), which in fact corresponds to the connected molecule of Th-BTz-Th@TA-BT-TA.

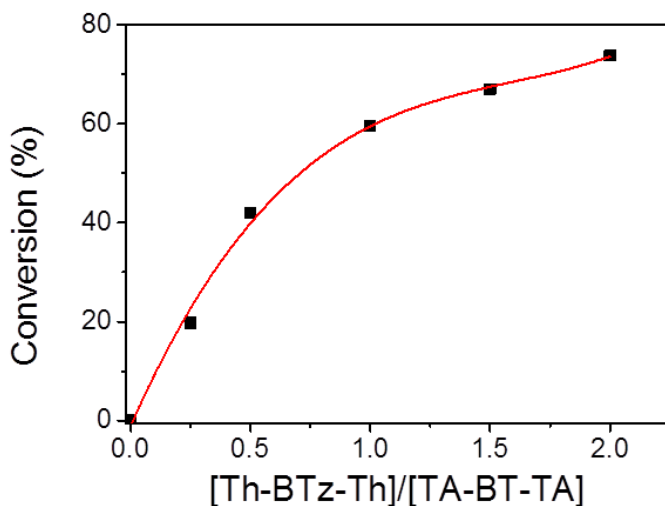


**Figure 5.37 Study of the impact of the OS ratio on the reaction conversion.**

However, when comparing the catalytic efficiency between the connected catalyst of Th-BTz-Th@TA-BT-TA and unconnected couple 2 with the same ratio between both OSs, only a decreased conversion was observed for the connected catalyst (Figure 5.38).

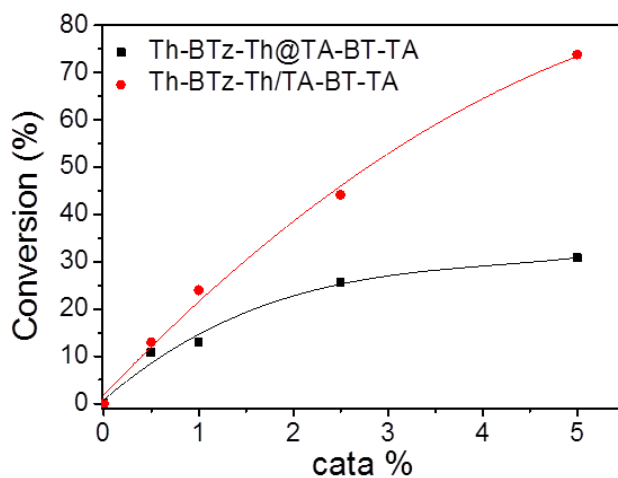


**Figure 5.38 Comparison between cooperative photocatalyst couple 2 with the C6-connected molecule Th-BTz-Th@TA-BT-TA**

In spite of the better electron transfer occurred within connected system, the reduced catalytic efficiency could be likely caused by the sterical hindrance within the large molecule or the competing charge recombination process, which limits the contact between the substrate and the individual OSs in the large molecule and efficient electron transfer between the catalyst and substrate. To overcome this limitation, new molecular bridges other than the C6 alkyl chain could be needed. This phenomenon is partially illustrated by the fluorescence quenching experiment between Th-BTz-Th@TA-BT-TA, Th-BTz-Th/TA-BT-TA and diethyl bromomalonate. The quenching rate decreased when two catalysts is connected, which indicates a weaker interaction between the connected catalyst and diethyl bromomalonate (Figure 5.39).

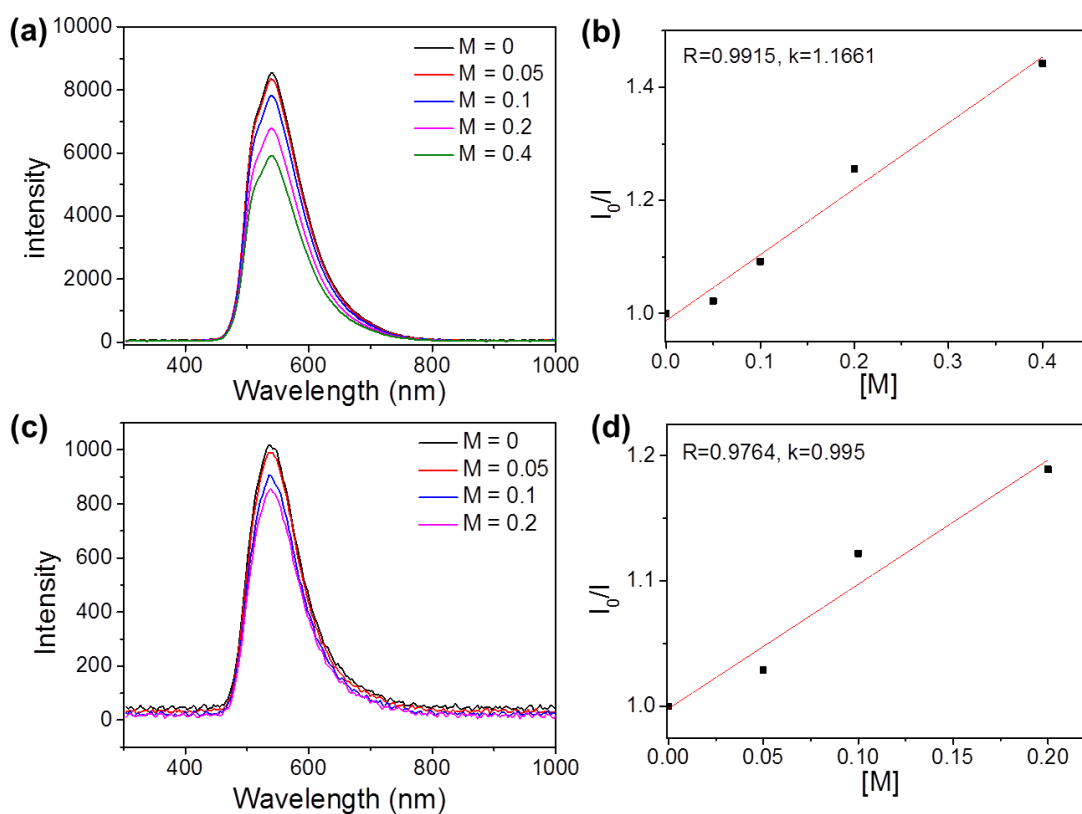


**Figure 5.39** Fluorescence quenching of (a) unconnected and (c) connected Th-BTz-Th/TA-BT-TA with diethyl bromomalonate and Stern-Volmer analysis of (b) unconnected and (d) connected Th-BTz-Th/TA-BT-TA with diethyl bromomalonate.

### 5.2.6 Conclusion

We have developed a new sacrificial reagent-free photoredox pathway by employing organic semiconductors as cooperative photocatalyst couple. The photocatalyst couple consists of organic semiconductors with complementary HOMO/LUMO band positions, leading to enhanced photo-induced intermolecular charge transfer between the organic semiconductors within the couple. By the cooperative photocatalyst design, no extra electron-donating sacrificial reagents are needed and a new paradigm in the photoredox reaction without undesired side reaction under the oxidation of the sacrificial reagents can be established.

## 5.3 Feasibility study of the small molecule organic semiconductors as photocatalysts for challenging reactions: molecular design for metal-free and photocatalytic aromatic C-C bond formation reaction

In the following chapter, a visible light driven aromatic cross coupling reaction is described. Due to the precise and tunable energy levels of small molecule organic semiconductors, namely HOMO/LUMO levels, the catalytic cycle can be designed firstly to achieve this high profile cross coupling reaction. A series of substrates are proved to undergo this reaction successfully with a good to excellent yield. A good selectivity between Br and I can be achieved in utilization of the difference in reductive potential. Cl and Br are also good leaving groups only if the reductive potential of halogen containing substrates is lower than the LUMO of the catalyst.

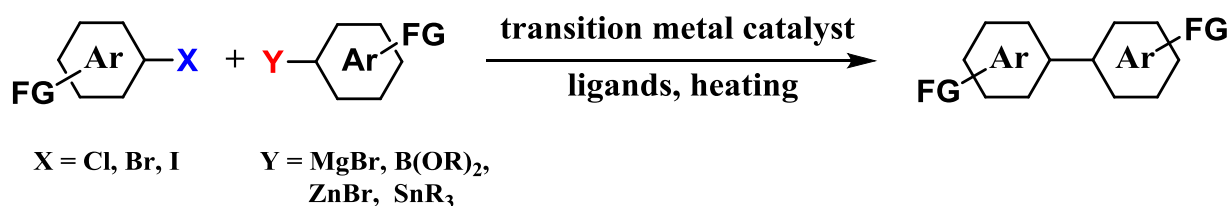
### 5.3.1 Motivation

C-C bond formation cross coupling reactions between aromatic rings show its superior research hit in the past decades and still attract the growing interest in extending this powerful synthetic method.<sup>219</sup> A fruitful research field utilizing this synthetic method is the synthesis of conjugated materials for fascinating electronic devices, such as organic thin film transistors (OTFT), organic solar cells (OSCs), organic light emitting diodes (OLED) and etc.<sup>188-189, 192</sup> The most commonly utilized method is the transition metal, typically palladium, nickel or copper, catalyzed C-C coupling, where the pre-functionalized organometallic starting compound reacts with aryl

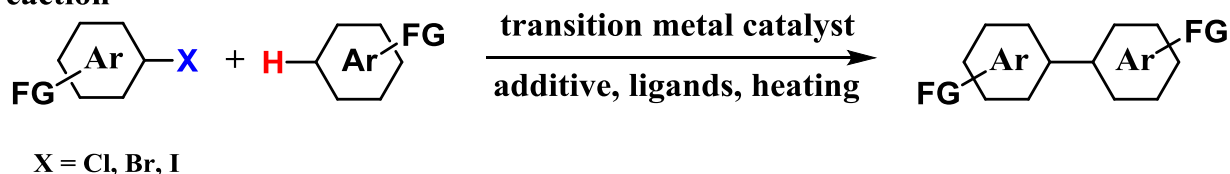


halides. Different reactions are named by the pre-functional group utilized, magnesium halogen, boronic acid and its derivatives, zinc halogen, and stannanes as Kumada, Suzuki, Negishi and Stille coupling respectively (Scheme 3a). A growing demand in streamlining of the overall synthesis to avoid the toxic or high active organometallic pre-functionalized groups results in the direct functionalization of the unreactive carbon-hydrogen bonds. Intensive efforts have been made to develop various reaction conditions for this direct cross coupling of challenging C-H bonds and aryl halides (Scheme 3b).<sup>220-221</sup>

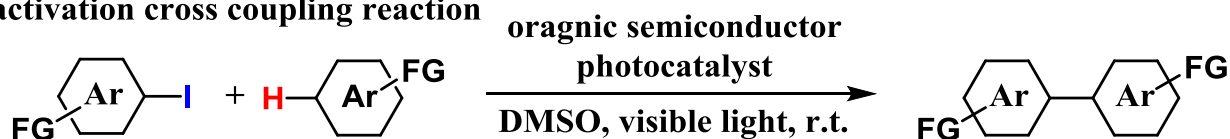
**a. transition metal catalyzed C-C cross coupling reaction**



**b. transition metal catalyzed C-H activation cross coupling reaction**



**c. organic semiconductor photocatalyst catalyzed C-H activation cross coupling reaction**



**Scheme 5.3** Transition metal catalyzed C-C, C-H and organic semiconductor photocatalyst catalyzed C-H cross coupling reactions.

Recent efforts in the field of visible light mediated photocatalyst shows its tremendous perspective for an alternative synthetic method under mild and environmental benign

conditions. Versatile photocatalysts, such as organic transition metal complexes and organic dyes, as well as the novel reactions were developed.<sup>6-8, 13, 222-224</sup> A typical single electron transfer (SET) process occurred between the light activated photocatalyst and substrates in photocatalytic cycle. Numerous inter- or intra-molecular addition reactions were reported using the free radical formed via the SET process.<sup>92, 194, 225-227</sup> However, the examples for the cross coupling using a photocatalyst method between different aromatic rings are rare.<sup>52, 94, 228</sup>

### 5.3.2 Catalytic cycle design

Based on our recent work in applying the organic semiconductors as efficient photocatalyst, we declared an electron flowing behavior between the catalyst and substrates benefited from the clear energy levels of the organic semiconductors. Also, a successful SET process happened and an intermolecular C-C bond formation reaction was conducted. Rechecking the proposed catalytic cycle in our catalyst system, it motivated us to think whether we could conduct the C-C bond formation cross coupling reaction between aromatic rings under the same manner (Scheme 5.3c). So, designing of new reactions by first drawing the catalytic cycle, then trying to find the proper organic semiconductor type photocatalyst and sacrificial reagent to enclose the catalytic cycle should be a possible way to achieve this high profile reaction. Based on the reaction mechanisms we have studied before, the similar catalytic cycle for the aromatic C-C bond formation reaction can be drawn as shown in Figure 5.40. After the formation of the aryl radical via single electron transfer from the LUMO of the excited catalyst, it reacted with a new aryl ring to form the intermediate. Then oxidation and reconstruction of the intermediate offered the desired product.

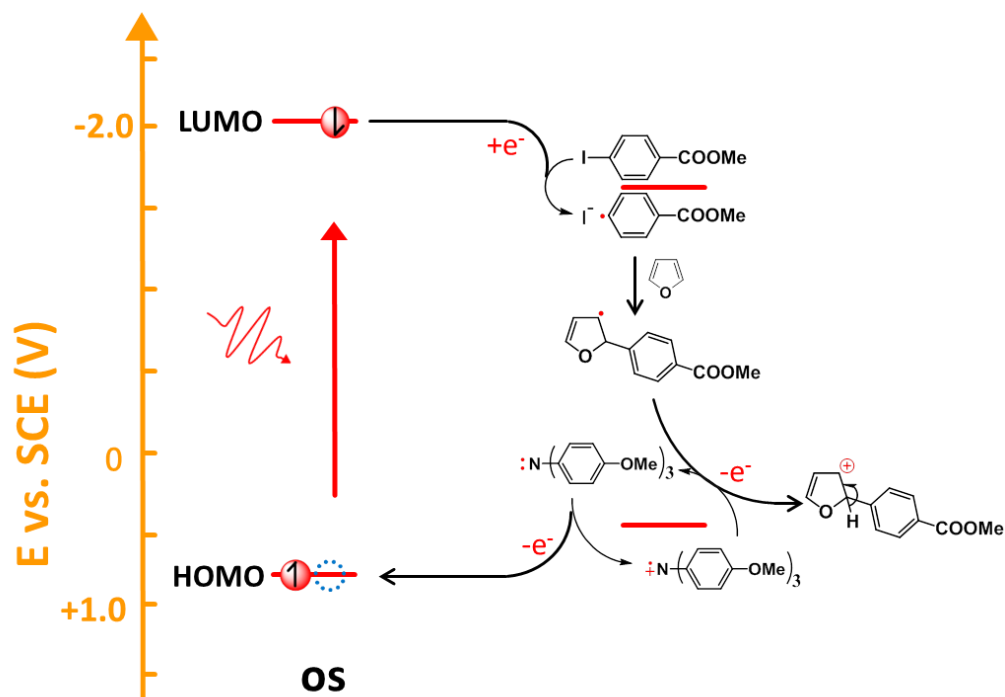


**Figure 5.40** Pre-designed mechanism for organic semiconductor photocatalyst catalyzed C-H cross coupling reactions.

The very first step in pre-drawn catalytic cycle (Figure 5.40) should be the formation of the free aryl radical through the electron transfer between the LUMO of the organic semiconductor and the aryl halogen substrate. Methyl 4-iodobenzoate was chosen here as a typical aryl halogen substrate which has reductive potential of -1.63 V (vs. SCE) (Figure 5.42), so the LUMO of the catalyst should be higher than this. To achieve extremely high LUMO band positions, we aim to fine-engineer molecular organic semiconductors on the molecular level. Three OSs were synthesized to demonstrate the structural design strategy, in particular, 4,7-di(thiophen-2-yl) benzo[c][1,2,5]thiadiazole (**Th-BT-Th**),<sup>229</sup> 2-butyl-4,7-di(thiophen-2-yl)-2H-benzo[d][1,2,3] triazole (**Th-BTz-Th**), and 2-butyl-4,7-bis(1-methyl-1H-pyrrol-2-yl)-2H-benzo[d][1,2,3]triazole (**Py-BTz-Py**). The structures and energy band positions of the OSs are shown in Figure 5.41. By replacing sulfur in the BT unit and introducing nitrogen as electron-donating moiety, the LUMO level could be elevated to -1.68 V vs SCE, as shown in Th-BTz-Th. By further replacement of sulfur by nitrogen in the adjacent thiophene units, the LUMO level could be gradually aligned to -2.04

V, as observed by Py-BTz-Py, which is high enough to make sure the electron transfer from the catalyst to the methyl 4-iodobenzoate.

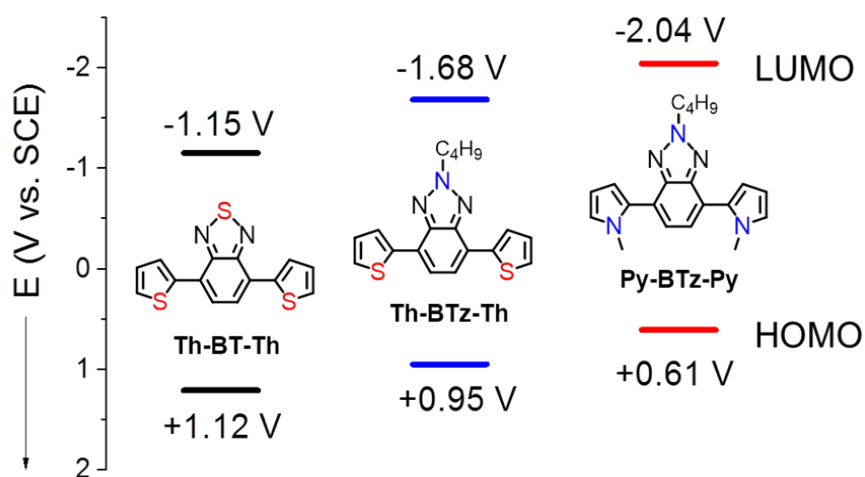


**Figure 5.41** Molecular engineering of OS type photocatalysts.

Based on our previous work that sacrificial reagent is first oxidized to give out one electron to the excited hole in HOMO, we are next searching for the proper substituted triphenyl anine whose oxidative potential is lower than the HOMO of the catalyst (+0.61 V vs. SCE) (Figure 5.41). Tri(4-methoxyl phenyl)anime, triphenyl amine substituted by three electron donating group, was a final choice whose oxidative potential is +0.48 V (vs. SCE) (Figure 5.42). Although, the oxidative potential of the new radical intermediate formed after the addition cannot be tested directly, it should be not so high that prevent the electron transfer to the oxidized reductant, as reported<sup>116</sup> and calculated by computed method before.

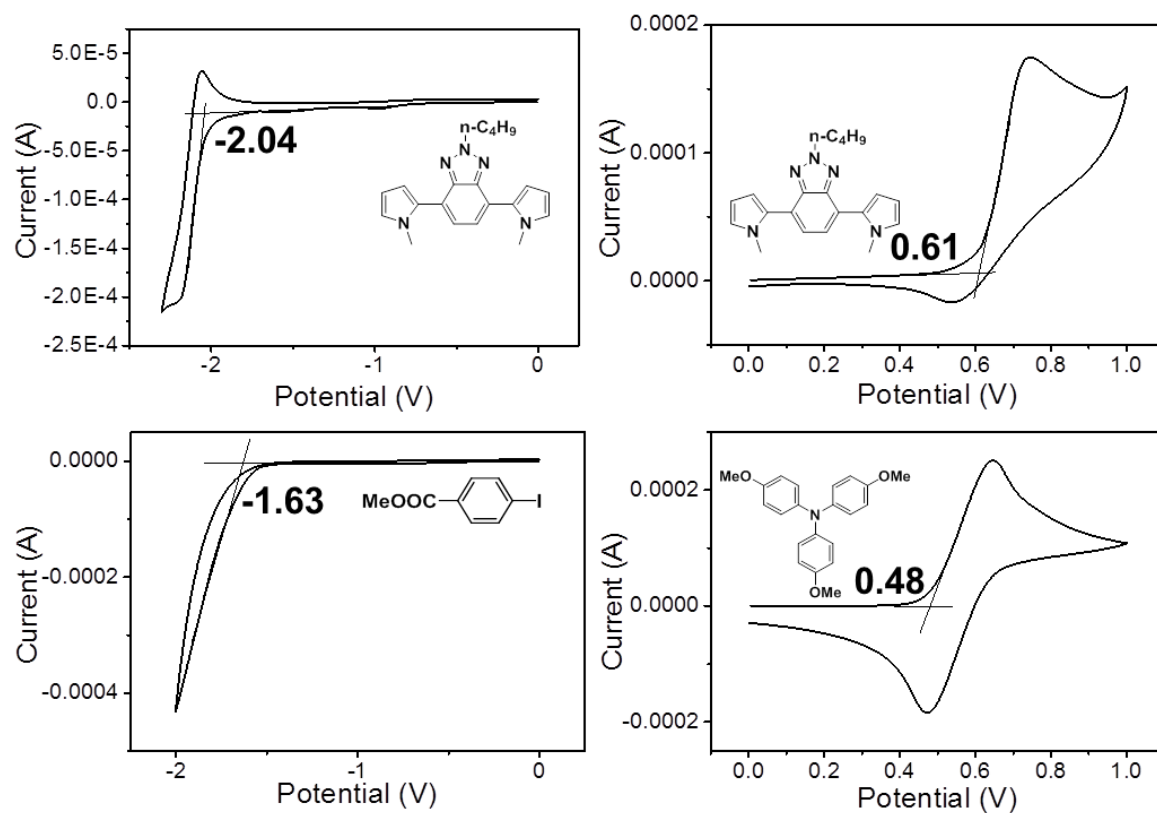
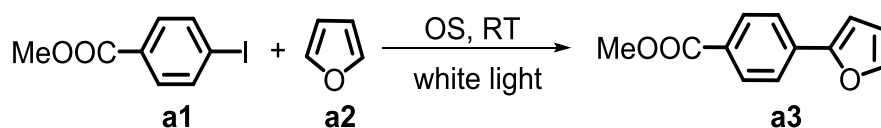


Figure 5.42 Proper energy levels designed for catalytic cycle.

### 5.3.3 Screening of the reaction condition

**Table 5.6 Reaction condition optimization of aromatic cross coupling reaction**



Entry	solvent	Catalyst/%	Amine/equiv.	Furan/equiv.	Conversion/% <sup>a</sup>
1	DMSO	5	1	20	55
2	DMF	5	1	20	43 <sup>b</sup>
3	MeCN	5	1	20	24
4 <sup>c</sup>	DMSO	5	1	20	66
5	DMSO	-	1	20	-
6	DMSO	5	-	20	-
7 <sup>d</sup>	DMSO	5	1	20	-

*Reaction conditions: 1 equiv (0.38 mmol) methyl 4-iodobenzoate, 20 equiv furan, 1 equiv amine, 5% catalyst in 2.5 ml solvent, white LED (0.16 W/cm<sup>2</sup>), RT, 24 h. [a] Conversion determined via GC-MS. [b] 30% methyl benzoate as side product. [c] 2 days reaction time. [d] reaction conducted without light.*

Initial study using 1 equiv (0.38 mmol) methyl 4-iodobenzoate, 5 equiv photocatalyst, 1 equiv sacrificial reagent and 20 equiv furan in 2.5 ml DMSO give the desired product with 55% conversion (Table 5.6, entry 1). Changing the solvent into DMF will result in the 30% de-iodine product as a side reaction (Table 5.6, entry 2), since the high reactive radical can abstract hydrogen from DMF.<sup>230</sup> Extend the reaction time to 2 days just slightly improved the conversion (Table 5.6, entry 4). And the control experiment that conducting reactions without catalyst (Table 5.6, entry 5), sacrificial reagent (Table 5.6, entry 6) and light (Table 5.6, entry 7) will not

lead to any consumption of the starting substrate, which indicates the robustness of the designed catalytic cycle.

#### 5.3.4 Screening of the aryl iodides and aromatic ring

To investigate the general feasibility of Py-BTz-Py as photocatalyst, we then tested various aryl substrates using the optimized reaction condition. The results are listed in Figure 5.43. A high functional group tolerance on the aryl substrates was observed. By scoping the reaction of various aryl iodides with furan, a clear tendency could be observed. The electron-withdrawing substituents such as cyano- or trifluoro- groups (b4-b9) generally led to higher reaction yields than the electron-donating substituents (b17-b20) (Figure 5.43a). However, single halide-containing substituents (b1-b3) did not lead to higher product yields than the model substrate methyl 4-iodobenzoate (b15). Nevertheless, multiply halogenated aryl iodides led to moderate product yields (b11-b13). The reactions with the other carbonyl-containing substrates showed similar product yields (b14 and b16).

The scope of different arenes ( $Ar^2$ ) as coupling partner showed that the reactions with electron-rich arenes such as pyrrole could be obtained in very high yields up to 99% (b21-b26). The reaction of methyl 4-iodobenzoate with thiophene led to a slightly lower yield than the model reaction with furan (b27). The reactions with electron deficient arenes such as phenyl (b28) and toluene (b29) showed a lower product yields than the ones with electron rich arenes. It is to note that three different products were obtained from the reaction with toluene. Mainly *ortho*-substituted C-C bonded product on toluene was obtained (b29).

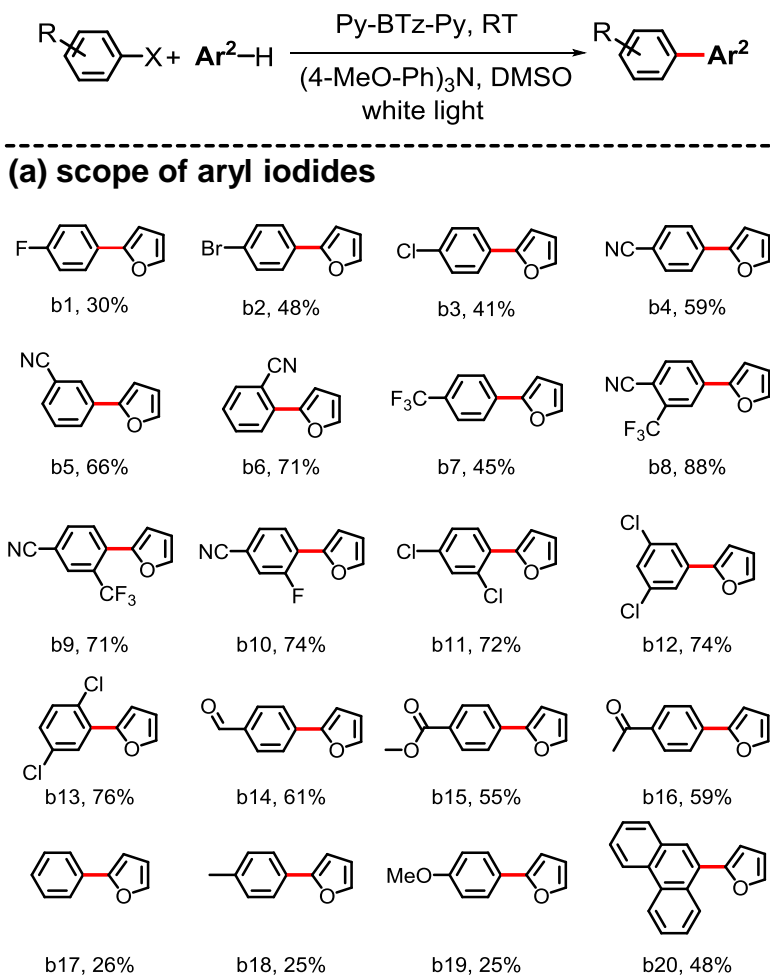
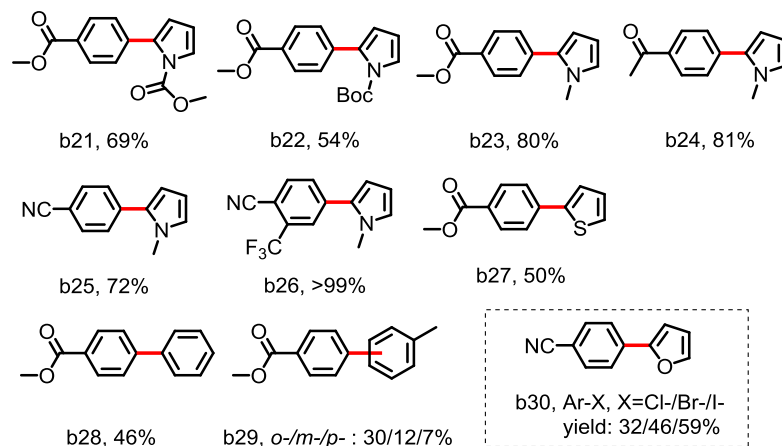
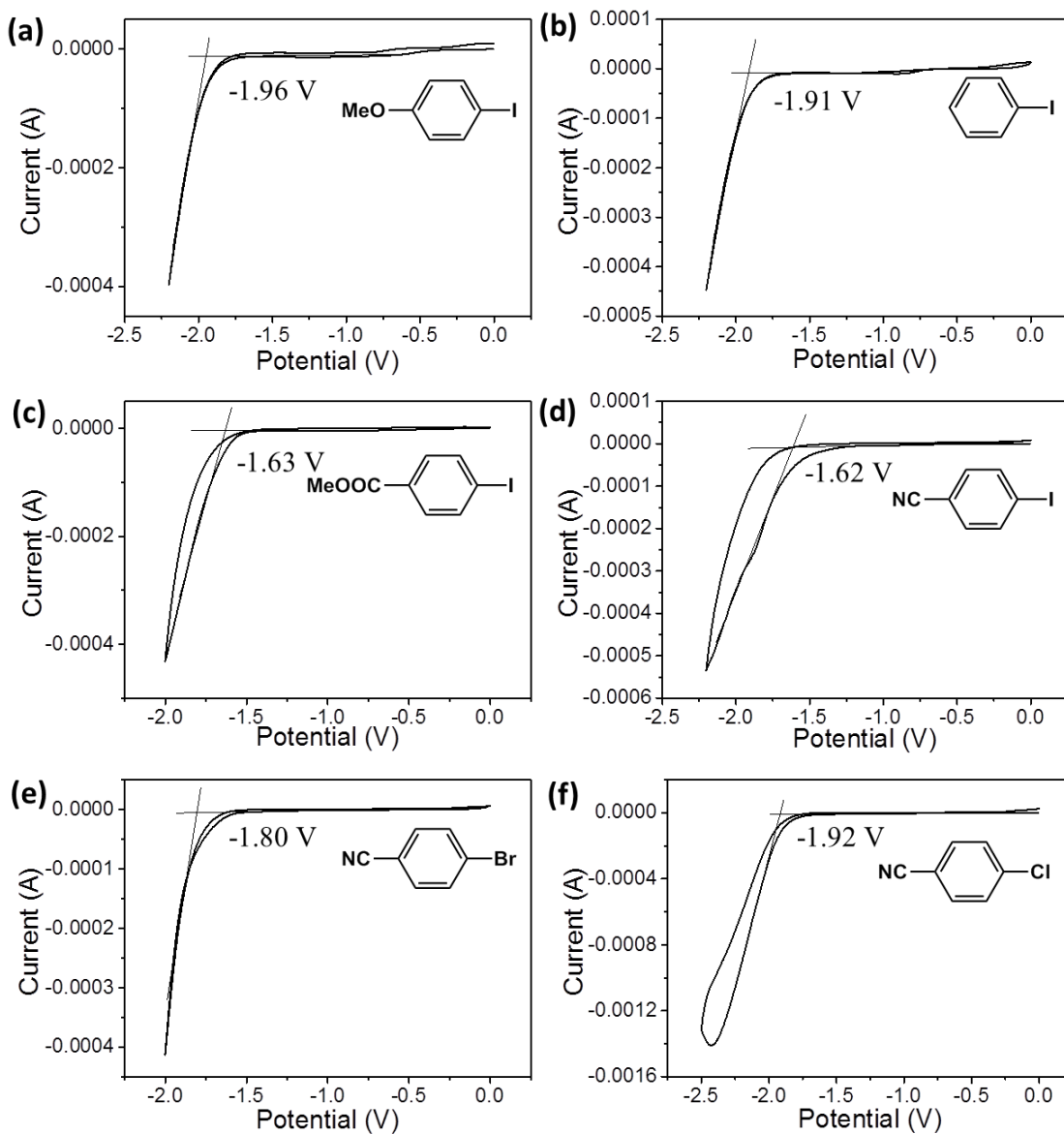
**(b) scope of Ar<sup>2</sup>**

Figure 5.43 Screening of the Ar-I and Ar for the photocatalytic C-C bond formation.



Additionally, the reduction potential dependence of the C-C bonded product yield of the aryl halides could be demonstrated by comparing the reaction of 4-chloro-, 4-bromo- and 4-iodobenzonitrile with furan. By decreasing reduction potential of the aryl halides, in particular, -1.92, -1.80, and -1.62 V vs. SCE respectively (Figure 5.44), increased product yields were obtained (b30).



**Figure 5.44** Reductive potential of (a) 4-iodoanisole, (b) iodobenzene, (c) methyl 4-iodobenzoate, (d) 4-iodobenzonitrile, (e) 4-bromobenzonitrile and (f) 4-chlorobenzonitrile.

### 5.3.5 Examination of the mechanism

Fluorescence quenching experiments show that the fluorescence of the catalyst can be strongly quenched by adding the sacrificial reagent tri(4-methoxyl phenyl) amine (Figure 5.45a and 5.45b). A slowly quenching between the catalyst and methyl 4-iodobenzoate can also be seen (Figure 5.45c and 5.45d), however, no product can be obtained when conducting the reaction without sacrificial reagent. It is accordance with our previous knowledge that fluorescence quenching can be seen between catalyst and halogen containing substance when the catalyst is more electron-rich, namely LUMO is higher. However the reductive quenching of the catalyst should be more efficient. Two roles of the sacrificial reagent exist here, first is the base to neutralize the HI formed as by product and second the electron donating reagent to accelerate the reaction rate. So, it is strongly declared here that the electron should originate from the tri(4-methoxyl phenyl) amine to the light generated hole in the HOMO of the catalyst.

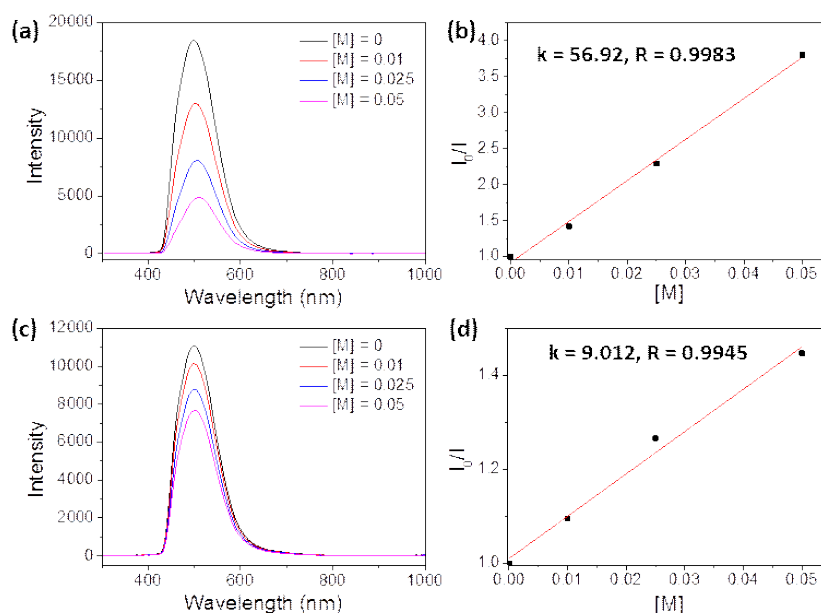


**Figure 5.45** Fluorescence quenching of (a) Py-BTz-Py with tri(4-methoxylohenyl)amine and (c) methyl 4-iodobenzoate, Stern-Volmer analysis of (b) Py-BTz-Py with tri(4-methoxylohenyl)amine and (d) methyl 4-iodobenzoate. [M]: concentration of the amine or the substrate.

To confirm the aryl radical-mediated reaction mechanism as illustrated in Figure 5.40, we then conducted the reduction reaction of methyl 4-iodobenzoate in the presence of Bu<sub>3</sub>N using 2,2,6,6-tetramethylpiperidin-1-yl)oxyl (TEMPO) as radical trapping agent. The trapped TEMPO-adduct could be determined by MS (291.7 g/mol in Figure 5.46).

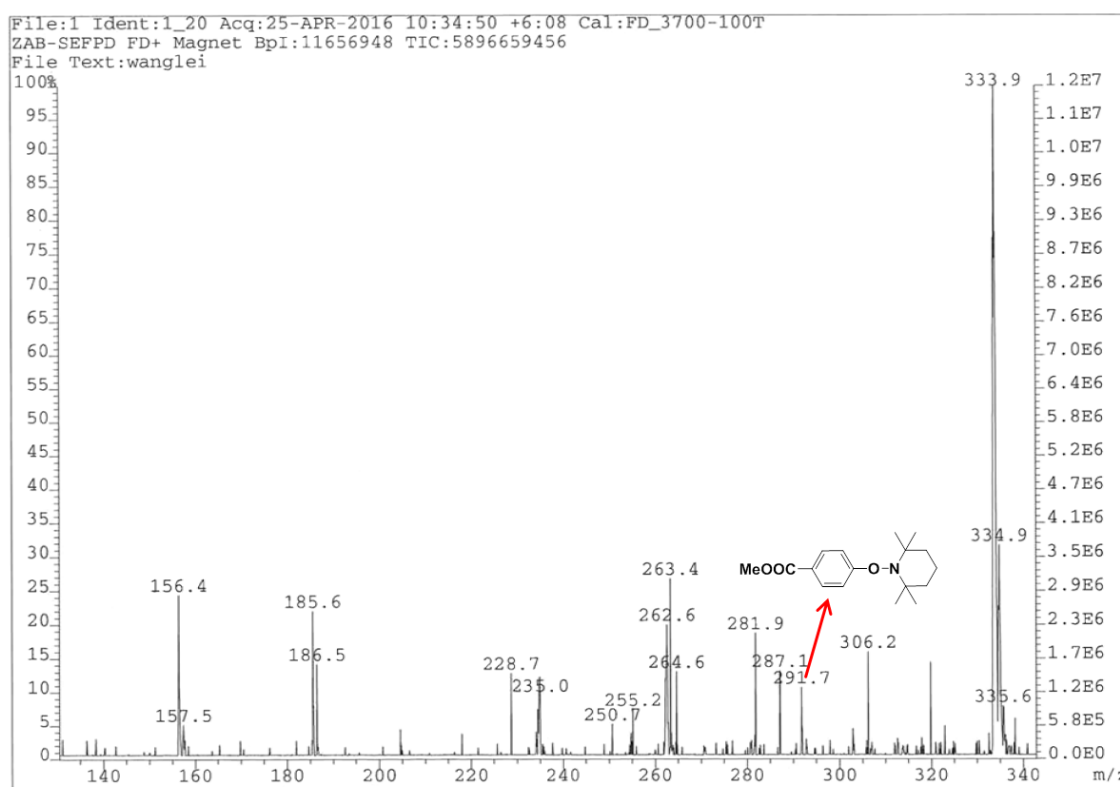
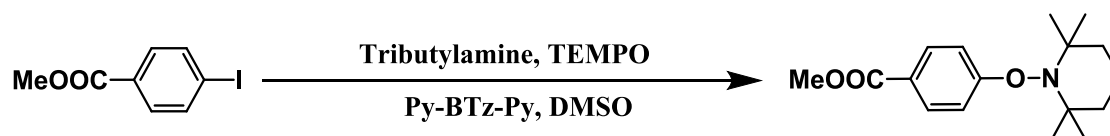


**Figure 5.46** Aryl radical trapping experiment using TEMPO. Reaction conditions: methyl 4-iodobenzoate (0.38 mmol, 1 equiv.), tributylamine (1.9 mmol, 5 equiv.), TEMPO (1.9 mmol, 5 equiv.), organic semiconductor photocatalyst (5%, 0.019 mmol), in 2.5 ml DMSO.

### 5.3.6 Conclusion

In summary, a precise molecular design of organic semiconductors for metal-free and visible light-driven aromatic C-C formation reactions was demonstrated. Via heteroatom engineering, the LUMO level of the organic semiconductor could be aligned to -2.04 V vs SCE and thereby possessing an extreme high photo-reductive potential. Various aryl halides could be reduced to aryl radicals, which could couple with other aromatic compounds to form the final C-C-bonded products. We believe that this study can provide a promising organic photocatalyst with extreme high reductive potential for C-C bond formations, which can also be applied in a wider range of radical-mediated bond formation reactions such as C-N, C-P etc.

## 5.4 Visible light-controlled atom transfer radical polymerization (ATRP) catalyzed by small molecule organic semiconductors

In the following chapter, a controllable atom transfer radical polymerization process is described, which can be achieved by the utilization of different small molecule organic semiconductors as photocatalyst. The redox potential of the organic photocatalysts, initiator, sacrificial reagents and monomers were precisely adjusted. The additive salt, in particular LiX (X: halide), played an important role in maintaining the living manner during the polymerization process to surpass the chain end to eliminate the side reaction. Under the optimized condition, well-defined polymers with narrow polydispersity, precisely identified chain end were synthesized. The controllability of the polymerization was proved by the chain extension with the purified polymer as macro-initiator to further prepare block copolymers.

### 5.4.1 Motivation

Controllable synthesis of polymer with precise molecular weight, molecular weight distributions and also molecular structures is of great importance in polymer chemistry. Unlike the living ionic polymerizations, controlled radical polymerization (CRP) is more applicable due to its great tolerance to solvents, functional groups and impurities.<sup>231-238</sup> Indeed, atom transfer radical polymerization (ATRP) has become one of the most utilized synthetic methods for the

preparation of polymers with controlled molecular weight, molecular weight distribution, and versatile chemical structures.<sup>239</sup> Recent efforts in improving the ATRP process leads to the photo polymerization driven by photocatalyst, which the control of the chain growth can be easily accomplished with light as external stimulus and the toxic metal purification process can be avoided by utilization of the organic catalysts.<sup>39-40, 42-43, 45, 240-243</sup> However, most reported organic photocatalysts for ATRP such as phenoxazines and dihydrophenazine illustrate extremely high reductive potential, which have an intrinsic disadvantage of UV activation and instability of storage. Therefore, the design of visible light induced photocatalyst with high stability and catalytic efficiency for ATRP is still urgent for polymer chemists.

In the previous sub-chapters, organic semiconductor (OS) photocatalysts have demonstrated their feasibility as promising alternative to noble metal or organic dye-containing photocatalysts. The advantage of tailorable electronic properties via versatile structural design was also demonstrated in this thesis. The high efficiency of single electron transfer (SET) process in OS type photocatalyst has been verified by C-C coupling reactions conducted under visible light, which the radical formed after the electron transfer from the LUMO of the catalyst to the relative substrate. We envisaged that this photo-induced radical formation process could also be applied for the photo controlled living radical polymerization. A proposed mechanism is shown in Figure 5.47. The initiating step of the polymerization is the electron transfer from the LUMO of the catalyst to alkyl halogen initiator to form the desired radical for chain propagation. In addition, the radical polymer chain end can be efficiently deactivated via the oxidation process, which one electron was migrated to the oxidized sacrificial reagent, accompanying with the regenerated alkyl halogen bond for further catalytic cycle. According to the proposed mechanism, a photocatalyst with slightly higher reductive potential than that of halide initiator and oxidative potential than that of sacrificial reagent should thermodynamically work for the electron transfer between photocatalyst and reactive reagents. Therefore, extremely high redox potentials could be totally avoided for the ATRP process, which makes it possible for radical generation and chain initiation in the visible light region.

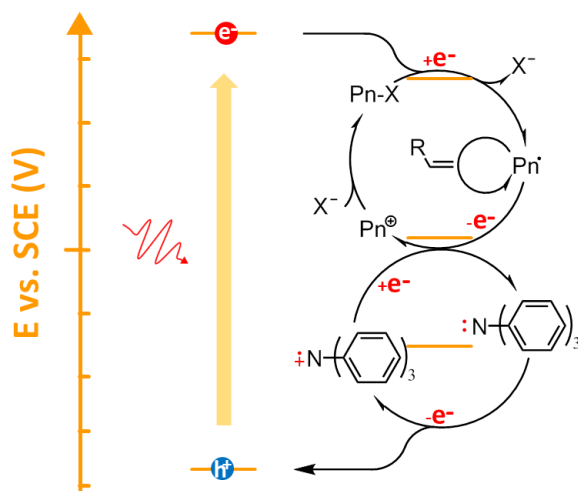


Figure 5.47 Proposed mechanism for the light-controlled ATRP process catalyzed by OS type photocatalysts.

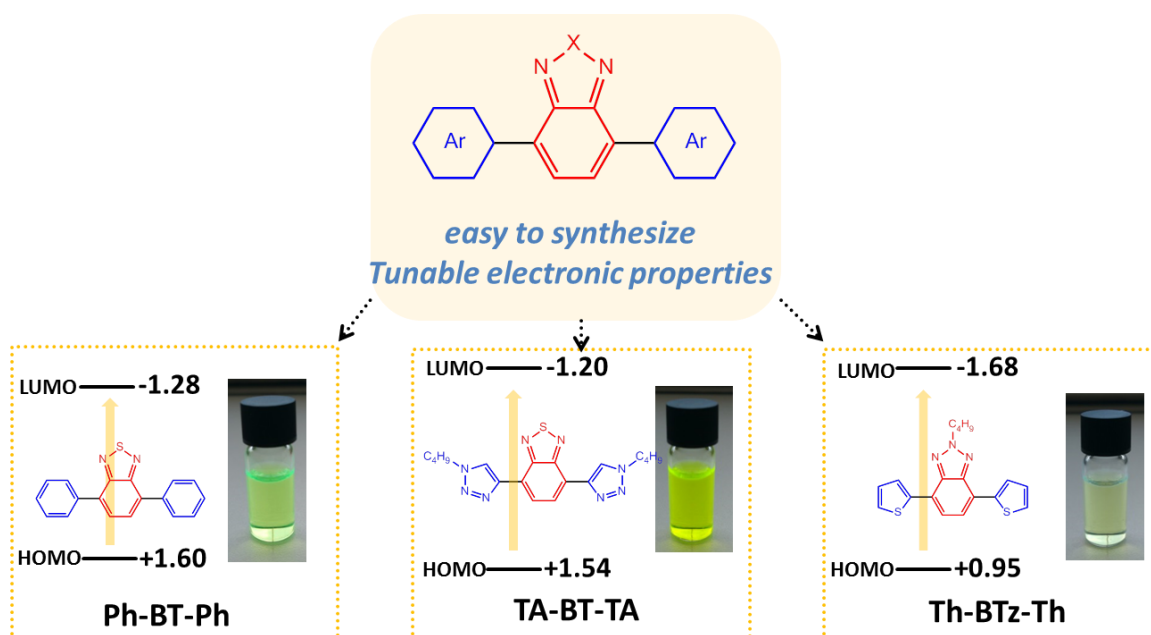
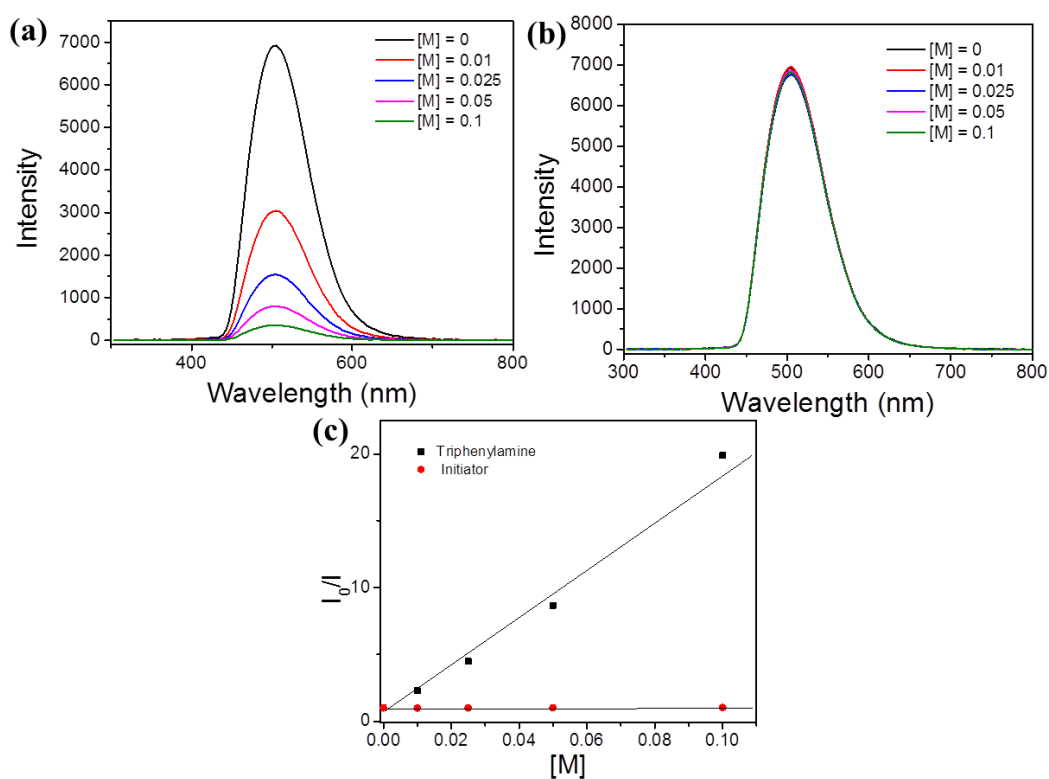


Figure 5.48 Illustration of the probably suitable OS type catalysts using in ATRP.

### 5.4.2 The role of sacrificial reagent

Before studying the light-controlled ATRP process, the role of the sacrificial reagent should be first clarified. Proven by the previous studies, usually, the fluorescence of the photocatalyst

with a lower reductive potential cannot or can only be slightly quenched by substrate containing alkyl halogen bonds. In comparison, the fluorescence of the photocatalyst can be strongly quenched by sacrificial reagent. However, for photocatalysts with high reductive potentials, the reductive quenching process via direct electron transfer from the photocatalyst to the alkyl halogen bond, could be possible.<sup>92</sup> To prove this, the fluorescence quenching experiments of the chosen photocatalyst, in particular, Ph-BT-Ph and ethyl  $\alpha$ -bromophenyl acetate as the radical initiator were carried out. The fluorescence of Ph-BT-Ph could not be quenched by the initiator, as shown in Figure 5.49. However, the successful quenching was shown by the sacrificial reagent (triphenylamine). Based on this observation, we aim to incorporate the sacrificial reagents in the designed catalytic system.



**Figure 5.49** Fluorescence quenching of Ph-BT-Ph with (a) triphenylamine, (b) ethyl  $\alpha$ -bromophenyl acetate, and (c) Stern-Volmer analysis.

### 5.4.3 Energy level study in the proposed catalytic cycle

To verify the demanded reductive/oxidative potentials for the photocatalyst, the reductive potential of the initiator and the living chain end, and the oxidative potentials of sacrificial reagent, triphenylamine used here, were first examined. As a result, the demand for the reductive potential of the photocatalyst should higher than -1.05 V (Figure 5.50b), which was the reductive potential for the C-Br bond at the chain end, and the oxidative potential should higher than 0.89 V (Figure 5.50c), which is the oxidative potential of the sacrificial reagent, triphenylamine in this case.

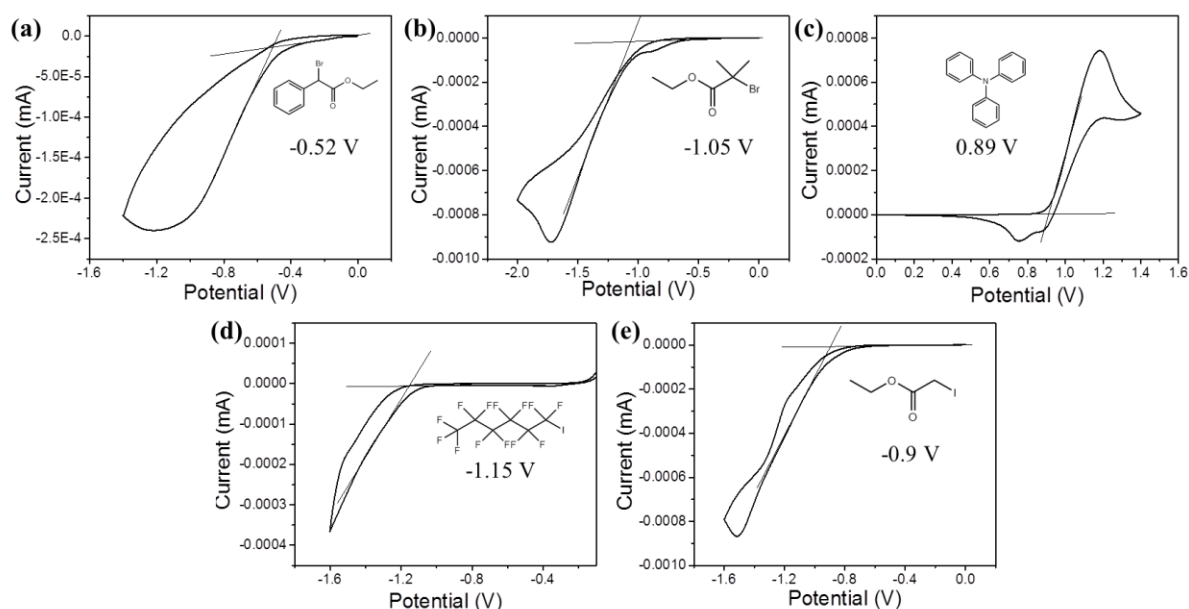


**Figure 5.50** (a) Reductive potential of initiator ethyl  $\alpha$ -bromophenyl acetate, (b) reductive potential of polymer chain end C-Br bond, (c) oxidative potential of sacrificial reagent triphenylamine, (d) reductive potential of initiator 1-iodoperfluorohexane, and (e) reductive potential of polymer chain end C-I bond, estimated by the analogue ethyl iodoacetate.



#### 5.4.4 Optimization of polymerization condition

The requirement for the energy levels can be accomplished by the designed OS type photocatalysts here. Initial study by employing 0.1% Th-BTz-Th, which occupies a reductive potential of -1.68 V and oxidative potential of 0.95 V, 5.6 mmol MMA, 2.5% ethyl  $\alpha$ -bromophenyl acetate and 10 % triphenylamine offered a polymer. However, carefully examined the polymer process showed a non-controlled behavior. The molecular weight unchanged and even decreased with prolonged reaction time (Figure 5.51a), while the consumption of the monomer increases.

It is also necessary to mention that, without sacrificial reagent, the polymerization process occurred in a more radical manner, resulting in the polymer with multi-distribution properties as illuminated in GPC curve, high molecular weight and broad PDI (Figure 5.51b).

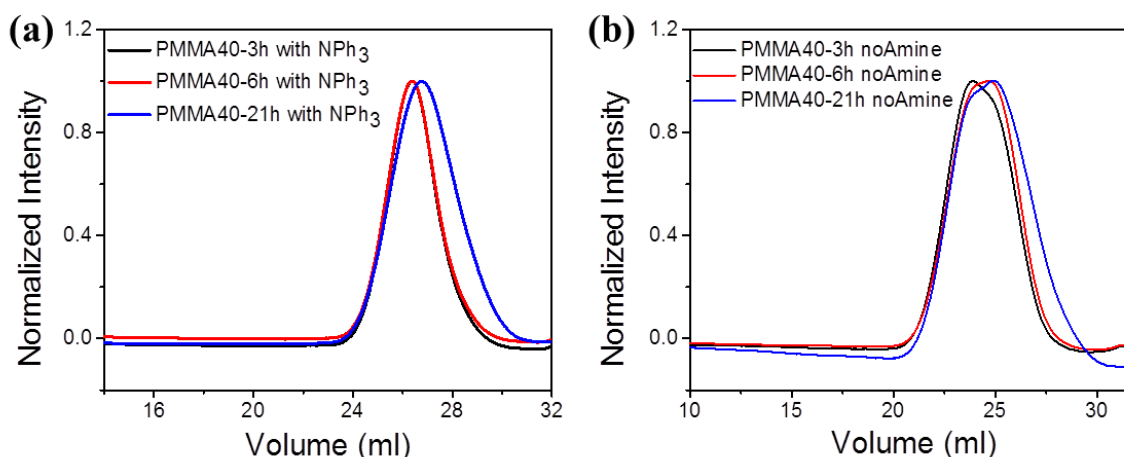


**Figure 5.51** Gel permeation chromatography traces of PMMA40 synthesized (a) with sacrificial reagent and (b) without sacrificial reagent. Reaction condition: MMA 5.6 mmol, 2.5% mol Initiator ethyl  $\alpha$ -bromophenyl acetate, 0.1% Th-BTz-Th as photocatalyst, 10% mol triphenylamine or not in 1.5 ml DMF with a white LED as light source.

Chain extension of the produced polymer with MMA showed shoulder peak in GPC curves (Figure 5.52a), which may be caused by the dead chain end that the molecular weight

unchanged. This component was more obvious for the polymer synthesized with 1-iodoperfluorohexane as initiator, whose polymer chain end should be the C-I bond (Figure 5.52b).

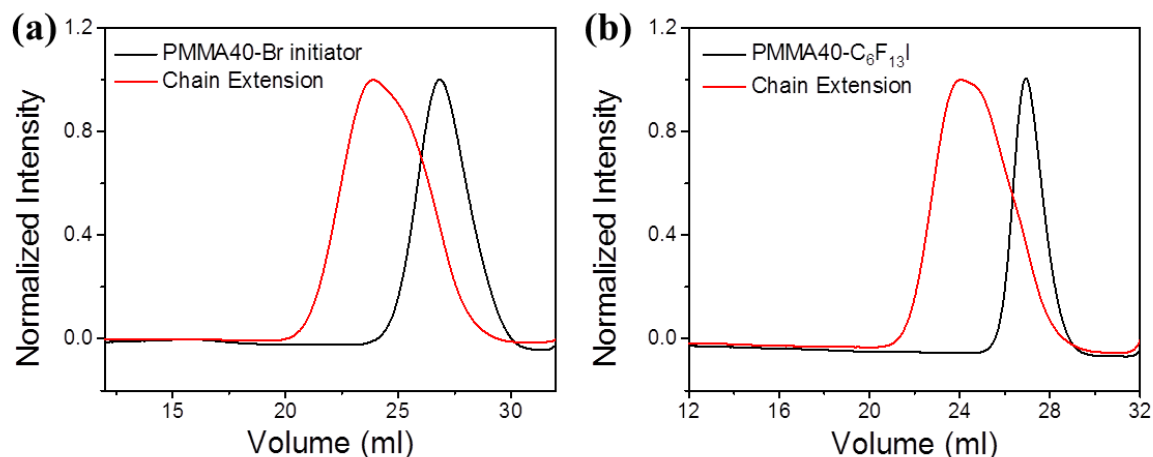


**Figure 5.52 Gel permeation chromatography traces of PMMA40 and chain extended PMMA40 synthesized (a) with ethyl  $\alpha$ -bromophenyl acetate as initiator and (b) with 1-iodoperfluorohexane as initiator. Reaction condition for the PMMA40: MMA 5.6 mmol, 2.5% mol Initiator, 0.1% Th-BTz-Th as photocatalyst, 10% mol triphenylamine in 1.5 ml DMF with a white LED as light source (5 hours reaction time for Br initiator and 20 h for the I initiator). Reaction condition for the chain extended PMMA40: MMA 5.6 mmol, 100 mg purified macroinitiator, 0.1% Th-BTz-Th as photocatalyst, 20% mol triphenylamine in 1.5 ml DMF with a white LED as light source (5 hours reaction time for Br initiated PMMA40 and 20h for the I initiated PMMA40).**

The failure of synthesizing the well-defined polymer and chain extended product forced us to reexamine the catalytic cycle. We realized that the sacrificial reagent, triphenylamine, could also act as a Lewis base. As shown in Figure 5.53, the positive carbon ion formed after the electron transfer process made the hydrogen at the adjacent carbon more acidic, which could be abstracted by the triphenylamine to form the eliminated product and finally formed an inactive chain end (dead chain).

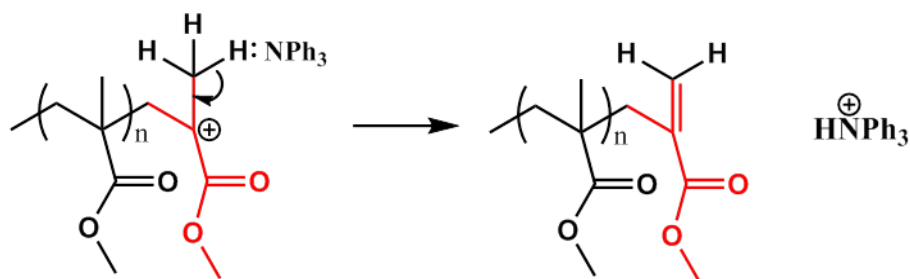


**Figure 5.53 Proposed elimination side reaction.**

To surpass this side reaction, more halogen negative ions should be supplied for a quicker recombination with the positive carbon ion to form the C-X bond. LiBr was added as an additive to improve the living polymerization behavior. Interestingly, the polymerization process conducted with 0.1% Th-BTz-Th as photocatalyst, 5.6 mmol MMA, 2.5% ethyl  $\alpha$ -bromophenyl acetate, 10% triphenylamine and 20% LiBr showed an improved living polymerization character. The molecule weight increased linearly with the consumption of the monomer (Figure 5.54a), and the plot of the  $\ln([M]_0/[M])$  versus exposure time was also in a linear function relationship (Figure 5.54d). However, the PDI also increased after the polymerization process.

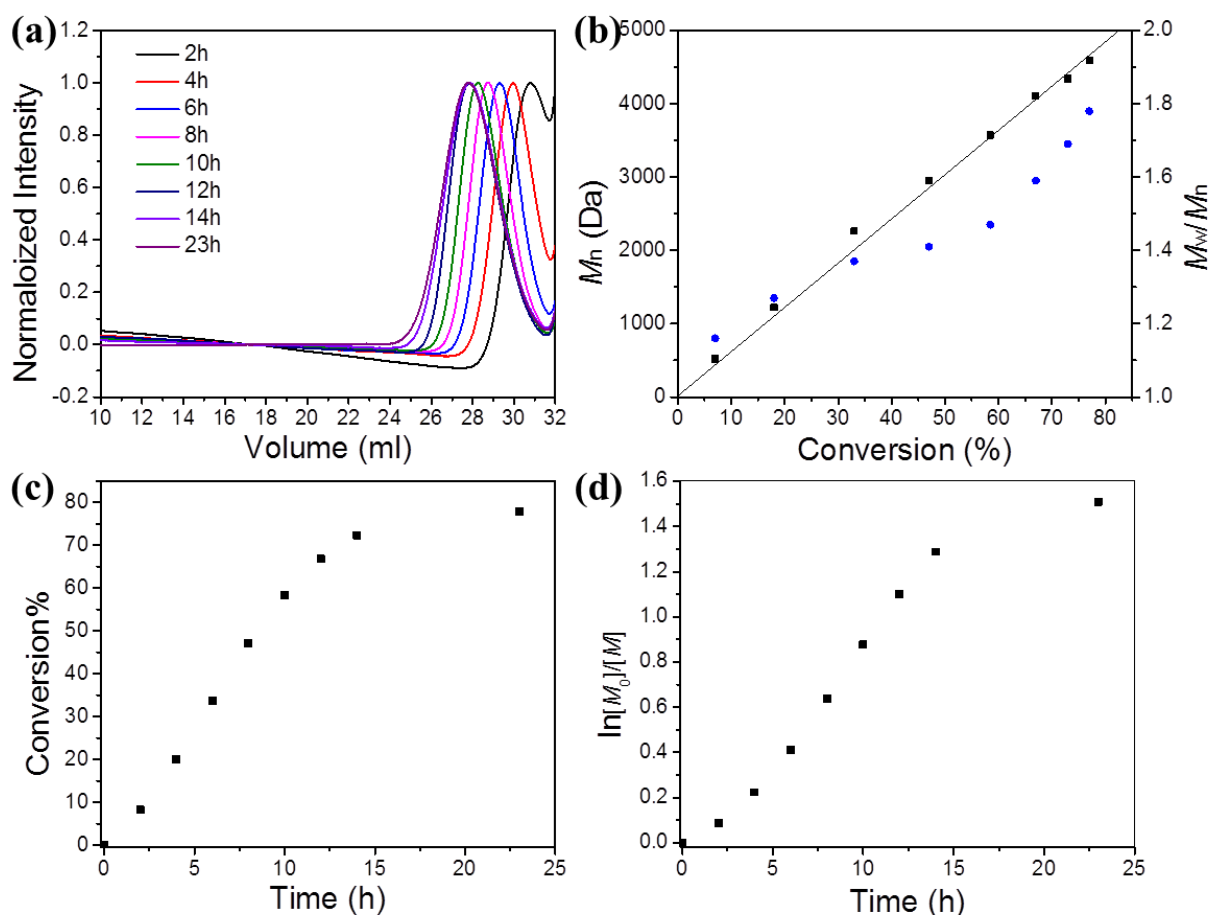


**Figure 5.54 (a) Gel permeation chromatography trace vs. reaction time, (b) molecular weight and molecular weight distribution vs. conversion, (c) conversion vs. reaction time and (d)  $\ln([M]_0/[M])$  as a function of time. Reaction condition: MMA 5.6 mmol, 2.5% mol Initiator ethyl  $\alpha$ -bromophenyl acetate, 0.1% Th-BTz-Th as photocatalyst, 10% mol triphenylamine, 20% LiBr in 1.5 ml DMF.**

Further attempt to improve this situation was involved the changing of the photocatalyst. By using TA-BT-TA as photocatalyst, which has a reductive potential of -1.20 V and oxidative potential of +1.54 V, a longer reaction time up to 60 hours was needed for a high conversion of the monomer (Figure 5.55c). This was likely due to the low “over potential” between the LUMO of the TA-BT-TA and reductive potential of chain end C-Br bond, which is consisted with the

result we got before. PDI during the whole polymerization process was quit high, up to 1.8 (Figure 5.55b).

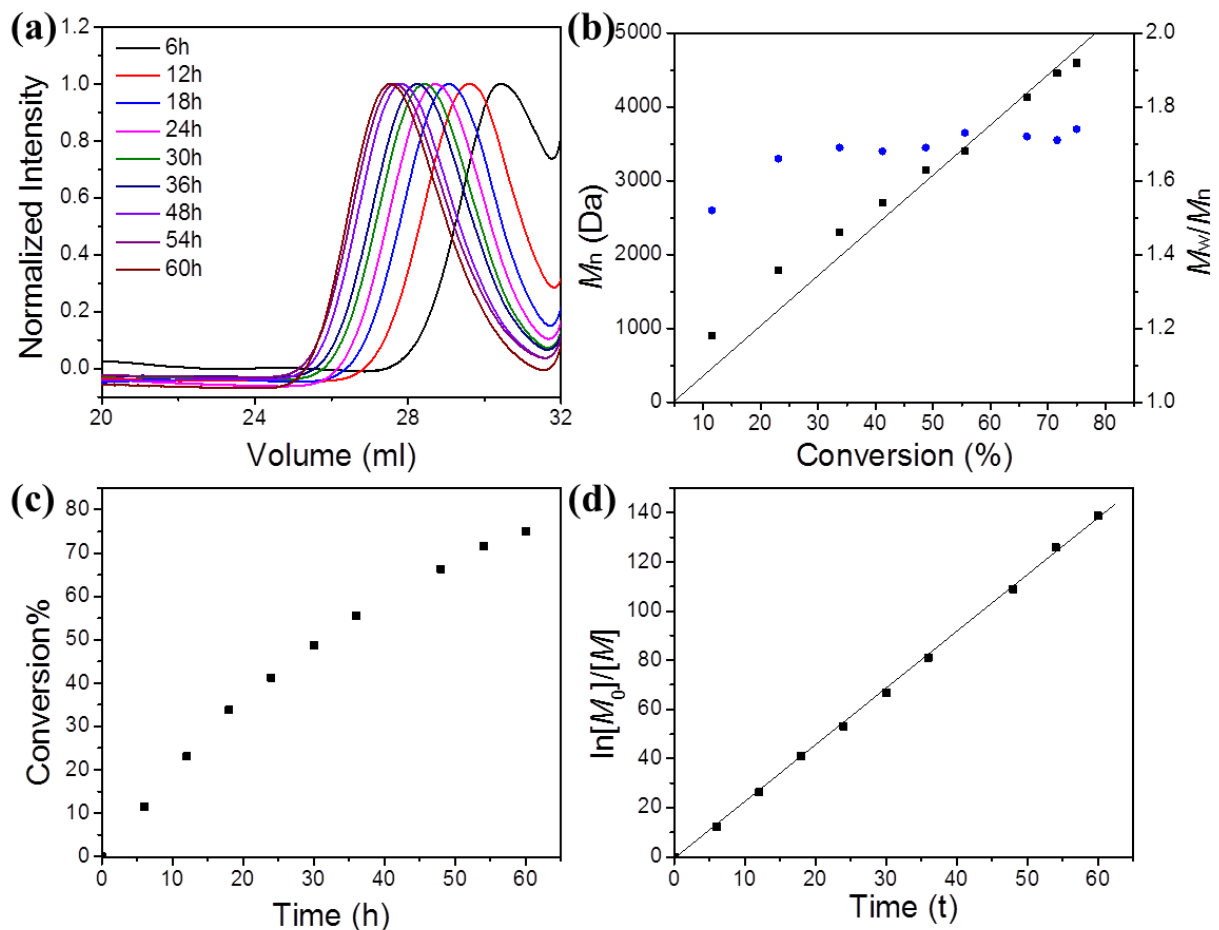


**Figure 5.55 (a) Gel permeation chromatography trace vs. reaction time, (b) molecular weight and molecular weight distribution vs. conversion, (c) conversion vs. reaction time, and (d)  $\ln([M]_0/[M])$  as a function of time. Reaction condition: MMA 5.6 mmol, 2.5% mol Initiator ethyl  $\alpha$ -bromophenyl acetate, 0.1% TA-BT-TA as photocatalyst, 10% mol triphenylamine, 20% LiBr in 1.5 ml DMF.**

To narrow the PDI, Ph-BT-Ph was used as photocatalyst, which exhibited the reductive potential and oxidative potential of -1.28 V and +1.6 V vs SCE, respectively. During the polymerization

process, the plots of the  $M_n$  versus conversion and  $\ln([M]_0/[M])$  versus exposure time appeared in a linear relationship (Figure 5.56b and 5.56d), and the PDI for the final product was 1.35.

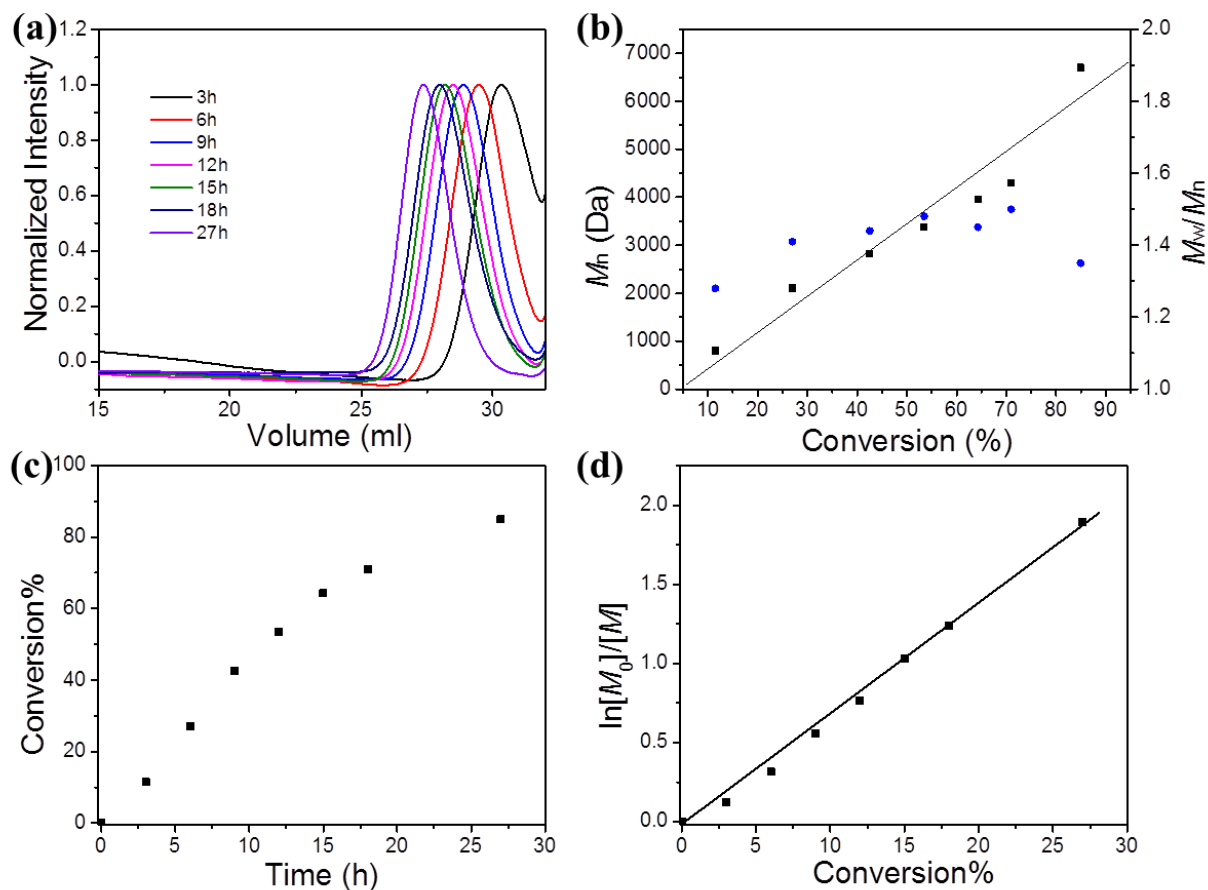


**Figure 5.56 (a) Gel permeation chromatography trace vs. reaction time, (b) molecular weight and molecular weight distribution vs. conversion, (c) conversion vs. reaction time and (d)  $\ln([M]_0/[M])$  as a function of time. Reaction condition: MMA 5.6 mmol, 2.5% mol Initiator ethyl  $\alpha$ -bromophenyl acetate, 0.1% Ph-BT-Ph as photocatalyst, 10% mol triphenylamine, 20% mol LiBr in 1.5 ml DMF.**

**Table 5.7 Results of the ATRP conducted with different catalysts.**

Entry	catalyst	<i>t</i> /h	<i>M<sub>n</sub></i> ,GPC/Da	PDI	Conversion/%	<i>I</i> <sup>b</sup>
1	Th-BTz-Th	23	4591	1.78	78	0.68
2	TA-BT-TA	60	4598	1.74	75	0.65
3	Ph-BT-Ph	27	6706	1.35	85	0.51

[a] Reaction condition: MMA (1 equiv, 5.6 mmol), initiator, catalyst,  $NPh_3$ , LiBr in DMF (1.5ml) at room temperature with a white LED as light source. [b] Initiating rate, calculated by  $Mn,theory/Mn, GPC$ .

#### 5.4.5 Living nature of the ATRP

The light controlled living manner of the polymerization process was further proved via the light “on-off” experiment. During the polymerization, the polymer chain could only propagate under light irradiation. In the absence of light, no consumption of the monomer (Figure 5.57a) or the increase of the molecular weight (Figure 5.57b) could be observed. Even after a long dark period up to 5 hours, no obvious change was observed. This strongly suggested that the polymerization was not in a free radical manner. The radical chain end could be quickly deactivated after the monomer addition via the oxidation process to form the C-Br bond.

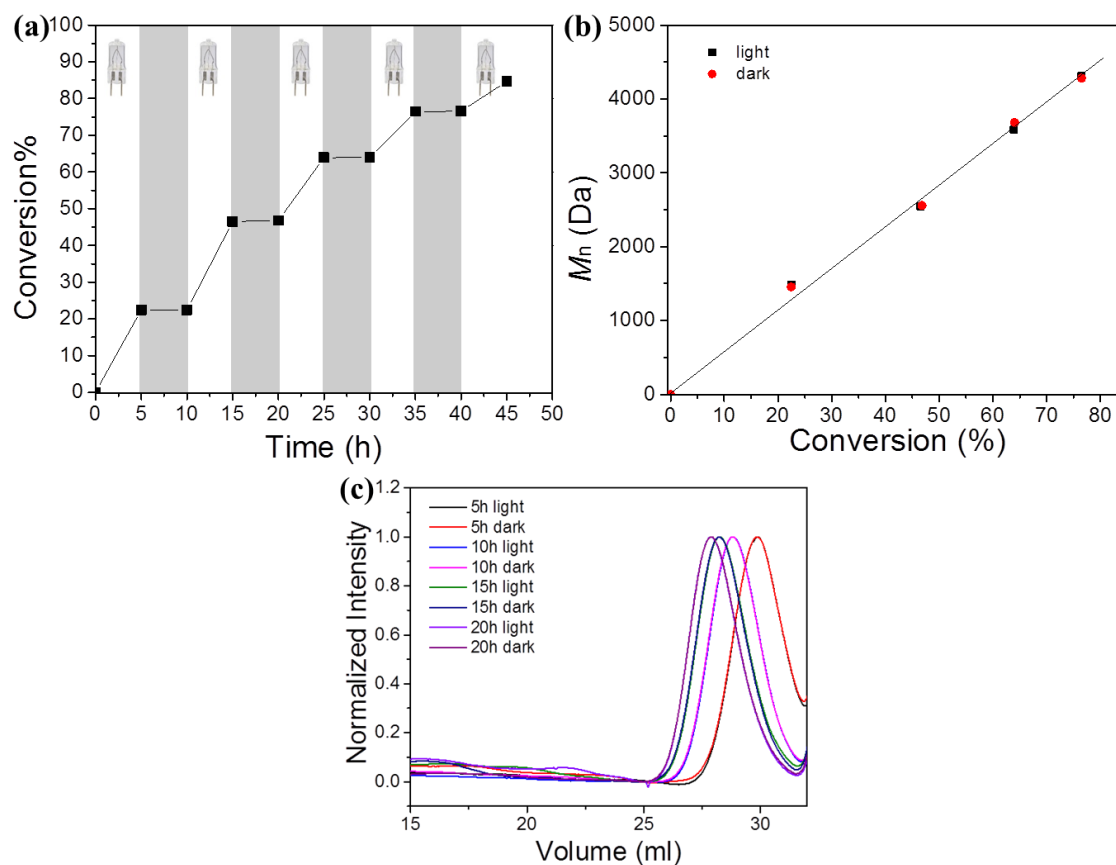


**Figure 5.57 (a) Conversion of the monomer within the controlled light “on-off” cycle, (b) relative molecular weight of each “on-off” cycle and (c) gel permeation chromatography trace at different time point.**

To further prove the living nature in this system, the polymer chain extension and the synthesis of a block copolymer were conducted. A PMMA macroinitiator was synthesized under the optimized condition using Ph-BT-Ph as photocatalyst under the exposure of light for 24 h. Then, the irradiation of the purified macroinitiator, MMA, triphenylamine, and Th-BTz-Th as photocatalyst offered a chain extended PMMA product (Figure 5.58a) with increased molecular weight. The GPC measurement showed a low polydispersity after 5h light irradiation. This suggested the maintaining of the living nature of the chain end C-Br bond during the whole polymerization process for further chain propagation. The block copolymer was also



successfully synthesized via adding the macroinitiator, benzyl methacrylate, triphenylamine and Th-BTz-Th as photocatalyst. The GPC measurement showed no signal of the starting macroinitiator (Figure 5.58b). This finding further supports our proposed mechanism, in which the ATRP process can also be accomplished with low reductive potential OS type photocatalyst.

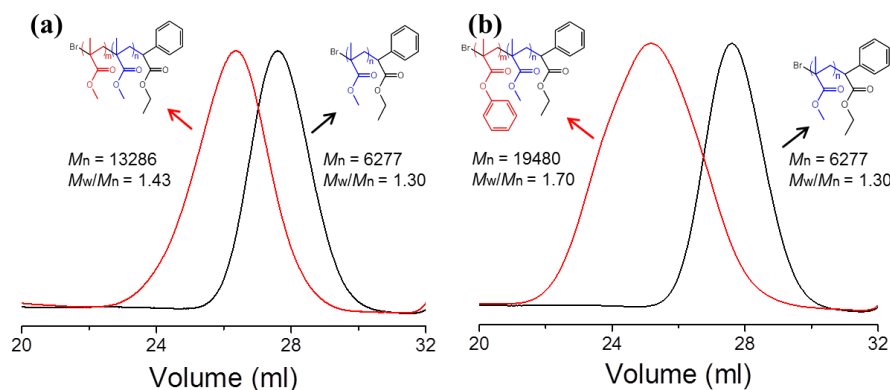
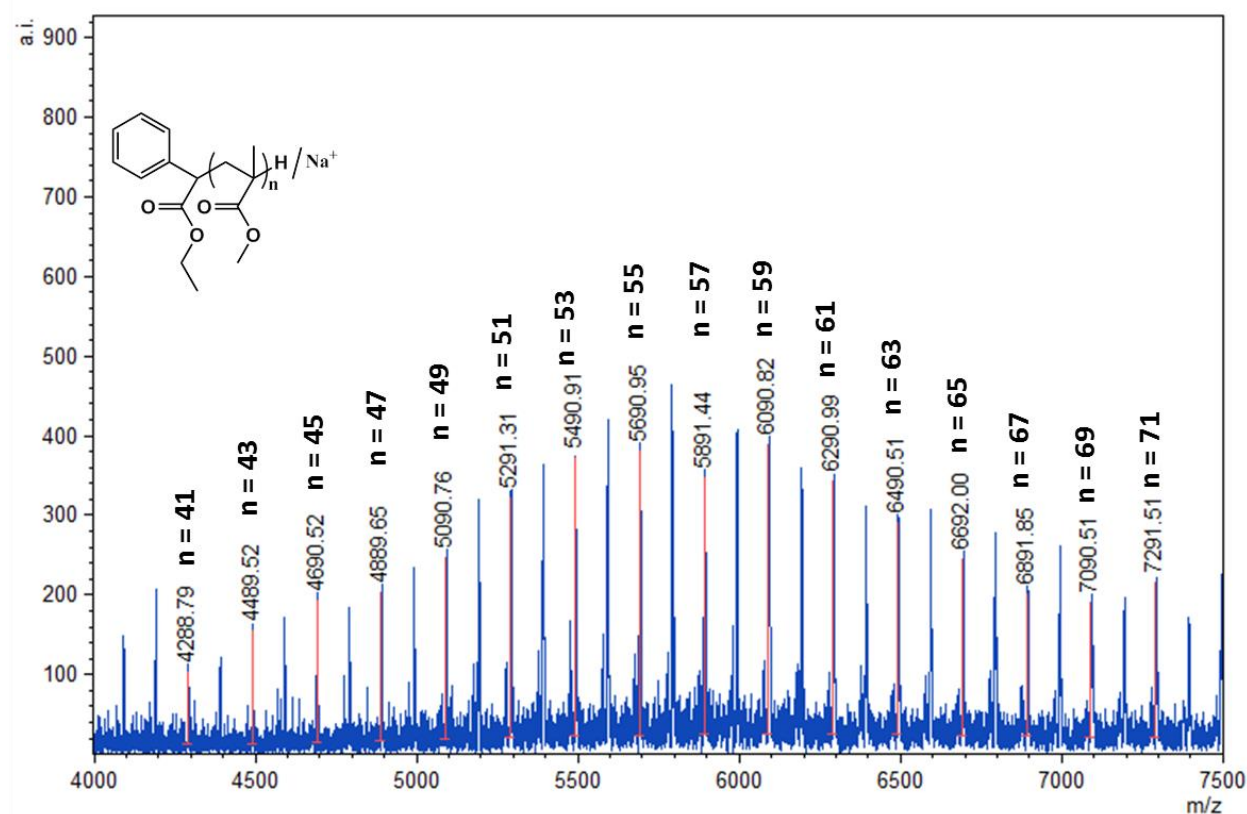


**Figure 5.58 (a) Gel permeation chromatography traces of PMMA before and after chain extension, and (b) Gel permeation chromatography traces of PMMA and PMMA-*b*-PBMA.**

Matrix-assisted laser desorption ionization-time of flight (MALDI-TOF) spectrum can directly give the insight of the molecular weight of single polymer chains, which can be used to calculate the composition of the polymer. For the PMMA samples synthesized by the standard condition with LiBr as additive, the generated polymers appeared extremely clean. Only a single series of peaks was presented, which was obviously associated with the theoretically expected molecular structure (Figure 5.59). The molecular weight could be calculated by the following equation:

$$163.07 (\alpha \text{ chain end}) + 100.05 (\text{repeating unit}) + 1.01 (\text{H}) + 23 (\text{Na}^+)$$

The missing of the Br atom was likely due to the ionization process and was discussed by other authors.<sup>43, 243-244</sup>



**Figurer 5.59** MALDI-TOF spectrum of the PMMA synthesized with the standard condition: MMA 5.6 mmol, 2.5% mol Initiator ethyl  $\alpha$ -bromophenyl acetate, 0.1% Ph-BT-Ph as photocatalyst, 10% mol triphenylamine, 20% LiBr in 1.5 ml DMF.

The PMMA sample synthesized without LiBr showed a complex pattern of peaks in the MALDI-TOF spectrum (Figure 5.60). The main series of peaks were associated with theoretic molecular weight, which indicates the living ATRP process. However, the other series of peaks that also differed in one MMA (100.05) repeating unit were observed. Among these, the series of peaks containing two  $\alpha$  chain end groups could be obtained by either the recombination of two radicals, or the re-addition of the double bonds at the polymer chain end, the later could be likely caused by the elimination process as we have assumed before.

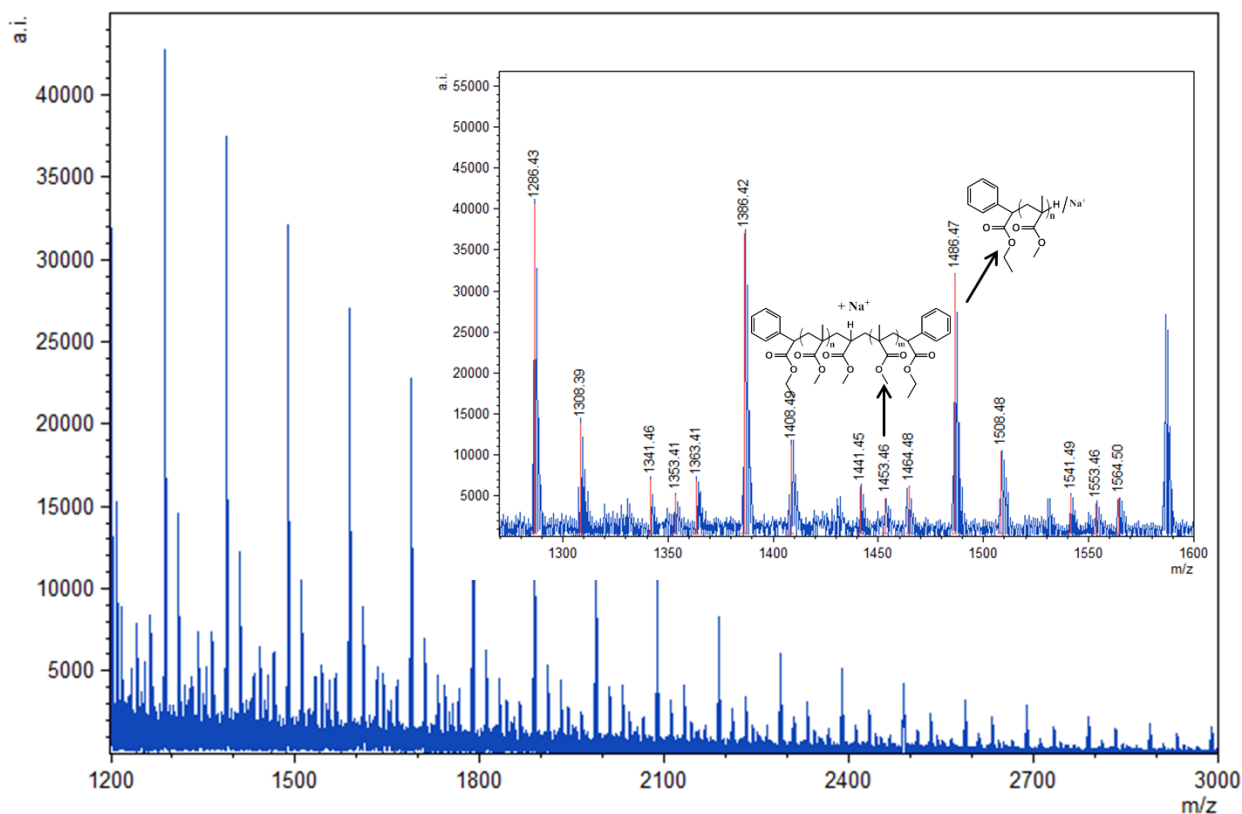


**Figure 5.60** MALDI-TOF spectrum of the PMMA synthesized without LiBr: MMA 5.6 mmol, 2.5% mol Initiator ethyl  $\alpha$ -bromophenyl acetate, 0.1% Ph-BT-Ph as photocatalyst, 10% mol triphenylamine in 1.5 ml DMF.

The flexibility of the small molecule organic semiconductor with low reductive potentials, which can efficiently catalyze the ATRP process, was further examined via the variation of the reaction conditions. Interestingly, lowering the amount of the sacrificial reagent and LiBr to 0.05 equiv and 0.1 equiv, respectively, did not influence the formation of the final polymer product (Table 5.8, entry 2 and 3). When increasing the amount of the photocatalyst to 0.5% equiv, the reaction time was not obviously shortened to reach similar conversions (Table 5.8, entry 4). This led to our hypothesis that the catalyst load did not influence the polymerization rate due to the fact that the concentration of the living chain end was low. Only a slightly decrease of the conversion and the final molecular weight of the polymer occurred when using a low catalyst concentration of 0.01% (Table 5.8, entry 5). This also showed the high catalytic efficiency of our OS type photocatalyst in low concentrations. However, due to the lower over potential

between the reductive potential of the photocatalyst and the C-Br bond of the living polymer chain end, a relative longer reaction time was needed compared to other photocatalysts. This phenomenon was observed in a more obvious manner when synthesizing PMMAs with high molecular weights.

**Table 5.8 Results of the OS catalyzed atom transfer radical polymerization.**

Entry <sup>a</sup>	[MMA]:[MBP]	NPh <sub>3</sub> <sup>b</sup>	LiBr <sup>b</sup>	Cata. <sup>b</sup>	t/h	Mn,GPC/Da	PDI	Conversion/%	I <sup>c</sup>
1	40	0.1	0.2	0.1%	24	6755	1.27	81.7	0.48
2	40	0.05	0.2	0.1%	24	6893	1.27	72.3	0.42
3	40	0.1	0.1	0.1%	24	7460	1.29	75	0.40
4	40	0.1	0.2	0.5%	24	7245	1.36	73.2	0.40
5	40	0.1	0.2	0.01%	24	5705	1.35	70.1	0.49
6	20	0.1	0.2	0.1%	17	2956	1.37	74.6	0.50
7	70	0.1	0.2	0.1%	26	9053	1.36	81	0.62
8	100	0.1	0.2	0.1%	30	15636	1.45	71	0.45
9	200	0.1	0.2	0.1%	36	16547	1.69	33.8	0.40

[a] Reaction condition: MMA (1 equiv, 5.6 mmol), initiator, catalyst, NPh<sub>3</sub>, LiBr in DMF (1.5 ml) at room temperature with a white LED as light source. [b] mol percent relative to MMA. [c] Initiating rate, calculated by Mn,theory/Mn,GPC.

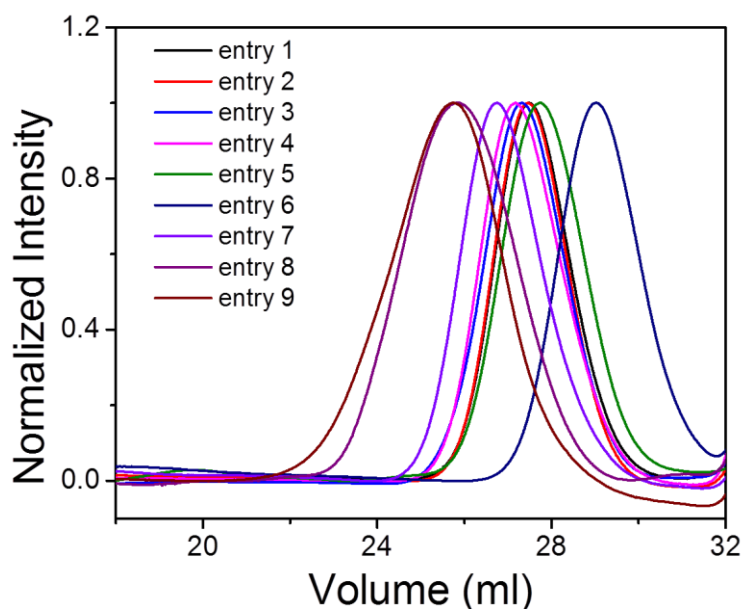


**Figure 5.61** Gel permeation chromatography traces of the polymer in Table 5.8.

#### **5.4.6 Improvement of the ATRP catalyzed by small molecule organic semiconductor**

As suggested in the traditional living polymerization process, the living character results from a “quick initiation, slow propagation, and no termination” process. This led us to further improve the ATRP process catalyzed by the designed OS type photocatalysts. Especially the polydispersity and reaction time were taken into account. The “quick initiation, slow propagation” manner could be easily controlled via controlling the energy difference in the reductive potentials of the initiator and the C-Br bond at the polymer chain end. For the initiator, i.e. ethyl  $\alpha$ -bromophenyl acetate, the reductive potential is -0.52 V, and the reductive potential of the polymer chain end is -1.05 V. Obviously, the initiator appeared to be reduced in a more efficient manner than the polymer chain end. This could guarantee the living character of the polymerization process. For the case, when the initiator owns a higher reductive potential than the polymer chain end, the polymerization process should be in a “slow

initiation, quick propagation” manner, which would result into less control of the polymerization process. No living nature of the polymerization could be guaranteed.

To confirm this observation, we employed 1-iodoperfluorohexane as initiator, which owns a reductive potential of -1.15 V (Figure 5.50d). The reductive potential of the C-I bond at the polymer chain end was estimated to be -0.9 V vs SCE (ethyl iodoacetate) (Figure 5.50e). This designed “slow initiation, quick propagation” process resulted into a polymer with a high molecular weight, which was considerably higher than theoretically expected. Additionally, the molecular weight decreased with the prolonged reaction time (Figure 5.62b), which indicates that more initiator was initiated in the polymerization process during the chain propagation period. However, the reaction rate was quicker due to the lower reductive potential of the C-I bond than C-Br bond at the chain end. It is worthy to mention that the PDI of the polymer obtained using the I-initiator was lower than that obtained by using the Br-initiator. We attributed this improved polydispersity to a quicker deactivated process between the negative iodide ion and the positive carbon ion, which was likely caused by the larger atom radius of the iodide ion.

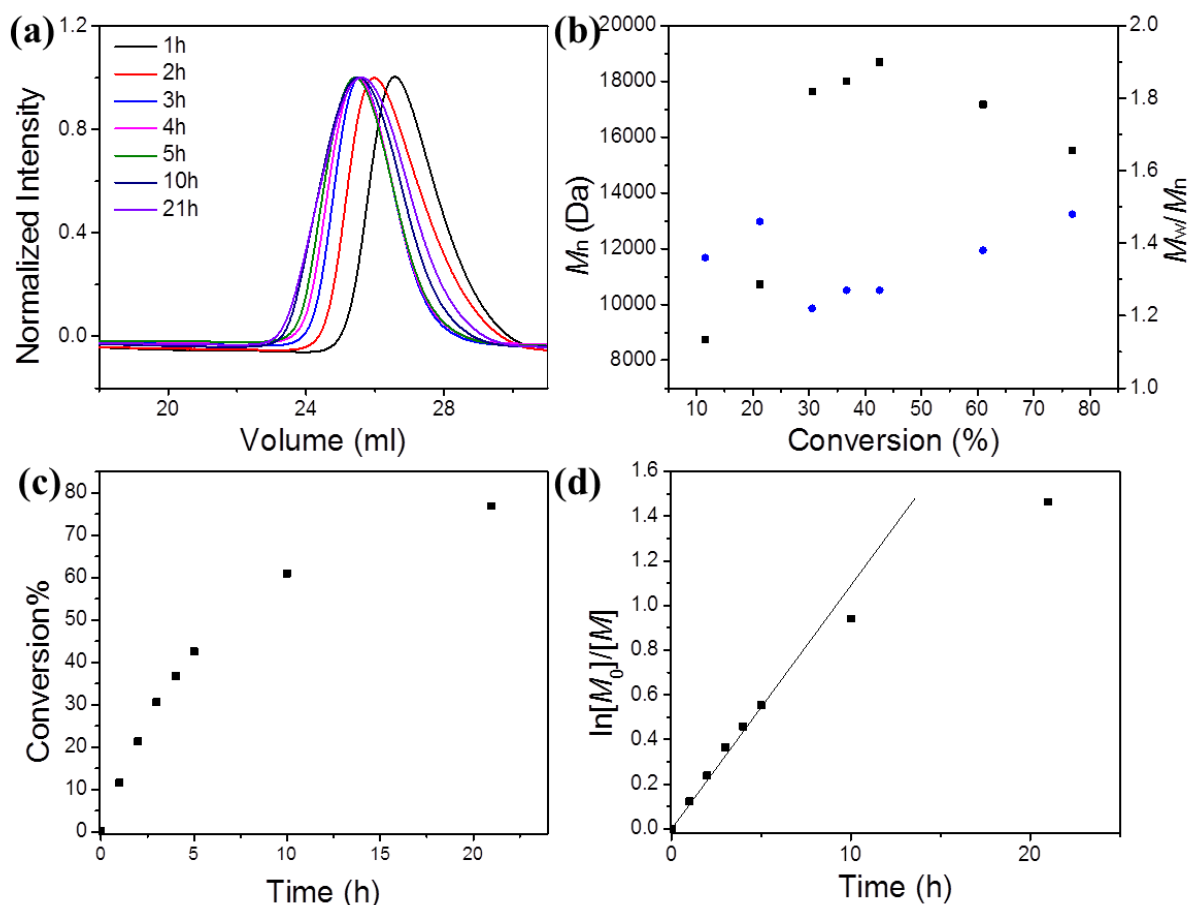


**Figure 5.62 (a) Gel permeation chromatography trace vs. reaction time (b) molecular weight and molecular weight distribution vs. conversion (c) conversion vs. reaction time and (d)  $\ln([M]_0/[M])$  as a function of time. Reaction condition: MMA 5.6 mmol, 2.5% mol initiator 1-iodoperfluorohexane, 0.1% Ph-BT-Ph as photocatalyst, 10% mol triphenylamine, 20% LiI in 1.5 ml DMF.**

The “ideal” potential conditions for the ATRP process catalyzed by small molecule organic semiconductor with low reductive potentials are illustrated in Figure 5.63. The initiator should own a lower reductive potential than the polymer chain end. This guarantees the initiating process. The LUMO of the photocatalyst should be proper to ensure a fast reaction rate. And a proper band gap of the photocatalyst is needed to capture protons, which can further improve the reaction rate. At last, iodides should function more effectively than bromines as additives.

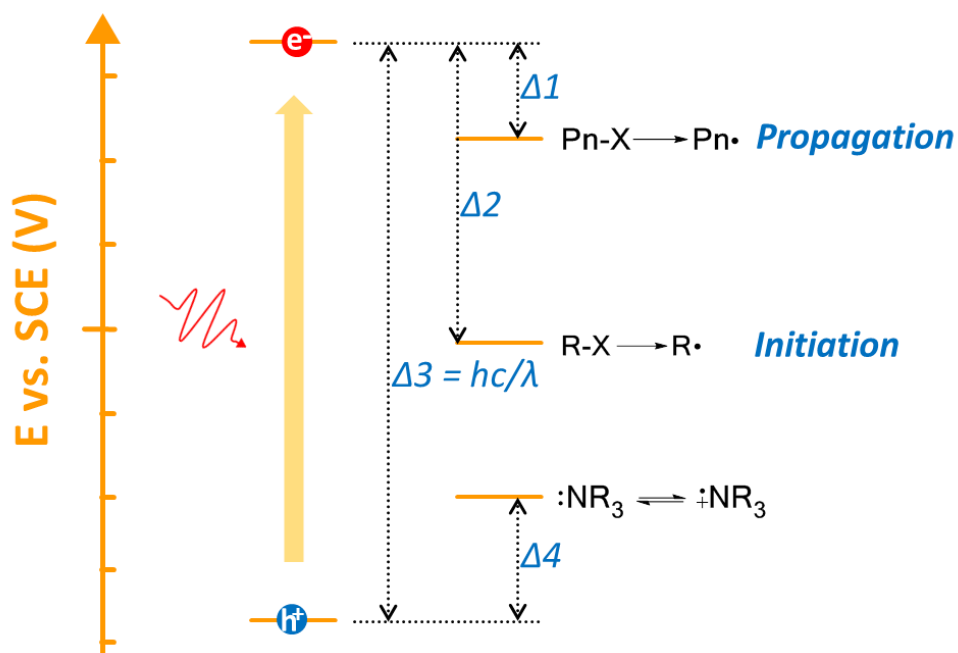


**Figure 5.63** The “ideal” potential conditions for the ATRP process catalyzed by small molecule organic semiconductor with low reductive potentials.

A quick test to this hypothesis was conducted via utilization of the Ph-BT-Ph as photocatalyst, ethyl  $\alpha$ -bromophenyl acetate as initiator, but Lil as additive. The result was demonstrated in Figure 5.63. Since the reductive potential of the polymer chain end is higher than initiator, not surprising that it will lead to a living polymerization process than 1-iodoperfluorohexane as initiator. The reaction rate was quicker, the molecular weight increases linear with the consumption of the monomer, and the polydispersity maintains in low level ( $<1.3$ ) during the whole polymerization process. This indicates the great potential of the OS type photocatalyst in ATRP process, and further improvement can be achieved via precisely tuning of the energy levels of photocatalyst, initiator and sacrificial reagent.



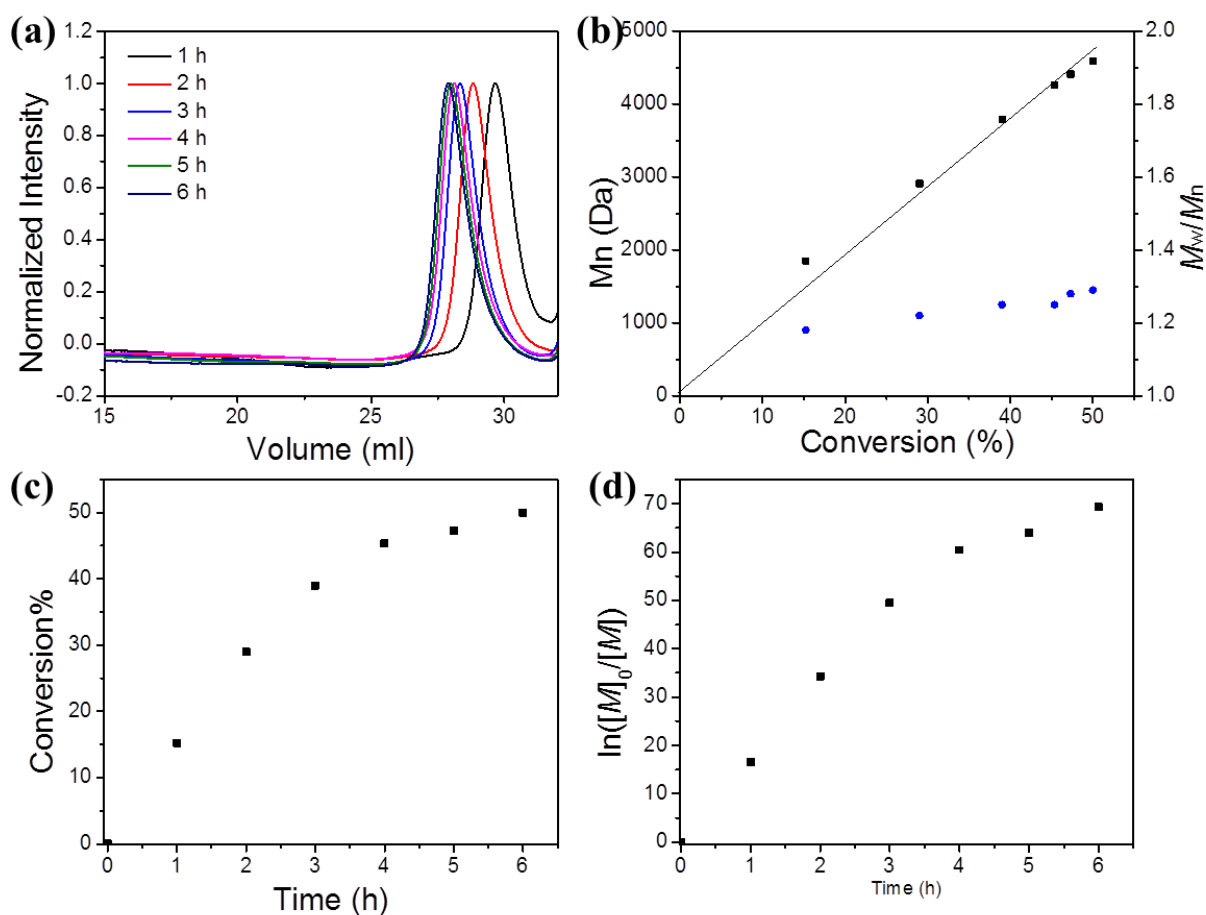


**Figure 5.64** (a) Gel permeation chromatography trace vs. reaction time, (b) molecular weight and molecular weight distribution vs. conversion, (c) conversion vs. reaction time and (d)  $\ln([M]_0/[M])$  as a function of time. Reaction condition: MMA 5.6 mmol, 2.5% mol initiator ethyl  $\alpha$ -bromophenyl acetate, 0.1% Ph-BT-Ph as photocatalyst, 10% mol triphenylamine, 20% Lil in 1.5 ml DMF.

### 5.4.7 Conclusion

In summary, the light-controlled atom transfer radical polymerization could be successfully catalyzed by OS type photocatalysts via precise control of the energy levels for various components involved in the catalytic cycle. Well-defined polymers with expected molecular weight and low polydispersity could be obtained. The control of the propagation process could

be achieved by using light as external stimulus. The synthesis of the polymer chain extension and formation of the block copolymers ensured the living nature of this designed process. This study offers a promising opportunity for the controllable ATRP process catalyzed by OS type photocatalysts.

## 6 Experimental Section

### 6.1 Structural design principle of small molecule organic semiconductors for metal-free, visible light-promoted photocatalysis

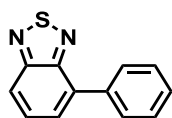
#### 6.1.1 Materials and methods

Chemicals were purchased from commercial sources and used as received without further purification. Glassware was dried using heating gun at 600 °C and cooled under vacuum prior to use if necessary. All photocatalytic reactions were conducted using common dry, inert atmosphere techniques via a Schlenk tube or a stopper capped vessel. A household energy saving light bulb (23 W, Osram) and blue LED (460 nm, 1.2 W/cm<sup>2</sup>, OSA Opto Light) were used as light source. UV-Vis absorption and emission spectra were recorded on a Perkin Elmer Lambda 100 spectrophotometer and J&M TIDAS spectrofluorometer at ambient temperature, respectively. Cyclic voltammetry measurement was performed on an Autolab PGSTAT204 potentiostat/galvanostat (Metrohm) using a three electrode cell system: glassy carbon electrode as the working electrode, Hg/HgCl<sub>2</sub> electrode as the reference electrode, platinum wire as the counter electrode, and Bu<sub>4</sub>NPF<sub>6</sub> (0.1 M Acetonitrile) as supporting electrolyte with a scan rate of 100 mV/s in the range of -2 eV to 2.5 eV. <sup>1</sup>H and <sup>13</sup>C spectra were recorded on a Bruker Avance 300 spectrometer, and *d*-CHCl<sub>3</sub> was used as solvent unless otherwise noted. GC-MS spectra were recorded on a SHIMADZU GCMS-QP2010 gas chromatograph mass spectrometer. Theoretical calculations of the oxidation potential of the intermediate was carried out using Gaussian 09, DFT 6-311G(d) method. Time-resolved photoluminescence (TRPL) on a nanosecond timescale was taken with a Streak Camera System (Hamamatsu C4742) in slow sweep mode. The excitation wavelength of 400 nm was provided using the frequency-

doubled output of a commercial titanium-sapphire amplifier (Coherent LIBRA-HE, 3.5 mJ, 1 kHz, 100 fs). The data was fitted with a monoexponential decay function.

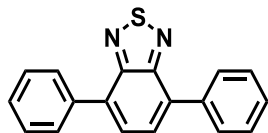
### 6.1.2 Synthesis of the small molecule organic semiconductors

Synthesis of BT-Ph:



4-bromo-2,1,3-benzothiadiazole was purchased from Santa Cruz Biotechnology Inc. and directly used without further purification. A 25ml Schlenk tube equipped with a stirring bar and stopper was heated under vacuum then cooling three times before 4-bromo-2,1,3-benzothiadiazole (430 mg, 2 mmol), phenylboronic acid (320 mg, 2.6 mmol), tetrakis(triphenylphosphine)palladium(0) (92 mg, 4 mol%) were added. 10 ml toluene and 4 ml  $K_2CO_3$  aqueous solution (4 g  $K_2CO_3$  dissolved in 20 ml water and degassed by argon for 30 min before using) were added via syringe. The reactor was degassed under vacuum and then back filled with argon three times. It was heated under 90 °C overnight, then pour into 100 ml water and extracted with  $CH_2Cl_2$  three times. The organic layer was washed with water twice, dried over by anhydrous  $MgSO_4$ , and the solvent was removed via evaporation. The product was purified via chromatography through silica gel using hexane as eluent to give a beige solid (225 mg, yield 53%).  $^1H$  NMR (300 MHz,  $CDCl_3$ )  $\delta$  : 8.03 - 7.98 (m, 1 H), 7.94 - 7.91 (m, 2 H), 7.71 - 7.68 (m, 2 H), 7.58 - 7.52 (m, 2 H), 7.49 - 7.43 (m, 1 H).  $^{13}C$  NMR (300 MHz,  $CDCl_3$ )  $\delta$  : 155.60, 153.53, 137.38, 134.61, 129.63, 129.27, 128.61, 128.42, 127.74, 120.54.

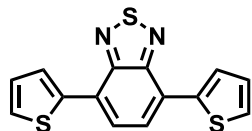
Synthesis of Ph-BT-Ph:



A 100ml Schlenk tube equipped with a stirring bar and stopper was heated under vacuum then cooling three times before 4,7-dibromo-2,1,3-benzothiadiazole (1.47 g, 5 mmol), phenylboronic

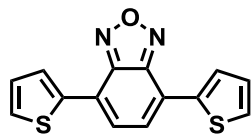
acid (1.24 g, 15 mmol),  $\text{Pd}(\text{PPh}_3)_4$  (289 mg, 5%) were added. After degassed by vacuum for 5 min, 25 ml anhydrous toluene and pre-degassed  $\text{K}_2\text{CO}_3$  solution (2.76 g in 10 ml water) were added via syringe and the reactor was degassed under vacuum and then back filled with argon three times. It was heated under 90 °C overnight, then poured into 200 ml water and extracted with  $\text{CH}_2\text{Cl}_2$  three times. The organic layer was washed with water twice, dried by anhydrous  $\text{MgSO}_4$ , solvent was removed under vacuum. Purified with a short column then crystalized from methanol gave a needle like green-yellow solid. (922 mg, 64%).  $^1\text{H}$  NMR (300 MHz,  $\text{CDCl}_3$ )  $\delta$  : 7.99 (m, 4H), 7.79 (s, 2H), 7.57 (m, 4H), 7.48 (t,  $J=7.5\text{Hz}$ , 2H).  $^{13}\text{C}$  NMR (300 MHz,  $\text{CDCl}_3$ )  $\delta$  : 128.13, 128.38, 128.64, 129.25, 133.38, 137.44, 154.11.

#### Synthesis of Th-BT-Th:



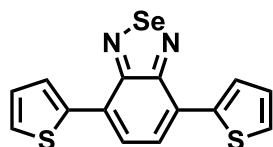
A 100ml Schlenk tube equipped with a stirring bar and stopper was heated under vacuum then cooling three times before 4,7-dibromo-2,1,3-benzoxadiazole (1.76 g, 6.00 mmol), 2-(tributylstannyl)thiophene (4.76 ml, 15 mmol) and  $\text{Pd}(\text{PPh}_3)_2\text{Cl}_2$  (201.60 mg, 5 mol%) were added. 30 ml anhydrous THF was added via syringe and the reactor was degassed under vacuum and then back filled with argon three times. It was heated under 90 °C overnight, then poured into 200 ml water and extracted with  $\text{CH}_2\text{Cl}_2$  three times. The organic layer was washed with water twice, dried by anhydrous  $\text{MgSO}_4$ , solvent was removed under vacuum. Purified with a short column then crystalized from methanol gave a needle like reddish solid (1.14 g, 63%).  $^1\text{H}$  NMR (300 MHz,  $\text{CDCl}_3$ )  $\delta$  : 8.13-8.11 (m, 2H), 7.88 (s, 2H), 7.48-7.45 (m, 2H), 7.23-7.20 (m, 2H).  $^{13}\text{C}$  NMR (300 MHz,  $\text{CDCl}_3$ )  $\delta$  : 152.66, 139.36, 128.02, 127.52, 126.81, 126.02, 125.79.

## Synthesis of Th-BO-Th:



A 100ml schlenk tube equipped with a stirring bar and stopper was heated under vacuum then cooling three times before 4,7-dibromobenzooxadiazole (590 mg, 2.12 mmol), 2-(tributylstannyl)thiophene (1.68 ml, 5.3 mmol) and  $\text{Pd}(\text{PPh}_3)_2\text{Cl}_2$  (74.4 mg, 5 mol%) were added. 20 ml anhydrous DMF was added via syringe and the reactor was degassed under vacuum and then back filled with argon three times. It was heated under 90 °C overnight, then poured into 200 ml water and extracted with  $\text{CH}_2\text{Cl}_2$  three times. The organic layer was washed with water twice, dried by anhydrous  $\text{MgSO}_4$ , solvent was removed under vacuum. Purified with a short column then crystalized from methanol gave a short needle-like red solid (187.6 mg, 66%).  $^1\text{H}$  NMR (300 MHz,  $\text{CDCl}_3$ )  $\delta$  : 8.13-8.11 (m, 2H), 7.62 (s, 2H), 7.46-7.43 (m, 2H), 7.23-7.20 (m, 2H).  $^{13}\text{C}$  NMR (300 MHz,  $\text{CDCl}_3$ )  $\delta$  : 147.90, 137.92, 128.75, 128.64, 126.98, 126.39, 122.15.

## Synthesis of Th-BS-Th:

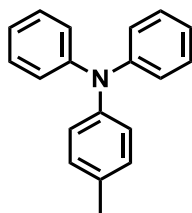


A 100ml schlenk tube equipped with a stirring bar and stopper was heated under vacuum then cooling three times before 4,7-dibromo-2,1,3-benzoselenadiazole (500 mg, 1.47 mmol), 2-(tributylstannyl)thiophene (1.2 ml, 3.8 mmol) and  $\text{Pd}(\text{PPh}_3)_2\text{Cl}_2$  (52 mg, 5 mol%) were added. 20 ml anhydrous DMF was added via syringe and the reactor was degassed under vacuum and then back filled with argon three times. It was heated under 90 °C overnight, then poured into

200 ml water and extracted with  $\text{CH}_2\text{Cl}_2$  three times. The organic layer was washed with water twice, dried by anhydrous  $\text{MgSO}_4$ , solvent was removed under vacuum. Purified with a short column then crystalized from methanol gave a long fiber-like dark purple solid (367.6 mg, 72%).  $^1\text{H}$  NMR (300 MHz,  $\text{CDCl}_3$ )  $\delta$  : 8.02-8.01 (m, 2H), 7.79 (s, 2H), 7.47-7.45 (m, 2H), 7.21-7.18 (m, 2H).  $^{13}\text{C}$  NMR (300 MHz,  $\text{CDCl}_3$ )  $\delta$  : 158.24, 139.68, 127.72, 127.52, 127.40, 127.12, 126.90.

### 6.1.3 Synthesis of sacrificial reagent

Synthesis of 4-Methyl-N,N-diphenylaniline:



An oven-dried two neck flask equipped with a stirring bar was heated under vacuum then cooling three times before diphenylamine (1.92 g, 11.6 mmol), 2,2'-bipyridine (72 mg, 4 mol%),  $\text{CuI}$  (86 mg, 4 mol%), and 4-iodotoluene (2.78 mg, 12.7 mmol) were added. 35 ml anhydrous toluene and 10 ml  $\text{KOtBu}$  (1.7 M in THF) were added sequently via syringe. The reactor was degassed under vacuum and then back filled with argon three times. It was heated under  $100^\circ\text{C}$  for 24 hours, then poured into 200 ml water and extracted with  $\text{CH}_2\text{Cl}_2$  three times. The organic layer was washed with water twice, dried by anhydrous  $\text{MgSO}_4$ , solvent was removed under vacuum. Purified on silica gel using hexane as eluent gave the product as a white solid (1.52 g, 51%).  $^1\text{H}$  NMR (300 MHz,  $\text{CDCl}_3$ )  $\delta$  : 7.23-7.18 (m, 4H), 7.07-7.04 (m, 6H), 7.01-7.93 (m, 4H), 2.30 (s, 3H).  $^{13}\text{C}$  NMR (300 MHz,  $\text{CDCl}_3$ )  $\delta$  : 148.06, 145.28, 132.75, 129.94, 129.13, 124.96, 123.63, 122.24, 20.84.

### 6.1.4 Fluorescence quenching experiments

Conditions for the fluorescence quenching experiments: in different vessels, 0.0114 mmol SMOs was dissolved in 3 ml DMF, different amounts of the quencher were added into

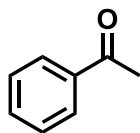
different vessels. The solution was degassed via freeze-pump-thaw method to remove the oxygen residue before the experiment. Concentrations of different quenchers were: 0.01 M, 0.025 M, 0.05 M, and 0.1 M (0.2 M is also conducted if necessary).

#### **6.1.5 General procedure of the dehalogenation reaction using the small molecule organic semiconductors**

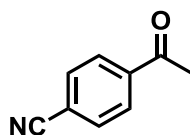
A 10 ml vessel equipped with a stirring bar and stopper was heated under vacuum then cooling for one time and then back filled with argon before  $\alpha$ -bromoacetophenone (1 mmol, 1 eq.), hantzsch ester (1.1 mmol, 1.1 eq.), N,N-diisopropylethylamine (2 mmol, 2 eq.), catalyst (1 mol%) and 2 ml DMF were added. The reactor was degassed via the freeze-pump-thaw method and irradiated under a table lamp. The reaction time for full conversion was determined by  $^1\text{H}$ -NMR when the signal of  $-\text{CH}_2\text{Br}$  totally disappeared. After the reaction was completed, the mixture was poured into 20 ml water and extracted with  $\text{CH}_2\text{Cl}_2$ , the organic layer was dried by anhydrous  $\text{MgSO}_4$ , and the solvent was removed under vacuum. The crude product was then purified over silica gel using the indicated solvent system to obtain the pure product.

#### **6.1.6 General procedure of the intermolecular C–H functionalization of electron-rich heterocycles with malonates catalyzed by the organic semiconductors**

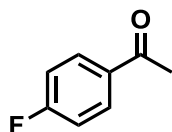
A 25 ml Schlenk tube equipped with a stirring bar and stopper was heated under vacuum then cooling for one time and then back filled with argon before heteroaromatic compound (0.38 mmol, 1 equiv), triphenylamine (0.76 mmol, 2 equiv), diethyl bromomalonate (0.76 mmol, 2.0 equiv), catalyst (1 mol%), 2.5 ml DMF were added. The reactor was degassed via the freeze-pump-thaw method and irradiated under a blue LED. The reaction time was determined by GC-MS when the signal of starting material totally disappeared. After the reaction was completed, the mixture was poured into 20 ml water and extracted by  $\text{CH}_2\text{Cl}_2$ , the organic layer was dried by anhydrous  $\text{MgSO}_4$ , and the solvent removed under vacuum. The crude product was purified on silica gel using the indicated solvent system to offer the desired product.

**6.1.7 Products data:**

Acetophenone. Follow the general procedure, hexane/ $\text{CH}_2\text{Cl}_2$  = 1/1 was used as eluent to give the product as a light yellow oil (87.7 mg, 76%).  $^1\text{H}$  NMR (300 MHz,  $\text{CDCl}_3$ )  $\delta$ : 7.97 - 7.94 (m, 2 H), 7.59 - 7.54 (m, 2 H), 7.49 - 7.43 (m, 2 H), 2.61 (s, 3 H).  $^{13}\text{C}$  NMR (300 MHz,  $\text{CDCl}_3$ )  $\delta$ : 198.16, 137.14, 133.11, 128.57, 128.31, 26.61.

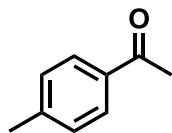


4-Acetylbenzonitrile. Follow the general procedure, hexane/ $\text{CH}_2\text{Cl}_2$  = 1/1 was used as eluent to give the product as a light yellow oil (120.5 mg, 83%).  $^1\text{H}$  NMR (300 MHz,  $\text{CDCl}_3$ )  $\delta$ : 8.05 (d,  $J$  = 7.5 Hz, 2 H), 7.78 (d,  $J$  = 7.5 Hz, 2 H), 2.64 (s, 1 H).  $^{13}\text{C}$  NMR (300 MHz,  $\text{CDCl}_3$ )  $\delta$ : 196.55, 139.92, 132.51, 128.70, 117.93, 116.37, 26.76.

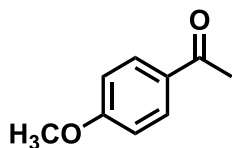


4-Fluoroacetophenone. Follow the general procedure, hexane/ $\text{CH}_2\text{Cl}_2$  = 1/1 was used as eluent to give the product as a pale yellow oil (106.4 mg, 77%).  $^1\text{H}$  NMR (300 MHz,  $\text{CDCl}_3$ )  $\delta$ : 8.03 - 7.98 (m, 2 H), 7.18 - 7.12 (m, 2 H), 2.59 (s, 3 H).  $^{13}\text{C}$  NMR (300 MHz,  $\text{CDCl}_3$ )  $\delta$ : 196.48, 167.46 (dd,  $J$  = 254 Hz), 133.62, 131.00, 115.80 (dd,  $J$  = 21.9 Hz), 26.53.

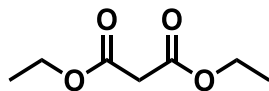




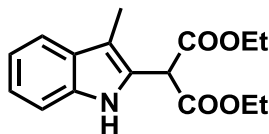
4-Methylacetophenone. Follow the general procedure, hexane/ $\text{CH}_2\text{Cl}_2$  = 1/1 was used as eluent to give the product as a slightly yellow oil (107 mg, 80%).  $\delta$  : 7.89 (d,  $J$  = 7.5Hz, 2 H), 7.29 (d,  $J$  = 7.5Hz, 2 H), 2.60 (s, 3 H), 2.43 (s, 3 H).  $^{13}\text{C}$  NMR (300 MHz,  $\text{CDCl}_3$ )  $\delta$  : 197.85, 143.87, 134.73, 129.24, 128.44, 26.53, 21.63.



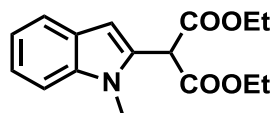
4-Methoxyacetophenone. Follow the general procedure, hexane/ $\text{CH}_2\text{Cl}_2$  = 1/1 was used as eluent to give the product as a slightly yellow oil (129 mg, 86%).  $^1\text{H}$  NMR (300 MHz,  $\text{CDCl}_3$ )  $\delta$  : 7.93 (d,  $J$  = 7.5Hz, 2 H), 6.93 (d,  $J$  = 7.5Hz, 2 H), 3.85 (s, 3 H), 2.54 (s, 3 H).  $^{13}\text{C}$  NMR (300 MHz,  $\text{CDCl}_3$ )  $\delta$  : 196.71, 163.47, 130.55, 130.31, 113.66, 55.43, 26.30.



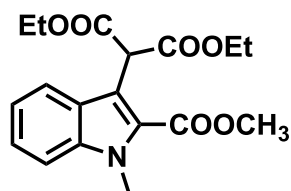
Diethyl malonate. Follow the general procedure, hexane/ $\text{CH}_2\text{Cl}_2$  = 1/1 was used as eluent to give the product as a colorless oil (139.3 mg, 87%).  $^1\text{H}$  NMR (300 MHz,  $\text{CDCl}_3$ )  $\delta$  : 4.23 - 4.15 (q, 4 H), 3.35 (s, 2 H), 1.27 (t, 3 H).  $^{13}\text{C}$  NMR (300 MHz,  $\text{CDCl}_3$ )  $\delta$  : 166.59, 61.44, 41.63, 14.00.



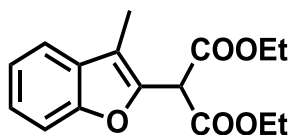
Diethyl 2-(1,3-dimethyl-1H-indole-2-yl)malonate. Follow the general procedure, hexane/CH<sub>2</sub>Cl<sub>2</sub> = 2/1 was used as eluent to give the product as a yellow solid (97 mg, 88%). <sup>1</sup>H NMR (300 MHz, CDCl<sub>3</sub>) δ : 8.93 (br, 1 H), 7.58 - 7.55 (m, 1 H), 7.39 - 7.36 (m, 1 H), 7.24 - 7.15 (m, 1 H), 7.19 - 7.10 (m, 1 H), 5.00 (s, 1 H), 4.34 - 4.18 (m, 4 H), 2.34 (s, 3 H), 1.31 (t, *J* = 7.5 Hz, 6 H). <sup>13</sup>C NMR (300 MHz, CDCl<sub>3</sub>) δ : 167.38, 135.83, 128.26, 124.53, 122.36, 119.22, 118.78, 111.09, 110.60, 62.29, 49.31, 14.03, 8.51.



Diethyl 2-(1-methyl-1H-indole-2-yl)malonate. Follow the general procedure, hexane/CH<sub>2</sub>Cl<sub>2</sub> = 1/1 was used as eluent to give the product as a yellow solid (86 mg, 78%). <sup>1</sup>H NMR (300 MHz, CDCl<sub>3</sub>) δ : 7.61 (d, *J* = 7.81 Hz, 1 H), 7.33 (d, *J* = 7.72 Hz, 1 H), 7.25 - 7.21 (m, 1 H), 7.13 - 7.08 (m, 1 H), 6.50 (s, 1 H), 4.93 (s, 1 H), 4.34 - 4.20 (m, 4 H), 3.73 (s, 3 H), 1.30 (t, *J* = 7.5 Hz, 6 H). <sup>13</sup>C NMR (300 MHz, CDCl<sub>3</sub>) δ : 166.99, 137.93, 130.90, 127.27, 121.97, 120.79, 119.71, 109.30, 103.01, 62.23, 51.32, 30.31, 14.05.



Diethyl 2-(2-(methoxycarbonyl)-1-methyl-1H-indole-3-yl)malonate. Follow the general procedure, hexane/CH<sub>2</sub>Cl<sub>2</sub> = 1/2 was used as eluent to give the product as a green-yellow solid (115 mg, 87%). <sup>1</sup>H NMR (300 MHz, CDCl<sub>3</sub>) δ : 7.77 (d, *J* = 8.21 Hz, 1 H), 7.41 - 7.34 (m, 2 H), 7.21 - 7.15 (m, 1 H), 5.79 (s, 1 H), 4.28 - 4.21 (m, 4 H), 4.03 (s, 3 H), 3.96 (s, 3 H), 1.27 (t, *J* = 7.5 Hz, 6 H). <sup>13</sup>C NMR (300 MHz, CDCl<sub>3</sub>) δ : 168.55, 162.51, 138.68, 126.15, 125.65, 125.36, 121.99, 120.77, 114.50, 110.35, 61.69, 51.77, 49.96, 32.28, 14.09.



Diethyl 2-(3-methyl-1H-2,3-benzofuran -2-yl)malonate (table 2, entry 6). Follow the general procedure, hexane/ $\text{CH}_2\text{Cl}_2$  = 1/1 was used as eluent to give the product as a yellow oil (99 mg, 90%).  $^1\text{H}$  NMR (300 MHz, DMSO)  $\delta$  : 7.63 - 7.60 (m, 1 H), 7.56 - 7.54 (m, 1 H), 7.37 - 7.26 (m, 2 H), 5.49 (s, 1 H), 4.26 - 4.14 (m, 4 H), 2.22 (s, 3 H), 1.22 (t,  $J$  = 7.5 Hz, 6 H).  $^{13}\text{C}$  NMR (300 MHz, DMSO)  $\delta$  : 165.93, 153.47, 144.29, 129.10, 124.67, 122.58, 119.66, 114.25, 110.92, 61.67, 50.00, 13.85, 7.42.

## 6.2 Sacrificial reagent-free photoredox catalysis using cooperative organic semiconductor couples

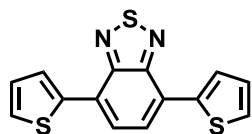
### 6.2.1 Materials and methods

Chemicals were purchased from commercial sources and used as received without further purification. Glassware was dried under heating by a heating gun at 600 °C and cooled under vacuum prior to use if necessary. All photocatalyst reactions were conducted using common dry, inert atmosphere techniques via a schlenk tube. White LED (Silent Air System White OL M-018) is a product of OSA Opto Light GmbH. UV-Vis absorption and emission spectra were recorded on a Perkin Elmer Lambda 100 spectrophotometer and J&M TIDAS spectrofluorometer at ambient temperature, respectively. Cyclic voltammetry measurement was performed with Autolab PGSTAT204 potentiostat/galvanostat of Metrohm (a three electrode cell system): glassy carbon electrode as the working electrode, Hg/HgCl<sub>2</sub> electrode as the reference electrode, platinum wire as the counter electrode, and Bu<sub>4</sub>NPF<sub>6</sub> (0.1 M Acetonitrile) as supporting electrolyte with a scan rate of 100 mV/s in the range of -2 eV to 2.5 eV.  $^1\text{H}$  and  $^{13}\text{C}$  spectra were recorded on a Bruker Avance 300 spectrometer, and *d*-CHCl<sub>3</sub> was used as solvent unless otherwise noted. GC-MS spectra were recorded on a SHIMADZU GCMS-

QP2010 gas chromatograph mass spectrometer. Time-resolved photoluminescence (TRPL) on a nanosecond timescale was taken with a Streak Camera System (Hamamatsu C4742) in slow sweep mode. The excitation wavelength of 400 nm was provided using the frequency-doubled output of a commercial titanium:sapphire amplifier (Coherent LIBRA-HE, 3.5 mJ, 1 kHz, 100 fs).

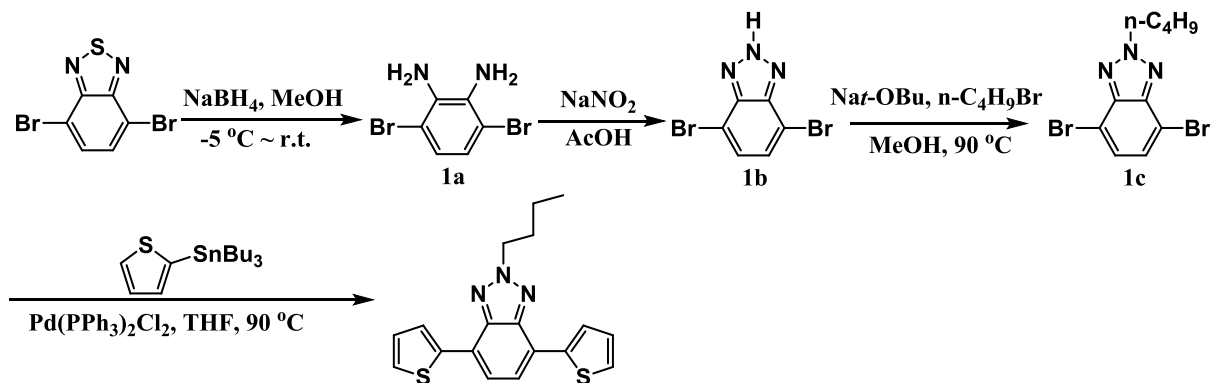
## 6.2.2 Synthesis of the organic semiconductors

Synthesis of Th-BT-Th



*See in Chapter 6.1.2*

Synthetic route of Th-BTz-Th



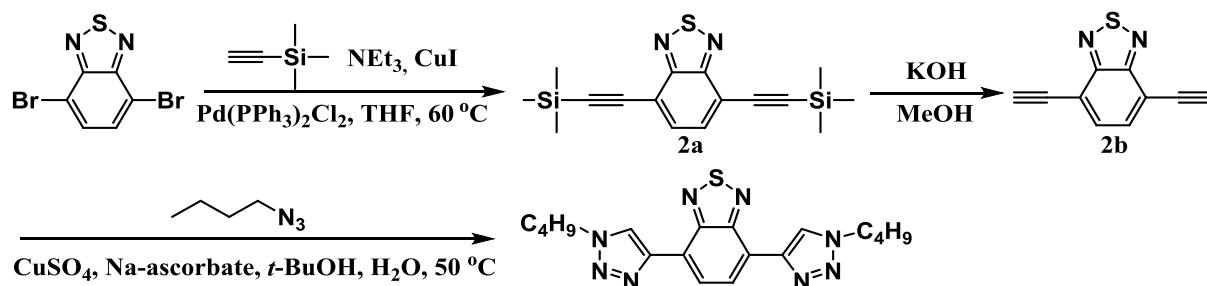
Synthesis of **1a**: The suspension of 4,7-dibromobenzo[c]-1,2,5-thiadiazole (2.94 g, 10 mmol) in 100 ml methanol was previously cooled to -5 °C in water-ice bath. Then sodium borohydride (8 g, 21.7 mmol) was added portionwise to the suspension. The mixture was warmed up to room temperature and stirred overnight. Then, 500 ml water was added, the mixture was extracted with CH<sub>2</sub>Cl<sub>2</sub>, the organic layer was washed with water twice, dried by anhydrous MgSO<sub>4</sub>, solvent was removed under vacuum to give the final product as a pale yellow solid in 80% yield. The H-NMR spectrum was consistent with the literature and used without further purification.<sup>245</sup>

Synthesis of **1b**: Dibromobenzene-1,2-diamine (2 g, 7.5 mmol) (**1a**) was added to a flask containing 15 ml glacial acetic acid. Sodium nitrite (1.03 g, 15 mmol) was dissolved in 10 ml water and added dropwise to the solution. The mixture was further reacted for another 3 hours before it was cooled by ice to 0 °C. The suspension was filtrated, washed with water until pH reaches 7. The crude product was dried in oven at 70 °C under vacuum overnight. The H-NMR spectrum was consistent with the literature<sup>245</sup> and used without further purification.

Synthesis of **1c**: To a 100 ml schlenk tube was added 4,7-dibromo-2H-benzo[d][1,2,3]triazole (2.4 g, 8.6 mmol) (**1b**) and Na<sup>t</sup>-OBu (1.24 g, 12.9 mmol), then 20 ml methanol and 1-bromobutyl (4.3 ml, 40 mmol) was added via syringe. The mixture was degassed under vacuum slightly then back filled with N<sub>2</sub> three times. After stirred under 90 °C for 24h, the mixture was poured into 200 ml water and extracted with CH<sub>2</sub>Cl<sub>2</sub> three times. The organic layer was washed with water twice, dried by anhydrous MgSO<sub>4</sub>, solvent was removed under vacuum. Purified with a column using CH<sub>2</sub>Cl<sub>2</sub>/hexane = 1 : 1 as eluent give the final product as white solid (1.28 g, 45%). <sup>1</sup>H NMR (300 MHz, CDCl<sub>3</sub>) δ : 7.37 (s, 2H), 4.72 (t, *J* = 7.4 Hz, 2H), 2.06 (m, 2H), 1.41-1.29 (m, 2H), 0.91 (t, *J* = 7.4 Hz, 3H). <sup>13</sup>C NMR (300 MHz, CDCl<sub>3</sub>) δ : 143.71, 129.51, 109.97, 57.22, 32.17, 19.82, 13.51.

Synthesis of **Th-BTz-Th**: A 100ml Schlenk tube equipped with a stirring bar and stopper was heated under vacuum then cooling three times before 4,7-dibromo-2-(n-butyl)-2H-benzo[d][1,2,3]triazole (1 g, 3.00 mmol) (**1c**), 2-(tributylstannyl)thiophene (2.38 ml, 7.5 mmol) and Pd(PPh<sub>3</sub>)<sub>2</sub>Cl<sub>2</sub> (100.8 mg, 5 mol%) were added. 15 ml anhydrous THF was added via syringe and the reactor was degassed under vacuum and then back filled with nitrogen three times. It was heated under 90 °C overnight, then poured into 200 ml water and extracted with CH<sub>2</sub>Cl<sub>2</sub> three times. The organic layer was washed with water twice, dried by anhydrous MgSO<sub>4</sub>, solvent was removed under vacuum. Purified with a column using CH<sub>2</sub>Cl<sub>2</sub>/hexane = 1 : 1 as eluent give the final product as light red solid (713 mg, 70%). <sup>1</sup>H NMR (300 MHz, CDCl<sub>3</sub>) δ : 8.03 (dd, *J* = 3.7, 1.2 Hz, 2H), 7.56 (s, 2H), 7.31 (dd, *J* = 5.1, 1.2 Hz, 2H), 7.12 (dd, *J* = 5.1, 3.7 Hz, 2H), 4.76 (t, *J* = 7.4 Hz, 2H), 2.16-2.07 (m, 2H), 1.44-1.34 (m, 2H), 0.94 (t, *J* = 7.4 Hz, 3H). <sup>13</sup>C NMR (300 MHz, CDCl<sub>3</sub>) δ : 142.10, 139.97, 128.12, 126.97, 125.55, 123.59, 122.78, 56.61, 32.08, 19.89, 13.57.

## Synthetic route of TA-BT-TA

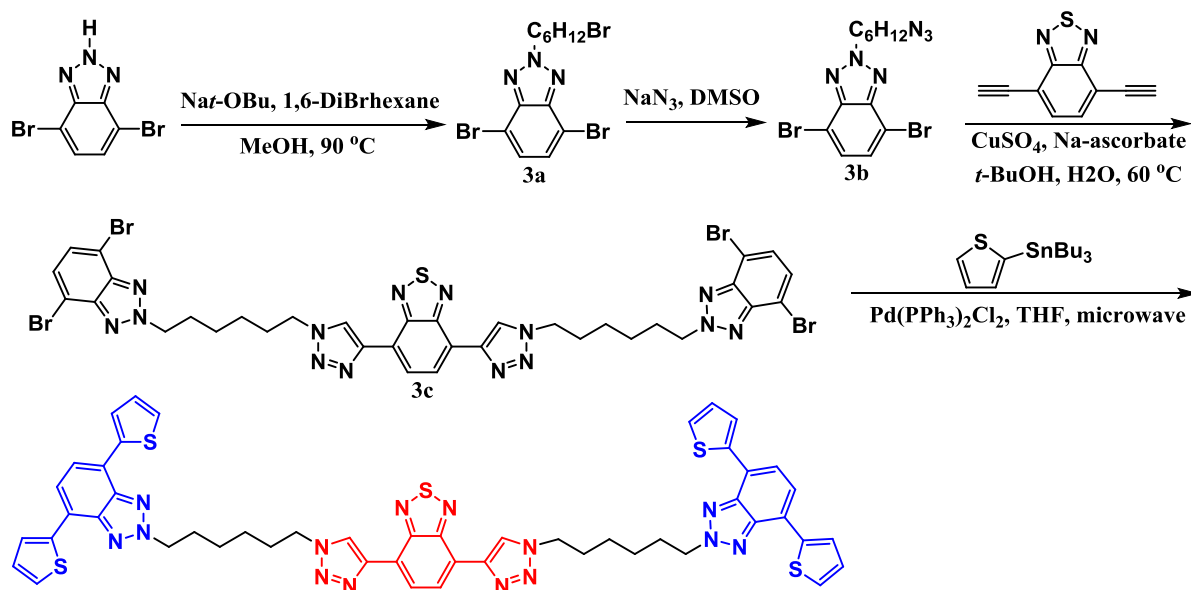


Synthesis of **2a**: A 100ml Schlenk tube equipped with a stirring bar and stopper was heated under vacuum then cooling three times before 4,7-dibromobenzothiadiazole (3 g, 10.2 mmol),  $\text{Pd(PPh}_3)_2\text{Cl}_2$  (143.2 mg, 2%),  $\text{CuI}$  (77 mg, 4%) were added. 30 ml THF and 10ml  $\text{NEt}_3$  were added via syringe. The mixture was cooled to freeze in liquid  $\text{N}_2$ , then trimethylsilyl acetylene (4 ml, 30.6 mmol) was added. The reactor was degassed via the freeze-pump-thaw method and reacted under  $50^\circ\text{C}$  overnight. Then it was poured into 100 ml water and extracted with  $\text{CH}_2\text{Cl}_2$  three times. The organic layer was washed with water twice, dried by anhydrous  $\text{MgSO}_4$ , solvent was removed under vacuum. Purified with a column using  $\text{CH}_2\text{Cl}_2/\text{hexane} = 1 : 1$  as eluent give the final product as light yellow solid (2.78 g, 83%). The H-NMR was consistent with the literature reported.<sup>246</sup>

Synthesis of **2b**: In a 100 ml two neck flask was added  $\text{KOH}$  methanol solution ( $1 \text{ mol L}^{-1}$ , 50 ml) and 4,7-bis[2-(trimethylsilyl)ethynyl]benzothiadiazole (1 g, 3 mmol)(**2a**). The solution was stirred under room temperature for 2 h, and then it was poured into 300 ml water and extracted with  $\text{CH}_2\text{Cl}_2$  three times. The organic layer was washed with water twice, dried by anhydrous  $\text{MgSO}_4$ , solvent was removed under vacuum. Purified with a column using  $\text{CH}_2\text{Cl}_2/\text{hexane} = 1 : 1$  as eluent give the final product as light brown solid (420 mg, 76%). The H-NMR was consistent with the literature reported.<sup>246</sup>

Synthesis of **TA-BT-TA**: 4,7-Diethynylbenzothiadiazole (400 mg, 2.17 mmol)(**2b**), 1-azidobutane (synthesized from 10 mmol 1-bromobutane, 20 mmol sodium azide in 100 ml DMSO, the mixture was poured into 500ml water and extracted with CH<sub>2</sub>Cl<sub>2</sub> then dried by anhydrous MgSO<sub>4</sub>, solvent was removed under vacuum, used as synthesized without column purification, the excessive amount of sodium azide in water phase was slowly added to a solution of NaOCl before deposition), CuSO<sub>4</sub> (51.4 mg, 0.32 mmol), Na-ascorbate (87 mg, 0.44 mmol), 20 ml *t*-BuOH, 2 ml H<sub>2</sub>O were added into a 100 ml two neck flask. The reactor was degassed under vacuum and then back filled with nitrogen three times. The mixture was heated under 60 °C overnight, then poured into 200 ml water and extracted with CH<sub>2</sub>Cl<sub>2</sub> three times. The organic layer was washed with water twice, dried by anhydrous MgSO<sub>4</sub>, solvent was removed under vacuum. Purified with a column using CH<sub>2</sub>Cl<sub>2</sub>/acetone = 10 : 1 as eluent then recrystallized from methanol give the final product as a sheet-like yellow solid (747 mg, 90%). <sup>1</sup>H NMR (300 MHz, CDCl<sub>3</sub>) δ : 8.67 (s, 2H), 8.61 (s, 2H), 4.44 (t, *J* = 7.4 Hz, 4H), 2.00-1.90 (m, 4H), 1.43-1.32 (m, 4H), 0.94 (t, *J* = 7.4 Hz, 6H). <sup>13</sup>C NMR (300 MHz, CDCl<sub>3</sub>) δ : 152.29, 143.10, 126.08, 123.74, 122.66, 50.27, 32.37, 19.79, 13.52.

Synthetic route of the connected catalyst Th-BT-Th@TA-BT-TA:



Synthesis of **3a**: To a 100 ml Schlenk tube was added 4,7-dibromo-2H-benzo[d][1,2,3]triazole (**3** g, 10.8 mmol) and NaI-OBu (1.56 g, 16.2 mmol), then 40 ml methanol and 1,6-dibromohexane (8.3 ml, 54 mmol) was added via syringe. The mixture was degassed under vacuum slightly then back filled with N<sub>2</sub> three times. After stirred under 90 °C for 24 h, the mixture was poured into 200 ml water and extracted with CH<sub>2</sub>Cl<sub>2</sub> three times. The organic layer was washed with water twice, dried by anhydrous MgSO<sub>4</sub>, solvent was removed under vacuum. Purified with a column using CH<sub>2</sub>Cl<sub>2</sub>/hexane = 1 : 1 as eluent give the final product as a white solid (1.82 g, 41%). <sup>1</sup>H NMR (300 MHz, CDCl<sub>3</sub>) δ : 7.38 (s, 2H), 4.73 (t, *J* = 7.4 Hz, 2H), 3.33 (t, *J* = 7.4 Hz, 2H), 2.16-2.06 (m, 2H), 1.84-1.75 (multi, 2H), 1.50-1.39 (multi, 2H), 1.34-1.29 (multi, 2H). <sup>13</sup>C NMR (300 MHz, CDCl<sub>3</sub>) δ : 143.76, 129.64, 110.00, 57.24, 33.58, 32.39, 29.99, 27.54, 25.70.

Synthesis of **3b**: 4,7-Dibromo-2-(bromohexane)-benzo[d][1,2,3]triazole (1.8 g, 2.27 mmol)(**3a**), sodium azide (295 mg, 4.54 mmol) were dissolved in 20 ml DMSO and stirred under room temperature overnight. Then the mixture was poured into 200 ml water and extracted with CH<sub>2</sub>Cl<sub>2</sub> three times. The organic layer was washed with water twice, dried by anhydrous MgSO<sub>4</sub>,



solvent was removed under vacuum. Product was used directly for the next step without any purification.

Synthesis of **3c**: In a 100 ml two neck flask was added 4,7-diethynylbenzothiadiazole (184 mg, 1 mmol)(**3b**), 4,7-dibromo-2-(bromohexane)-benzo[d][1,2,3]triazole, CuSO<sub>4</sub> (24 mg, 0.15 mmol), Na-ascorbate (41 mg, 0.21 mmol), 10 ml *t*-BuOH, 1 ml H<sub>2</sub>O. The reactor was degassed under vacuum and then back filled with nitrogen three times. The suspension was stirred under heating at 60 °C for two days, then it was poured into 100 ml water and extracted with CH<sub>2</sub>Cl<sub>2</sub> three times. The organic layer was washed with water twice, dried by anhydrous MgSO<sub>4</sub>, solvent was removed under vacuum. Purified with a column using CH<sub>2</sub>Cl<sub>2</sub>/acetone = 20 : 1 as eluent give the final product as a yellow solid (750 mg, 76%). <sup>1</sup>H NMR (300 MHz, CDCl<sub>3</sub>) δ : 8.66 (s, 2H), 8.59 (s, 2H), 7.36 (s, 4H), 4.72 (t, *J* = 7.4 Hz, 4H), 4.42 (t, *J* = 7.4 Hz, 4H), 2.16-2.07 (m, 4H), 2.00-1.94 (m, 4H), 1.42-1.39 (m, 8H). <sup>13</sup>C NMR (300 MHz, CDCl<sub>3</sub>) δ : 152.26, 143.74, 143.14, 129.65, 126.15, 123.82, 122.58, 109.98, 57.12, 50.30, 30.11, 29.86, 25.94.

Synthesis of the **connected catalyst (Th-BT-Th@TA-BT-TA)**: In a capped vial, **3c** (750 mg, 0.76 mmol), 2-(tributylstannyl)thiophene (1.64 ml, 4.56 mmol) and Pd(PPh<sub>3</sub>)<sub>2</sub>Cl<sub>2</sub> (53 mg, 10 mol%) were added. 10 ml anhydrous THF was added via syringe and the reactor was degassed via bubbling nitrogen for 5 min. The vial was put in a microwave reactor (120 °C, 0.8 T) for 1 h, then poured into 100 ml water and extracted with CH<sub>2</sub>Cl<sub>2</sub> three times. The organic layer was washed with water twice, dried by anhydrous MgSO<sub>4</sub>, solvent was removed under vacuum. Purified with a column using CH<sub>2</sub>Cl<sub>2</sub>/acetone = 20 : 1 as eluent give the final product as a yellow-red solid (403 mg, 53%). <sup>1</sup>H NMR (300 MHz, CDCl<sub>3</sub>) δ : 8.59 (s, 2H), 8.55 (s, 2H), 7.98 (dd, *J* = 3.7, 1.2 Hz, 4H), 7.52 (s, 4H), 7.29-7.27 (m, 4H), 7.08 (dd, *J* = 5.1, 3.7 Hz, 4H), 4.74 (t, *J* = 7.4 Hz, 4H), 4.39 (t, *J* = 7.4 Hz, 4H), 2.16-2.12 (m, 4H), 1.98-1.93 (m, 4H), 1.45-1.42 (m, 8H). <sup>13</sup>C NMR (300 MHz, CDCl<sub>3</sub>) δ : 152.21, 143.15, 142.09, 139.84, 128.10, 126.92, 126.04, 125.63, 123.72, 123.55, 122.82, 122.59, 56.52, 50.30, 30.15, 29.70, 26.03, 25.97.

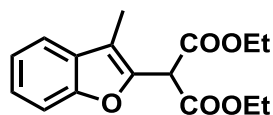
### 6.2.3 General procedure for the sacrificial reagent free and photocatalytic C-C coupling reactions using cooperative photocatalyst systems

A 25 ml Schlenk tube equipped with a stirring bar and stopper was heated under vacuum then cooling for one time and then back filled with argon before the electron-rich heteroaromatics (3-methyl benzofuran *et al.*) (0.38 mmol, 1 equiv), cooperative photocatalyst couple system (declared amount and ratio as described in Table 5.5), diethyl bromomalonate (0.76 mmol, 2.0 equiv), 2.5 ml DMF were added. The reactor was degassed via the freeze-pump-thaw method and irradiated under a white LED for 24 h. The conversion was determined via GC-MS and the pure product was obtained via chromatography.

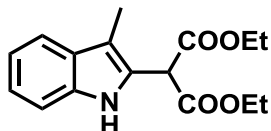
### 6.2.4 Comparison control experiment for the C-C coupling reaction between 3-methylbenzofuran and ethyl bromoacetate using Th-BTz-Th as catalyst and 4-methoxytriphenylamine as sacrificial reagent.

A 25 ml Schlenk tube equipped with a stirring bar and stopper was heated under vacuum then cooling for one time and then back filled with argon before 3-methylbenzofuran (0.38 mmol, 1 equiv), 4-methoxytriphenylamine (0.76 mmol, 2 equiv), ethyl bromomalonate (0.76 mmol, 2.0 equiv), Th-BTz-Th (1 mol%), 2.5 ml DMF were added. The reactor was degassed via the freeze-pump-thaw method and irradiated under a white LED. The reaction time was determined by GC-MS when the signal of starting material totally disappeared. After the reaction was completed, the mixture was poured into 20 ml water and extracted by CH<sub>2</sub>Cl<sub>2</sub>, the organic layer was dried by anhydrous MgSO<sub>4</sub>, and the solvent removed under vacuum. The crude product was purified on silica gel using the indicated solvent system to offer the desired product.

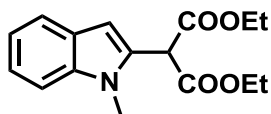
### 6.2.5 Products NMR data:



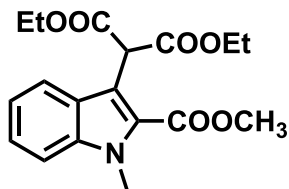
**Diethyl 2-(3-methyl-1H-2,3-benzofuran-2-yl)malonate.** Follow the general procedure, hexane/ $\text{CH}_2\text{Cl}_2$  = 1/1 was used as eluent to give the product as a yellow oil (99 mg, 90%).  $^1\text{H}$  NMR (300 MHz, DMSO)  $\delta$  : 7.63 - 7.60 (m, 1 H), 7.56 - 7.54 (m, 1 H), 7.37 - 7.26 (m, 2 H), 5.49 (s, 1 H), 4.26 - 4.14 (m, 4 H), 2.22 (s, 3 H), 1.22 (t,  $J$  = 7.4 Hz, 6 H).  $^{13}\text{C}$  NMR (300 MHz, DMSO)  $\delta$  : 165.93, 153.47, 144.29, 129.10, 124.67, 122.58, 119.66, 114.25, 110.92, 61.67, 50.00, 13.85, 7.42.



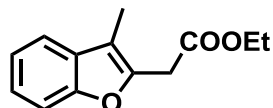
**Diethyl 2-(1,3-dimethyl-1H-indole-2-yl)malonate.** Follow the general procedure, hexane/ $\text{CH}_2\text{Cl}_2$  = 2/1 was used as eluent to give the product as a yellow solid (97 mg, 88%).  $^1\text{H}$  NMR (300 MHz,  $\text{CDCl}_3$ )  $\delta$  : 8.93 (br, 1 H), 7.58 - 7.55 (m, 1 H), 7.39 - 7.36 (m, 1 H), 7.24 - 7.15 (m, 1 H), 7.19 - 7.10 (m, 1 H), 5.00 (s, 1 H), 4.34 - 4.18 (m, 4 H), 2.34 (s, 3 H), 1.31 (t,  $J$  = 7.4 Hz, 6 H).  $^{13}\text{C}$  NMR (300 MHz,  $\text{CDCl}_3$ )  $\delta$  : 167.38, 135.83, 128.26, 124.53, 122.36, 119.22, 118.78, 111.09, 110.60, 62.29, 49.31, 14.03, 8.51.



**Diethyl 2-(1-methyl-1H-indole-2-yl)malonate.** Follow the general procedure, hexane/ $\text{CH}_2\text{Cl}_2$  = 1/1 was used as eluent to give the product as a yellow solid (86 mg, 78%).  $^1\text{H}$  NMR (300 MHz,  $\text{CDCl}_3$ )  $\delta$  : 7.61 (d,  $J$  = 7.81 Hz, 1 H), 7.33 (d,  $J$  = 7.72 Hz, 1 H), 7.25 - 7.21 (m, 1 H), 7.13 - 7.08 (m, 1 H), 6.50 (s, 1 H), 4.93 (s, 1 H), 4.34 - 4.20 (m, 4 H), 3.73 (s, 3 H), 1.30 (t,  $J$  = 7.4 Hz, 6 H).  $^{13}\text{C}$  NMR (300 MHz,  $\text{CDCl}_3$ )  $\delta$  : 166.99, 137.93, 130.90, 127.27, 121.97, 120.79, 119.71, 109.30, 103.01, 62.23, 51.32, 30.31, 14.05.



**Diethyl 2-(2-(methoxycarbonyl)-1-methyl-1H-indole-3-yl)malonate.** Follow the general procedure, hexane/CH<sub>2</sub>Cl<sub>2</sub> = 1/2 was used as eluent to give the product as a green-yellow solid (115 mg, 87%). <sup>1</sup>H NMR (300 MHz, CDCl<sub>3</sub>) δ : 7.77 (d, *J* = 8.21 Hz, 1 H), 7.41 - 7.34 (m, 2 H), 7.21 - 7.15 (m, 1 H), 5.79 (s, 1 H), 4.28 - 4.21 (m, 4 H), 4.03 (s, 3 H), 3.96 (s, 3 H), 1.27 (t, *J* = 7.4 Hz, 6 H). <sup>13</sup>C NMR (300 MHz, CDCl<sub>3</sub>) δ : 168.55, 162.51, 138.68, 126.15, 125.65, 125.36, 121.99, 120.77, 114.50, 110.35, 61.69, 51.77, 49.96, 32.28, 14.09.



**Ethyl 2-(3-methyl-1H-2,3-benzofuran-2-yl)acetate.**

<sup>1</sup>H NMR (300 MHz, DMSO) δ : 7.41 - 7.37 (m, 1 H), 7.35 - 7.32 (m, 1 H), 7.20 - 7.17 (m, 1 H), 7.16 - 7.11 (m, 1 H), 4.15 - 4.08 (m, 2 H), 3.68 (s, 2 H), 2.13 (s, 3 H), 1.19 (t, 3 H). <sup>13</sup>C NMR (300 MHz, DMSO) δ : 169.14, 154.15, 146.12, 129.91, 123.92, 122.23, 119.13, 112.81, 110.95, 61.35, 32.84, 14.19, 7.97.

### 6.3 Feasibility study of the small molecule organic semiconductors as photocatalysts for challenging reactions: molecular design for metal-free and photocatalytic aromatic C-C bond formation reaction

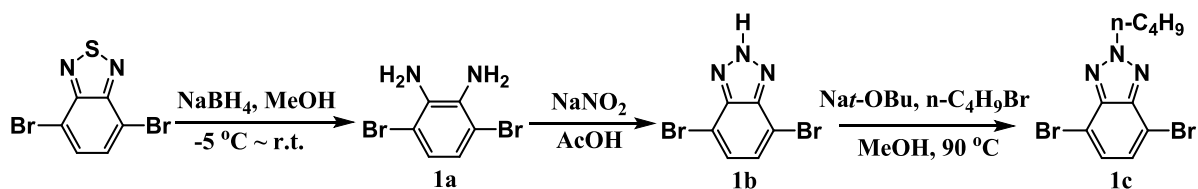
#### 6.3.1 Materials and methods.

Chemicals were purchased from commercial sources and used as received without further purification. Glassware was dried under heating by a heating gun at 600 °C and cooled under vacuum prior to use if necessary. All photocatalyst reactions were conducted using common dry, inert atmosphere techniques via a schlenk tube. White LED (Silent Air System White OL M-018) is a product of OSA Opto Light GmbH. UV-Vis absorption and emission spectra were recorded on a Perkin Elmer Lambda 100 spectrophotometer and J&M TIDAS spectrofluorometer at ambient temperature, respectively. Cyclic voltammetry measurement was performed with Autolab PGSTAT204 potentiostat/galvanostat of Metrohm (a three electrode cell system): glassy carbon electrode as the working electrode, Hg/HgCl<sub>2</sub> electrode as

the reference electrode, platinum wire as the counter electrode, and  $\text{Bu}_4\text{NPF}_6$  (0.1 M Acetonitrile) as supporting electrolyte with a scan rate of 100 mV/s in the range of -2 eV to 2.5 eV.  $^1\text{H}$  and  $^{13}\text{C}$  spectra were recorded on a Bruker Avance 300 spectrometer, and  $d\text{-CHCl}_3$  was used as solvent unless otherwise noted. GC-MS spectra were recorded on a SHIMADZU GCMS-QP2010 gas chromatograph mass spectrometer.

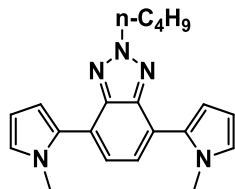
### 6.3.2 Synthesis of the molecular organic semiconductors and sacrificial reagent

Synthetic route of 4,7-Dibromo-2-(n-butyl)-2H-benzo[d]-[1,2,3]triazole



*See in chapter 6.2.2.*

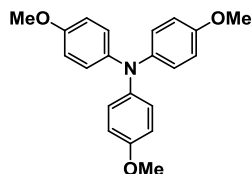
Py-BTz-Py



A 100 ml Schlenk tube equipped with a stirring bar and stopper was heated under vacuum then cooling three times before 4,7-dibromo-2-(n-butyl)-2H-benzo[d]-[1,2,3]triazole (1 g, 3.00 mmol), 1-methyl-2-(tributylstannyl)pyrrole (2.14 ml, 6.5 mmol) and  $\text{Pd}(\text{PPh}_3)_2\text{Cl}_2$  (100.8 mg, 5 mol%) were added. 15 ml anhydrous DMF was added via syringe and the reactor was degassed under vacuum and then back filled with nitrogen three times. It was heated under 90 °C overnight, then poured into 200 ml water and extracted with  $\text{CH}_2\text{Cl}_2$  three times. The organic layer was washed with water twice, dried by anhydrous  $\text{MgSO}_4$ , solvent was removed under vacuum. Purified with a column using  $\text{CH}_2\text{Cl}_2/\text{hexane} = 1 : 1$  as eluent give the final product as light red solid (650 mg, 65%).  $^1\text{H}$  NMR (300 MHz,  $\text{CDCl}_3$ )  $\delta$  : 7.27 (s, 2H), 6.76-6.75 (m, 2H), 6.50-6.49 (m, 2H), 6.23-6.21 (m, 2H), 4.65 (t,  $J=7.4$  Hz, 2H), 3.68 (s, 6H), 2.07-1.97 (m, 2H), 1.37-1.25

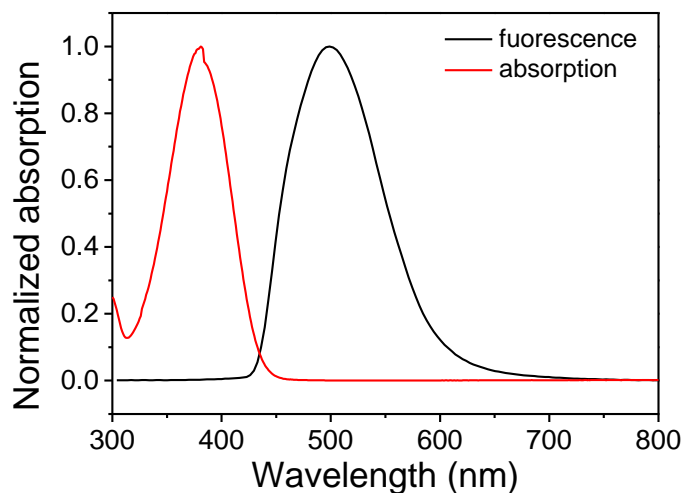
(m, 2H), 0.88 (t,  $J=7.4$  Hz, 3H).  $^{13}\text{C}$  NMR (300 MHz,  $\text{CDCl}_3$ )  $\delta$  : 143.49, 130.49, 125.46, 124.66, 122.22, 111.19, 108.28, 56.42, 35.78, 32.15, 19.82, 13.56.

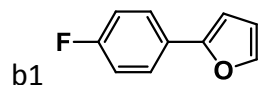
#### Synthesis of the tri(4-methoxyphenyl)amine



4-Methoxyaniline (6.06 g, 50 mmol), 4-Iodoanisole (29 g, 125 mmol) were added into a 100 ml two neck flask was equipped with a stirring bar and stopper, then 50 ml toluene was added and the mixture was stirred for dissolving.  $\text{CuCl}$  (193 mg, 3.9%), 1,10-phenanthroline (360 mg, 4%),  $\text{KOH}$  (21 g, 390 mmol) were added, and the reactor was degased for 10 min. It was heated to  $120^\circ\text{C}$  for 24 h then poured into 300 ml water and extracted with  $\text{CH}_2\text{Cl}_2$  three times. The organic layer was washed with water twice, dried by anhydrous  $\text{MgSO}_4$ , solvent was removed under vacuum. Purified with a column using  $\text{CH}_2\text{Cl}_2/\text{hexane} = 1:2$  as eluent then recrystallized from methanol give the final product as white solid.  $^1\text{H}$  NMR (300 MHz,  $\text{DMSO}$ )  $\delta$  : 6.90-6.82 (m, 12 H), 3.71 (s,  $J=7.4$  Hz, 9 H).  $^{13}\text{C}$  NMR (300 MHz,  $\text{CDCl}_3$ )  $\delta$  : 154.55, 141.31, 124.41, 114.68, 55.15.

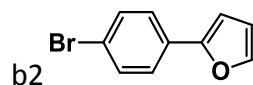
#### 6.3.3 Absorption and fluorescence spectrum of photocatalyst Py-BTz-Py



**6.3.4 Product characterization**

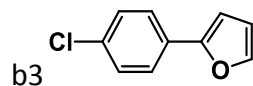
$^1\text{H}$  NMR (300 MHz,  $\text{CDCl}_3$ )  $\delta$  : 7.59-7.54 (m, 2 H), 7.38 (m, 1 H), 7.00 (m, 2 H), 6.51-6.50 (m, 1 H), 6.40-6.38 (m, 1 H).

$^{13}\text{C}$  NMR (300 MHz,  $\text{CDCl}_3$ )  $\delta$  : 163.75, 160.48, 153.16, 142.04, 125.59, 125.48, 115.82, 115.53, 111.68, 104.62.



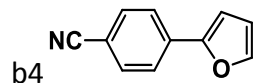
$^1\text{H}$  NMR (300 MHz,  $\text{CDCl}_3$ )  $\delta$  : 7.46-7.38 (m, 5 H), 6.57-6.55 (m, 1 H), 6.39-6.37 (m, 1 H).

$^{13}\text{C}$  NMR (300 MHz,  $\text{CDCl}_3$ )  $\delta$  : 152.95, 142.40, 131.81, 129.80, 125.30, 121.08, 111.82, 105.56.



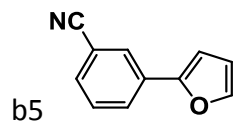
$^1\text{H}$  NMR (300 MHz,  $\text{CDCl}_3$ )  $\delta$  : 7.54 (d,  $J = 7.5\text{Hz}$ , 2 H), 7.40-7.39 (m, 1 H), 7.30-7.26 (d,  $J = 7.5\text{Hz}$ , 2 H), 7.57-7.56 (m, 1 H), 6.41-6.39 (m, 1 H).

$^{13}\text{C}$  NMR (300 MHz,  $\text{CDCl}_3$ )  $\delta$  : 152.94, 142.35, 132.96, 129.37, 128.89, 125.02, 111.80, 105.44.



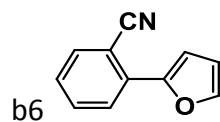
$^1\text{H}$  NMR (300 MHz,  $\text{CDCl}_3$ )  $\delta$  : 7.68 (d,  $J = 7.5\text{Hz}$ , 2 H), 7.59 (d,  $J = 7.5\text{Hz}$ , 2 H), 7.46 (m, 1 H), 6.75-6.73 (m, 1 H), 6.46-6.44 (m, 1 H).

$^{13}\text{C}$  NMR (300 MHz,  $\text{CDCl}_3$ )  $\delta$  : 151.97, 143.71, 134.64, 132.61, 123.95, 118.89, 112.28, 110.27, 108.19.



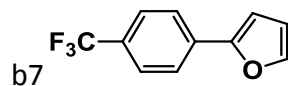
$^1\text{H}$  NMR (300 MHz,  $\text{CDCl}_3$ )  $\delta$  : 7.82 (s, 1 H), 7.77-7.75 (m, 1 H), 7.43-7.35 (m, 3 H), 6.65-6.64 (m, 1 H), 6.43-6.41 (m, 1 H).

$^{13}\text{C}$  NMR (300 MHz,  $\text{CDCl}_3$ )  $\delta$  : 151.56, 143.19, 131.93, 130.40, 129.54, 127.65, 127.11, 118.68, 112.97, 112.05, 106.91.



$^1\text{H}$  NMR (300 MHz,  $\text{CDCl}_3$ )  $\delta$  : 7.81-7.79 (m, 1 H), 7.60-7.58 (m, 1 H), 7.54-7.46 (m, 2 H), 7.25-7.20 (m, 2 H), 6.48-6.46 (m, 1 H).

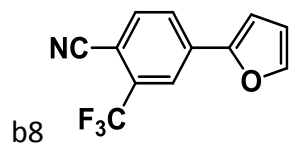
$^{13}\text{C}$  NMR (300 MHz,  $\text{CDCl}_3$ )  $\delta$  : 149.76, 143.34, 134.14, 133.21, 132.95, 127.12, 125.93, 119.03, 112.27, 110.45, 106.83.



$^1\text{H}$  NMR (300 MHz,  $\text{CDCl}_3$ )  $\delta$  : 7.71-7.67 (m, 2 H), 7.57-7.54 (m, 2 H), 7.45-7.44 (m, 1 H), 6.70 (d,  $J$  = 3.4 Hz, 1 H), 6.45-6.43 (m, 1 H).

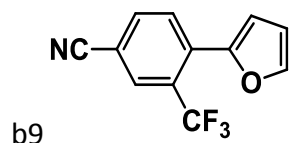
$^{13}\text{C}$  NMR (300 MHz,  $\text{CDCl}_3$ )  $\delta$  : 152.51, 143.09, 133.94, 125.73, 125.68, 125.63, 123.77, 111.97, 106.96.





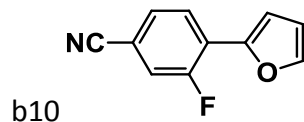
$^1\text{H}$  NMR (300 MHz,  $\text{CDCl}_3$ )  $\delta$  : 7.93 (s, 1 H), 7.83-7.79 (m, 1 H), 7.74-7.71 (d, 1 H), 7.50 (m, 1 H), 6.85-6.83 (m, 1 H), 6.50-6.48 (m, 1 H).

$^{13}\text{C}$  NMR (300 MHz,  $\text{CDCl}_3$ )  $\delta$  : 150.63, 144.62, 135.19, 134.91, 134.18, 133.66, 133.14, 132.62, 126.28, 124.51, 121.57, 121.49, 121.42, 121.34, 120.15, 115.72, 112.67, 109.80, 107.33.



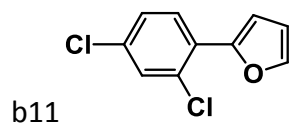
$^1\text{H}$  NMR (300 MHz,  $\text{CDCl}_3$ )  $\delta$  : 7.92 (s, 1 H), 7.88 (m, 1 H), 7.75-7.72 (m, 1 H), 7.53-7.52 (m, 1 H), 6.86-6.85 (m, 1 H), 6.49-6.47 (m, 1 H).

$^{13}\text{C}$  NMR (300 MHz,  $\text{CDCl}_3$ )  $\delta$  : 148.33, 144.60, 134.97, 133.46, 130.86, 130.78, 130.69, 130.61, 129.85, 127.05, 126.61, 126.23, 125.83, 124.71, 121.11, 117.51, 113.29, 113.23, 113.18, 113.12, 112.51, 111.06.



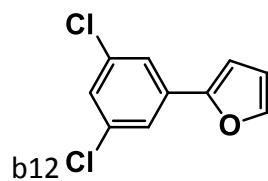
$^1\text{H}$  NMR (300 MHz,  $\text{CDCl}_3$ )  $\delta$  : 7.85-7.80 (m, 1 H), 7.49-7.48 (m, 1 H), 7.41-7.37 (m, 1 H), 7.33-7.29 (m, 1 H), 6.94-6.9 (m, 1 H), 6.50-6.48 (m, 1 H).

$^{13}\text{C}$  NMR (300 MHz,  $\text{CDCl}_3$ )  $\delta$  : 159.12, 155.76, 146.21, 143.65, 128.38, 126.45, 123.67, 123.51, 119.76, 119.43, 117.76, 113.44, 113.28, 112.62, 110.85, 110.72.



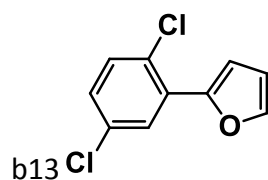
$^1\text{H}$  NMR (300 MHz,  $\text{CDCl}_3$ )  $\delta$  : 7.74-7.71 (m, 1 H), 7.44 (m, 1 H), 7.38 (m, 1 H), 7.24-7.20 (m, 1 H), 7.06-7.05 (m, 1 H), 6.47-6.45 (m, 1 H).

$^{13}\text{C}$  NMR (300 MHz,  $\text{CDCl}_3$ )  $\delta$  : 149.30, 142.34, 132.99, 130.51, 130.39, 128.58, 127.84, 127.27, 111.84, 111.21.



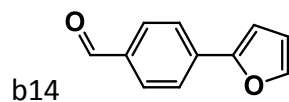
$^1\text{H}$  NMR (300 MHz,  $\text{CDCl}_3$ )  $\delta$  : 7.46-7.45 (m, 2 H), 7.42-7.41 (m, 1 H), 7.16-7.14 (m, 1 H), 6.63-6.62 (m, 1 H), 6.43-6.41 (m, 1 H).

$^{13}\text{C}$  NMR (300 MHz,  $\text{CDCl}_3$ )  $\delta$  : 151.23, 143.18, 135.37, 133.44, 126.99, 122.05, 112.02, 107.16.



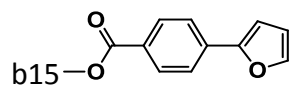
$^1\text{H}$  NMR (300 MHz,  $\text{CDCl}_3$ )  $\delta$  : 7.78-7.77 (m, 1 H), 7.44 (m, 1 H), 7.28-7.25 (m, 1 H), 7.11-7.10 (m, 1 H), 7.08-7.04 (m, 1 H), 6.46-6.44 (m, 1 H).

$^{13}\text{C}$  NMR (300 MHz,  $\text{CDCl}_3$ )  $\delta$  : 148.93, 142.62, 132.92, 131.81, 130.42, 128.05, 127.76, 127.46, 111.93, 111.87.



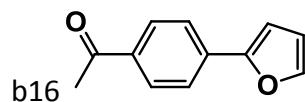
$^1\text{H}$  NMR (300 MHz,  $\text{CDCl}_3$ )  $\delta$  : 9.92 (s, 1 H), 7.84 (d,  $J$  = 7.5Hz, 2 H), 7.76 (d,  $J$  = 7.5Hz, 2 H), 7.48 (m, 1 H), 6.78-6.77 (m, 1 H), 6.47-6.46 (m, 1 H).

$^{13}\text{C}$  NMR (300 MHz,  $\text{CDCl}_3$ )  $\delta$  : 191.62, 152.62, 143.65, 136.11, 134.89, 130.39, 123.93, 112.26, 108.16.



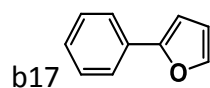
$^1\text{H}$  NMR (300 MHz,  $\text{CDCl}_3$ )  $\delta$  : 7.99 (d,  $J$  = 7.5Hz, 2 H), 7.66 (d,  $J$  = 7.5Hz, 2 H), 7.44 (m, 1 H), 6.71-6.70 (m, 1 H), 6.44-6.42 (m, 1 H).

$^{13}\text{C}$  NMR (300 MHz,  $\text{CDCl}_3$ )  $\delta$  : 166.81, 152.93, 143.14, 134.77, 130.11, 128.54, 123.40, 112.03, 107.24, 52.11.



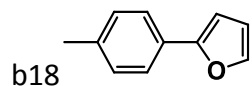
$^1\text{H}$  NMR (300 MHz,  $\text{CDCl}_3$ )  $\delta$  : 7.92 (d,  $J$  = 7.5Hz, 2 H), 7.69 (d,  $J$  = 7.5Hz, 2 H), 7.46 (m, 1 H), 6.74-6.73 (m, 1 H), 6.46-6.44 (m, 1 H), 2.54 (s, 3 H).

$^{13}\text{C}$  NMR (300 MHz,  $\text{CDCl}_3$ )  $\delta$  : 197.46, 152.85, 143.29, 125.55, 134.89, 128.97, 123.56, 112.10, 107.48, 26.58.



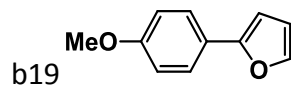
$^1\text{H}$  NMR (300 MHz,  $\text{CDCl}_3$ )  $\delta$  : 7.62-7.59 (m, 2 H), 7.40 (m, 1 H), 7.34-7.29 (m, 2 H), 7.21-7.16 (m, 1H), 6.59-6.85 (m, 1 H), 6.41-6.39 (m, 1 H).

$^{13}\text{C}$  NMR (300 MHz,  $\text{CDCl}_3$ )  $\delta$  : 151.91, 142.05, 130.89, 128.75, 127.17, 123.79, 111.63, 104.94.



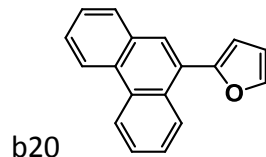
$^1\text{H}$  NMR (300 MHz,  $\text{CDCl}_3$ )  $\delta$  : 7.50 (d,  $J$  = 7.5Hz, 2 H), 7.37 (m, 1 H), 7.12 (d,  $J$  = 7.5Hz, 2 H), 6.52-6.50 (m, 1H), 6.38-6.37 (m, 1 H), 2.28 (s, 3 H).

$^{13}\text{C}$  NMR (300 MHz,  $\text{CDCl}_3$ )  $\delta$  : 154.23, 141.67, 137.16, 129.36, 128.25, 123.78, 111.55, 104.22, 21.28.



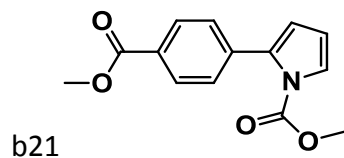
$^1\text{H}$  NMR (300 MHz,  $\text{CDCl}_3$ )  $\delta$  : 7.54 (d,  $J$  = 7.5Hz, 2 H), 7.35 (m, 1 H), 6.86 (d,  $J$  = 7.5Hz, 2 H), 6.44-6.43 (m, 1H), 6.37-6.36 (m, 1 H), 3.75 (s, 3 H).

$^{13}\text{C}$  NMR (300 MHz,  $\text{CDCl}_3$ )  $\delta$  : 159.02, 154.05, 141.39, 125.24, 124.05, 114.12, 111.54, 103.38, 55.32.



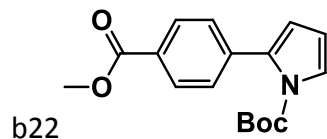
$^1\text{H}$  NMR (300 MHz,  $\text{CDCl}_3$ )  $\delta$  : 8.70-8.67 (m, 1 H), 8.63-8.60 (m, 1 H), 8.35-8.32 (m, 1 H), 7.91 (s, 1H), 7.85-7.82 (m, 1 H), 7.62-7.50 (m, 5 H), 6.71-6.69 (m, 1 H), 6.55-6.54 (m, 1 H).

$^{13}\text{C}$  NMR (300 MHz,  $\text{CDCl}_3$ )  $\delta$  : 153.41, 142.50, 131.34, 130.77, 130.23, 129.65, 128.97, 127.44, 127.37, 127.09, 126.94, 126.90, 126.69, 126.33, 123.03, 122.57, 111.39, 109.60.



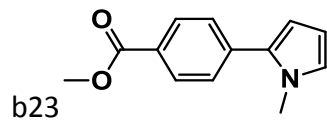
$^1\text{H}$  NMR (300 MHz,  $\text{CDCl}_3$ )  $\delta$  : 7.96 (d,  $J$  = 7.5Hz, 2 H), 7.37 (d,  $J$  = 7.5Hz, 2 H), 7.33-7.31 (m, 1 H), 6.23-6.17 (m, 2 H), 3.85 (s, 3 H), 3.75 (s, 3 H).

$^{13}\text{C}$  NMR (300 MHz,  $\text{CDCl}_3$ )  $\delta$  : 166.95, 151.09, 138.07, 134.48, 128.83, 123.33, 120.07, 115.92, 112.47, 111.66, 53.94, 52.11.



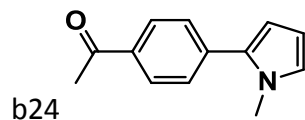
$^1\text{H}$  NMR (300 MHz,  $\text{CDCl}_3$ )  $\delta$  : 7.96 (d,  $J$  = 7.5Hz, 2 H), 7.36 (d,  $J$  = 7.5Hz, 2 H), 7.31-7.30 (m, 1 H), 6.18-6.16 (m, 2 H), 3.85 (s, 3 H), 1.30 (s, 9 H).

$^{13}\text{C}$  NMR (300 MHz,  $\text{CDCl}_3$ )  $\delta$  : 167.00, 149.18, 138.92, 133.95, 128.93, 128.55, 123.51, 115.46, 110.87, 84.09, 52.14, 27.65.



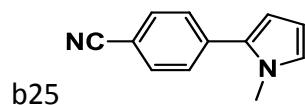
$^1\text{H}$  NMR (300 MHz,  $\text{CDCl}_3$ )  $\delta$  : 8.00 (d,  $J$  = 7.5Hz, 2 H), 7.41 (d,  $J$  = 7.5Hz, 2 H), 6.69-6.68 (m, 1 H), 6.27-6.25 (m, 2 H), 6.16-6.13 (m, 1 H), 3.85 (s, 3 H), 3.63 (s, 3 H).

$^{13}\text{C}$  NMR (300 MHz,  $\text{CDCl}_3$ )  $\delta$  : 167.00, 137.75, 133.52, 129.78, 127.92, 127.89, 125.16, 110.06, 108.30, 52.15, 35.45.



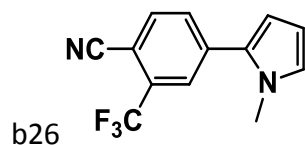
$^1\text{H}$  NMR (300 MHz,  $\text{CDCl}_3$ )  $\delta$  : 7.89 (d,  $J$  = 7.5Hz, 2 H), 7.41 (d,  $J$  = 7.5Hz, 2 H), 6.67-6.66 (m, 1 H), 6.26-6.24 (m, 1 H), 6.14-6.11 (m, 1 H), 3.61 (s, 3 H), 2.51 (s, 3 H).

$^{13}\text{C}$  NMR (300 MHz,  $\text{CDCl}_3$ )  $\delta$  : 197.58, 137.94, 134.92, 133.40, 128.63, 127.95, 125.39, 110.27, 108.40, 35.48, 26.61.



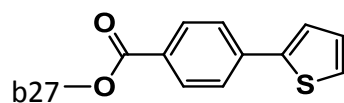
$^1\text{H}$  NMR (300 MHz,  $\text{CDCl}_3$ )  $\delta$  : 7.58 (d,  $J$  = 7.5Hz, 2 H), 7.42 (d,  $J$  = 7.5Hz, 2 H), 6.70-6.68 (m, 1 H), 6.27-6.25 (m, 1 H), 6.15-6.13 (m, 1 H), 3.62 (s, 3 H).

$^{13}\text{C}$  NMR (300 MHz,  $\text{CDCl}_3$ )  $\delta$  : 137.72, 132.63, 132.29, 128.29, 125.92, 119.10, 110.79, 109.67, 108.62, 35.51.



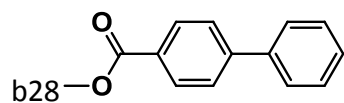
$^1\text{H}$  NMR (300 MHz,  $\text{CDCl}_3$ )  $\delta$  : 7.77-7.72 (m, 2 H), 7.61-7.57 (m, 1 H), 7.76-7.74 (m, 1 H), 6.37-6.34 (m, 1 H), 6.18-6.16 (m, 1 H), 3.67 (s, 3 H).

$^{13}\text{C}$  NMR (300 MHz,  $\text{CDCl}_3$ )  $\delta$  : 138.05, 134.90, 133.80, 133.29, 132.77, 132.26, 131.25, 130.30, 127.15, 125.43, 124.58, 120.23, 115.83, 112.10, 109.12, 106.67, 35.66.



$^1\text{H}$  NMR (300 MHz,  $\text{CDCl}_3$ )  $\delta$  : 7.99 (d,  $J$  = 7.5Hz, 2 H), 7.62 (d,  $J$  = 7.5Hz, 2 H), 7.36-7.34 (m, 1 H), 7.30-7.28 (m, 1 H), 7.06-7.03 (m, 1 H), 3.86 (s, 3 H).

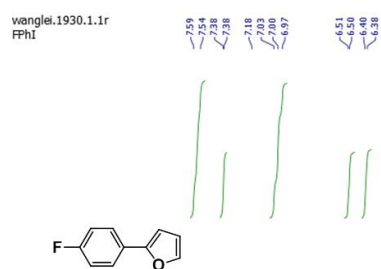
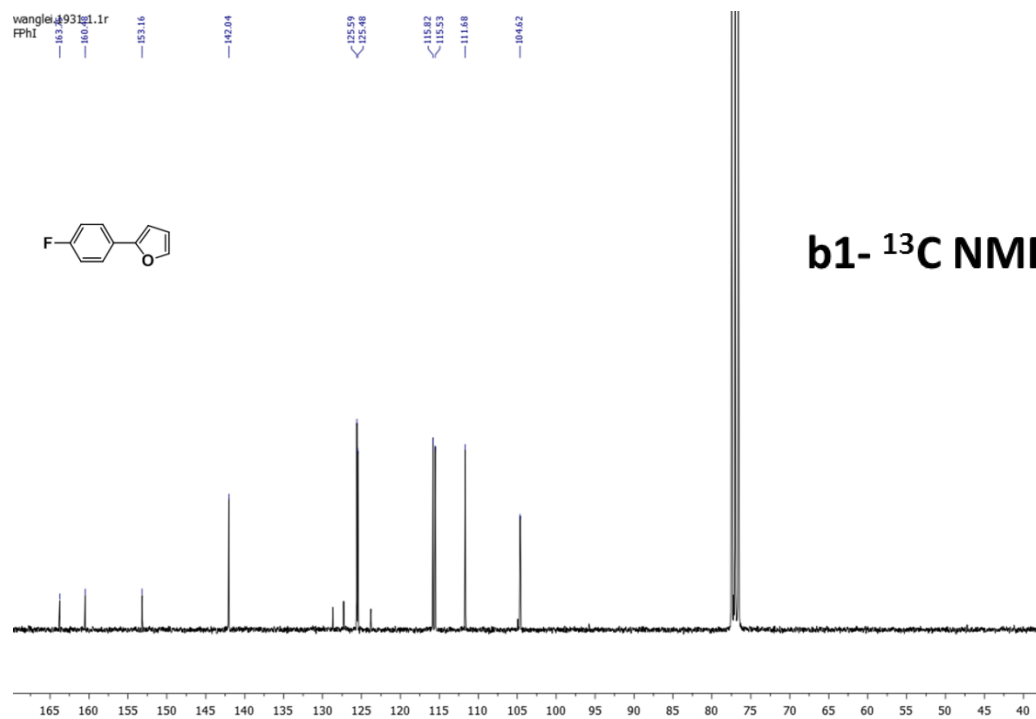
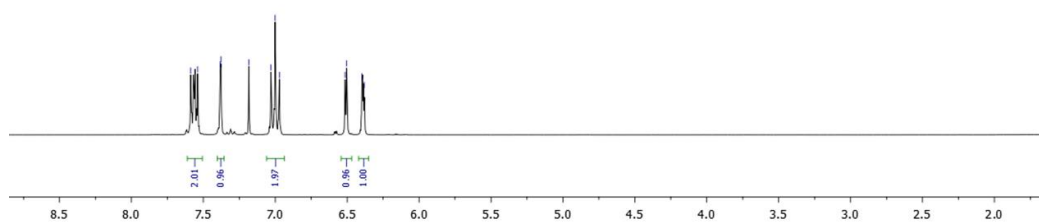
$^{13}\text{C}$  NMR (300 MHz,  $\text{CDCl}_3$ )  $\delta$  : 166.79, 143.08, 138.64, 130.30, 128.77, 128.35, 126.32, 125.53, 124.51, 52.18.



$^1\text{H}$  NMR (300 MHz,  $\text{CDCl}_3$ )  $\delta$  : 8.05 (d,  $J$  = 7.5Hz, 2 H), 7.60 (d,  $J$  = 7.5Hz, 2 H), 7.57-7.54 (m, 2 H), 7.42-7.37 (m, 2 H), 7.35-7.29 (m, 1 H), 3.87 (s, 3 H).

$^{13}\text{C}$  NMR (300 MHz,  $\text{CDCl}_3$ )  $\delta$  : 167.02, 145.64, 140.01, 130.11, 128.93, 128.15, 127.29, 127.06, 52.14.

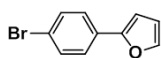
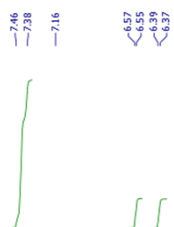
## 6.3.5 NMR spectrum of the isolate products

b1-  $^1\text{H}$  NMRb1-  $^{13}\text{C}$  NMR

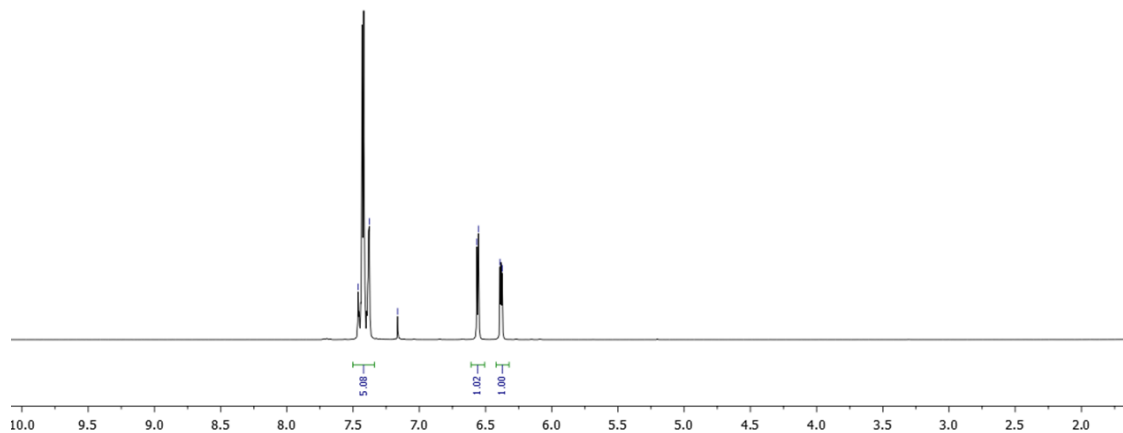


# Experiment Section

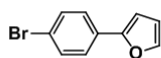
wanglei.1940.1.1r  
BrPhI



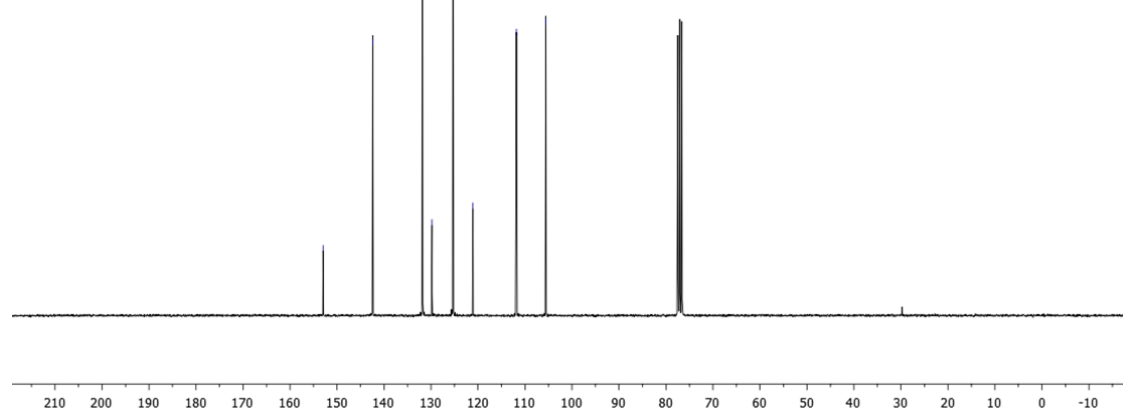
b2- <sup>1</sup>H NMR



wanglei.1941.1.1r  
BrPhI



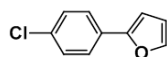
b2- <sup>13</sup>C NMR



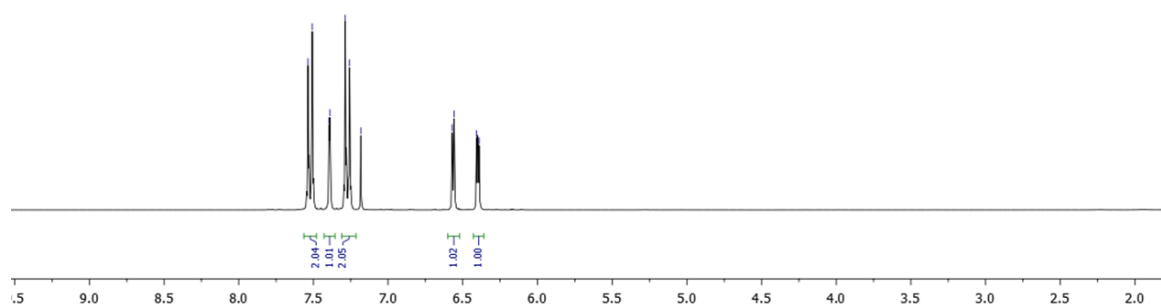
# Experiment Section

wanglei.1950.1.1r  
ClPhI

7.54  
7.51  
7.40  
7.39  
7.29  
7.28  
7.18  
6.57  
6.56  
6.54  
6.39

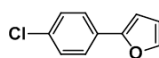


**b3- <sup>1</sup>H NMR**

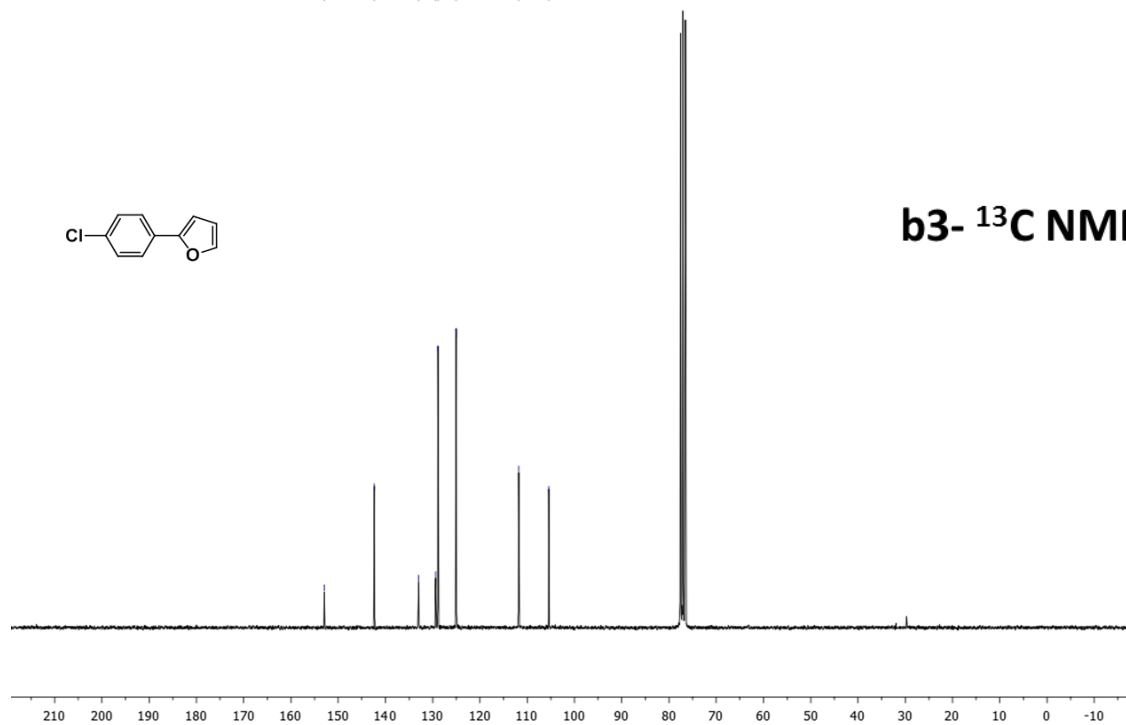


wanglei.295.1.1r  
ClPhI

152.94  
142.35  
132.96  
128.37  
128.89  
125.62  
111.80  
105.44

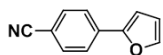
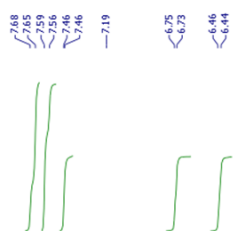


**b3- <sup>13</sup>C NMR**

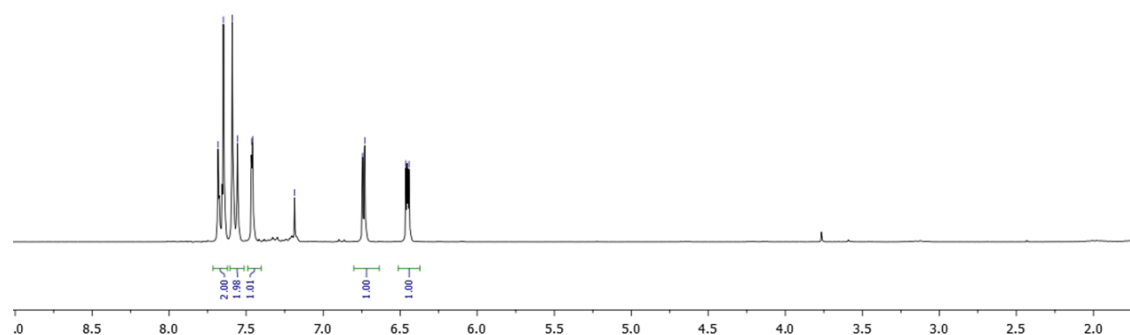


# Experiment Section

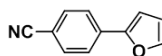
wanglei.283.1.1r  
CNPhI



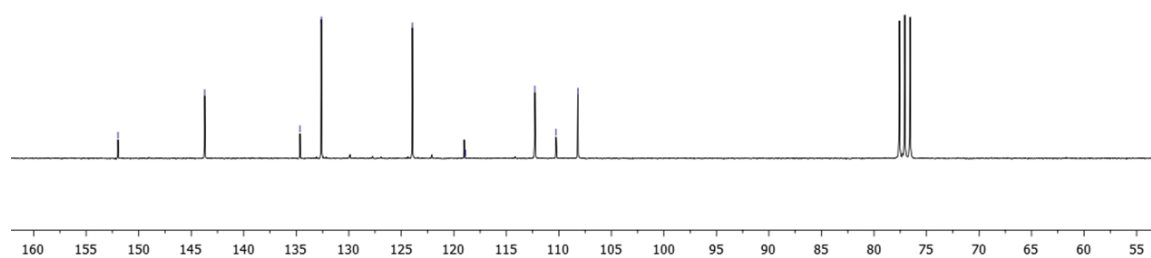
**b4- <sup>1</sup>H NMR**



wanglei.285.1.1r  
CNPhI

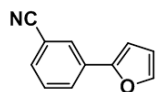
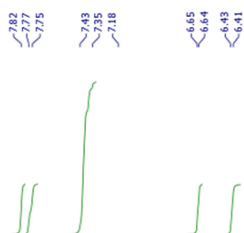


**b4- <sup>13</sup>C NMR**

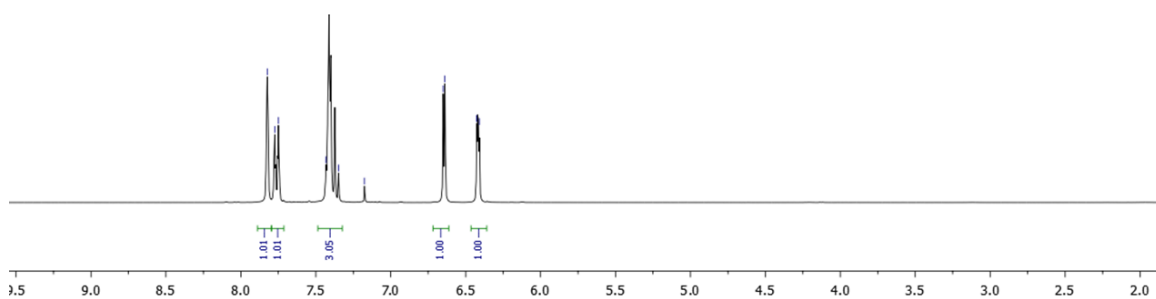


# Experiment Section

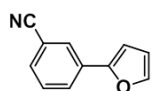
wanglei.2060.1.1r  
3-CNPhI



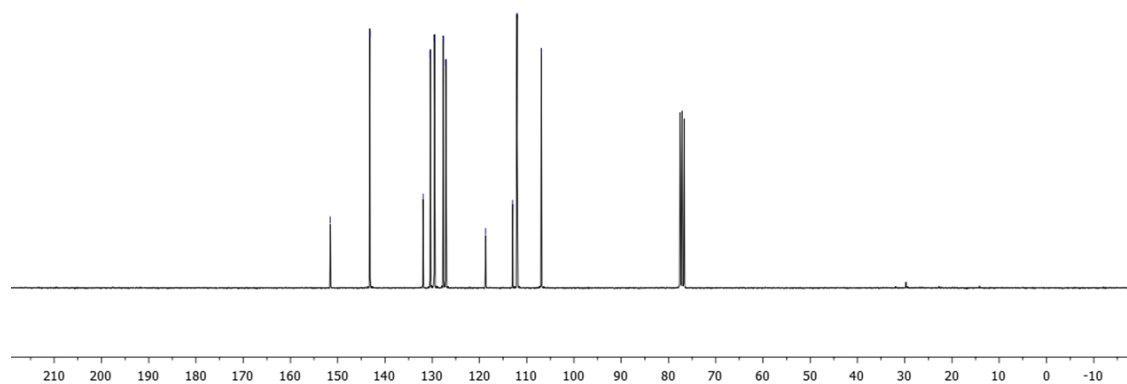
**b5- <sup>1</sup>H NMR**



wanglei.2061.1.1r  
3-CNPhI

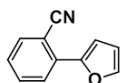
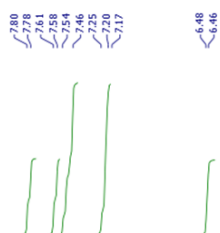


**b5- <sup>13</sup>C NMR**

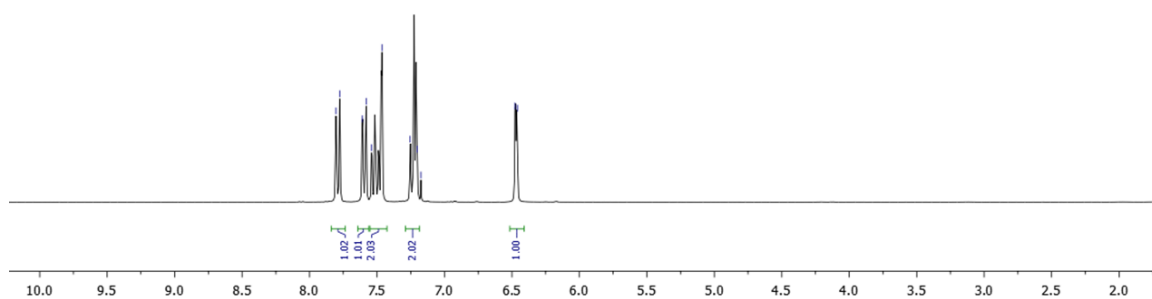


# Experiment Section

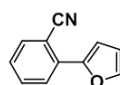
wanglei.2050.1.1r  
2-CNPhI



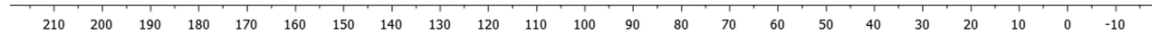
**b6- <sup>1</sup>H NMR**



wanglei.2051.1.1r  
2-CNPhI

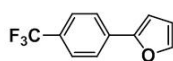
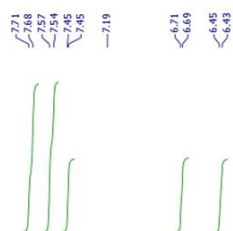


**b6- <sup>13</sup>C NMR**

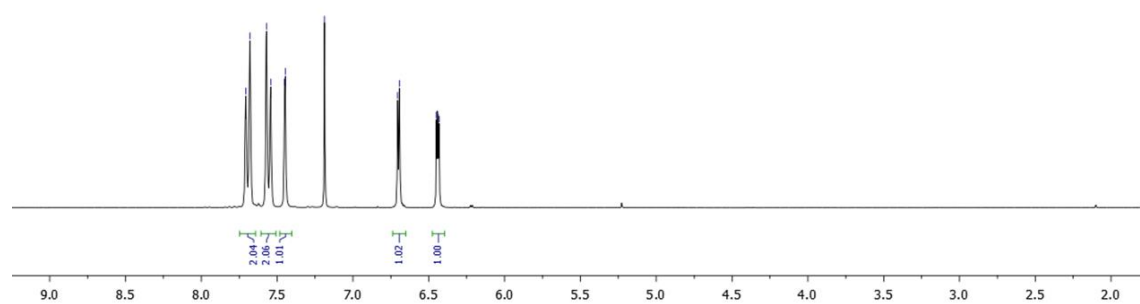


# Experiment Section

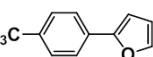
wanglei.2010.1.1r  
CF3PhI



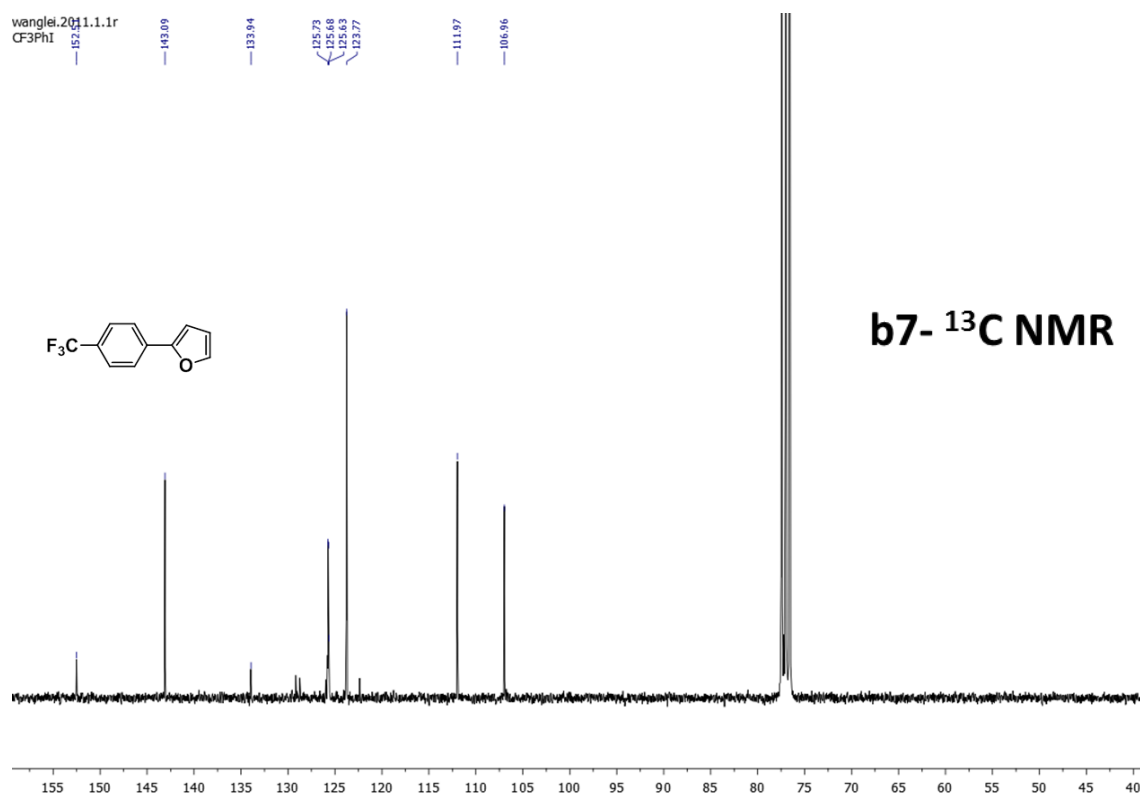
**b7- <sup>1</sup>H NMR**



wanglei.2011.1.1r  
CF3PhI

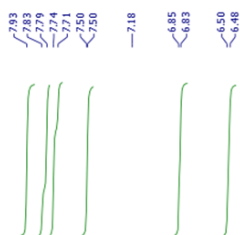


**b7- <sup>13</sup>C NMR**

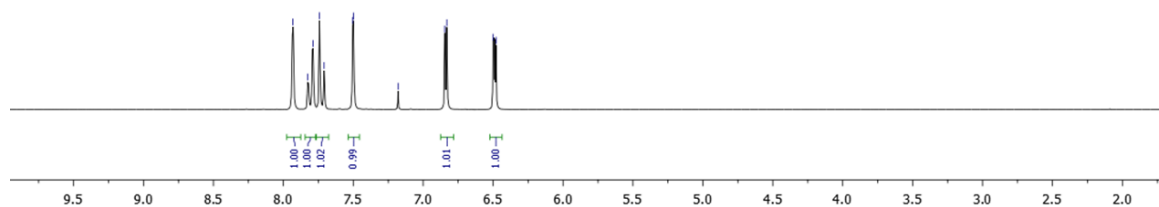
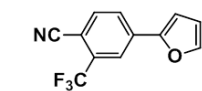


# Experiment Section

wanglei.326.1.1r  
4-I-2CF<sub>3</sub>-CNPh



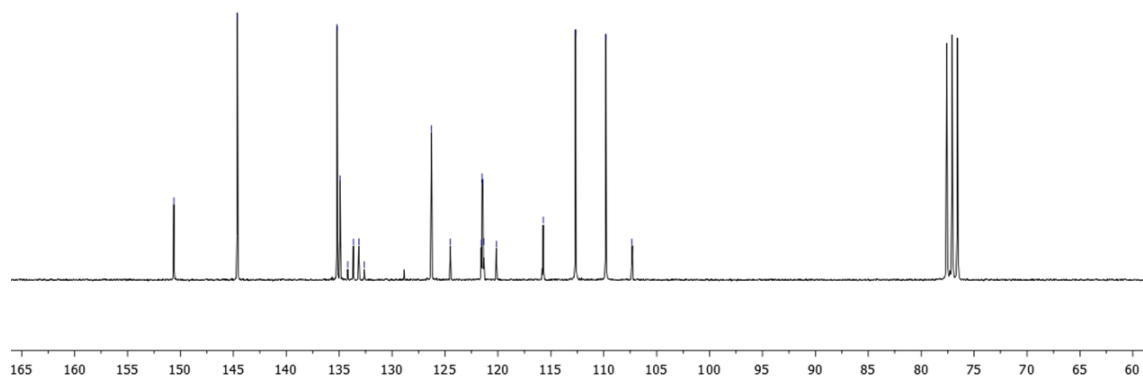
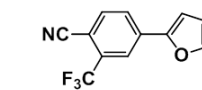
**b8- <sup>1</sup>H NMR**



wanglei.327.1.1r  
4-I-2-CF<sub>3</sub>-CNPh

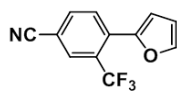
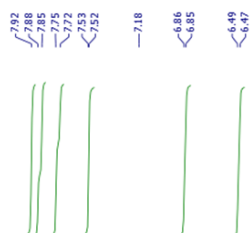


**b8- <sup>13</sup>C NMR**

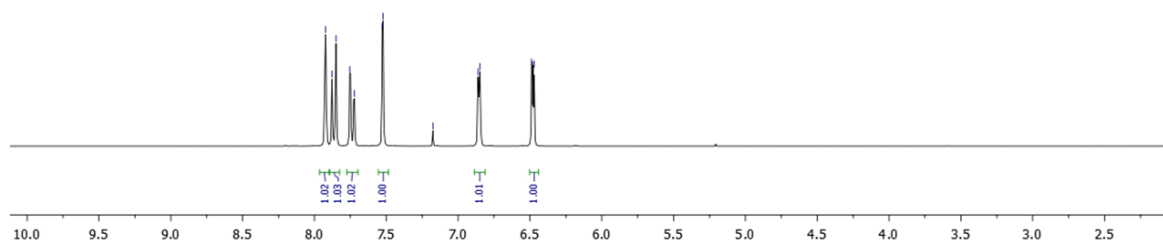


# Experiment Section

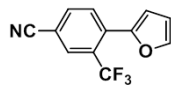
wanglei.2100.1.1r  
4-1-3-CF<sub>3</sub>-CNPh



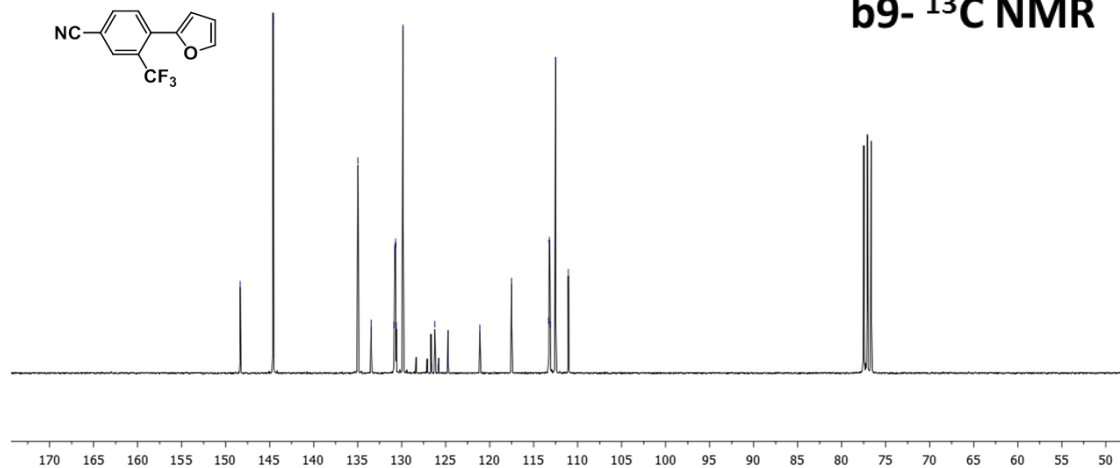
**b9- <sup>1</sup>H NMR**



wanglei.2101.1.1r  
4-1-3-CF<sub>3</sub>-CNPh



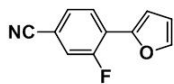
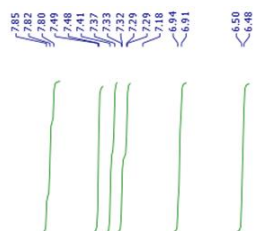
**b9- <sup>13</sup>C NMR**



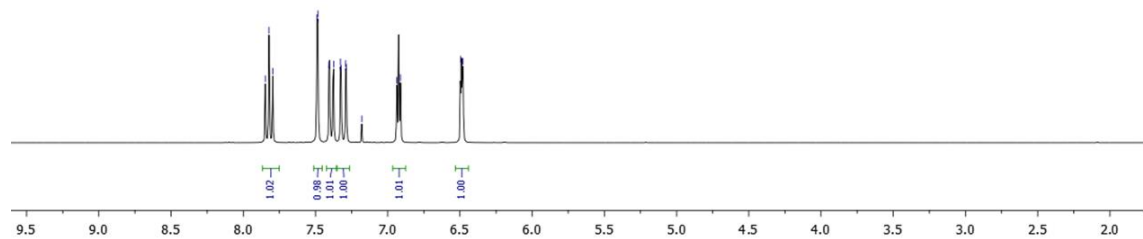


## Experiment Section

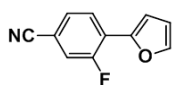
wanglei.2090.1.1r  
4-1-2-F-CNPh



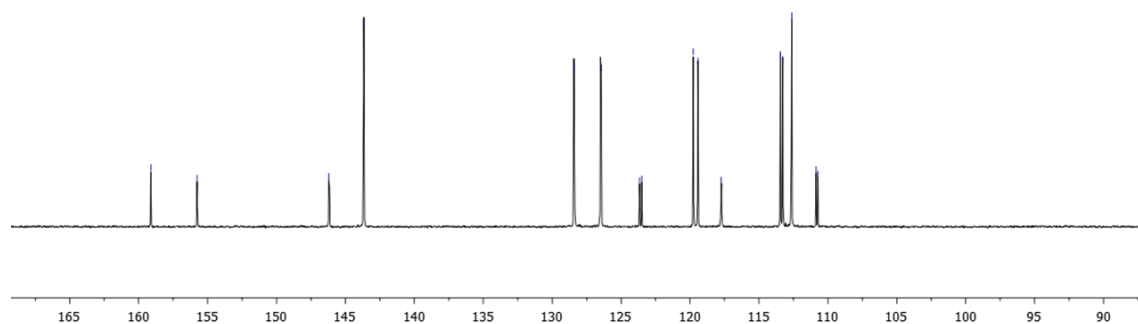
**b10-  $^1\text{H}$  NMR**



wanglei.2091.1.1r  
4-1-2-F-CNPh

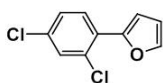
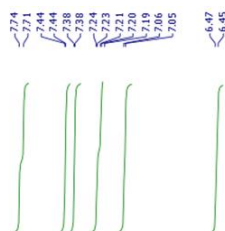


**b10-  $^{13}\text{C}$  NMR**

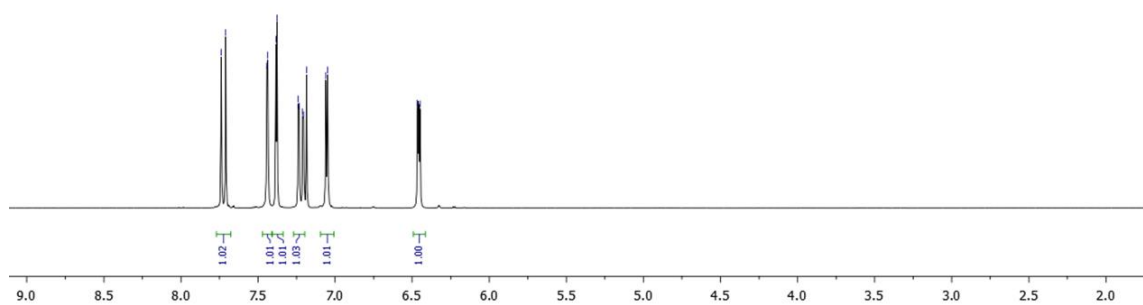


# Experiment Section

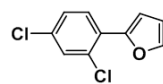
wanglei.2080.1.1r  
2,4-DiCl-1-I-Ph



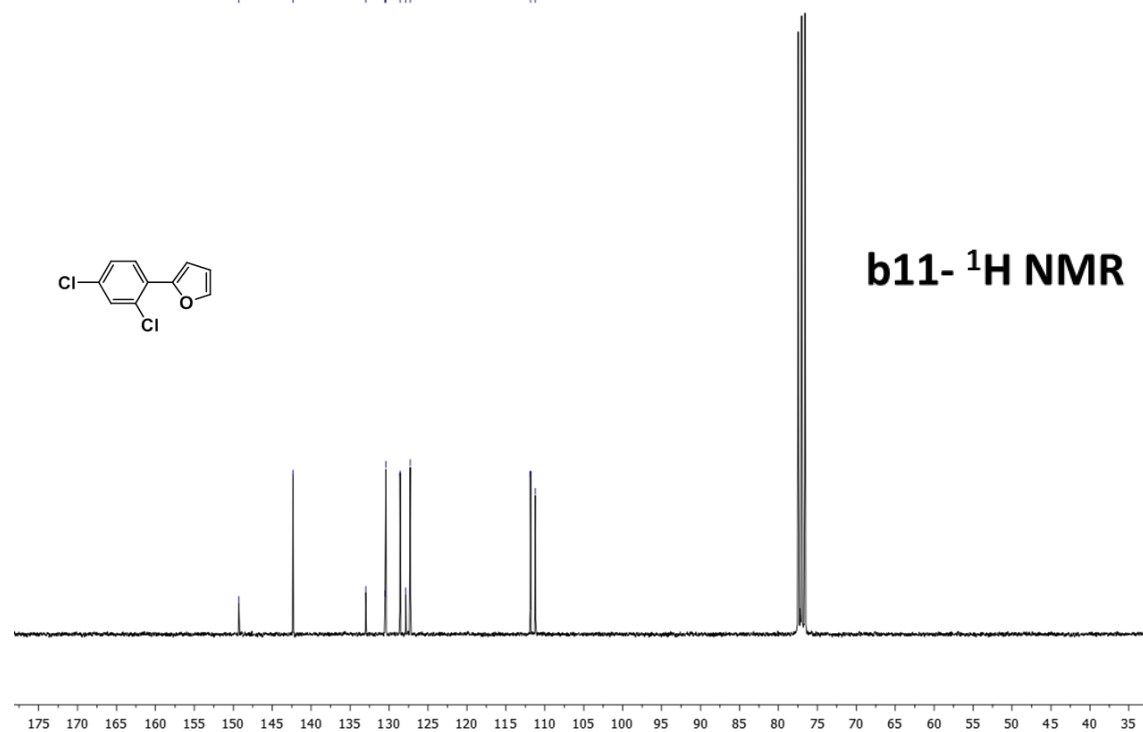
**b11- <sup>1</sup>H NMR**



wanglei.2081.1.1r  
2,4-DiCl-1-I-Ph

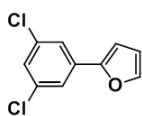
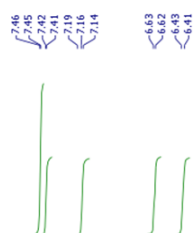


**b11- <sup>1</sup>H NMR**

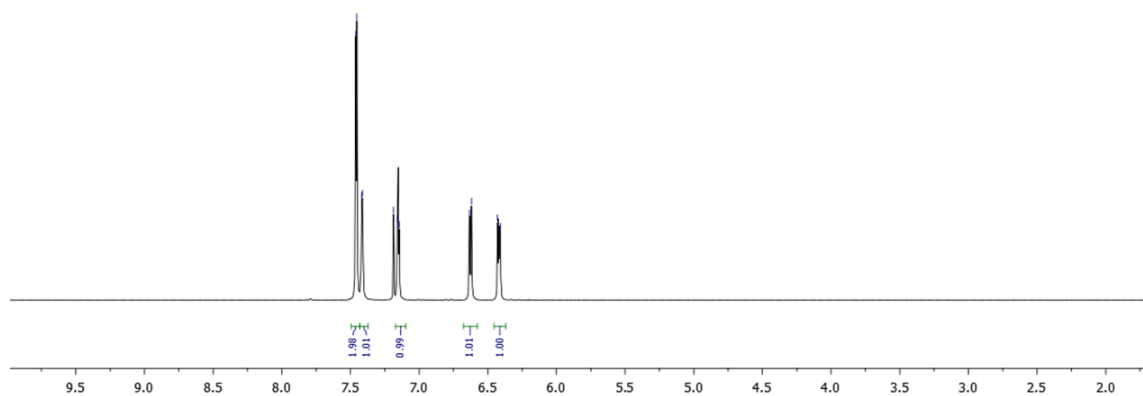


# Experiment Section

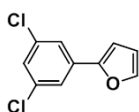
wanglei.340.1.1r  
3,5-DiCl-1-IPh



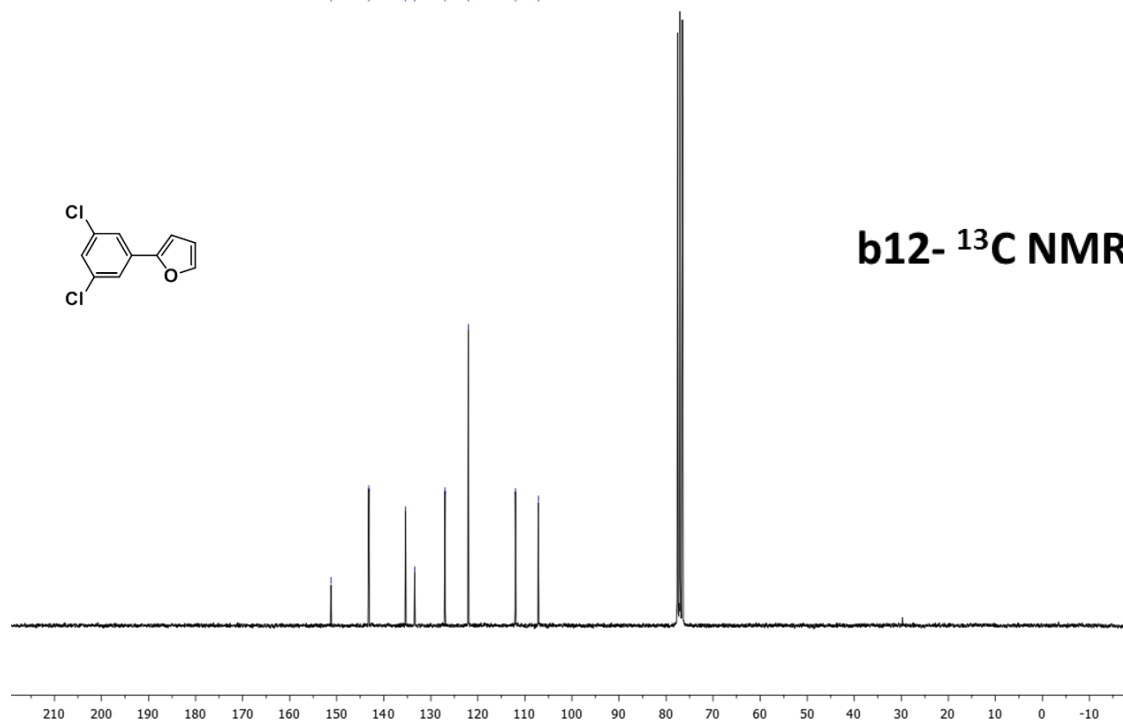
**b12- <sup>1</sup>H NMR**



wanglei.341.1.1r  
3,5-DiCl-1-IPh

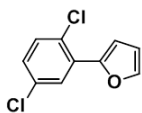
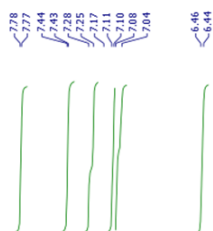


**b12- <sup>13</sup>C NMR**

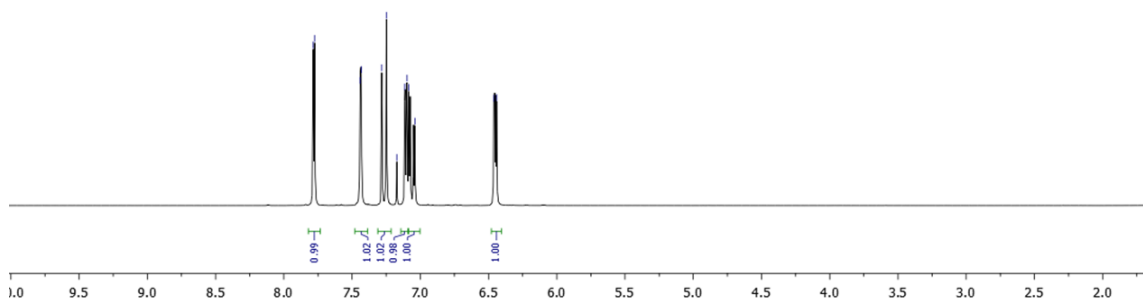


# Experiment Section

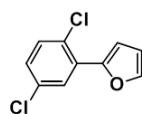
wanglei.321.1.1r



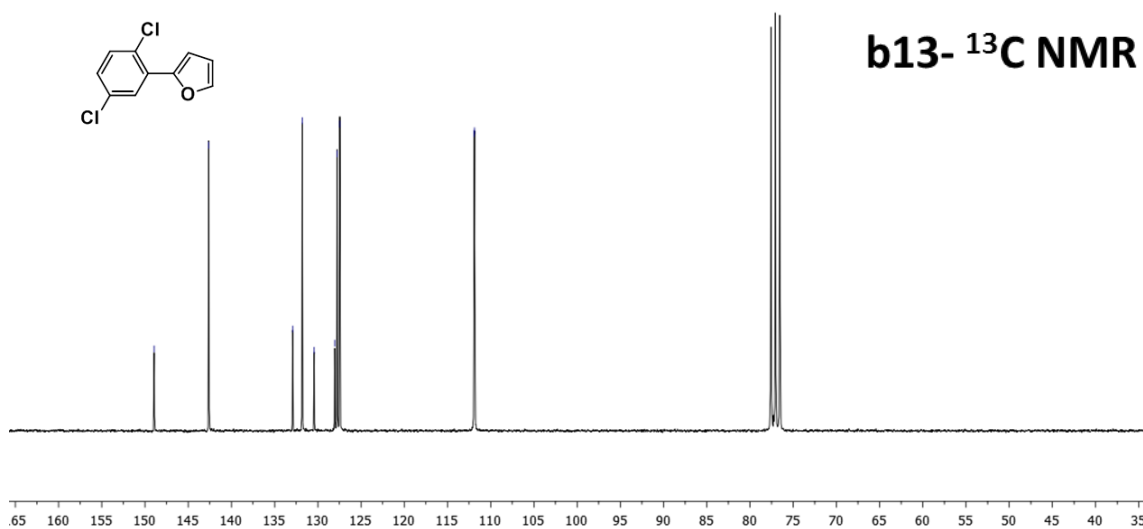
**b13- <sup>1</sup>H NMR**



wanglei.322.1.1r  
1,4-DiCl-2-1-Ph

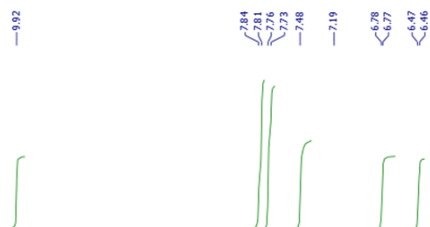


**b13- <sup>13</sup>C NMR**

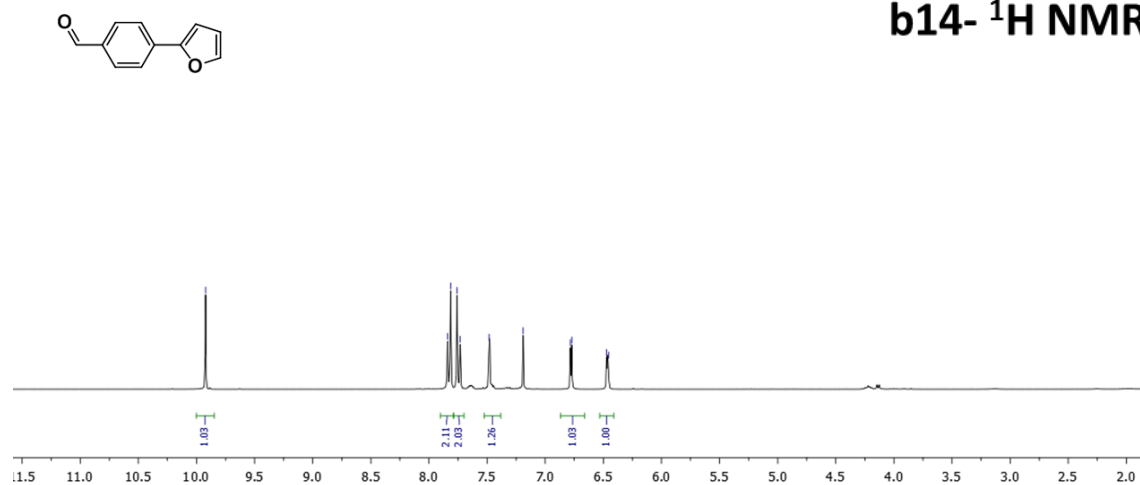


## Experiment Section

wanglei.2000.1.1r  
CHOPH1



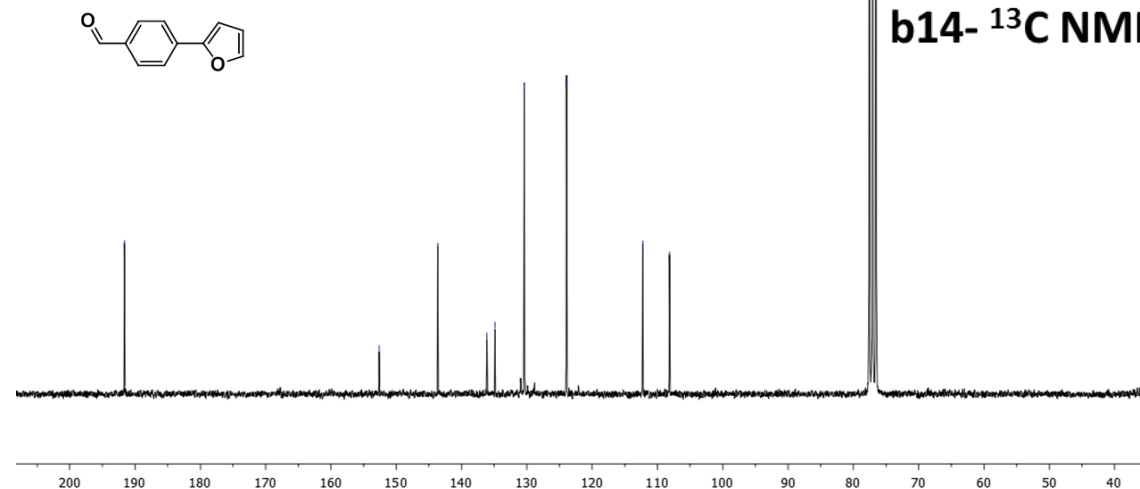
**b14-  $^1\text{H}$  NMR**



wanglei.300.1.1r  
CHOPH1

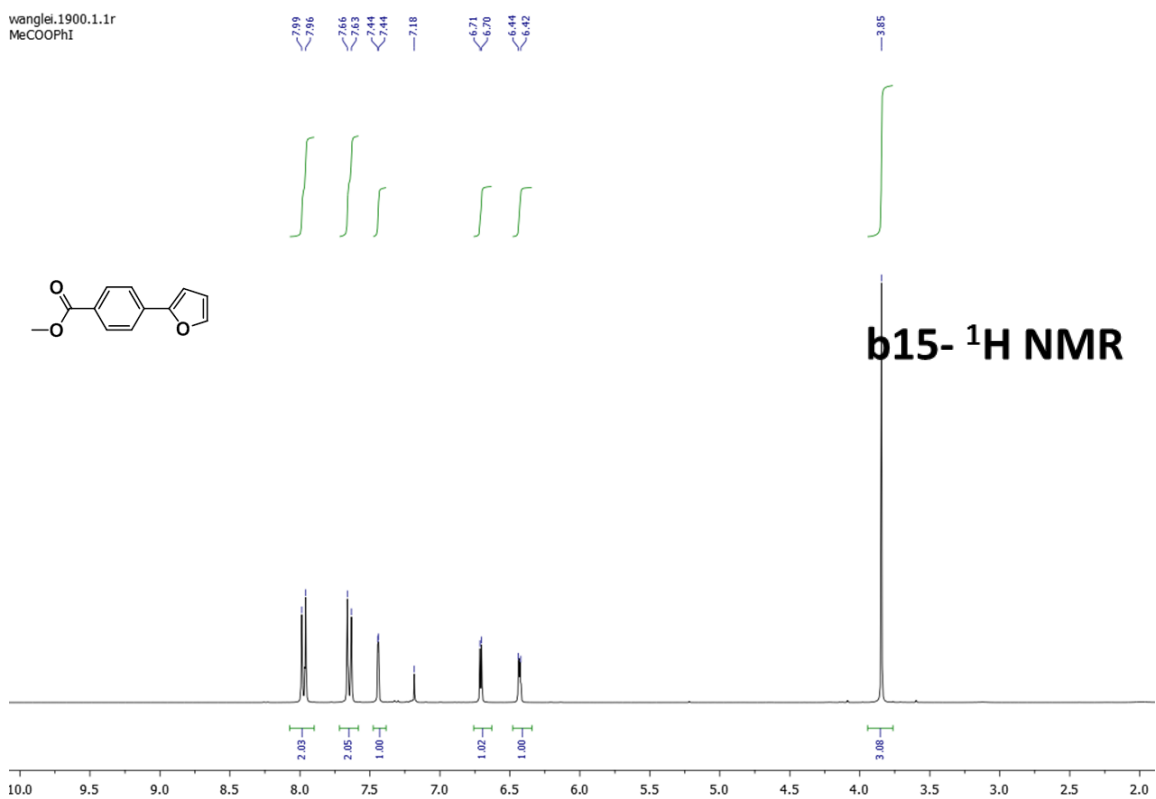


**b14-  $^{13}\text{C}$  NMR**

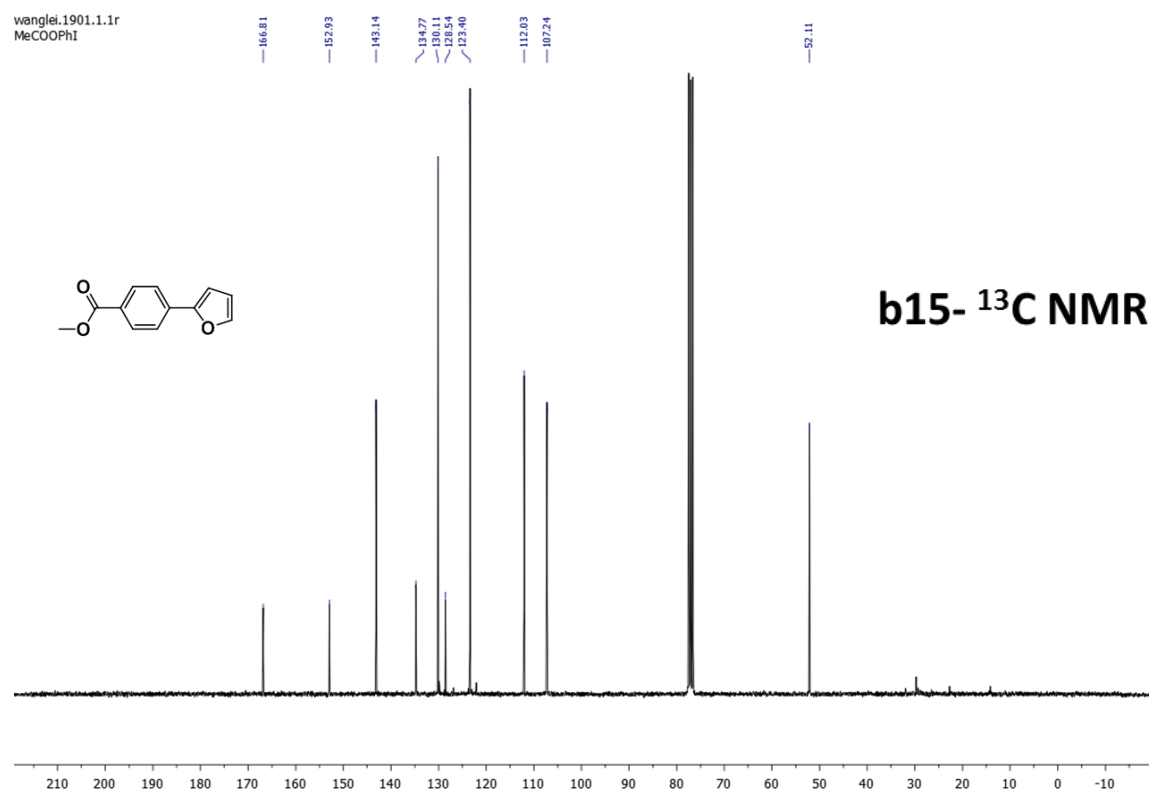


# Experiment Section

wanglei.1900.1.1r  
MeCOOPhI

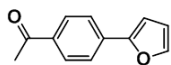
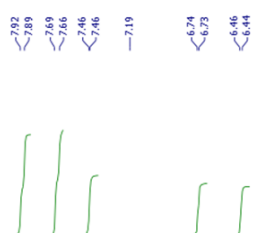


wanglei.1901.1.1r  
MeCOOPhI

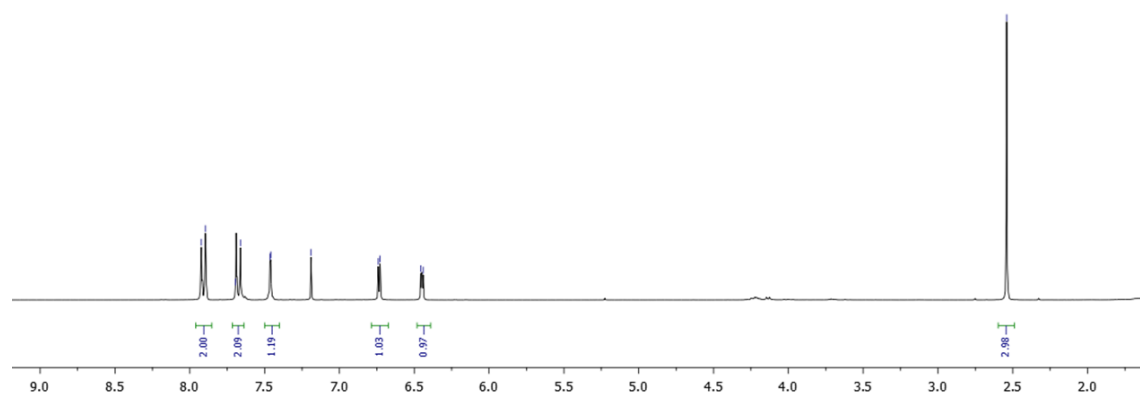


# Experiment Section

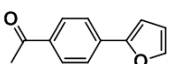
wanglei.1911.1.1r  
MeCOPhI



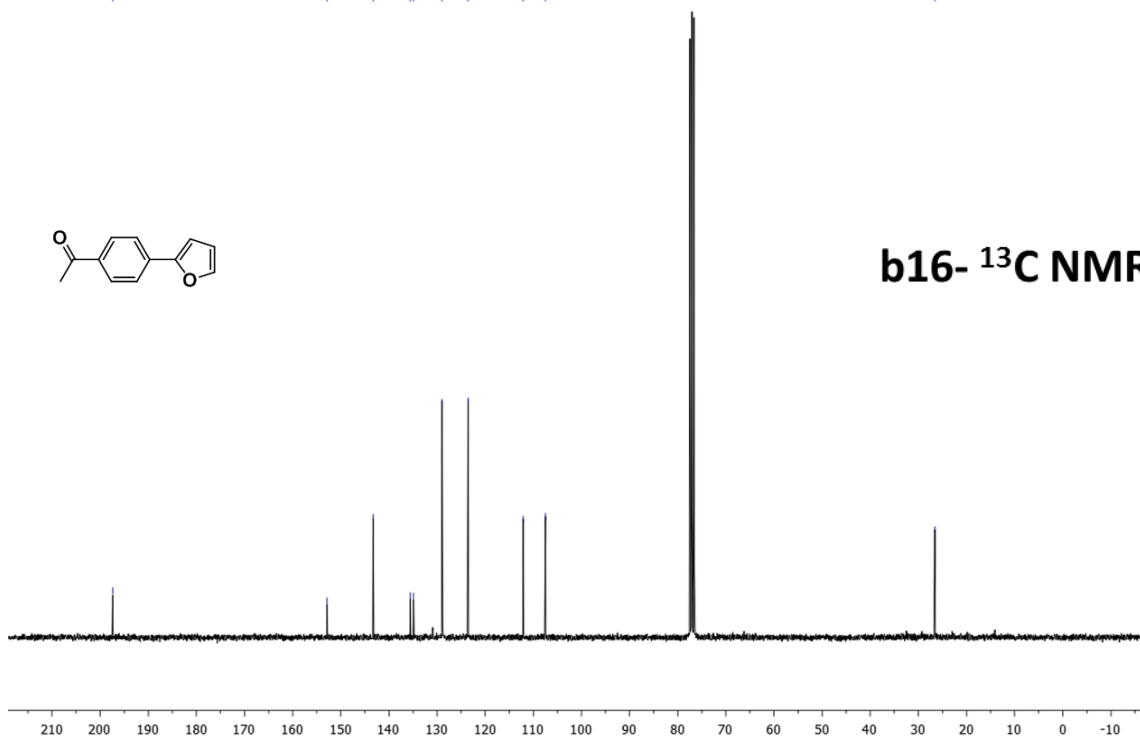
**b16-  $^1\text{H}$  NMR**



wanglei.1910.1.1e  
MeCOPhI

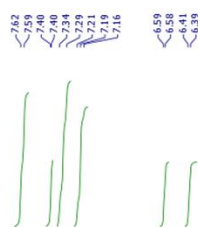
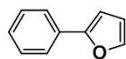


**b16-  $^{13}\text{C}$  NMR**

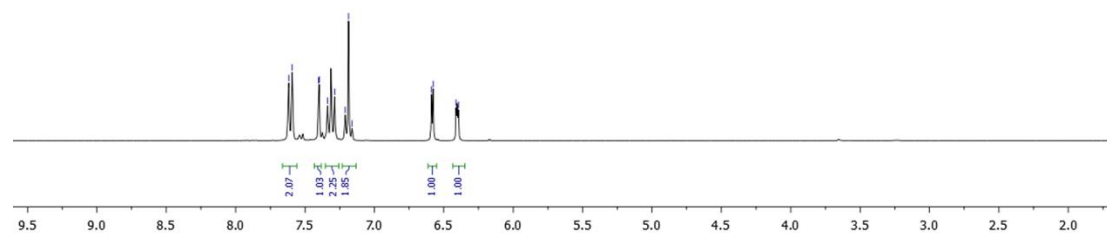


# Experiment Section

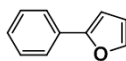
wanglei.1920.1.1r  
PhI



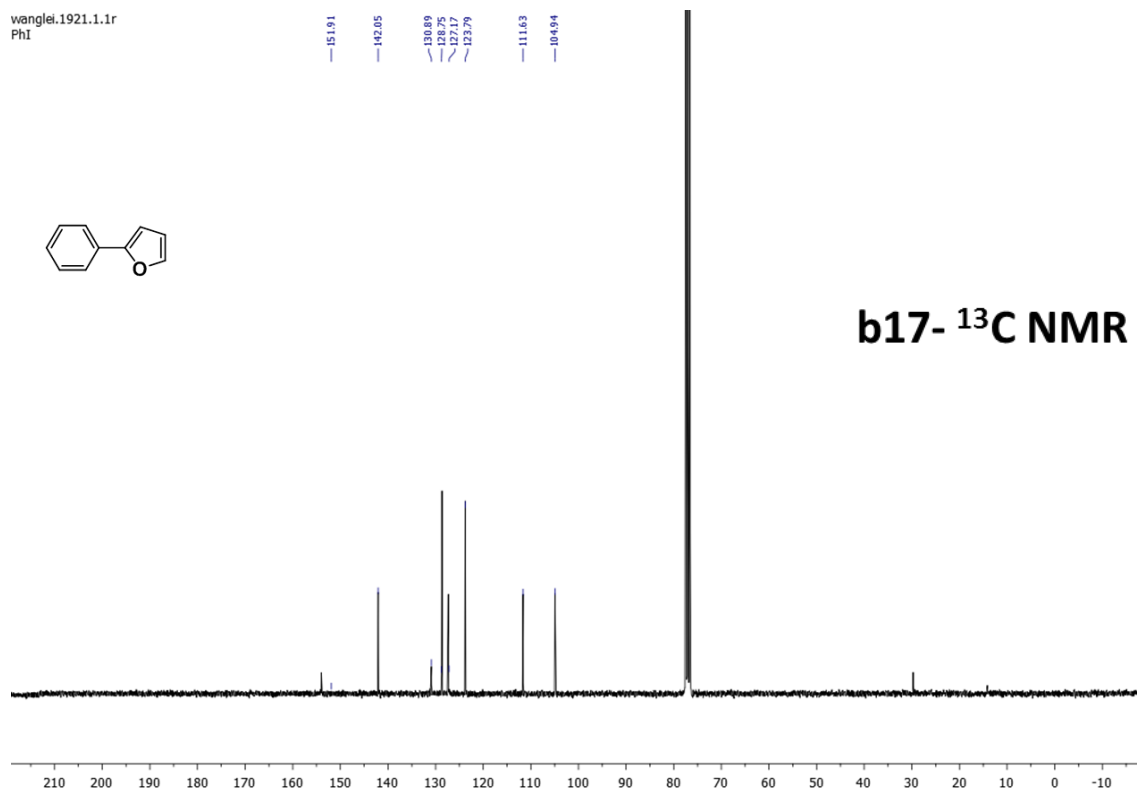
**b17-  $^1\text{H}$  NMR**



wanglei.1921.1.1r  
PhI



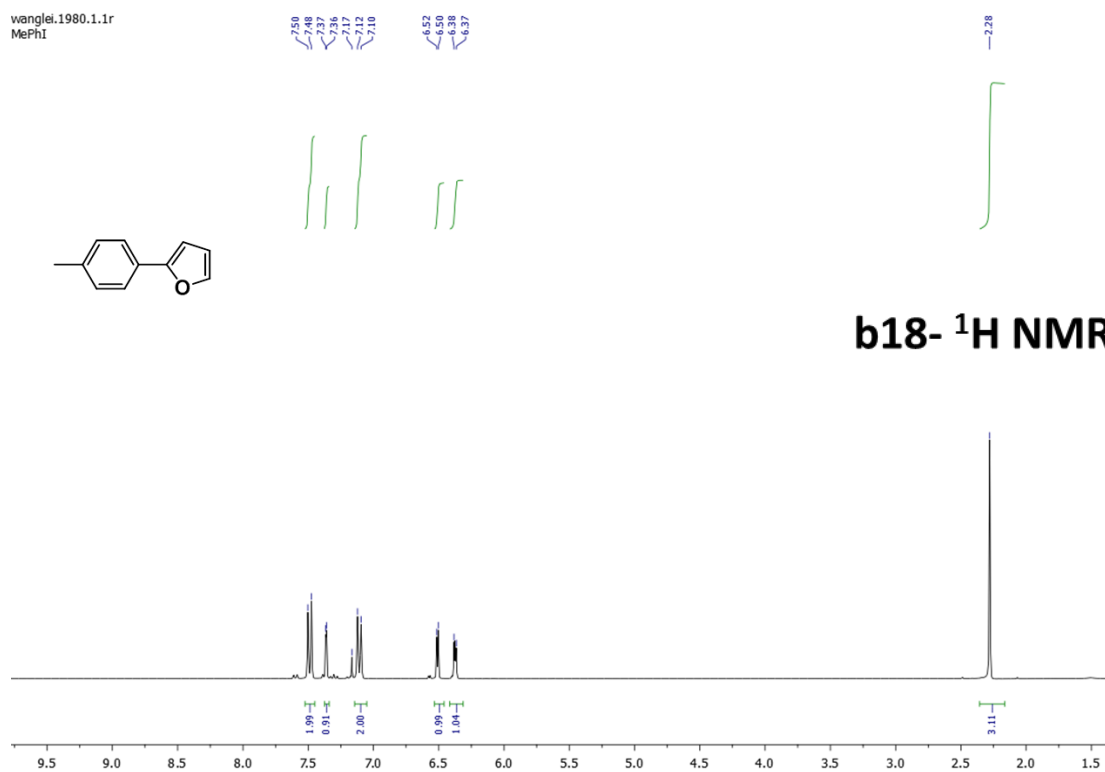
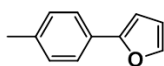
**b17-  $^{13}\text{C}$  NMR**



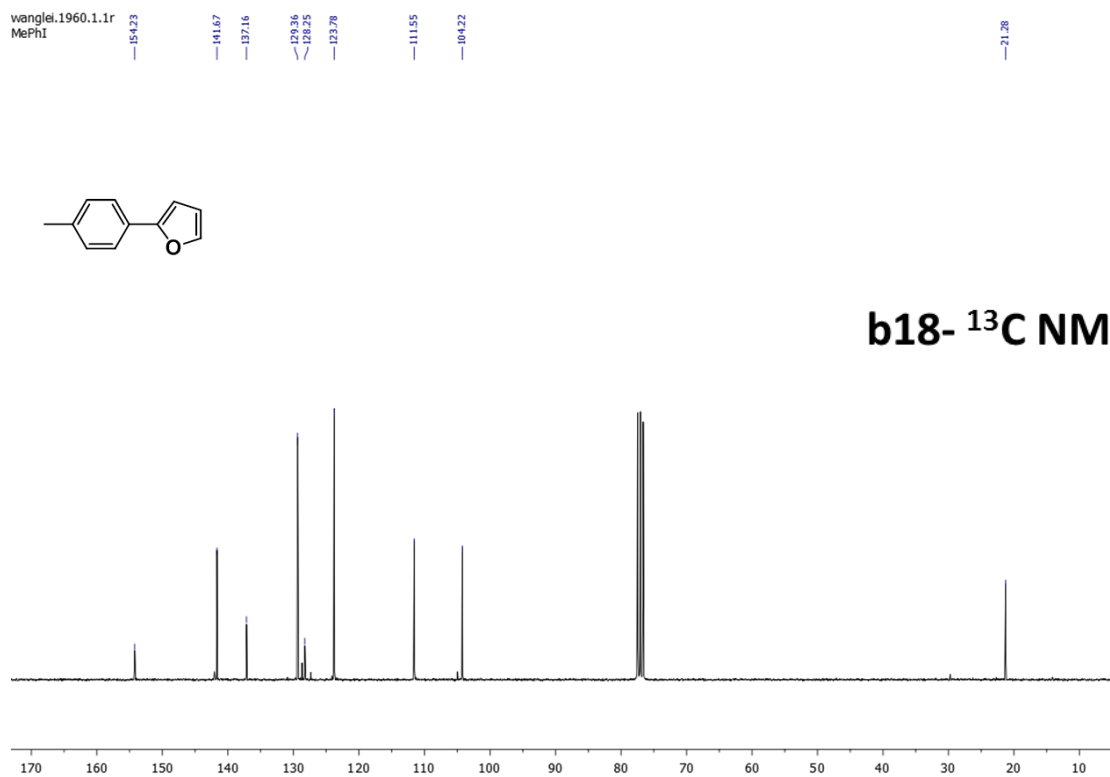
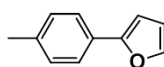


# Experiment Section

wanglei.1980.1.1r  
MePhI

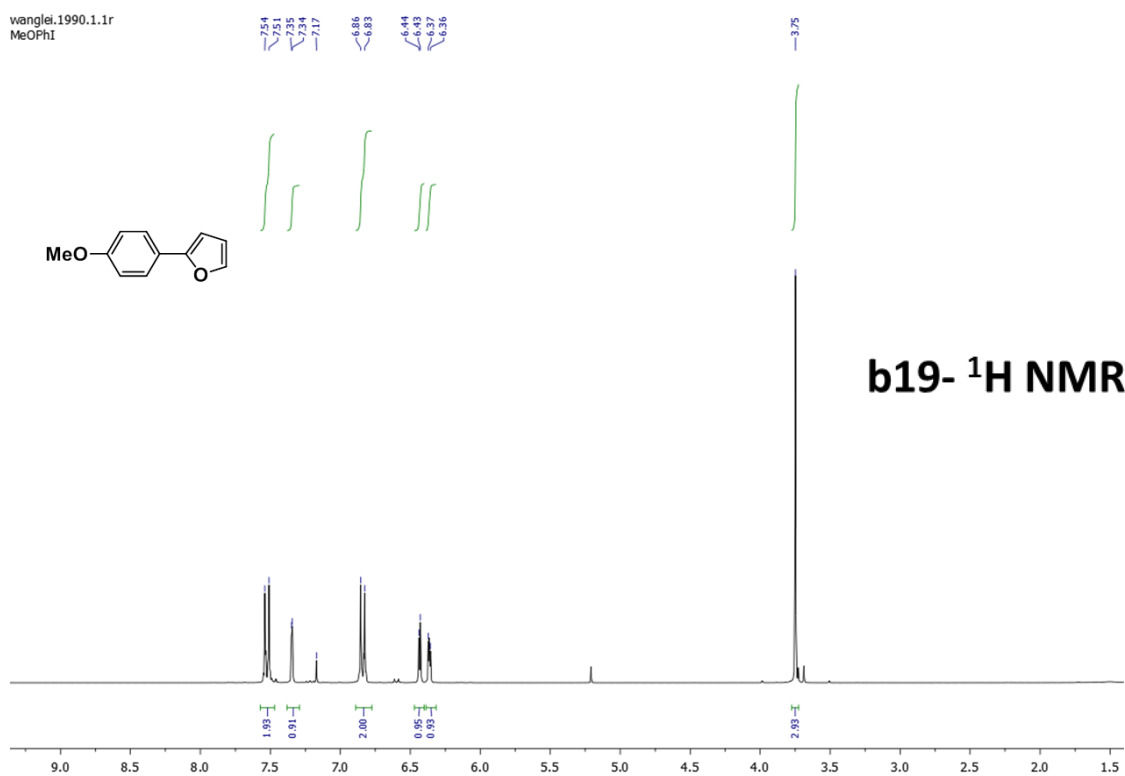


wanglei.1960.1.1r  
MePhI

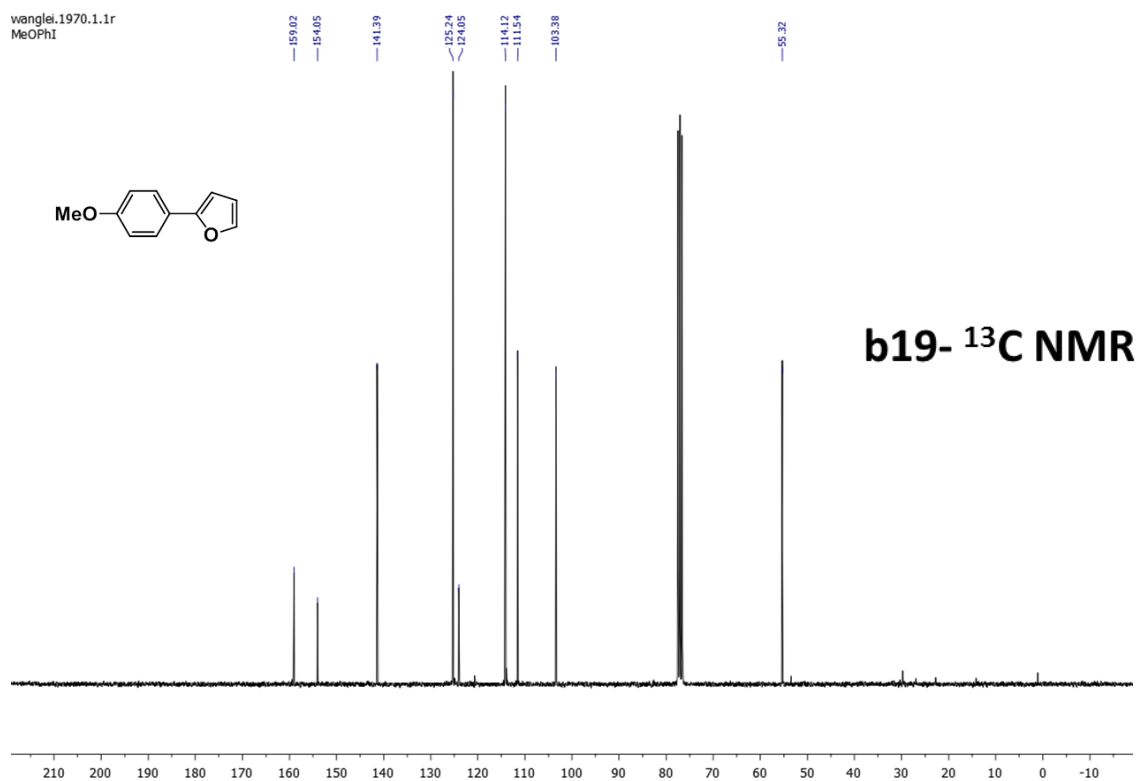


# Experiment Section

wanglei.1990.1.1r  
MeOPhI

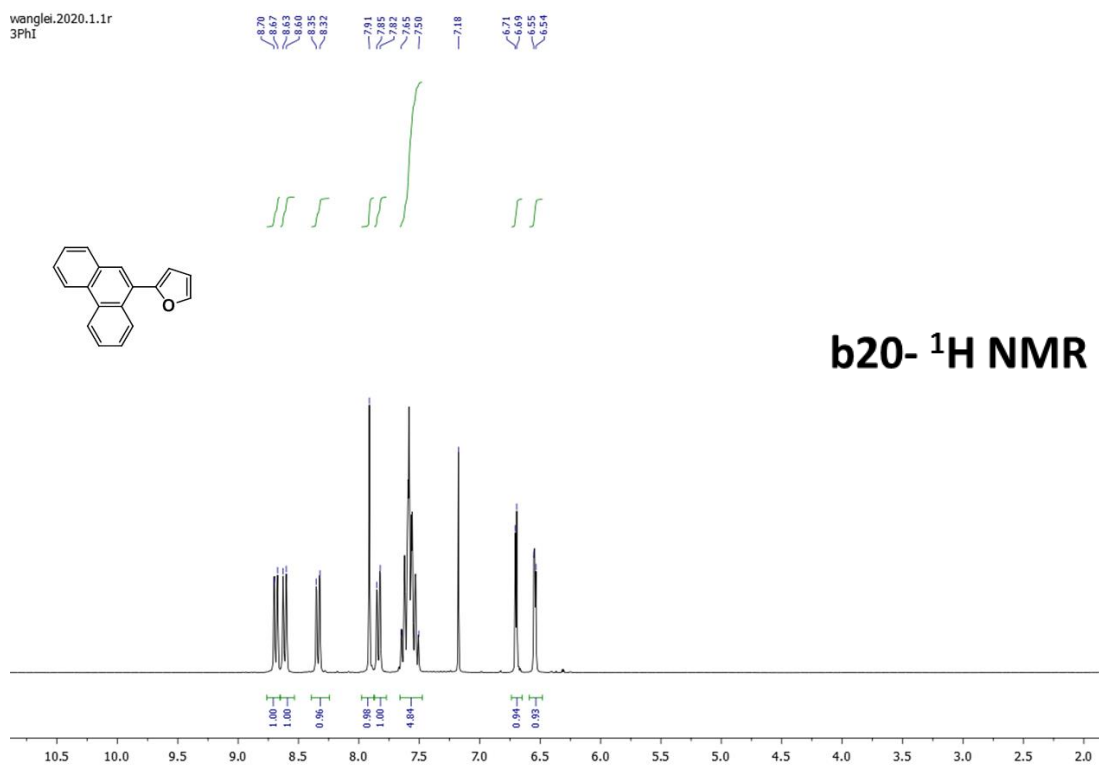
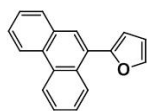


wanglei.1970.1.1r  
MeOPhI

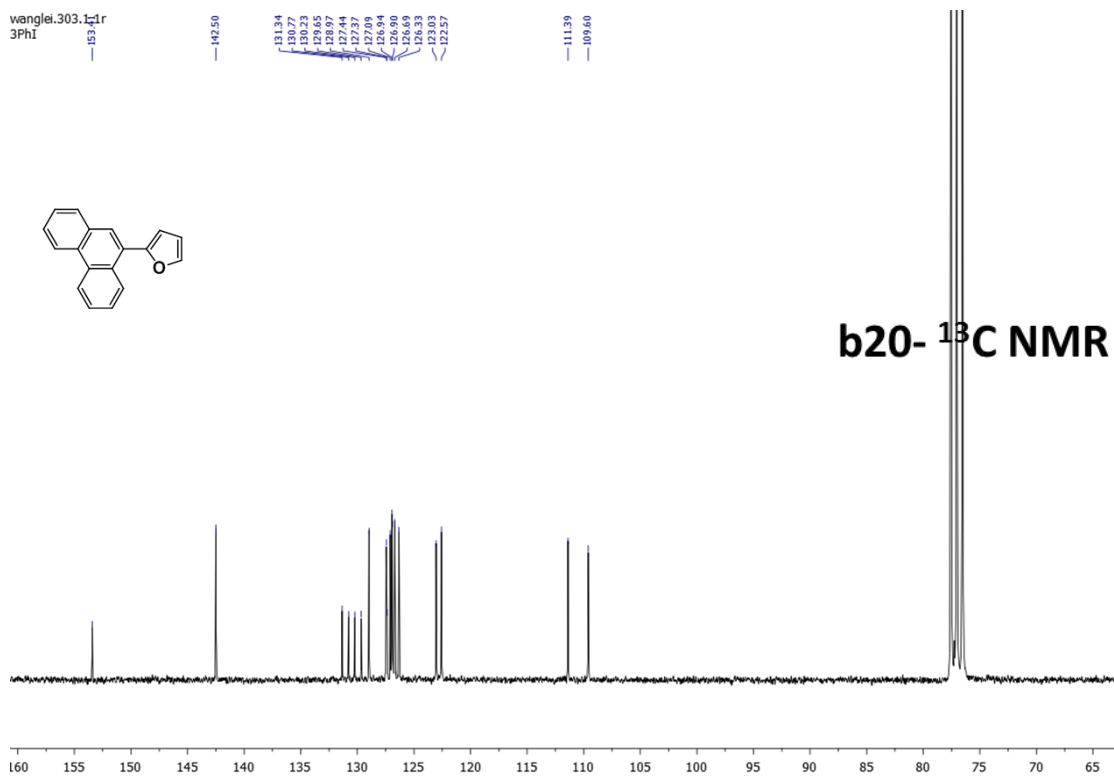
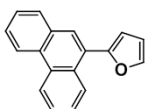


# Experiment Section

wanglei.2020.1.1r  
3Phi



wanglei.303.1.1r  
3Phi



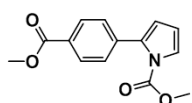
# Experiment Section

wanglei.2110.1.1r  
NAcPyrrole

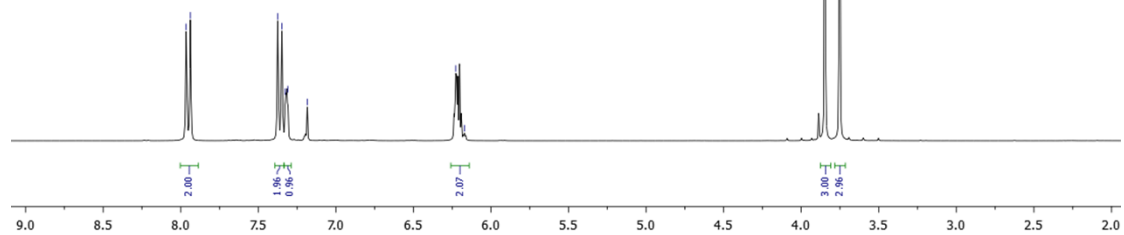
7.86  
7.84  
7.37  
7.35  
7.31  
7.18

6.33  
6.17

3.85  
3.75



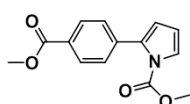
**b21- <sup>1</sup>H NMR**



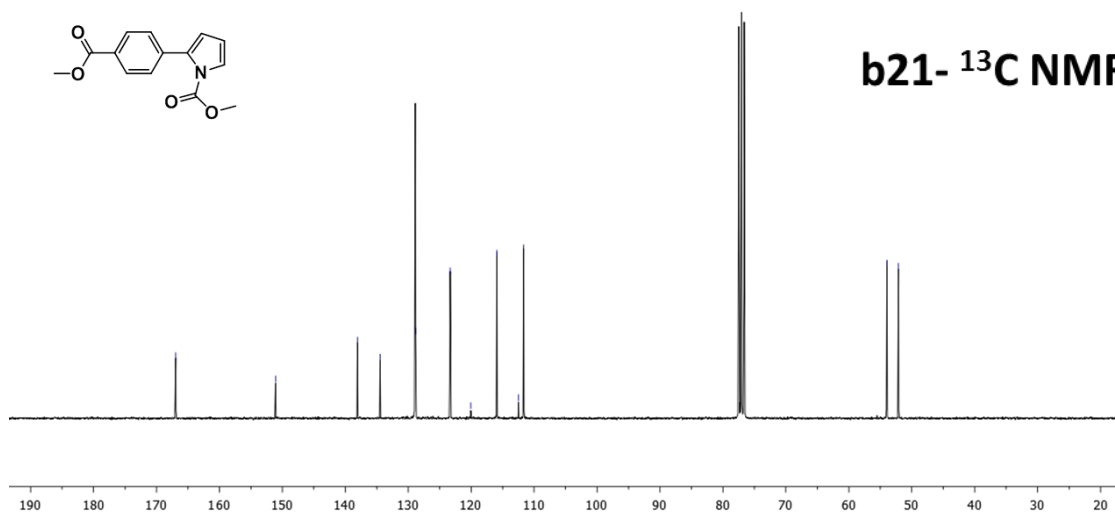
wanglei.2111.1.1r  
NAcPyrrole

166.95  
151.09  
138.07  
134.48  
128.83  
123.33  
120.07  
115.92  
112.47  
111.66

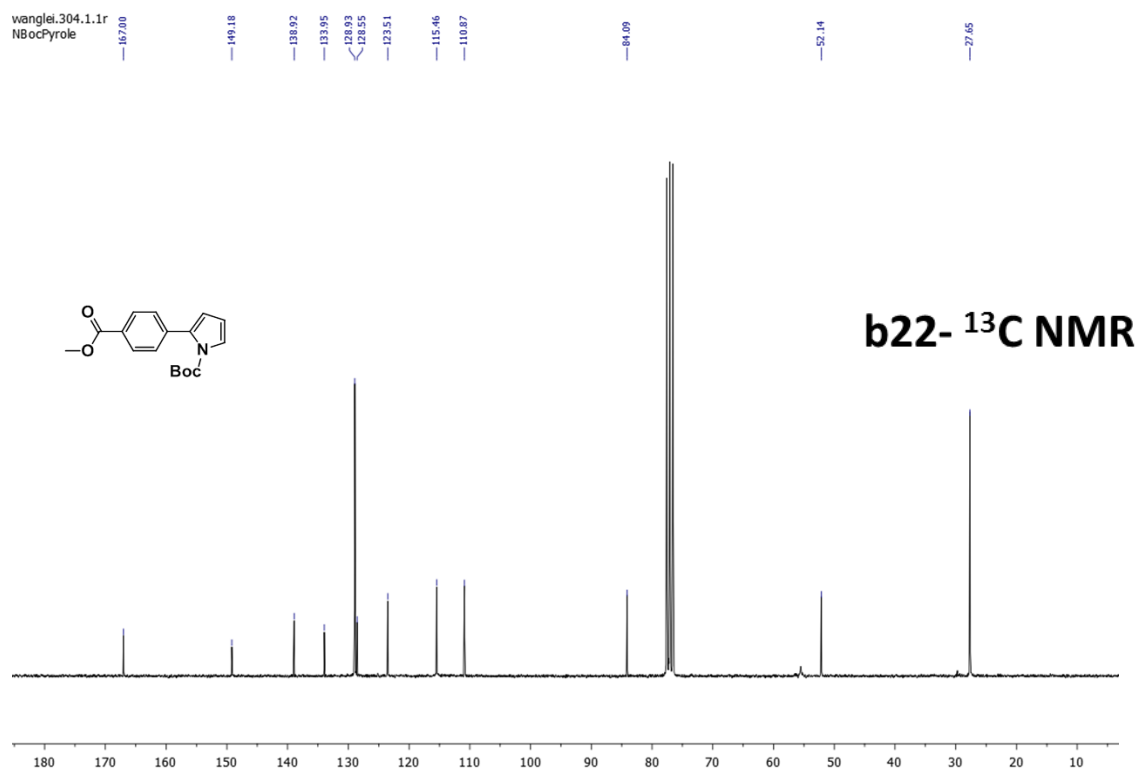
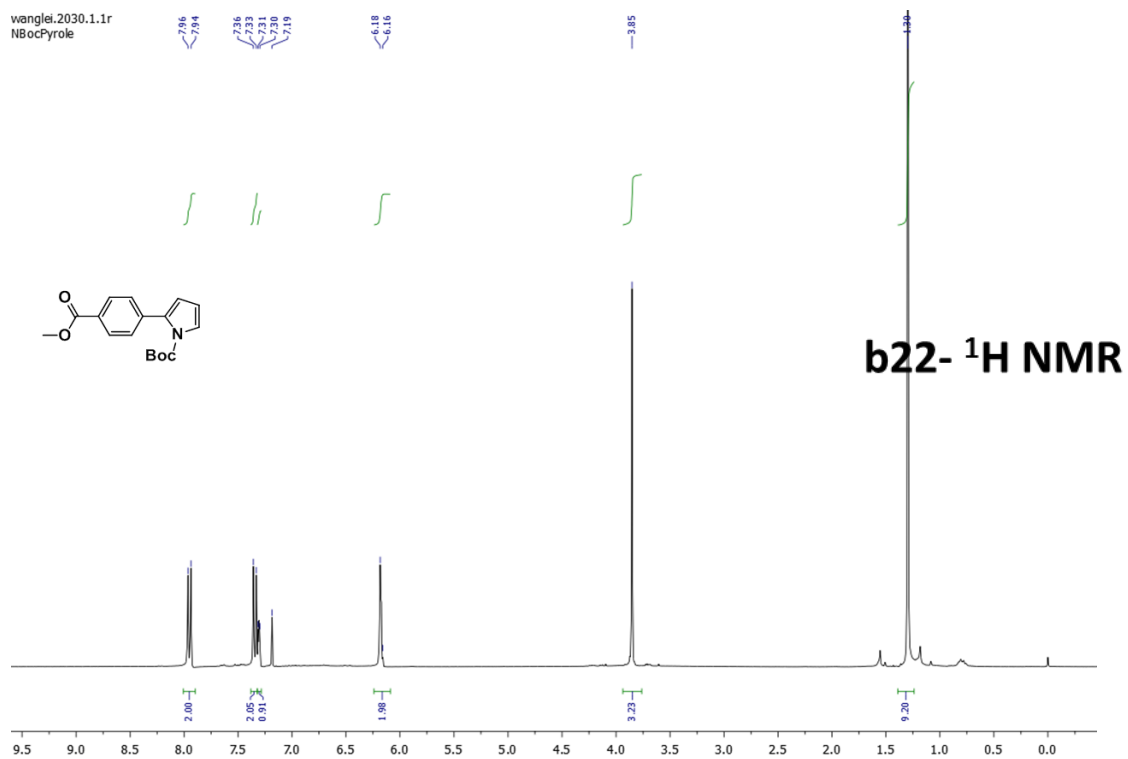
53.94  
52.11



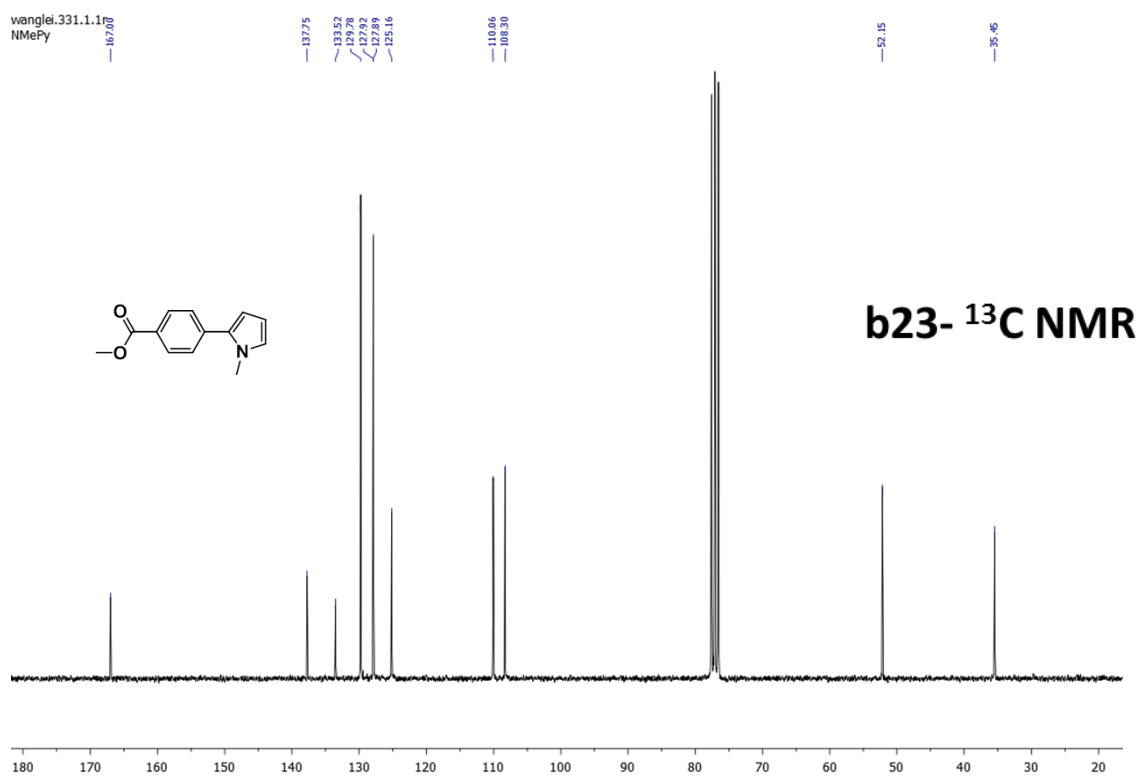
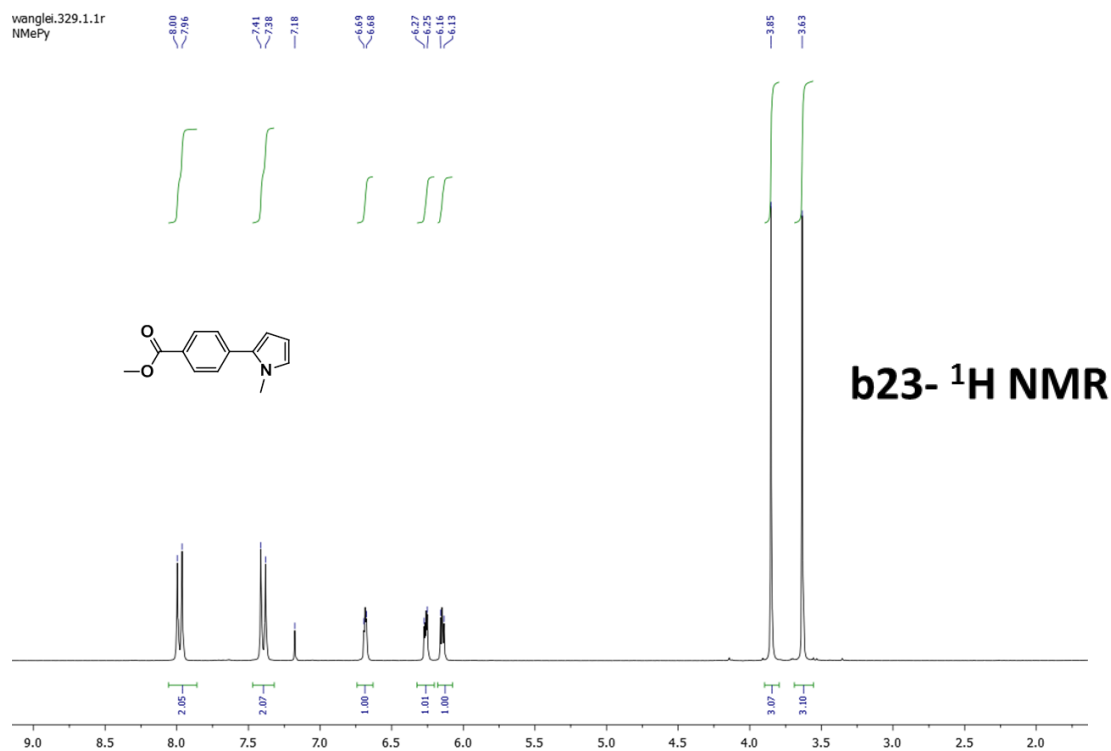
**b21- <sup>13</sup>C NMR**



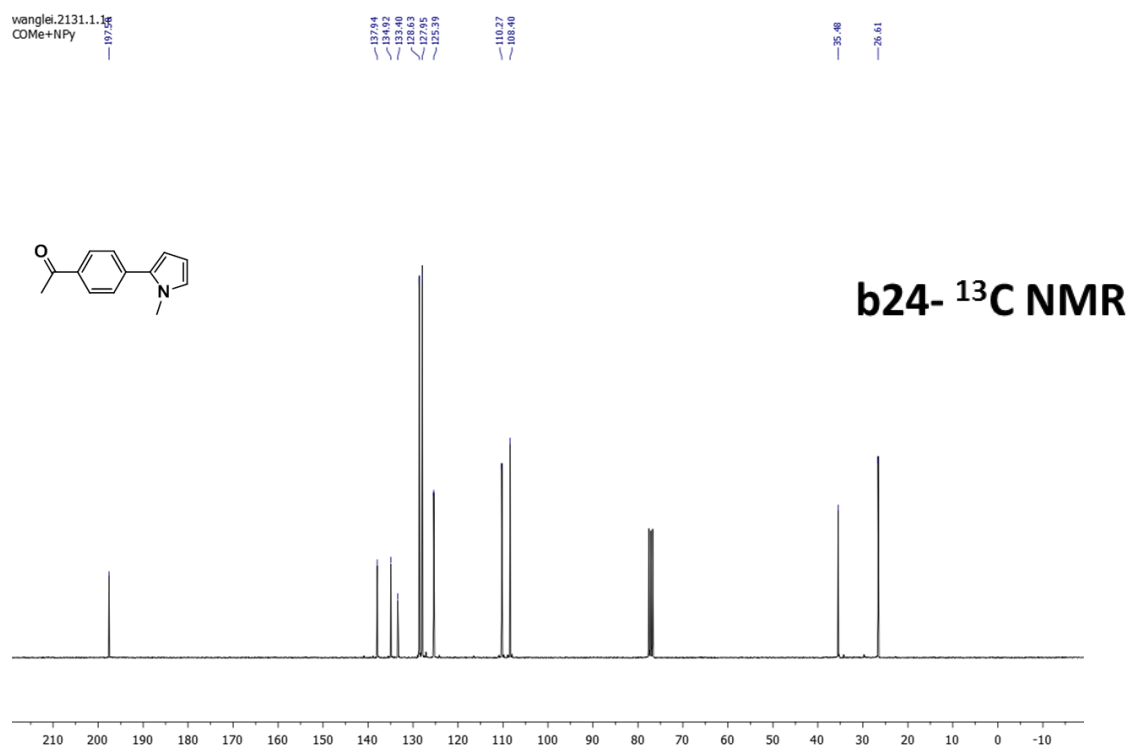
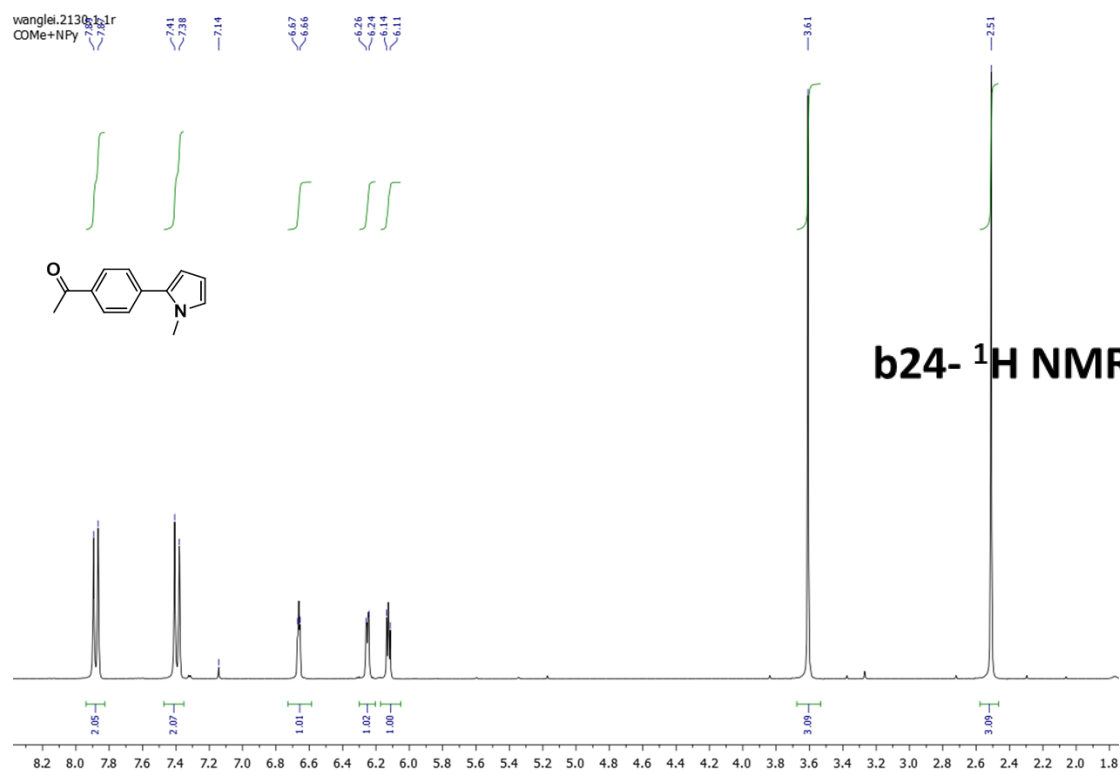
# Experiment Section



# Experiment Section

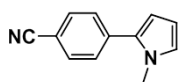
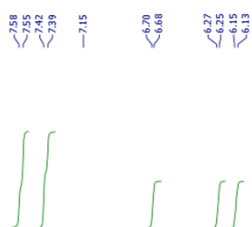


# Experiment Section



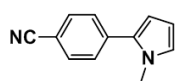
# Experiment Section

wanglei.2140.1.1r  
CN+NPy



**b25- <sup>1</sup>H NMR**

wanglei.2141.1.1r  
CN+NPy

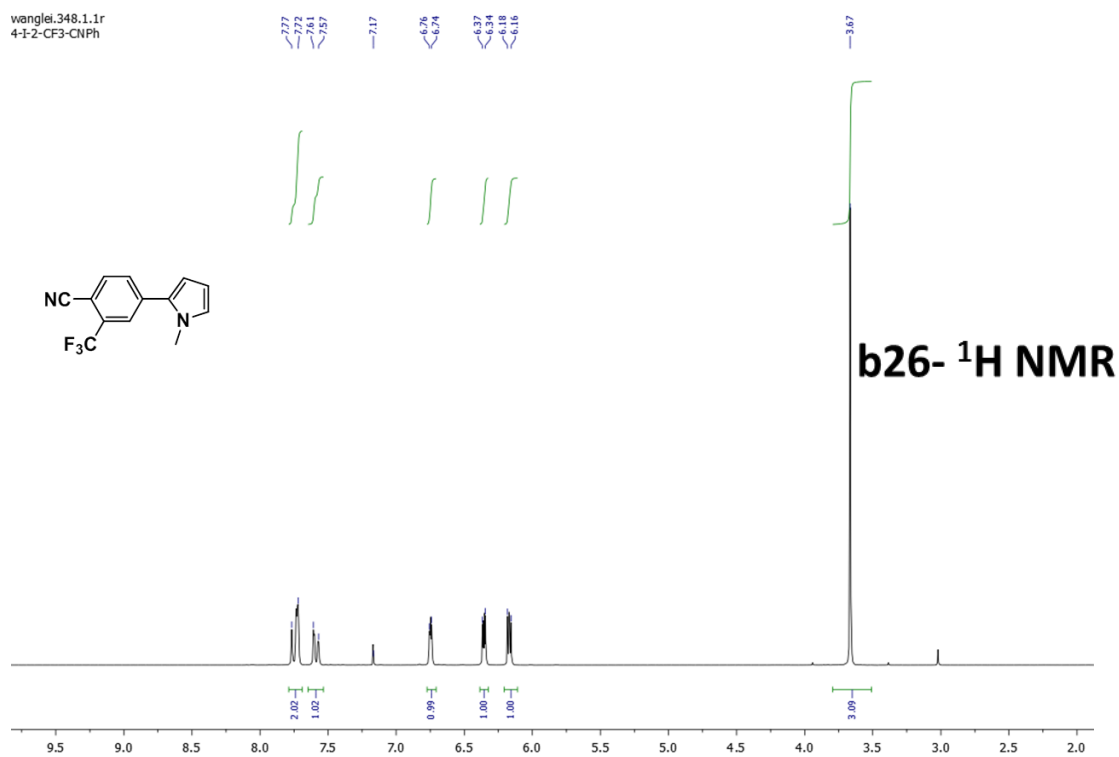
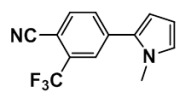


**b25- <sup>13</sup>C NMR**

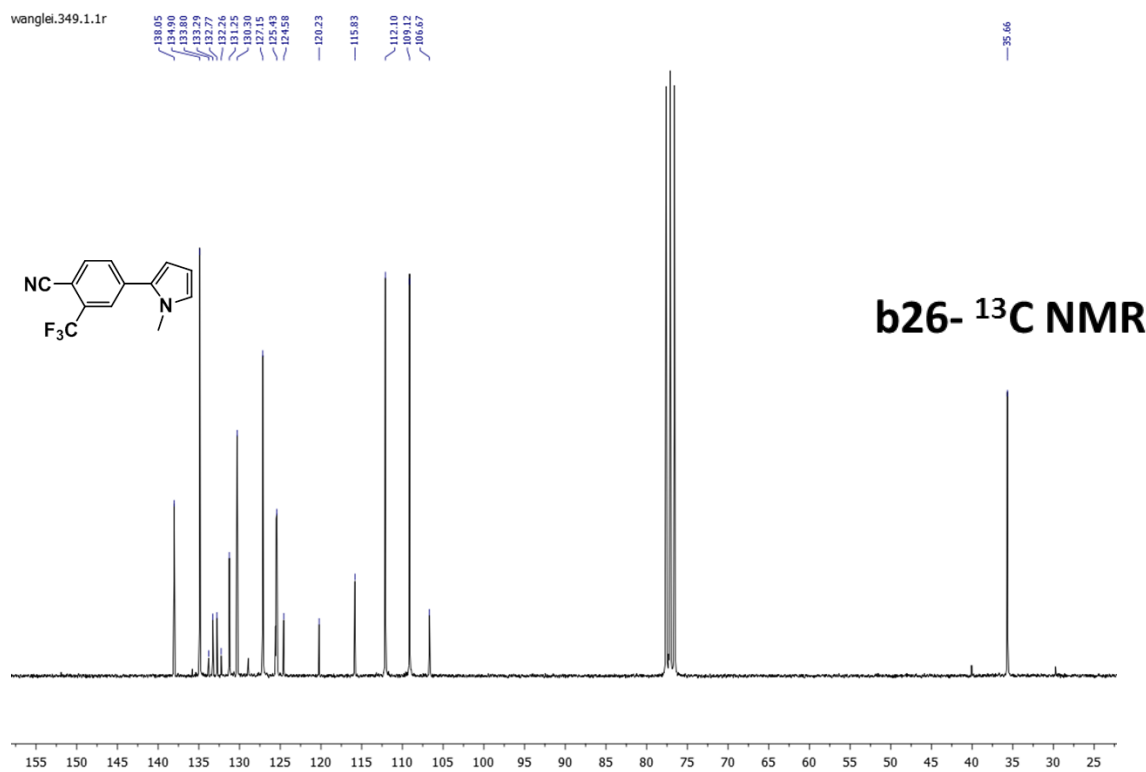
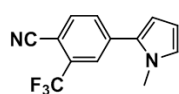


# Experiment Section

wanglei.348.1.1r  
4-(2-CF<sub>3</sub>-CNPh)



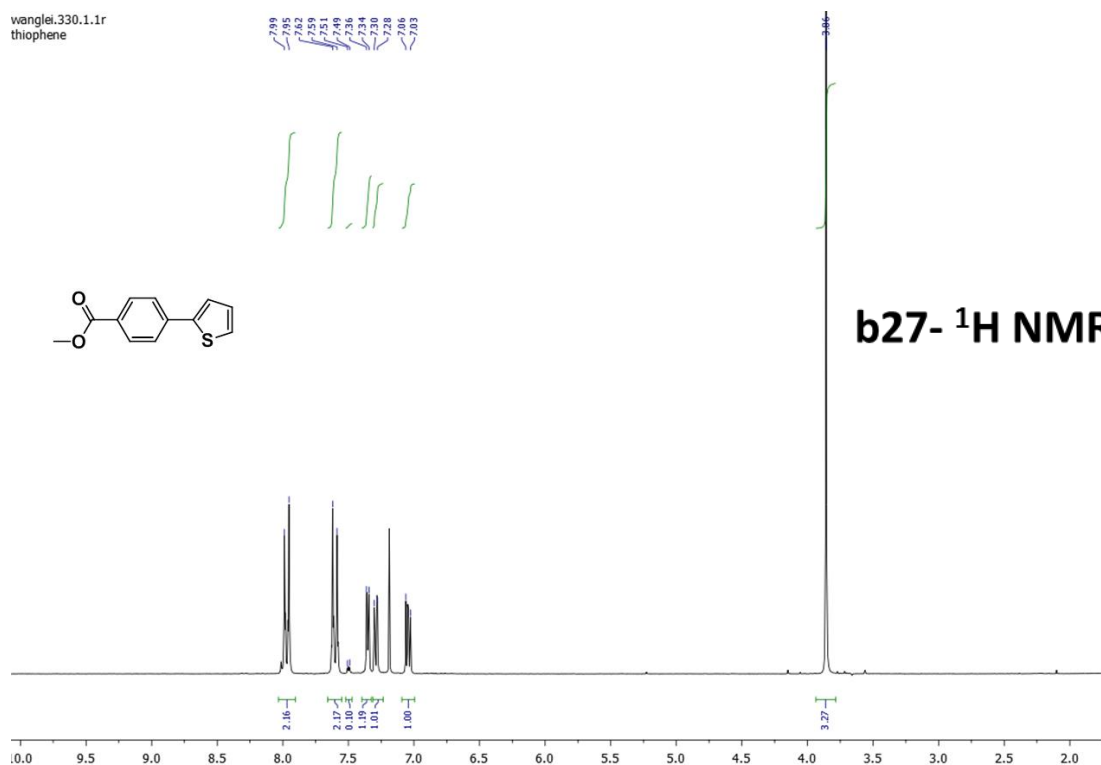
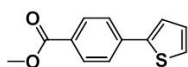
wanglei.349.1.1r



# Experiment Section

wanglei.330.1.1r  
thiophene

7.79  
7.78  
7.75  
7.59  
7.51  
7.36  
7.34  
7.30  
7.28  
7.26  
7.23



wanglei.332.1.1r  
thiophene

166.79

143.08

138.64

130.30

128.57

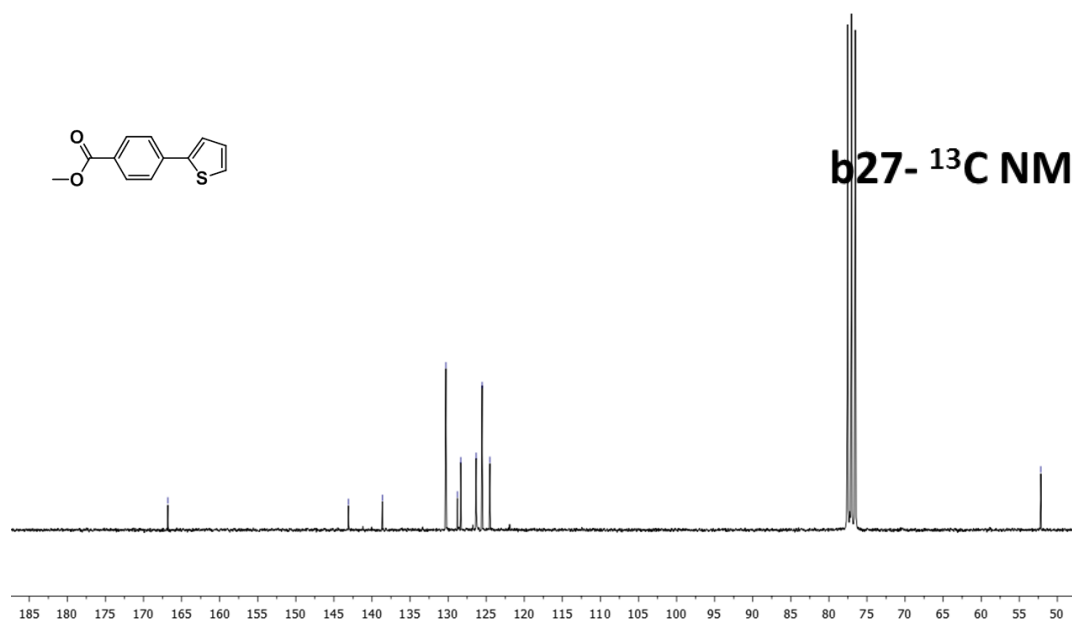
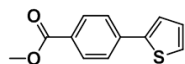
126.35

126.32

125.53

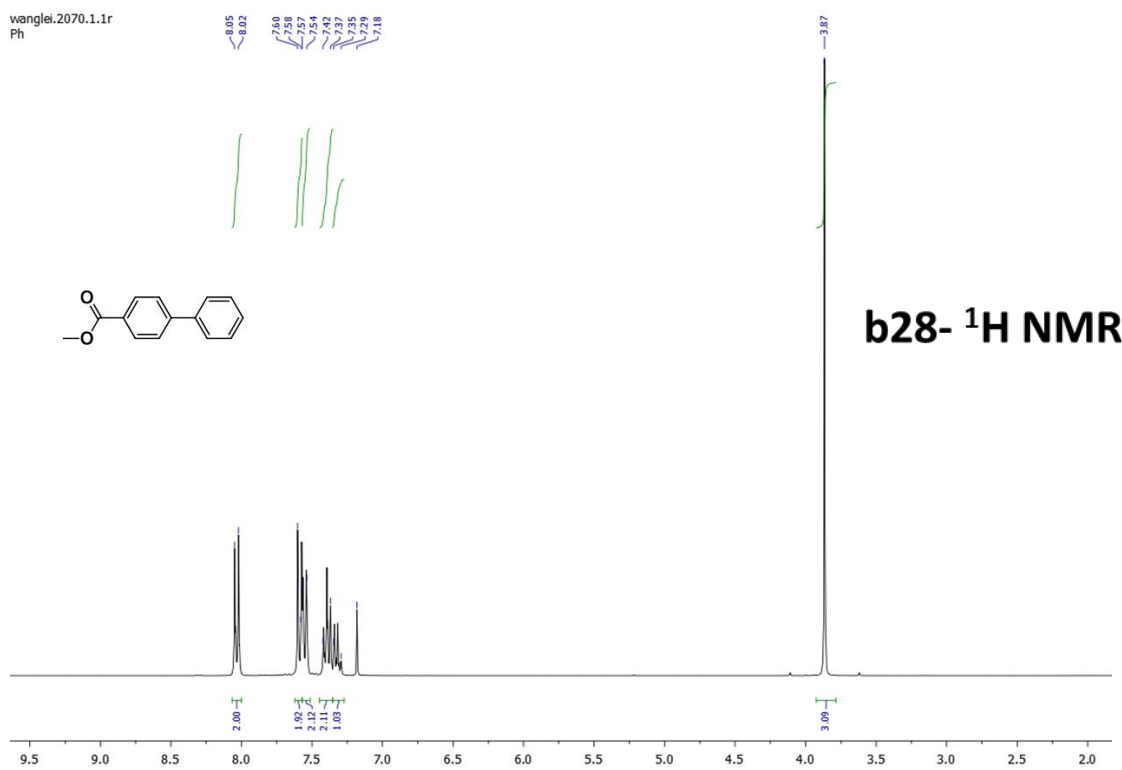
124.51

52.18

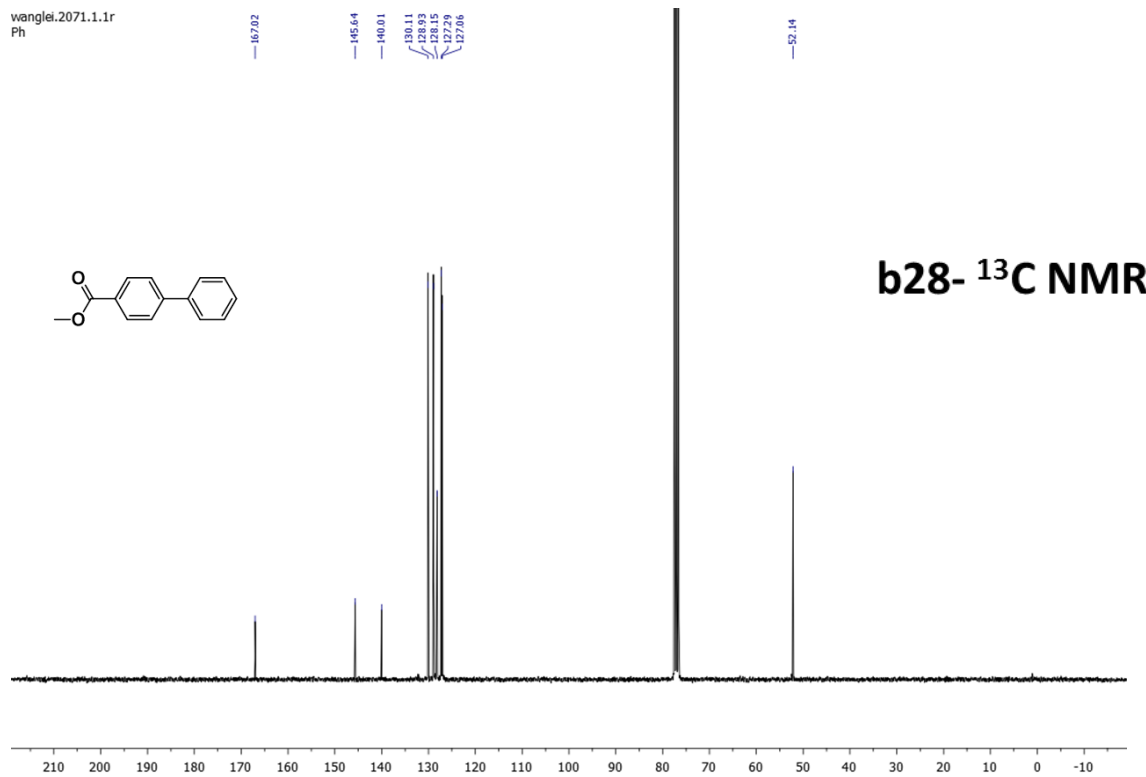


# Experiment Section

wanglei.2070.1.1r  
Ph

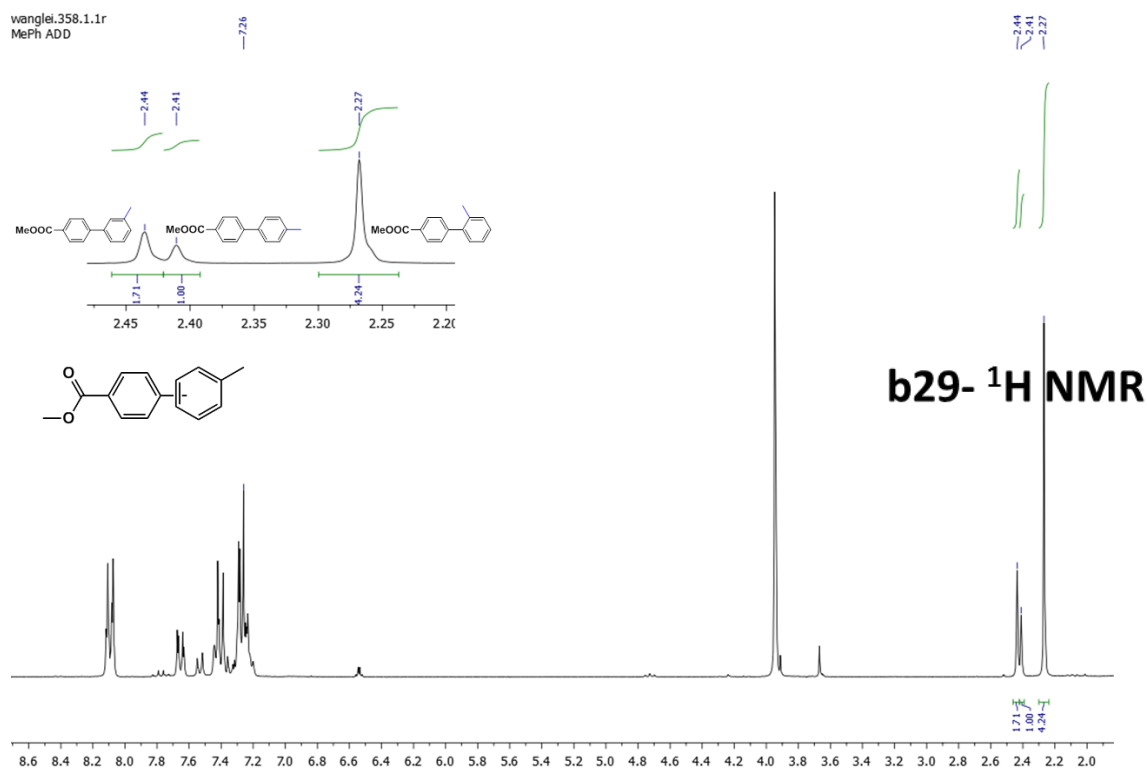


wanglei.2071.1.1r  
Ph

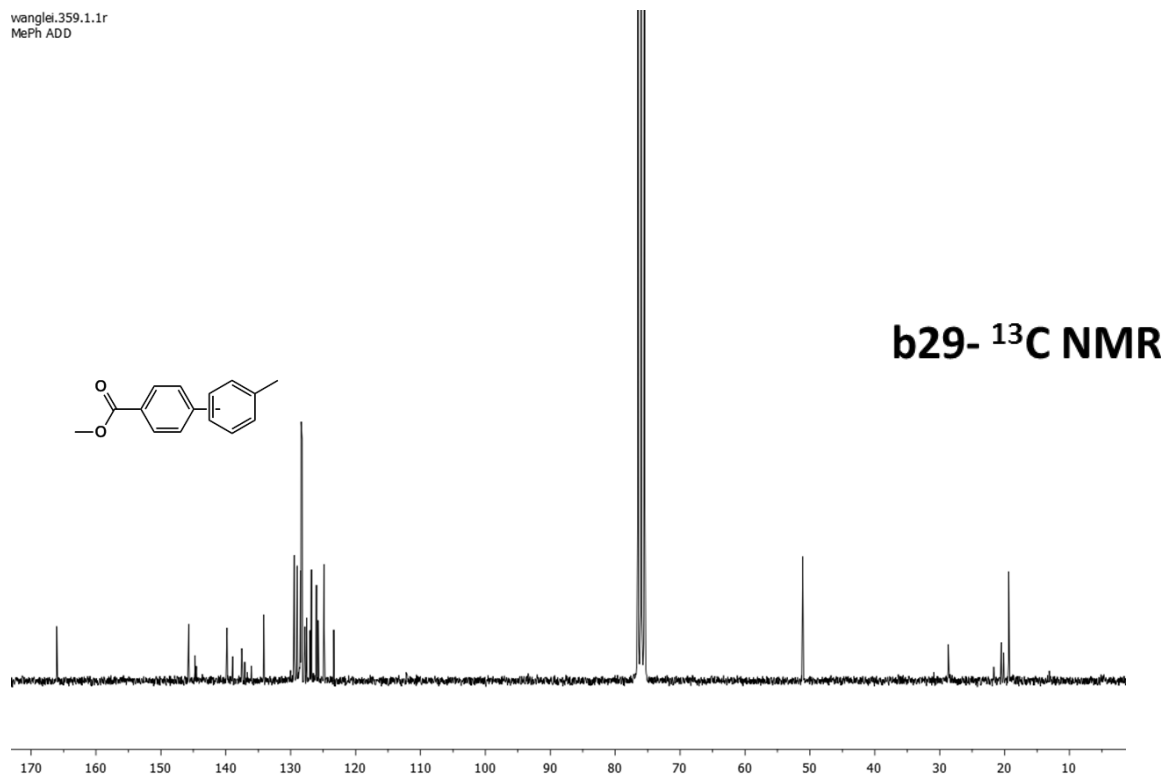


# Experiment Section

wanglei.358.1.1r  
MePh ADD



wanglei.359.1.1r  
MePh ADD



## **6.4 Atom transfer radical polymerization (ATRP) catalyzed by visible-light-absorbed small molecule organic semiconductors**

### **6.4.1 Materials and methods**

Chemicals were purchased from commercial sources and used as received without further purification. Glassware was dried using heating gun at 600 °C and cooled under vacuum prior to use if necessary. All photocatalytic reactions were conducted using common dry, inert atmosphere (N<sub>2</sub>) techniques via a Schlenk tube in ambient condition. White LED (OSA Opto Light) was used as light source. UV-Vis absorption and emission spectra were recorded on a Perkin Elmer Lambda 100 spectrophotometer and J&M TIDAS spectrofluorometer at ambient temperature, respectively. Cyclic voltammetry measurement was performed on an Autolab PGSTAT204 potentiostat/galvanostat (Metrohm) using a three electrode cell system: glassy carbon electrode as the working electrode, Hg/HgCl<sub>2</sub> electrode as the reference electrode, platinum wire as the counter electrode, and Bu<sub>4</sub>NPF<sub>6</sub> (0.1 M Acetonitrile) as supporting electrolyte with a scan rate of 100 mV/s in the range of -2 eV to 2.5 eV. GPC traces were recorded using a device of Agilent Technologies 1260 Infinity, THF as eluent, PMMA as standard and refractive index 1260 detector (RID) as indicator.

### **6.4.2 Fluorescence quenching experiments**

Conditions for the fluorescence quenching experiments: in different vessels, 0.0114 mmol Ph-BT-Ph was dissolved in 3 ml DMF, different amounts of the quencher were added into different vessels. The solution was degassed via N<sub>2</sub> bulb to remove the oxygen residue before the experiment. Concentrations of different quenchers were: 0.01 M, 0.025 M, 0.05 M, and 0.1 M.

### **6.4.3 General procedure for polymerization**

A 25 ml Schlenk tube equipped with a stirring bar and stopper was heated under vacuum then cooling for one time and then back filled with argon before MMA, Initiator, photocatalyst, triphenylamine, LiX if necessary, DMF is added. Then the reactor was degassed via the freeze-pump-thaw method and irradiated under a white LED. The mixture was dropwise added into

the MeOH or a mixture of MeOH/H<sub>2</sub>O for participation of the polymer. The polymer was collected via filtration and dried under vacuum to give the desired product.

## 7 Conclusion

In this thesis, small molecule organic semiconductors (SMOS) containing electron donor and acceptor moieties have been designed as metal-free, visible light-active and stable photocatalysts for organic transformation reactions as a promising alternative to the traditional transition metal complexes. The work has been conducted starting with the observation of a general design principle via donor and acceptor combinations, followed by the comprehensive study of the reaction mechanism using photophysical methods, and the utilization of the SMOSs for challenging organic photoredox reactions.

First, a general structural design principle of the small molecule organic semiconductor-based photocatalysts has been established via the investigation of various electron donor and acceptor combinations in order to fulfill the following crucial requirements: (i) visible light absorption; (ii) sufficient photoredox potential; (iii) long lifetime of photogenerated excitons. The structural impact on the photocatalytic efficiency was studied via the C-H functionalization reaction between electron-rich heteroaromatics and malonate derivatives as the model reaction. A mechanistic study focusing on the variation of the photoredox potential of the catalysts and sacrificial reagents was conducted. It could be demonstrated that the catalytic efficiency of the small molecule organic semiconductor were absolutely comparable with the state-of-the-art photocatalytic systems consisting of transition metal complexes.

Second, to precisely study the photo-generated charge separation, the electron transfer and the interaction between the organic catalysts, substrates and possible sacrificial reagents during the photocatalytic process, we focused on an important issue for photo-redox reactions, i.e. the mandatory use of electron donating sacrificial reagents. Here, a new conceptual study using a double photocatalyst system made of cooperative organic semiconductor couples was

conducted. By the cooperative photocatalyst design, an extra intermolecular electron transfer could occur between the SMOSs, leading to enhanced photo-generated electron/hole separation and thereby more stable reductive and oxidative species which can give out one electron to the diethyl bromomalonate or get one electron back from the intermediate directly. The C-H functionalization reaction between electron-rich heteroaromatics and malonate derivatives can be conducted successfully without triphenylamine as sacrificial reagent. Advanced photophysical studies illustrate the excitons separation process between OS couples in a direct way. Precisely tuning the energy levels of the photocatalysts will improve the excitons separation process, further influence the reaction rate.

To demonstrate the feasibility of the SMOSs for challenging organic photoredox reactions, a SMOS with an extremely high reduction potential of -2.04 V vs. SCE was designed. Aromatic carbon-carbon bond formation reactions could be successfully conducted via the reductive dehalogenation of various aryl halides by the SMOS.

An additional study for light-controlled atom transfer radical polymerization using SMOSs as photocatalysts was successfully carried out via precise control of the energy levels for various components involved, i.e. the organic photocatalysts, radical starter, sacrificial reagents and monomers in the catalytic cycle. The living nature of the polymerization process was confirmed by the controllable growth of the molecular weight in a light “on-off” cycle, successful synthesis of the chain extension and a di-block copolymer, and the defined molecular weight distribution of the polymer chain.

The studies conducted in this thesis demonstrated that the donor–acceptor (D–A) based small-molecule organic semiconductors (SMOS) can act as a new class of pure organic and metal-free photocatalytic systems for visible light-driven organic photoredox reactions. With their tunable absorption range, defined and appropriate energy band positions, and long exciton lifetimes, the SMOSs can be used as a promising alternative to the traditional transition metal complexes.

## 8 List of Abbreviations

A	Acceptor
Ar	Arene
ATRP	Atom transfer radical polymerization
BHJ	Bulk-heterojunction
BO	Benzooxadiazole
BS	Benzoselenadiazole
BT	Benzothiadiazole
BTz	Benzo[d]1,2,3]triazole
CPP	Conjugated porous polymer
CRP	Controlled radical polymerization
CT	Charge transfer
CV	Cyclic voltammetry
D	Donor
DAS	Decay associated spectra
DFT	Density functional theory
DMF	Dimethylformamide
DMSO	Dimethylsulfoxide



## List of Abbreviations

---

DIPEA	Diisopropylethylamine
ET	Electron transfer
EET	Excited energy transfer
FG	Functional group
GC-MS	Gas chromatography-mass spectrometry
GPC	Gel permeation chromatography
HOMO	Highest occupied molecular orbital
LUMO	Lowest unoccupied molecular orbital
LED	Light emitting diode
MALDI-TOF	Matrix-assisted laser desorption ionization-time of flight
MLCT	Metal to ligand charge transfer
MMA	Methyl methacrylate
Mn	Number average molecular weight
OLED	Organic light emitting diode
OPV	Organic photovoltaic
OS	Organic semiconductor
OSC	Organic solar cell

## References

---

OTFT	Organic thin film transistor
PCE	Power conversion efficiency
PDI	Polydispersity index
PMMA	Poly(methyl methacrylate)
Ph	Phenyl ring
Py	Pyrrole
SCE	Saturated calomel electrode
SET	Single electron transfer
SMOS	Small molecule organic semiconductor
TA	1-Butyl-1H-1,2,3-triazol
TEMPO	(2,2,6,6-Tetramethylpiperidin-1-yl)oxyl
Th	Thiophene
TRPL	Time-resolved photoluminescence

## 9 References

1. Fox, M. A.; Dulay, M. T., Heterogeneous Photocatalysis. *Chem Rev* **1993**, *93* (1), 341-357.
2. Ma, Y.; Wang, X. L.; Jia, Y. S.; Chen, X. B.; Han, H. X.; Li, C., Titanium Dioxide-Based Nanomaterials for Photocatalytic Fuel Generations. *Chem Rev* **2014**, *114* (19), 9987-10043.

3. Schneider, J.; Matsuoka, M.; Takeuchi, M.; Zhang, J. L.; Horiuchi, Y.; Anpo, M.; Bahnemann, D. W., Understanding TiO<sub>2</sub> Photocatalysis: Mechanisms and Materials. *Chem Rev* **2014**, *114* (19), 9919-9986.
4. White, J. L.; Baruch, M. F.; Pander, J. E.; Hu, Y.; Fortmeyer, I. C.; Park, J. E.; Zhang, T.; Liao, K.; Gu, J.; Yan, Y.; Shaw, T. W.; Abelev, E.; Bocarsly, A. B., Light-Driven Heterogeneous Reduction of Carbon Dioxide: Photocatalysts and Photoelectrodes. *Chem Rev* **2015**, *115* (23), 12888-12935.
5. Ong, W. J.; Tan, L. L.; Ng, Y. H.; Yong, S. T.; Chai, S. P., Graphitic Carbon Nitride (g-C<sub>3</sub>N<sub>4</sub>)-Based Photocatalysts for Artificial Photosynthesis and Environmental Remediation: Are We a Step Closer To Achieving Sustainability? *Chem Rev* **2016**, *116* (12), 7159-7329.
6. Prier, C. K.; Rankic, D. A.; MacMillan, D. W. C., Visible Light Photoredox Catalysis with Transition Metal Complexes: Applications in Organic Synthesis. *Chem Rev* **2013**, *113* (7), 5322-5363.
7. Ravelli, D.; Fagnoni, M.; Albini, A., Photoorganocatalysis. What for? *Chem Soc Rev* **2013**, *42* (1), 97-113.
8. Zeitler, K., Photoredox Catalysis with Visible Light. *Angew Chem Int Edit* **2009**, *48* (52), 9785-9789.
9. Staveness, D.; Bosque, I.; Stephenson, C. R. J., Free Radical Chemistry Enabled by Visible Light-Induced Electron Transfer. *Accounts Chem Res* **2016**, *49* (10), 2295-2306.
10. Koike, T.; Akita, M., Fine Design of Photoredox Systems for Catalytic Fluoromethylation of Carbon-Carbon Multiple Bonds. *Accounts Chem Res* **2016**, *49* (9), 1937-1945.
11. Hopkinson, M. N.; Tlahuext-Aca, A.; Glorius, F., Merging Visible Light Photoredox and Gold Catalysis. *Accounts Chem Res* **2016**, *49* (10), 2261-2272.
12. Chatterjee, T.; Iqbal, N.; You, Y.; Cho, E. J., Controlled Fluoroalkylation Reactions by Visible-Light Photoredox Catalysis. *Accounts Chem Res* **2016**, *49* (10), 2284-2294.
13. Nicewicz, D. A.; Nguyen, T. M., Recent Applications of Organic Dyes as Photoredox Catalysts in Organic Synthesis. *Acs Catal* **2014**, *4* (1), 355-360.

14. Margrey, K. A.; Nicewicz, D. A., A General Approach to Catalytic Alkene Anti-Markovnikov Hydrofunctionalization Reactions via Acridinium Photoredox Catalysis. *Accounts Chem Res* **2016**, *49* (9), 1997-2006.
15. Pitre, S. P.; McTiernan, C. D.; Scaiano, J. C., Understanding the Kinetics and Spectroscopy of Photoredox Catalysis and Transition-Metal-Free Alternatives. *Accounts Chem Res* **2016**, *49* (6), 1320-1330.
16. Majek, M.; Jacobi von Wangelin, A., Mechanistic Perspectives on Organic Photoredox Catalysis for Aromatic Substitutions. *Accounts Chem Res* **2016**, *49* (10), 2316-2327.
17. Shirakawa, H.; Louis, E. J.; Macdiarmid, A. G.; Chiang, C. K.; Heeger, A. J., Synthesis of Electrically Conducting Organic Polymers - Halogen Derivatives of Polyacetylene, (Ch)X. *J Chem Soc Chem Comm* **1977**, (16), 578-580.
18. Tsumura, A.; Koezuka, H.; Ando, T., Macromolecular Electronic Device - Field-Effect Transistor with a Polythiophene Thin-Film. *Appl Phys Lett* **1986**, *49* (18), 1210-1212.
19. Tang, C. W.; Vanslyke, S. A., Organic Electroluminescent Diodes. *Appl Phys Lett* **1987**, *51* (12), 913-915.
20. Boudreault, P. L. T.; Najari, A.; Leclerc, M., Processable Low-Bandgap Polymers for Photovoltaic Applications. *Chem Mater* **2011**, *23* (3), 456-469.
21. Li, Y. F., Molecular Design of Photovoltaic Materials for Polymer Solar Cells: Toward Suitable Electronic Energy Levels and Broad Absorption. *Accounts Chem Res* **2012**, *45* (5), 723-733.
22. Horvath, I. T.; Anastas, P. T., Innovations and green chemistry. *Chem Rev* **2007**, *107* (6), 2169-2173.
23. Farran, A.; Cai, C.; Sandoval, M.; Xu, Y. M.; Liu, J.; Hernaiz, M. J.; Linhardt, R. J., Green Solvents in Carbohydrate Chemistry: From Raw Materials to Fine Chemicals. *Chem Rev* **2015**, *115* (14), 6811-6853.
24. Shoda, S.; Uyama, H.; Kadokawa, J.; Kimura, S.; Kobayashi, S., Enzymes as Green Catalysts for Precision Macromolecular Synthesis. *Chem Rev* **2016**, *116* (4), 2307-2413.
25. Fujishima, A.; Honda, K., Electrochemical Photolysis of Water at a Semiconductor Electrode. *Nature* **1972**, *238* (5358), 37-+.

26. Kudo, A.; Miseki, Y., Heterogeneous photocatalyst materials for water splitting. *Chem Soc Rev* **2009**, *38* (1), 253-278.
27. Maeda, K., Photocatalytic water splitting using semiconductor particles: History and recent developments. *J Photoch Photobio C* **2011**, *12* (4), 237-268.
28. Abe, R., Recent progress on photocatalytic and photoelectrochemical water splitting under visible light irradiation. *J Photoch Photobio C* **2010**, *11* (4), 179-209.
29. Matsunaga, T.; Tomoda, R.; Nakajima, T.; Wake, H., Photoelectrochemical Sterilization of Microbial-Cells by Semiconductor Powders. *Fems Microbiol Lett* **1985**, *29* (1-2), 211-214.
30. Sunada, K.; Watanabe, T.; Hashimoto, K., Studies on photokilling of bacteria on TiO<sub>2</sub> thin film. *J Photoch Photobio A* **2003**, *156* (1-3), 227-233.
31. McCullagh, C.; Robertson, J. M. C.; Bahnemann, D. W.; Robertson, P. K. J., The application of TiO<sub>2</sub> photocatalysis for disinfection of water contaminated with pathogenic micro-organisms: a review. *Res Chem Intermediat* **2007**, *33* (3-5), 359-375.
32. Peller, J. R.; Whitman, R. L.; Griffith, S.; Harris, P.; Peller, C.; Scalzitti, J., TiO<sub>2</sub> as a photocatalyst for control of the aquatic invasive alga, *Cladophora*, under natural and artificial light. *J Photoch Photobio A* **2007**, *186* (2-3), 212-217.
33. Caballero, L.; Whitehead, K. A.; Allen, N. S.; Verran, J., Inactivation of *Escherichia coli* on immobilized TiO<sub>2</sub> using fluorescent light. *J Photoch Photobio A* **2009**, *202* (2-3), 92-98.
34. Qiao, J. L.; Liu, Y. Y.; Hong, F.; Zhang, J. J., A review of catalysts for the electroreduction of carbon dioxide to produce low-carbon fuels. *Chem Soc Rev* **2014**, *43* (2), 631-675.
35. Inoue, T.; Fujishima, A.; Konishi, S.; Honda, K., Photoelectrocatalytic Reduction of Carbon-Dioxide in Aqueous Suspensions of Semiconductor Powders. *Nature* **1979**, *277* (5698), 637-638.
36. Shaw, M. H.; Twilton, J.; MacMillan, D. W. C., Photoredox Catalysis in Organic Chemistry. *J Org Chem* **2016**, *81* (16), 6898-6926.
37. Neumann, M.; Fuldner, S.; Konig, B.; Zeitler, K., Metal-Free, Cooperative Asymmetric Organophotoredox Catalysis with Visible Light. *Angew Chem Int Edit* **2011**, *50* (4), 951-954.
38. Hernandez-Perez, A. C.; Collins, S. K., Heteroleptic Cu-Based Sensitizers in Photoredox Catalysis. *Accounts Chem Res* **2016**, *49* (8), 1557-1565.

39. Treat, N. J.; Sprafke, H.; Kramer, J. W.; Clark, P. G.; Barton, B. E.; de Alaniz, J. R.; Fors, B. P.; Hawker, C. J., Metal-Free Atom Transfer Radical Polymerization. *J Am Chem Soc* **2014**, *136* (45), 16096-16101.
40. Theriot, J. C.; Lim, C. H.; Yang, H.; Ryan, M. D.; Musgrave, C. B.; Miyake, G. M., Organocatalyzed atom transfer radical polymerization driven by visible light. *Science* **2016**, *352* (6289), 1082-1086.
41. Poelma, S. O.; Burnett, G. L.; Discekici, E. H.; Mattson, K. M.; Treat, N. J.; Luo, Y. D.; Hudson, Z. M.; Shankel, S. L.; Clark, P. G.; Kramer, J. W.; Hawker, C. J.; de Alaniz, J. R., Chemoselective Radical Dehalogenation and C-C Bond Formation on Aryl Halide Substrates Using Organic Photoredox Catalysts. *J Org Chem* **2016**, *81* (16), 7155-7160.
42. Pearson, R. M.; Lim, C. H.; McCarthy, B. G.; Musgrave, C. B.; Miyake, G. M., Organocatalyzed Atom Transfer Radical Polymerization Using N-Aryl Phenoxazines as Photoredox Catalysts. *J Am Chem Soc* **2016**, *138* (35), 11399-11407.
43. Miyake, G. M.; Theriot, J. C., Perylene as an Organic Photocatalyst for the Radical Polymerization of Functionalized Vinyl Monomers through Oxidative Quenching with Alkyl Bromides and Visible Light. *Macromolecules* **2014**, *47* (23), 8255-8261.
44. McTiernan, C. D.; Pitre, S. P.; Scaiano, J. C., Photocatalytic Dehalogenation of Vicinal Dibromo Compounds Utilizing Sexithiophene and Visible-Light Irradiation. *Acs Catal* **2014**, *4* (11), 4034-4039.
45. Lim, C. H.; Ryan, M. D.; McCarthy, B. G.; Theriot, J. C.; Sartor, S. M.; Damrauer, N. H.; Musgrave, C. B.; Miyake, G. M., Intramolecular Charge Transfer and Ion Pairing in N,N-Diaryl Dihydrophenazine Photoredox Catalysts for Efficient Organocatalyzed Atom Transfer Radical Polymerization. *J Am Chem Soc* **2017**, *139* (1), 348-355.
46. Wang, Z. J.; Ghasimi, S.; Landfester, K.; Zhang, K. A. I., Molecular Structural Design of Conjugated Microporous Poly(Benzooxadiazole) Networks for Enhanced Photocatalytic Activity with Visible Light. *Adv Mater* **2015**, *27* (40), 6265-6270.
47. Luo, J.; Zhang, X.; Zhang, J., Carbazolic Porous Organic Framework as an Efficient, Metal-Free Visible-Light Photocatalyst for Organic Synthesis. *Acs Catal* **2015**, *5* (4), 2250-2254.

48. Li, R.; Ma, B. C.; Huang, W.; Wang, L.; Wang, D.; Lu, H.; Landfester, K.; Zhang, K. A. I., Photocatalytic Regioselective and Stereoselective [2+2] Cycloaddition of Styrene Derivatives Using a Heterogeneous Organic Photocatalyst. *Acs Catal* **2017**, 7 (5), 3097-3101.
49. Huang, W.; Wang, Z. J.; Ma, B. C.; Ghasimi, S.; Gehrig, D.; Laquai, F.; Landfester, K.; Zhang, K. A. I., Hollow nanoporous covalent triazine frameworks via acid vapor-assisted solid phase synthesis for enhanced visible light photoactivity. *J Mater Chem A* **2016**, 4 (20), 7555-7559.
50. Nguyen, J. D.; D'Amato, E. M.; Narayanam, J. M. R.; Stephenson, C. R. J., Engaging unactivated alkyl, alkenyl and aryl iodides in visible-light-mediated free radical reactions. *Nat Chem* **2012**, 4 (10), 854-859.
51. Grandjean, J. M. M.; Nicewicz, D. A., Synthesis of Highly Substituted Tetrahydrofurans by Catalytic Polar-Radical-Crossover Cycloadditions of Alkenes and Alkenols. *Angew Chem Int Edit* **2013**, 52 (14), 3967-3971.
52. Hari, D. P.; Schroll, P.; Konig, B., Metal-Free, Visible-Light-Mediated Direct C-H Arylation of Heteroarenes with Aryl Diazonium Salts. *J Am Chem Soc* **2012**, 134 (6), 2958-2961.
53. Ohkubo, K.; Fujimoto, A.; Fukuzumi, S., Metal-free oxygenation of cyclohexane with oxygen catalyzed by 9-mesityl-10-methylacridinium and hydrogen chloride under visible light irradiation. *Chem Commun* **2011**, 47 (30), 8515-8517.
54. Ohkubo, K.; Mizushima, K.; Iwata, R.; Fukuzumi, S., Selective photocatalytic aerobic bromination with hydrogen bromide via an electron-transfer state of 9-mesityl-10-methylacridinium ion. *Chem Sci* **2011**, 2 (4), 715-722.
55. Pitre, S. P.; McTiernan, C. D.; Ismaili, H.; Scaiano, J. C., Mechanistic Insights and Kinetic Analysis for the Oxidative Hydroxylation of Arylboronic Acids by Visible Light Photoredox Catalysis: A Metal-Free Alternative. *J Am Chem Soc* **2013**, 135 (36), 13286-13289.
56. Pitre, S. P.; McTiernan, C. D.; Ismaili, H.; Scaiano, J. C., Metal-Free Photocatalytic Radical Trifluoromethylation Utilizing Methylene Blue and Visible Light Irradiation. *Acs Catal* **2014**, 4 (8), 2530-2535.
57. Riener, M.; Nicewicz, D. A., Synthesis of cyclobutane lignans via an organic single electron oxidant-electron relay system. *Chem Sci* **2013**, 4 (6), 2625-2629.

58. Wilger, D. J.; Gesmundo, N. J.; Nicewicz, D. A., Catalytic hydrotrifluoromethylation of styrenes and unactivated aliphatic alkenes via an organic photoredox system. *Chem Sci* **2013**, *4* (8), 3160-3165.
59. Fukuzumi, S.; Mochizuki, S.; Tanaka, T., Photocatalytic Reduction of Phenacyl Halides by 9,10-Dihydro-10-Methylacridine - Control between the Reductive and Oxidative Quenching Pathways of Tris(Bipyridine)Ruthenium Complex Utilizing an Acid Catalysis. *J Phys Chem-US* **1990**, *94* (2), 722-726.
60. Narayanam, J. M. R.; Tucker, J. W.; Stephenson, C. R. J., Electron-Transfer Photoredox Catalysis: Development of a Tin-Free Reductive Dehalogenation Reaction. *J Am Chem Soc* **2009**, *131* (25), 8756-+.
61. Hironaka, K.; Fukuzumi, S.; Tanaka, T., Tris(Bipyridyl)Ruthenium(II)-Photosensitized Reaction of 1-Benzyl-1,4-Dihydronicotinamide with Benzyl Bromide. *J Chem Soc Perk T 2* **1984**, (10), 1705-1709.
62. Hirao, T.; Shiori, J.; Okahata, N., Ruthenium-bipyridine complex-catalyzed photo-induced reduction of nitrobenzenes with hydrazine. *B Chem Soc Jpn* **2004**, *77* (9), 1763-1764.
63. Gazi, S.; Ananthakrishnan, R., Metal-free-photocatalytic reduction of 4-nitrophenol by resin-supported dye under the visible irradiation. *Appl Catal B-Environ* **2011**, *105* (3-4), 317-325.
64. Yang, X. J.; Chen, B.; Zheng, L. Q.; Wu, L. Z.; Tung, C. H., Highly efficient and selective photocatalytic hydrogenation of functionalized nitrobenzenes. *Green Chem* **2014**, *16* (3), 1082-1086.
65. Chen, Y. Y.; Kamlet, A. S.; Steinman, J. B.; Liu, D. R., A biomolecule-compatible visible-light-induced azide reduction from a DNA-encoded reaction-discovery system. *Nat Chem* **2011**, *3* (2), 146-153.
66. Hedstrand, D. M.; Kruizinga, W. H.; Kellogg, R. M., Light-Induced and Dye Accelerated Reductions of Phenacyl Onium Salts by 1,4-Dihydropyridines. *Tetrahedron Lett* **1978**, (14), 1255-1258.
67. Vanbergen, T. J.; Hedstrand, D. M.; Kruizinga, W. H.; Kellogg, R. M., Chemistry of Dihydropyridines .9. Hydride Transfer from 1,4-Dihydropyridines to Sp<sup>3</sup>-Hybridized Carbon in



- Sulfonium Salts and Activated Halides - Studies with Nad(P)H Models. *J Org Chem* **1979**, *44* (26), 4953-4962.
68. Nakamura, K.; Fujii, M.; Mekata, H.; Oka, S.; Ohno, A., Nad(P)<sup>+</sup>-Nad(Ph) Model .58. Desulfonylation of Beta-Keto Sulfones with the Hantzsch Ester, an Nad(P)H Model. *Chem Lett* **1986**, (1), 87-88.
69. Yang, D. T.; Meng, Q. Y.; Zhong, J. J.; Xiang, M.; Liu, Q.; Wu, L. Z., Metal-Free Desulfonylation Reaction Through Visible-Light Photoredox Catalysis. *Eur J Org Chem* **2013**, *2013* (33), 7528-7532.
70. Larraufie, M. H.; Pellet, R.; Fensterbank, L.; Goddard, J. P.; Lacote, E.; Malacria, M.; Ollivier, C., Visible-Light-Induced Photoreductive Generation of Radicals from Epoxides and Aziridines. *Angew Chem Int Edit* **2011**, *50* (19), 4463-4466.
71. Xuan, J.; Xia, X. D.; Zeng, T. T.; Feng, Z. J.; Chen, J. R.; Lu, L. Q.; Xiao, W. J., Visible-Light-Induced Formal [3+2] Cycloaddition for Pyrrole Synthesis under Metal-Free Conditions. *Angew Chem Int Edit* **2014**, *53* (22), 5653-5656.
72. Fukuzumi, S.; Kotani, H.; Ohkubo, K.; Ogo, S.; Tkachenko, N. V.; Lemmetyinen, H., Electron-transfer state of 9-mesityl-10-methylacridinium ion with a much longer lifetime and higher energy than that of the natural photosynthetic reaction center. *J Am Chem Soc* **2004**, *126* (6), 1600-1601.
73. Tucker, J. W.; Nguyen, J. D.; Narayanam, J. M. R.; Krabbe, S. W.; Stephenson, C. R. J., Tin-free radical cyclization reactions initiated by visible light photoredox catalysis. *Chem Commun* **2010**, *46* (27), 4985-4987.
74. Kim, H.; Lee, C., Visible-Light-Induced Photocatalytic Reductive Transformations of Organohalides. *Angew Chem Int Edit* **2012**, *51* (49), 12303-12306.
75. Tucker, J. W.; Stephenson, C. R. J., Tandem Visible Light-Mediated Radical Cyclization-Divinylcyclopropane Rearrangement to Tricyclic Pyrrolidinones. *Org Lett* **2011**, *13* (20), 5468-5471.
76. Kern, J. M.; Sauvage, J. P., Photoassisted C-C Coupling Via Electron-Transfer to Benzylic Halides by a Bis(Di-Imine) Copper(1) Complex. *J Chem Soc Chem Comm* **1987**, (8), 546-548.

77. Maji, T.; Karmakar, A.; Reiser, O., Visible-Light Photoredox Catalysis: Dehalogenation of Vicinal Dibromo-,  $\alpha$ -Halo-, and  $\alpha,\alpha$ -Dibromocarbonyl Compounds. *J Org Chem* **2011**, 76 (2), 736-739.
78. Maidan, R.; Willner, I., Photochemical and Chemical Enzyme Catalyzed Debromination of Meso-1,2-Dibromostilbene in Multiphase Systems. *J Am Chem Soc* **1986**, 108 (5), 1080-1082.
79. Canoyelo, H.; Deronzier, A., Photo-Oxidation of Some Carbinols by the Ru(II) Polypyridyl Complex Aryl Diazonium Salt System. *Tetrahedron Lett* **1984**, 25 (48), 5517-5520.
80. Zou, Y. Q.; Chen, J. R.; Liu, X. P.; Lu, L. Q.; Davis, R. L.; Jorgensen, K. A.; Xiao, W. J., Highly Efficient Aerobic Oxidative Hydroxylation of Arylboronic Acids: Photoredox Catalysis Using Visible Light. *Angew Chem Int Edit* **2012**, 51 (3), 784-788.
81. Ohkubo, K.; Kobayashi, T.; Fukuzumi, S., Direct Oxygenation of Benzene to Phenol Using Quinolinium Ions as Homogeneous Photocatalysts. *Angew Chem Int Edit* **2011**, 50 (37), 8652-8655.
82. Tucker, J. W.; Narayanam, J. M. R.; Shah, P. S.; Stephenson, C. R. J., Oxidative photoredox catalysis: mild and selective deprotection of PMB ethers mediated by visible light. *Chem Commun* **2011**, 47 (17), 5040-5042.
83. Ohkubo, K.; Fujimoto, A.; Fukuzumi, S., Visible-Light-Induced Oxygenation of Benzene by the Triplet Excited State of 2,3-Dichloro-5,6-dicyano-p-benzoquinone. *J Am Chem Soc* **2013**, 135 (14), 5368-5371.
84. Hernandez-Perez, A. C.; Collins, S. K., A Visible-Light-Mediated Synthesis of Carbazoles. *Angew Chem Int Edit* **2013**, 52 (48), 12696-12700.
85. Mohlmann, L.; Baar, M.; Riess, J.; Antonietti, M.; Wang, X. C.; Blechert, S., Carbon Nitride-Catalyzed Photoredox C-C Bond Formation with N-Aryltetrahydroisoquinolines. *Adv Synth Catal* **2012**, 354 (10), 1909-1913.
86. Condie, A. G.; Gonzalez-Gomez, J. C.; Stephenson, C. R. J., Visible-Light Photoredox Catalysis: Aza-Henry Reactions via C-H Functionalization. *J Am Chem Soc* **2010**, 132 (5), 1464-+.
87. Rueping, M.; Zhu, S. Q.; Koenigs, R. M., Visible-light photoredox catalyzed oxidative Strecker reaction. *Chem Commun* **2011**, 47 (47), 12709-12711.

88. Zhao, G. L.; Yang, C.; Guo, L.; Sun, H. N.; Chen, C.; Xia, W. J., Visible light-induced oxidative coupling reaction: easy access to Mannich-type products. *Chem Commun* **2012**, 48 (17), 2337-2339.
89. Rueping, M.; Vila, C.; Koenigs, R. M.; Poscharny, K.; Fabry, D. C., Dual catalysis: combining photoredox and Lewis base catalysis for direct Mannich reactions. *Chem Commun* **2011**, 47 (8), 2360-2362.
90. Rueping, M.; Zhu, S. Q.; Koenigs, R. M., Photoredox catalyzed C-P bond forming reactions-visible light mediated oxidative phosphorylations of amines. *Chem Commun* **2011**, 47 (30), 8679-8681.
91. Freeman, D. B.; Furst, L.; Condie, A. G.; Stephenson, C. R. J., Functionally Diverse Nucleophilic Trapping of Iminium Intermediates Generated Utilizing Visible Light. *Org Lett* **2012**, 14 (1), 94-97.
92. Wallentin, C. J.; Nguyen, J. D.; Finkbeiner, P.; Stephenson, C. R. J., Visible Light-Mediated Atom Transfer Radical Addition via Oxidative and Reductive Quenching of Photocatalysts. *J Am Chem Soc* **2012**, 134 (21), 8875-8884.
93. Singh, A.; Arora, A.; Weaver, J. D., Photoredox-Mediated C-H Functionalization and Coupling of Tertiary Aliphatic Amines with 2-Chloroazoles. *Org Lett* **2013**, 15 (20), 5390-5393.
94. Ghosh, I.; Ghosh, T.; Bardagi, J. I.; Konig, B., Reduction of aryl halides by consecutive visible light-induced electron transfer processes. *Science* **2014**, 346 (6210), 725-728.
95. Arora, A.; Teegardin, K. A.; Weaver, J. D., Reductive Alkylation of 2-Bromoazoles via Photoinduced Electron Transfer: A Versatile Strategy to Csp(2)-Csp(3) Coupled Products. *Org Lett* **2015**, 17 (15), 3722-3725.
96. Arora, A.; Weaver, J. D., Photocatalytic Generation of 2-Azoly radicals: Intermediates for the Azolylolation of Arenes and Heteroarenes via C-H Functionalization. *Org Lett* **2016**, 18 (16), 3996-3999.
97. Pirtsch, M.; Paria, S.; Matsuno, T.; Isobe, H.; Reiser, O., [Cu(dap)<sub>2</sub>Cl] As an Efficient Visible-Light-Driven Photoredox Catalyst in Carbon-Carbon Bond-Forming Reactions. *Chem-Eur J* **2012**, 18 (24), 7336-7340.

98. Park, S.; Joo, J. M.; Cho, E. J., Synthesis of beta-Trifluoromethylated Ketones from Propargylic Alcohols by Visible Light Photoredox Catalysis. *Eur J Org Chem* **2015**, (19), 4093-4097.
99. Roh, G. B.; Iqbal, N.; Cho, E. J., Trifluoroethylation of Alkynes: Synthesis of Allylic-CF<sub>3</sub> Compounds by Visible-Light Photocatalysis. *Chinese J Chem* **2016**, 34 (5), 459-464.
100. Yu, C.; Iqbal, N.; Park, S.; Cho, E. J., Selective difluoroalkylation of alkenes by using visible light photoredox catalysis. *Chem Commun* **2014**, 50 (85), 12884-12887.
101. Choi, Y.; Yu, C.; Kim, J. S.; Cho, E. J., Visible-Light-Induced Arylthiofluoroalkylations of Unactivated Heteroaromatics and Alkenes. *Org Lett* **2016**, 18 (13), 3246-3249.
102. Choi, S.; Kim, Y. J.; Kim, S. M.; Yang, J. W.; Kim, S. W.; Cho, E. J., Hydrotrifluoromethylation and iodotrifluoromethylation of alkenes and alkynes using an inorganic electride as a radical generator. *Nat Commun* **2014**, 5.
103. Straathof, N. J. W.; Gemoets, H. P. L.; Wang, X.; Schouten, J. C.; Hessel, V.; Noel, T., Rapid Trifluoromethylation and Perfluoroalkylation of Five-Membered Heterocycles by Photoredox Catalysis in Continuous Flow. *ChemSuschem* **2014**, 7 (6), 1612-1617.
104. Jung, J.; Kim, E.; You, Y.; Cho, E. J., Visible Light-Induced Aromatic Difluoroalkylation. *Adv Synth Catal* **2014**, 356 (13), 2741-2748.
105. Kalyani, D.; McMurtrey, K. B.; Neufeldt, S. R.; Sanford, M. S., Room-Temperature C-H Arylation: Merger of Pd-Catalyzed C-H Functionalization and Visible-Light Photocatalysis. *J Am Chem Soc* **2011**, 133 (46), 18566-18569.
106. Xue, D.; Jia, Z. H.; Zhao, C. J.; Zhang, Y. Y.; Wang, C.; Xiao, J. L., Direct Arylation of N-Heteroarenes with Aryldiazonium Salts by Photoredox Catalysis in Water. *Chem-Eur J* **2014**, 20 (10), 2960-2965.
107. Zhang, J.; Chen, J.; Zhang, X. Y.; Lei, X. G., Total Syntheses of Menisporphine and Daurioxoisoporphine C Enabled by Photoredox-Catalyzed Direct C-H Arylation of Isoquinoline with Aryldiazonium Salt. *J Org Chem* **2014**, 79 (21), 10682-10688.
108. Hari, D. P.; Hering, T.; Konig, B., Visible Light Photocatalytic Synthesis of Benzothiophenes. *Org Lett* **2012**, 14 (20), 5334-5337.

109. Schroll, P.; Hari, D. P.; Konig, B., Photocatalytic Arylation of Alkenes, Alkynes and Enones with Diazonium Salts. *Chemistryopen* **2012**, *1* (3), 130-133.
110. Hering, T.; Hari, D. P.; Konig, B., Visible-Light-Mediated  $\alpha$ -Arylation of Enol Acetates Using Aryl Diazonium Salts. *J Org Chem* **2012**, *77* (22), 10347-10352.
111. Yao, C. J.; Sun, Q.; Rastogi, N.; Konig, B., Intermolecular Formyloxyarylation of Alkenes by Photoredox Meerwein Reaction. *Acs Catal* **2015**, *5* (5), 2935-2938.
112. Natarajan, P.; Bala, A.; Mehta, S. K.; Bhasin, K. K., Visible-light photocatalyzed synthesis of 2-aryl N-methylpyrroles, furans and thiophenes utilizing arylsulfonyl chlorides as a coupling partner. *Tetrahedron* **2016**, *72* (19), 2521-2526.
113. Xia, J. D.; Deng, G. B.; Zhou, M. B.; Liu, W.; Xie, P.; Li, J. H., Reusable Visible Light Photoredox Catalysts; Catalyzed Benzylic C(sp<sup>3</sup>)-H Functionalization/Carbocyclization Reactions. *Synlett* **2012**, (18), 2707-2713.
114. Deng, G. B.; Wang, Z. Q.; Xia, J. D.; Qian, P. C.; Song, R. J.; Hu, M.; Gong, L. B.; Li, J. H., Tandem Cyclizations of 1,6-Enynes with Arylsulfonyl Chlorides by Using Visible-Light Photoredox Catalysis. *Angew Chem Int Edit* **2013**, *52* (5), 1535-1538.
115. Mizoguchi, H.; Oikawa, H.; Oguri, H., Biogenetically inspired synthesis and skeletal diversification of indole alkaloids. *Nat Chem* **2014**, *6* (1), 57-64.
116. Nagib, D. A.; MacMillan, D. W. C., Trifluoromethylation of arenes and heteroarenes by means of photoredox catalysis. *Nature* **2011**, *480* (7376), 224-228.
117. Fearnley, A. F.; An, J.; Jackson, M.; Lindovska, P.; Denton, R. M., Synthesis of quaternary aryl phosphonium salts: photoredox-mediated phosphine arylation. *Chem Commun* **2016**, *52* (28), 4987-4990.
118. Neufeldt, S. R.; Sanford, M. S., Combining Transition Metal Catalysis with Radical Chemistry: Dramatic Acceleration of Palladium-Catalyzed C-H Arylation with Diaryliodonium Salts. *Adv Synth Catal* **2012**, *354* (18), 3517-3522.
119. Liu, Y. X.; Xue, D.; Wang, J. D.; Zhao, C. J.; Zou, Q. Z.; Wang, C.; Xiao, J. L., Room-Temperature Arylation of Arenes and Heteroarenes with Diaryliodonium Salts by Photoredox Catalysis. *Synlett* **2013**, *24* (4), 507-513.

120. Baralle, A.; Fensterbank, L.; Goddard, J. P.; Ollivier, C., Aryl Radical Formation by Copper(I) Photocatalyzed Reduction of Diaryliodonium Salts: NMR Evidence for a Cu-II/Cu-I Mechanism. *Chem-Eur J* **2013**, *19* (33), 10809-10813.
121. Mizuta, S.; Verhoog, S.; Engle, K. M.; Khotavivattana, T.; O'Duill, M.; Wheelhouse, K.; Rassias, G.; Medebielle, M.; Gouverneur, V., Catalytic Hydrotrifluoromethylation of Unactivated Alkenes. *J Am Chem Soc* **2013**, *135* (7), 2505-2508.
122. Yasu, Y.; Koike, T.; Akita, M., Three-component Oxytrifluoromethylation of Alkenes: Highly Efficient and Regioselective Difunctionalization of C=C Bonds Mediated by Photoredox Catalysts. *Angew Chem Int Edit* **2012**, *51* (38), 9567-9571.
123. Yasu, Y.; Arai, Y.; Tomita, R.; Koike, T.; Akita, M., Highly Regio- and Diastereoselective Synthesis of CF<sub>3</sub>-Substituted Lactones via Photoredox-Catalyzed Carbolactonization of Alkenoic Acids. *Org Lett* **2014**, *16* (3), 780-783.
124. Noto, N.; Miyazawa, K.; Koike, T.; Akita, M., Anti-Diastereoselective Synthesis of CF<sub>3</sub>-Containing Spirooxazolines and Spirooxazines via Regiospecific Trifluoromethylative Spirocyclization by Photoredox Catalysis. *Org Lett* **2015**, *17* (15), 3710-3713.
125. Yasu, Y.; Koike, T.; Akita, M., Intermolecular Aminotrifluoromethylation of Alkenes by Visible-Light-Driven Photoredox Catalysis. *Org Lett* **2013**, *15* (9), 2136-2139.
126. Noto, N.; Koike, T.; Akita, M., Diastereoselective Synthesis of CF<sub>3</sub>- and CF<sub>2</sub>H-Substituted Spiroethers from Aryl-Fused Cycloalkenylalkanols by Photoredox Catalysis. *J Org Chem* **2016**, *81* (16), 7064-7071.
127. Tomita, R.; Yasu, Y.; Koike, T.; Akita, M., Combining Photoredox-Catalyzed Trifluoromethylation and Oxidation with DMSO: Facile Synthesis of alpha-Trifluoromethylated Ketones from Aromatic Alkenes. *Angew Chem Int Edit* **2014**, *53* (28), 7144-7148.
128. Yasu, Y.; Koike, T.; Akita, M., Visible-light-induced synthesis of a variety of trifluoromethylated alkenes from potassium vinyltrifluoroborates by photoredox catalysis. *Chem Commun* **2013**, *49* (20), 2037-2039.
129. Tomita, R.; Yasu, Y.; Koike, T.; Akita, M., Direct C-H trifluoromethylation of di- and trisubstituted alkenes by photoredox catalysis. *Beilstein J Org Chem* **2014**, *10*, 1099-1106.

130. Tomita, R.; Koike, T.; Akita, M., Photoredox-Catalyzed Stereoselective Conversion of Alkynes into Tetrasubstituted Trifluoromethylated Alkenes. *Angew Chem Int Edit* **2015**, *54* (44), 12923-12927.
131. Ischay, M. A.; Anzovino, M. E.; Du, J.; Yoon, T. P., Efficient visible light photocatalysis of [2+2] enone cycloadditions. *J Am Chem Soc* **2008**, *130* (39), 12886-+.
132. Zhao, G. L.; Yang, C.; Guo, L.; Sun, H. N.; Lin, R.; Xia, W. J., Reactivity Insight into Reductive Coupling and Aldol Cyclization of Chalcones by Visible Light Photocatalysis. *J Org Chem* **2012**, *77* (14), 6302-6306.
133. Tarantino, K. T.; Liu, P.; Knowles, R. R., Catalytic Ketyl-Olefin Cyclizations Enabled by Proton-Coupled Electron Transfer. *J Am Chem Soc* **2013**, *135* (27), 10022-10025.
134. Du, J. N.; Espelt, L. R.; Guzei, I. A.; Yoon, T. P., Photocatalytic reductive cyclizations of enones: Divergent reactivity of photogenerated radical and radical anion intermediates. *Chem Sci* **2011**, *2* (11), 2115-2119.
135. Lu, Z.; Shen, M. H.; Yoon, T. P., [3+2] Cycloadditions of Aryl Cyclopropyl Ketones by Visible Light Photocatalysis. *J Am Chem Soc* **2011**, *133* (5), 1162-1164.
136. Hurtley, A. E.; Cismesia, M. A.; Ischay, M. A.; Yoon, T. R., Visible light photocatalysis of radical anion hetero-Diels-Alder cycloadditions. *Tetrahedron* **2011**, *67* (24), 4442-4448.
137. Du, J. N.; Skubi, K. L.; Schultz, D. M.; Yoon, T. P., A Dual-Catalysis Approach to Enantioselective [2+2] Photocycloadditions Using Visible Light. *Science* **2014**, *344* (6182), 392-396.
138. Amador, A. G.; Sherbrook, E. M.; Yoon, T. P., Enantioselective Photocatalytic [3+2] Cycloadditions of Aryl Cyclopropyl Ketones. *J Am Chem Soc* **2016**, *138* (14), 4722-4725.
139. Espelt, L. R.; McPherson, I. S.; Wiensch, E. M.; Yoon, T. P., Enantioselective Conjugate Additions of  $\alpha$ -Amino Radicals via Cooperative Photoredox and Lewis Acid Catalysis. *J Am Chem Soc* **2015**, *137* (7), 2452-2455.
140. Nakajima, K.; Miyake, Y.; Nishibayashi, Y., Synthetic Utilization of  $\alpha$ -Aminoalkyl Radicals and Related Species in Visible Light Photoredox Catalysis. *Accounts Chem Res* **2016**, *49* (9), 1946-1956.

141. Kohls, P.; Jadhav, D.; Pandey, G.; Reiser, O., Visible Light Photoredox Catalysis: Generation and Addition of N-Aryltetrahydroisoquinoline-Derived  $\alpha$ -Amino Radicals to Michael Acceptors. *Org Lett* **2012**, *14* (3), 672-675.
142. Miyake, Y.; Nakajima, K.; Nishibayashi, Y., Visible-Light-Mediated Utilization of  $\alpha$ -Aminoalkyl Radicals: Addition to Electron-Deficient Alkenes Using Photoredox Catalysts. *J Am Chem Soc* **2012**, *134* (7), 3338-3341.
143. Zhu, S. Q.; Das, A.; Bui, L.; Zhou, H. J.; Curran, D. P.; Rueping, M., Oxygen Switch in Visible-Light Photoredox Catalysis: Radical Additions and Cyclizations and Unexpected C-C-Bond Cleavage Reactions. *J Am Chem Soc* **2013**, *135* (5), 1823-1829.
144. Espelt, L. R.; Wiensch, E. M.; Yoon, T. P., Bronsted Acid Cocatalysts in Photocatalytic Radical Addition of  $\alpha$ -Amino C-H Bonds across Michael Acceptors. *J Org Chem* **2013**, *78* (8), 4107-4114.
145. Dai, X. J.; Cheng, D. P.; Guan, B. C.; Mao, W. J.; Xu, X. L.; Li, X. N., The Coupling of Tertiary Amines with Acrylate Derivatives via Visible-Light Photoredox Catalysis. *J Org Chem* **2014**, *79* (15), 7212-7219.
146. Dai, X. J.; Mao, R. J.; Guan, B. C.; Xu, X. L.; Li, X. N., Visible light photoredox catalysis: regioselective radical addition of aminoalkyl radicals to 2,3-allenoates. *Rsc Adv* **2015**, *5* (68), 55290-55294.
147. Hepburn, H. B.; Melchiorre, P., Bronsted acid-catalysed conjugate addition of photochemically generated  $\alpha$ -amino radicals to alkenylpyridines. *Chem Commun* **2016**, *52* (17), 3520-3523.
148. Yoon, U. C.; Mariano, P. S., Mechanistic and Synthetic Aspects of Amine Enone Single Electron-Transfer Photochemistry. *Accounts Chem Res* **1992**, *25* (5), 233-240.
149. Cho, D. W.; Yoon, U. C.; Mariano, P. S., Studies Leading to the Development of a Single-Electron Transfer (SET) Photochemical Strategy for Syntheses of Macrocyclic Polyethers, Polythioethers, and Polyamides. *Accounts Chem Res* **2011**, *44* (3), 204-215.
150. Miyake, Y.; Ashida, Y.; Nakajima, K.; Nishibayashi, Y., Visible-light-mediated addition of  $\alpha$ -aminoalkyl radicals generated from  $\alpha$ -silylamines to  $\alpha,\beta$ -unsaturated carbonyl compounds. *Chem Commun* **2012**, *48* (55), 6966-6968.



151. Nakajima, K.; Kitagawa, M.; Ashida, Y.; Miyake, Y.; Nishibayashi, Y., Synthesis of nitrogen heterocycles via alpha-aminoalkyl radicals generated from alpha-silyl secondary amines under visible light irradiation. *Chem Commun* **2014**, 50 (64), 8900-8903.
152. Lenhart, D.; Bauer, A.; Pothig, A.; Bach, T., Enantioselective Visible-Light-Induced Radical-Addition Reactions to 3-Alkylidene Indolin-2-ones. *Chem-Eur J* **2016**, 22 (19), 6519-6523.
153. Chu, L. L.; Ohta, C.; Zuo, Z. W.; MacMillan, D. W. C., Carboxylic Acids as A Traceless Activation Group for Conjugate Additions: A Three-Step Synthesis of (+/-)-Pregabalin. *J Am Chem Soc* **2014**, 136 (31), 10886-10889.
154. Miyake, Y.; Nakajima, K.; Nishibayashi, Y., Direct  $sp^3$  C-H Amination of Nitrogen-Containing Benzoheterocycles Mediated by Visible-Light-Photoredox Catalysts. *Chem-Eur J* **2012**, 18 (51), 16473-16477.
155. Zhou, H. X.; Lu, P.; Gu, X. Y.; Li, P. X., Visible-Light-Mediated Nucleophilic Addition of an alpha-Aminoalkyl Radical to Isocyanate or Isothiocyanate. *Org Lett* **2013**, 15 (22), 5646-5649.
156. Uraguchi, D.; Kinoshita, N.; Kizu, T.; Ooi, T., Synergistic Catalysis of Ionic Bronsted Acid and Photosensitizer for a Redox Neutral Asymmetric alpha-Coupling of N-Arylaminoethanes with Aldimines. *J Am Chem Soc* **2015**, 137 (43), 13768-13771.
157. Fava, E.; Millet, A.; Nakajima, M.; Loescher, S.; Rueping, M., Reductive Umpolung of Carbonyl Derivatives with Visible-Light Photoredox Catalysis: Direct Access to Vicinal Diamines and Amino Alcohols via alpha-Amino Radicals and Ketyl Radicals. *Angew Chem Int Edit* **2016**, 55 (23), 6775-6778.
158. Wang, C. Y.; Qin, J.; Shen, X. D.; Riedel, R.; Harms, K.; Meggers, E., Asymmetric Radical-Radical Cross-Coupling through Visible-Light-Activated Iridium Catalysis. *Angew Chem Int Edit* **2016**, 55 (2), 685-688.
159. Miyazawa, K.; Koike, T.; Akita, M., Hydroaminomethylation of Olefins with Aminomethyltrifluoroborate by Photoredox Catalysis. *Adv Synth Catal* **2014**, 356 (13), 2749-2755.
160. Ju, X. H.; Li, D. J.; Li, W. F.; Yu, W.; Bian, F. L., The Reaction of Tertiary Anilines with Maleimides under Visible Light Redox Catalysis. *Adv Synth Catal* **2012**, 354 (18), 3561-3567.

161. Lenhart, D.; Bach, T., Visible-light-induced, Ir-catalyzed reactions of N-methyl-N-((trimethylsilyl)methyl) aniline with cyclic  $\alpha,\beta$ -unsaturated carbonyl compounds. *Beilstein J Org Chem* **2014**, *10*, 890-896.
162. Liang, Z. W.; Xu, S.; Tian, W. Y.; Zhang, R. H., Eosin Y-catalyzed visible-light-mediated aerobic oxidative cyclization of N,N-dimethylanilines with maleimides. *Beilstein J Org Chem* **2015**, *11*, 425-430.
163. Lowry, M. S.; Goldsmith, J. I.; Slinker, J. D.; Rohl, R.; Pascal, R. A.; Malliaras, G. G.; Bernhard, S., Single-layer electroluminescent devices and photoinduced hydrogen production from an ionic iridium(III) complex. *Chem Mater* **2005**, *17* (23), 5712-5719.
164. Miyake, Y.; Nakajima, K.; Nishibayashi, Y., Visible light-mediated oxidative decarboxylation of arylacetic acids into benzyl radicals: addition to electron-deficient alkenes by using photoredox catalysts. *Chem Commun* **2013**, *49* (71), 7854-7856.
165. Lang, S. B.; O'Nele, K. M.; Tunge, J. A., Decarboxylative Allylation of Amino Alkanoic Acids and Esters via Dual Catalysis. *J Am Chem Soc* **2014**, *136* (39), 13606-13609.
166. McNally, A.; Prier, C. K.; MacMillan, D. W. C., Discovery of an  $\alpha$ -Amino C-H Arylation Reaction Using the Strategy of Accelerated Serendipity. *Science* **2011**, *334* (6059), 1114-1117.
167. Zuo, Z. W.; MacMillan, D. W. C., Decarboxylative Arylation of  $\alpha$ -Amino Acids via Photoredox Catalysis: A One-Step Conversion of Biomass to Drug Pharmacophore. *J Am Chem Soc* **2014**, *136* (14), 5257-5260.
168. Zuo, Z. W.; Gong, H.; Li, W.; Choi, J.; Fu, G. C.; MacMillan, D. W. C., Enantioselective Decarboxylative Arylation of  $\alpha$ -Amino Acids via the Merger of Photoredox and Nickel Catalysis. *J Am Chem Soc* **2016**, *138* (6), 1832-1835.
169. Noble, A.; MacMillan, D. W. C., Photoredox  $\alpha$ -Vinylolation of  $\alpha$ -Amino Acids and N-Aryl Amines. *J Am Chem Soc* **2014**, *136* (33), 11602-11605.
170. Ventre, S.; Petronijevic, F. R.; MacMillan, D. W. C., Decarboxylative Fluorination of Aliphatic Carboxylic Acids via Photoredox Catalysis. *J Am Chem Soc* **2015**, *137* (17), 5654-5657.
171. Johnston, C. P.; Smith, R. T.; Allmendinger, S.; MacMillan, D. W. C., Metallaphotoredox-catalysed  $sp^3$ - $sp^3$  cross-coupling of carboxylic acids with alkyl halides. *Nature* **2016**, *536* (7616), 322-325.

172. Noble, A.; McCarver, S. J.; MacMillan, D. W. C., Merging Photoredox and Nickel Catalysis: Decarboxylative Cross-Coupling of Carboxylic Acids with Vinyl Halides. *J Am Chem Soc* **2015**, *137* (2), 624-627.
173. Nawrat, C. C.; Jamison, C. R.; Slutskyy, Y.; MacMillan, D. W. C.; Overman, L. E., Oxalates as Activating Groups for Alcohols in Visible Light Photoredox Catalysis: Formation of Quaternary Centers by Redox-Neutral Fragment Coupling. *J Am Chem Soc* **2015**, *137* (35), 11270-11273.
174. Chu, L. L.; Lipshultz, J. M.; MacMillan, D. W. C., Merging Photoredox and Nickel Catalysis: The Direct Synthesis of Ketones by the Decarboxylative Arylation of  $\alpha$ -Oxo Acids. *Angew Chem Int Edit* **2015**, *54* (27), 7929-7933.
175. Zhang, X. H.; MacMillan, D. W. C., Alcohols as Latent Coupling Fragments for Metallaphotoredox Catalysis:  $sp^3$ - $sp^2$  Cross-Coupling of Oxalates with Aryl Halides. *J Am Chem Soc* **2016**, *138* (42), 13862-13865.
176. Roth, H. G.; Romero, N. A.; Nicewicz, D. A., Experimental and Calculated Electrochemical Potentials of Common Organic Molecules for Applications to Single-Electron Redox Chemistry. *Synlett* **2016**, *27* (5), 714-723.
177. Hamilton, D. S.; Nicewicz, D. A., Direct Catalytic Anti-Markovnikov Hydroetherification of Alkenols. *J Am Chem Soc* **2012**, *134* (45), 18577-18580.
178. Nguyen, T. M.; Nicewicz, D. A., Anti-Markovnikov Hydroamination of Alkenes Catalyzed by an Organic Photoredox System. *J Am Chem Soc* **2013**, *135* (26), 9588-9591.
179. Morse, P. D.; Nicewicz, D. A., Divergent regioselectivity in photoredox-catalyzed hydrofunctionalization reactions of unsaturated amides and thioamides. *Chem Sci* **2015**, *6* (1), 270-274.
180. Wilger, D. J.; Grandjean, J. M. M.; Lammert, T. R.; Nicewicz, D. A., The direct anti-Markovnikov addition of mineral acids to styrenes. *Nat Chem* **2014**, *6* (8), 720-726.
181. Romero, N. A.; Nicewicz, D. A., Mechanistic Insight into the Photoredox Catalysis of Anti-Markovnikov Alkene Hydrofunctionalization Reactions. *J Am Chem Soc* **2014**, *136* (49), 17024-17035.
182. Niimi, K.; Shinamura, S.; Osaka, I.; Miyazaki, E.; Takimiya, K., Dianthra[2,3-b:2'3'-f]thieno[3,2-b]thiophene (DATF): Synthesis, Characterization, and FET Characteristics of New pi-

- Extended Heteroarene with Eight Fused Aromatic Rings. *J Am Chem Soc* **2011**, *133* (22), 8732-8739.
183. Havinga, E. E.; Tenhoeve, W.; Wynberg, H., A New Class of Small Band-Gap Organic Polymer Conductors. *Polym Bull* **1992**, *29* (1-2), 119-126.
184. Bundgaard, E.; Krebs, F. C., Low band gap polymers for organic photovoltaics. *Sol. Energ. Mat. Sol. Cells* **2007**, *91* (11), 954-985.
185. Brocks, G.; Tol, A., Small band gap semiconducting polymers made from dye molecules: Polysquaraines. *J Phys Chem-Us* **1996**, *100* (5), 1838-1846.
186. Newman, C. R.; Frisbie, C. D.; da Silva, D. A.; Bredas, J. L.; Ewbank, P. C.; Mann, K. R., Introduction to organic thin film transistors and design of n-channel organic semiconductors. *Chem Mater* **2004**, *16* (23), 4436-4451.
187. Zhang, J. S.; Zhang, G. G.; Chen, X. F.; Lin, S.; Mohlmann, L.; Dolega, G.; Lipner, G.; Antonietti, M.; Blechert, S.; Wang, X. C., Co-Monomer Control of Carbon Nitride Semiconductors to Optimize Hydrogen Evolution with Visible Light. *Angew Chem Int Edit* **2012**, *51* (13), 3183-3187.
188. Mei, J. G.; Diao, Y.; Appleton, A. L.; Fang, L.; Bao, Z. N., Integrated Materials Design of Organic Semiconductors for Field-Effect Transistors. *J Am Chem Soc* **2013**, *135* (18), 6724-6746.
189. Cheng, Y. J.; Yang, S. H.; Hsu, C. S., Synthesis of Conjugated Polymers for Organic Solar Cell Applications. *Chem Rev* **2009**, *109* (11), 5868-5923.
190. Li, C.; Liu, M. Y.; Pschirer, N. G.; Baumgarten, M.; Mullen, K., Polyphenylene-Based Materials for Organic Photovoltaics. *Chem Rev* **2010**, *110* (11), 6817-6855.
191. Huang, Y.; Kramer, E. J.; Heeger, A. J.; Bazan, G. C., Bulk Heterojunction Solar Cells: Morphology and Performance Relationships. *Chem Rev* **2014**, *114* (14), 7006-7043.
192. Grimsdale, A. C.; Chan, K. L.; Martin, R. E.; Jokisz, P. G.; Holmes, A. B., Synthesis of Light-Emitting Conjugated Polymers for Applications in Electroluminescent Devices. *Chem Rev* **2009**, *109* (3), 897-1091.
193. Wang, C. L.; Dong, H. L.; Hu, W. P.; Liu, Y. Q.; Zhu, D. B., Semiconducting pi-Conjugated Systems in Field-Effect Transistors: A Material Odyssey of Organic Electronics. *Chem Rev* **2012**, *112* (4), 2208-2267.

194. Cuthbertson, J. D.; MacMillan, D. W. C., The direct arylation of allylic sp<sup>3</sup> C-H bonds via organic and photoredox catalysis. *Nature* **2015**, *519* (7541), 74-77.
195. Tyson, E. L.; Ament, M. S.; Yoon, T. P., Transition Metal Photoredox Catalysis of Radical Thiol-Ene Reactions. *J Org Chem* **2013**, *78* (5), 2046-2050.
196. Nicewicz, D. A.; MacMillan, D. W. C., Merging photoredox catalysis with organocatalysis: The direct asymmetric alkylation of aldehydes. *Science* **2008**, *322* (5898), 77-80.
197. Ohkubo, K.; Mizushima, K.; Iwata, R.; Souma, K.; Suzuki, N.; Fukuzumi, S., Simultaneous production of p-tolualdehyde and hydrogen peroxide in photocatalytic oxygenation of p-xylene and reduction of oxygen with 9-mesityl-10-methylacridinium ion derivatives. *Chem Commun* **2010**, *46* (4), 601-603.
198. Li, R.; Wang, Z. J.; Wang, L.; Ma, B. C.; Ghasimi, S.; Lu, H.; Landfester, K.; Zhang, K. A. I., Photocatalytic Selective Bromination of Electron-Rich Aromatic Compounds Using Microporous Organic Polymers with Visible Light. *Acs Catal* **2016**, *6* (2), 1113-1121.
199. Furst, L.; Matsuura, B. S.; Narayanam, J. M. R.; Tucker, J. W.; Stephenson, C. R. J., Visible Light-Mediated Intermolecular C-H Functionalization of Electron-Rich Heterocycles with Malonates. *Org Lett* **2010**, *12* (13), 3104-3107.
200. Belletete, M.; Mazerolle, L.; Desrosiers, N.; Leclerc, M.; Durocher, G., Spectroscopy and Photophysics of Some Oligomers and Polymers Derived from Thiophenes. *Macromolecules* **1995**, *28* (25), 8587-8597.
201. Kawai, T.; Sakata, T., Conversion of Carbohydrate into Hydrogen Fuel by a Photocatalytic Process. *Nature* **1980**, *286* (5772), 474-476.
202. Wang, X. C.; Maeda, K.; Thomas, A.; Takanabe, K.; Xin, G.; Carlsson, J. M.; Domen, K.; Antonietti, M., A metal-free polymeric photocatalyst for hydrogen production from water under visible light. *Nat Mater* **2009**, *8* (1), 76-80.
203. Schneider, J.; Bahnemann, D. W., Undesired Role of Sacrificial Reagents in Photocatalysis. *J Phys Chem Lett* **2013**, *4* (20), 3479-3483.
204. Wang, L.; Huang, W.; Li, R.; Gehrig, D.; Blom, P. W. M.; Landfester, K.; Zhang, K. A. I., Structural Design Principle of Small-Molecule Organic Semiconductors for Metal-Free, Visible-Light-Promoted Photocatalysis. *Angew Chem Int Edit* **2016**, *55* (33), 9783-9787.

205. Romero, N. A.; Nicewicz, D. A., Organic Photoredox Catalysis. *Chem Rev* **2016**, *116* (17), 10075-10166.
206. Zhang, K.; Kopetzki, D.; Seeberger, P. H.; Antonietti, M.; Vilela, F., Surface Area Control and Photocatalytic Activity of Conjugated Microporous Poly(benzothiadiazole) Networks. *Angew Chem Int Edit* **2013**, *52* (5), 1432-1436.
207. Kang, N.; Park, J. H.; Ko, K. C.; Chun, J.; Kim, E.; Shin, H. W.; Lee, S. M.; Kim, H. J.; Ahn, T. K.; Lee, J. Y.; Son, S. U., Tandem Synthesis of Photoactive Benzodifuran Moieties in the Formation of Microporous Organic Networks. *Angew Chem Int Edit* **2013**, *52* (24), 6228-6232.
208. Zhang, K.; Vobecka, Z.; Tauer, K.; Antonietti, M.; Vilela, F., pi-Conjugated polyHIPEs as highly efficient and reusable heterogeneous photosensitizers. *Chem Commun* **2013**, *49* (95), 11158-11160.
209. Sprick, R. S.; Jiang, J. X.; Bonillo, B.; Ren, S. J.; Ratvijitvech, T.; Guiglion, P.; Zwijnenburg, M. A.; Adams, D. J.; Cooper, A. I., Tunable Organic Photocatalysts for Visible-Light-Driven Hydrogen Evolution. *J Am Chem Soc* **2015**, *137* (9), 3265-3270.
210. Ghasimi, S.; Prescher, S.; Wang, Z. J.; Landfester, K.; Yuan, J. Y.; Zhang, K. A. I., Heterophase Photocatalysts from Water-Soluble Conjugated Polyelectrolytes: An Example of Self-Initiation under Visible Light. *Angew Chem Int Edit* **2015**, *54* (48), 14549-14553.
211. Yang, C.; Ma, B. C.; Zhang, L. Z.; Lin, S.; Ghasimi, S.; Landfester, K.; Zhang, K. A. I.; Wang, X. C., Molecular Engineering of Conjugated Polybenzothiadiazoles for Enhanced Hydrogen Production by Photosynthesis. *Angew Chem Int Edit* **2016**, *55* (32), 9202-9206.
212. Sprick, R. S.; Bonillo, B.; Clowes, R.; Guiglion, P.; Brownbill, N. J.; Slater, B. J.; Blanc, F.; Zwijnenburg, M. A.; Adams, D. J.; Cooper, A. I., Visible-Light-Driven Hydrogen Evolution Using Planarized Conjugated Polymer Photocatalysts. *Angew Chem Int Edit* **2016**, *55* (5), 1824-1828.
213. Zhang, G. G.; Lan, Z. A.; Wang, X. C., Conjugated Polymers: Catalysts for Photocatalytic Hydrogen Evolution. *Angew Chem Int Edit* **2016**, *55* (51), 15712-15727.
214. Brimiouille, R.; Lenhart, D.; Maturi, M. M.; Bach, T., Enantioselective Catalysis of Photochemical Reactions. *Angew Chem Int Edit* **2015**, *54* (13), 3872-3890.
215. Heeger, A. J., 25th Anniversary Article: Bulk Heterojunction Solar Cells: Understanding the Mechanism of Operation. *Adv Mater* **2014**, *26* (1), 10-28.

216. Dennler, G.; Scharber, M. C.; Brabec, C. J., Polymer-Fullerene Bulk-Heterojunction Solar Cells. *Adv Mater* **2009**, *21* (13), 1323-1338.
217. Lu, L. Y.; Zheng, T. Y.; Wu, Q. H.; Schneider, A. M.; Zhao, D. L.; Yu, L. P., Recent Advances in Bulk Heterojunction Polymer Solar Cells. *Chem Rev* **2015**, *115* (23), 12666-12731.
218. Scharber, M. C.; Sariciftci, N. S., Efficiency of bulk-heterojunction organic solar cells. *Prog Polym Sci* **2013**, *38* (12), 1929-1940.
219. Seechurn, C. C. C. J.; Kitching, M. O.; Colacot, T. J.; Snieckus, V., Palladium-Catalyzed Cross-Coupling: A Historical Contextual Perspective to the 2010 Nobel Prize. *Angew Chem Int Edit* **2012**, *51* (21), 5062-5085.
220. Ackermann, L., Carboxylate-Assisted Transition-Metal-Catalyzed C-H Bond Functionalizations: Mechanism and Scope. *Chem Rev* **2011**, *111* (3), 1315-1345.
221. Mercier, L. G.; Leclerc, M., Direct (Hetero)Arylation: A New Tool for Polymer Chemists. *Accounts Chem Res* **2013**, *46* (7), 1597-1605.
222. Schultz, D. M.; Yoon, T. P., Solar Synthesis: Prospects in Visible Light Photocatalysis. *Science* **2014**, *343* (6174), 985-+.
223. Xuan, J.; Xiao, W. J., Visible-Light Photoredox Catalysis. *Angew Chem Int Edit* **2012**, *51* (28), 6828-6838.
224. Yoon, T. P.; Ischay, M. A.; Du, J. N., Visible light photocatalysis as a greener approach to photochemical synthesis. *Nat Chem* **2010**, *2* (7), 527-532.
225. Hari, D. P.; Konig, B., The Photocatalyzed Meerwein Arylation: Classic Reaction of Aryl Diazonium Salts in a New Light. *Angew Chem Int Edit* **2013**, *52* (18), 4734-4743.
226. Jin, J.; MacMillan, D. W. C., Alcohols as alkylating agents in heteroarene C-H functionalization. *Nature* **2015**, *525* (7567), 87-90.
227. Yoon, T. P., Visible Light Photocatalysis: The Development of Photocatalytic Radical Ion Cycloadditions. *Acs Catal* **2013**, *3* (5), 895-902.
228. Meyer, A. U.; Slanina, T.; Yao, C. J.; Konig, B., Metal-Free Perfluoroarylation by Visible Light Photoredox Catalysis. *Acs Catal* **2016**, *6* (1), 369-375.

229. Wang, L.; Huang, W.; Li, R.; Gehrig, D.; Blom, P. W.; Landfester, K.; Zhang, K. A., Structural Design Principle of Small-Molecule Organic Semiconductors for Metal-Free, Visible-Light-Promoted Photocatalysis. *Angew. Chem. Int. Ed.* **2016**, *55* (33), 9783-7.
230. Dai, C.; Meschini, F.; Narayanam, J. M. R.; Stephenson, C. R. J., Friedel-Crafts Amidoalkylation via Thermolysis and Oxidative Photocatalysis. *J Org Chem* **2012**, *77* (9), 4425-4431.
231. Ouchi, M.; Terashima, T.; Sawamoto, M., Transition Metal-Catalyzed Living Radical Polymerization: Toward Perfection in Catalysis and Precision Polymer Synthesis. *Chem Rev* **2009**, *109* (11), 4963-5050.
232. Kamigaito, M.; Ando, T.; Sawamoto, M., Metal-catalyzed living radical polymerization. *Chem Rev* **2001**, *101* (12), 3689-3745.
233. Matyjaszewski, K.; Xia, J. H., Atom transfer radical polymerization. *Chem Rev* **2001**, *101* (9), 2921-2990.
234. Tsarevsky, N. V.; Matyjaszewski, K., "Green" atom transfer radical polymerization: From process design to preparation of well-defined environmentally friendly polymeric materials. *Chem Rev* **2007**, *107* (6), 2270-2299.
235. Hawker, C. J.; Bosman, A. W.; Harth, E., New polymer synthesis by nitroxide mediated living radical polymerizations. *Chem Rev* **2001**, *101* (12), 3661-3688.
236. Barner-Kowollik, C.; Davis, T. P.; Heuts, J. P. A.; Stenzel, M. H.; Vana, P.; Whittaker, M., RAFTing down under: Tales of missing radicals, fancy architectures, and mysterious holes. *J Polym Sci Pol Chem* **2003**, *41* (3), 365-375.
237. Perrier, S.; Takolpuckdee, P., Macromolecular design via reversible addition-fragmentation chain transfer (RAFT)/Xanthates (MADIX) polymerization. *J Polym Sci Pol Chem* **2005**, *43* (22), 5347-5393.
238. Sciannamea, V.; Jerome, R.; Detrembleur, C., In-situ nitroxide-mediated radical polymerization (NMP) processes: Their understanding and optimization. *Chem Rev* **2008**, *108* (3), 1104-1126.
239. Matyjaszewski, K., Atom Transfer Radical Polymerization (ATRP): Current Status and Future Perspectives. *Macromolecules* **2012**, *45* (10), 4015-4039.



240. Corrigan, N.; Shanmugam, S.; Xu, J. T.; Boyer, C., Photocatalysis in organic and polymer synthesis. *Chem Soc Rev* **2016**, 45 (22), 6165-6212.
241. Fors, B. P.; Hawker, C. J., Control of a Living Radical Polymerization of Methacrylates by Light. *Angew Chem Int Edit* **2012**, 51 (35), 8850-8853.
242. Treat, N. J.; Fors, B. P.; Kramer, J. W.; Christianson, M.; Chiu, C. Y.; de Alaniz, J. R.; Hawker, C. J., Controlled Radical Polymerization of Acrylates Regulated by Visible Light. *Acs Macro Lett* **2014**, 3 (6), 580-584.
243. Liu, X. D.; Zhang, L. F.; Cheng, Z. P.; Zhu, X. L., Metal-free photoinduced electron transfer-atom transfer radical polymerization (PET-ATRP) via a visible light organic photocatalyst. *Polym Chem-Uk* **2016**, 7 (3), 689-700.
244. Barner-Kowollik, C.; Davis, T. P.; Stenzel, M. H., Probing mechanistic features of conventional, catalytic and living free radical polymerizations using soft ionization mass spectrometric techniques. *Polymer* **2004**, 45 (23), 7791-7805.
245. Kim, J.-H.; Kim, H. U.; Song, C. E.; Kang, I.-N.; Lee, J.-K.; Shin, W. S.; Hwang, D.-H., Benzotriazole-based donor-acceptor type semiconducting polymers with different alkyl side chains for photovoltaic devices. *Sol. Energ. Mat. Sol. Cells* **2013**, 108, 113-125.
246. Lei, Y.; Li, H.; Gao, W.; Liu, M.; Chen, J.; Ding, J.; Huang, X.; Wu, H., Highly sensitive conjugated polymer fluorescent sensors based on benzochalcogendiazole for nickel ions in real-time detection. *J. Mater. Chem. C* **2014**, 2, 7402-7410.

## 10 List of Related Publications

Lei Wang, Wei Huang, Run Li, Dominik Gehrig, Paul W. M. Blom, Katharina Landfester, and Kai A. I. Zhang, "Structural Design Principle of Small-Molecule Organic Semiconductors for Metal-Free, Visible-Light-Promoted Photocatalysis", *Angew. Chem. Int. Ed.*, 2016, 55, 9783 –9787.

Run Li, Zi Jun Wang, Lei Wang, Beatriz Chiyin Ma, Saman Ghasimi, Hao Lu, Katharina Landfester, and Kai. A. I. Zhang\*, "Photocatalytic Selective Bromination of Electron-Rich Aromatic

Compounds Using Microporous Organic Polymers with Visible Light”, **ACS Catal.**, 2016, 6, 1113–1121.

Run Li, Beatriz Chiyin Ma, Wei Huang, Lei Wang, Di Wang, Hao Lu, Katharina Landfester, and Kai A. I. Zhang\*, “Photocatalytic Regioselective and Stereoselective [2 + 2] Cycloaddition of Styrene Derivatives Using a Heterogeneous Organic Photocatalyst”, **ACS Catal.**, 2017, 7, 3097–3101.

Wei Huang, Beatriz Chiyin Ma, Di Wang, Zi Jun Wang, Run Li, Lei Wang, Katharina Landfester and Kai A. I. Zhang\*, “A fixed-bed photoreactor using conjugated nanoporous polymer-coated glass fibers for visible light-promoted continuous photoredox reactions”, **J. Mater. Chem. A**, 2017, 5, 3792–3797.

Wei Huang, Beatriz Chiyin Ma, Hao Lu, Run Li, Lei Wang, Katharina Landfester, and Kai A. I. Zhang\*, “Visible Light-Promoted Selective Oxidation of Alcohols Using a Covalent Triazine Framework”, **ACS Catal.**, 2017, 7, 5438–5442.